Four–Terminal Perovskite–CIGS Tandem Solar Cells with Improved Near–Infrared Response

Zur Erlangung des akademischen Grades eines

DOKTOR-INGENIEURS

von der KIT–Fakultät für
Elektrotechnik und Informationstechnik
des Karlsruher Instituts für Technologie (KIT)

genehmigte

DISSERTATION

von

M.Sc. Moritz Schultes

geb. in Pinneberg

Erklärung

Moritz Schultes
Gallusstr. 41
70569 Stuttgart

Ich versichere wahrheitsgemäß, die Dissertation bis auf die dort angegebene Hilfe selbständig angefertigt, alle benutzten Hilfsmittel vollständig und genau angegeben und alles kenntlich gemacht zu haben, was aus Arbeiten anderer und eigenen Veröffentlichungen unverändert oder mit Änderungen entnommen wurde.
Hiermit bestätige ich, dass die eingereichte elektronische und gedruckte Version meiner Dissertation mit der vom KIT nach Maßgabe der einschlägigen Promotionsordnung genehmigten Fassung in Form und Inhalt übereinstimmt.

Karlsruhe, 22.04.2020

Unterschrift

Abstract

Perovskite-CIGS tandem solar cells are promising candidates for next-generation photovoltaic applications due to their potential power conversion efficiency beyond 30 %. One limitation of the efficiency is unfavourable parasitic absorption of low energetic light in the electrode layers. This dissertation focuses on the development of highly efficient semitransparent perovskite solar cells with minimized parasitic absorption and their combination with CIGS solar cells into stacked tandem devices.

In the progress, opaque perovskite solar cells are efficiency-optimized by implementation of an additional fullerene-based electron transport layer. A new nanoparticle based method for improving the layer formation is designed to support the fabrication.

Suitable transparent electrode layers of hydrogen-doped indium oxide (IO:H) and indium zinc oxide (IZO) are developed by sputter deposition under addition of oxygen or hydrogen as reactive gas components. Especially the reduction of the NIR-absorption by post deposition crystallization of amorphous IO:H films proves to be advantageous for the application in tandems.

Semitransparent perovskite solar cells that are equipped with these electrode layers achieve high efficiencies of over 15 % while the average NIR-transmittance of the device is increased from 55 % to 75 % compared to commercial electrode materials such as indium tin oxide (ITO).

In a tandem setup the CIGS bottom cell profits from the increased transmittance of the top cell and a combined tandem efficiency of 23.0 % is demonstrated on an active area of $0.5\,cm^2$. The simulation based analysis of the optical loss mechanisms of different tandem cells shows that the contribution of the electrodes to the total parasitic absorption is reduced from 60 % to 40 %.

Zusammenfassung

Perowskit-CIGS-Tandem-Solarzellen zeigen großes Potenzial Wirkungsgrade von über 30 % zu erreichen und damit die Kommerzialisierung der Dünnschicht-Photovoltaik zu revolutionieren. Parasitäre Verlustmechanismen wie etwa eine unerwünschte Absorption von langwelligem Licht in den Kontaktschichten limitieren jedoch die maximale Effizienz der Tandem-Solarzellen. Diese Dissertation beschäftigt sich mit der Entwicklung hocheffizienter, semitransparenter Perowskitsolarzellen, der Minimierung parasitärer Verluste in deren Kontaktschichten und mit der Herstellung von gestapelten Tandem-Solarzellen mit CIGS als Partnerzelle.

Dafür wird zunächst die Effizienz von opaken Perowskitsolarzellen durch die Implementierung einer zusätzlichen Fulleren-basierten Elektronenleiterschicht optimiert, was durch die Entwicklung eines neuartigen Nanopartikel-basierten Verfahrens zur Verbesserung der Benetzbarkeit unterstützt wird.

Die Entwicklung spezieller transparenter Kontaktschichten aus Wasserstoff-dotiertem Indiumoxid (IO:H) und Indiumzinkoxid (IZO) erfolgt durch Kathodenzerstäubung unter variabler Zugabe von Sauerstoff- bzw. Wasserstoffgas. Die nachträgliche Kristallisation von amorphem IO:H führt zu besonders niedrigen Absorptionseigenschaften im nahen Infrarotbereich, was für die Anwendung in Tandem-Solarzellen von entscheidendem Vorteil ist.

Semitransparente Perowskitzellen, die mit diesen Kontakten ausgestattet sind, erreichen hohe Effizienzen von über 15 % und ermöglichen eine Steigerung der mittleren Zell-Transmission von 55 % auf 75 % verglichen mit kommerziellen Kontaktschichten wie Indiumzinnoxid (ITO).

Durch diese Transmissionssteigerung werden Tandem-Solarzellen realisiert, die eine gemeinsame Zellfläche von 0.5 cm^2 und einen verbesserten Wirkungsgrad von bis zu 23.0 % aufweisen. Die Analyse der optischen Verlustmechanismen der verschiedenen Tandem-Solarzellen mittels Simulations-gestützter Methoden zeigt unter anderem auf, dass der Beitrag der Kontaktschichten zu den parasitären Gesamtabsorptionsverlusten von ca. 60 % auf 40 % gesenkt werden kann.

Preface

Vorweg bedanke ich mich dei denen, die mir auf diesem Weg geholfen haben.

Michael Powalla, Achim Hartschuh, Erik Ahlswede, Tim Helder, Jonas Hanisch, Tina Wahl, Meltem Aygüler, Thomas Schnabel, Cordula Wessendorf, Daniela Müller, Julia Zillner, Johannes Küffner, allen Kollegen aus der GIGS Abteilung, allen anderen Kollegen auf deren Unterstützung ich zählen konnte, allen Kooperationspartnern und Freunden an der LMU und am KIT.

Ich bedanke mich ausserdem bei meinen Eltern, die mir diesen Weg eröffnet haben.

Ich bedanke mich vor allem bei Julia und Theda, die mich auf diesem Weg begleitet haben.

Ich bedanke mich zuletzt bei meiner Schwester, die mich auf allen Wegen ermuntert.

List of contents

Symbols and Abbreviations

Abbreviations

2T	two-terminal
4P	four-point-probe
4T	four-terminal
a-**IO:H**	amorphous hydrogenated indium oxide
Al$_2$O$_3$-NP	aluminium oxide nanoparticle
AM1.5	AM1.5G solar spectrum
Ar	argon
ARF	anti reflection foil
ARC	anti reflection coating
BCP	conductive copper complex (2,9-Dimethyl-4,7-diphenyl-1,10-phenanthroline (bathocuproine))
C$_{60}$–SAM	C$_{60}$-based self-assembled monolayer (4-(1',5'-Dihydro-1'methyl-2'H-[5,6]fullereno-C$_{60}$-I$_h$-[1,9-c]pyrrol-2'-yl)benzoic acid)
CB	chlorobenzene
CdS	cadmium sulfide
CIGS	copper indium gallium diselenide (CuIn$_x$Ga$_{1-x}$Se$_2$)
CIGS$_a$	CIGS cell with E_g = 1.1 eV
CIGS$_b$	CIGS cell with E_g = 1.0 eV
CLSM	confocal laser scanning microscopy
CsI	caesium iodide
CsFAMAPIBr	mixed ionic perovskite (Cs$_{0.05}$(FA$_{0.83}$MA$_{0.17}$)$_{0.95}$Pb(I$_{0.83}$Br$_{0.17}$)$_3$)
c-SnO$_2$	compact tin oxide
c-TiO$_2$	compact titanium oxide
DC	direct current

DCB	dichlorobenzene
DMF	dimethylformamide
DMSO	dimethylsulfoxide
EBPVD	electron-beam physical vapor deposition
EDOT-Amide-TPA	conductive amide (N^5, N^7-bis(4-(bis(4-methoxyphenyl)amino)phenyl)-2,3-dihydrothieno[3,4-b][1,4]dioxine-5,7-dicarboxamide)
ETL	electron transport layer
EQE	external quantum efficiency
FA$^+$	formamidinium $((NH_2-CH=NH_2)^+)$
FAI	formamidinium iodide
FCA	free carrier absorption
FF	fill factor
FIB	focused ion beam
FTO	fluorine doped tin oxide
fwd	forward
FWHM	full width at half maximum
FWHM$_{inst}$	instrumental diffraction peak broadening
FWHM$_{struct}$	structural diffraction peak broadening
GBL	γ–butyrolactone
GDOES	glow discharge optical emission spectroscopy
GGI	gallium to indium ratio ([Ga]/([Ga] + [In]))
GIXRD	grazing incidence x-ray diffraction
H$_2$	hydrogen
H$_2$O	water
HTL	hole transport layer
i-ZnO	intrinsic zinc oxide
IV	current–voltage dependency
IMEC	Interuniversity Microelectronics Centre
In$_2$O$_3$	indium oxide
IO:H	hydrogen-doped indium oxide

IOOH	indium oxide hydroxide
IPA	isopropanol
ITO	indium tin oxide
IZO	indium zinc oxide $((In_2O_3)_{0.9}(ZnO)_{0.1})$
JV	current-density–voltage dependency
KIT	Karlsruher Institut für Technologie
LMU	Ludwig-Maximilian-Universität München
MA⁺	methylammonium $((CH_3-NH_3)^+)$
MABr	methylammonium bromide
MAI	methylammonium iodide
MAPI	$MAPbI_3$
MgF₂	magnesium fluoride
Mo	molybdenum
MoO₃	molybdenum oxide
MPP	maximum power point
n-i-p	n-type–intrinsic–p-type
NIR	near-infrared
NP	nanoparticle
O₂	oxygen
PCBM	C_{61} fullerene derivate ([6,6]-phenyl-C_{61}-butyric acid methyl ester)
PCE	power conversion efficiency at standard test conditions
PCE_f	power conversion efficiency under a filtered AM1.5G spectrum
PCE_MPP	power conversion efficiency at steady state conditions
PCE_Sim	power conversion efficiency obtained from single diode model simulation
PDC	post-deposition-crystallisation
PDC–IO:H	post-deposition-crystallised hydrogenated indium oxide
PbBr₂	lead bromide
PbI₂	lead iodide
PET	polyethylene terephthalate

p-i-n	p-type–intrinsic–n-type
PMMA	poly(methyl methacrylate)
PSC	perovskite solar cell
PSC$_a$	perovskite solar cell with PDC-IO:H front electrode
PSC$_b$	perovskite solar cell with ITO front electrode
PTAA	conductive polyamine (poly[bis(4-phenyl)(2,4,6-trimethylphenyl)amine])
PV	photovoltaic
PVD	physical vapor deposition
RbCsFAPbIBr	wide band gap perovskite ($Rb_{0.05}Cs_{0.17}FA_{0.78}Pb(I_{0.60}Br_{0.40})_3$)
RF	radio frequency
rvs	reverse
RMS	root mean square
SC	spin coating
SCAPS	SCAPS simulation software
SE	spectroscopic ellipsometry
SEM	scanning electron microscopy
SiO$_2$	silicon oxide
SiO$_2$-NP	silicon oxide nanoparticle
SnO$_2$	tin oxide
SnO$_2$-NP	tin oxide nanoparticle
Spiro-OMeTAD	conductive fluorene (2,2',7,7'-Tetrakis[N,N-di(4-methoxyphenyl)amino]-9,9'-spirobifluorene)
STEM	scanning transmission electron microscopy
TCO	transparent conductive oxide
TiO$_2$	titanium oxide
TLD	through-lens-detector
TMM	transfer matrix method
UHV	ultra high vacuum
UV	ultra violet

UV/Vis	ultra violet to visible
WBG	wide band gap
XRD	x-ray diffraction
XRR	x-ray reflectometry
ZAO	aluminium doped zinc oxide $Zn_xAl_{1-x}O$
ZMO	zinc magnesium oxide $Zn_xMg_{1-x}O$
ZSW	Zentrum für Sonnenenergie- und Wasserstoff-Forschung Baden-Württemberg

Constants

π	Circle constant $(3{,}14159\ldots)$
h	Planck constant $(6.626\,070\,15 \times 10^{-34}\,\text{J s})$
k	Boltzmann constant $(1.380\,649 \times 10^{-23}\,\text{J K}^{-1})$
m_0	electron resting mass $(9.109\,383\,701\,5 \times 10^{-31}\,\text{kg})$
q	elementary charge $(1.602\,176\,634 \times 10^{-34}\,\text{C})$

Latin Variables

Minuscule

d	film thickness (nm)
f_{rot}	rotational frequency (s^{-1})
$h\nu$	photon energy (eV)
$k(\lambda)$	imaginary part of the complex refractive index or extinction coefficient
m_e^*	effective electron mass
N	complex refractive index
n	diode ideality factor
$n(\lambda)$	real part of the complex refractive index or phase velocity

Capital

A	absorptance (%)
A_{act}	active area (cm^2)

A_{wt}	weighted average absorptance (%)
E_g	band gap (eV)
F_{HYS}	hysteresis factor (%)
I_{PH}	photocurrent (mA)
J	current density (mA cm^{-2})
J_0	reverse saturation current density (mA cm^{-2})
J_{Abs}	current density equivalent of the parasitic absorption loss (mA cm^{-2})
J_{EQE}	photo current density obtained by EQE measurement (mA cm^{-2})
J_{ph}	photo current density (mA cm^{-2})
J_{Rec}	current density equivalent of the recombination loss (mA cm^{-2})
J_{Ref}	current density equivalent of the reflection loss (mA cm^{-2})
J_{SC}	short circuit current density (mA cm^{-2})
J_{Sim}	photo current density obtained by EQE simulation (mA cm^{-2})
J_{Trn}	current density equivalent of the transmission (mA cm^{-2})
N_e	electron density (cm^{-3})
qN_{ph}	current density equivalent of the photon flux (mA cm^{-2})
R	reflectance (%)
R^2	coefficient of determination
R_a	arithmetic average roughness (nm)
R_p	parallel resistance (kΩ)
R_s	series resistance (Ω)
R_{sq}	sheet resistance ($\Omega_\square$)
T	transmittance (%)
T_f	transmittance after the fundamental absorption edge (%)
T_d	thickness factor
T_{wt}	weighted average transmittance (%)
V	voltage (V)
V_{OC}	open circuit voltage (mV)

Greek Variables

α	absorption coefficient (cm^{-1})
λ	wavelength (nm)
ϵ	microstrain (%)
$\epsilon_{\mathbf{wt}}$	weighted microstrain (%)
μ	charge carrier mobility ($\text{cm}^2\,\text{V}^{-1}\text{s}^{-1}$)
$\mu_{\mathbf{att}}$	linear attenuation coefficient (cm^{-1})
τ	penetration depth (nm)
$\overline{\tau}$	relaxation time (s)
ω	incident angle (°)
$\omega_{\mathbf{c}}$	critical angle (°)
ρ	resistivity ($\Omega\,\text{cm}$)
2θ	diffracted angle (°)

1   Introduction

Photovoltaics play a central role in the transition from fossil to renewable energy. The sun is the most significant source of energy that provides a constant supply to planet earth. In order to exploit solar energy, more efficient and cost-effective photovoltaic (PV) devices are required. Additionally, new PV technologies are desired that provide more versatile functionalities e.g. for building integration, mobile applications, curved surfaces, or individual shapes, colours and form factors.

In contrast to silicon PV technology, two thin-film technologies with a certificated power conversion efficiency (PCE) above 23 % could allow cost-effective, lightweight and potentially flexible all-thin-film devices to meet the new demands of the future: perovskite solar cells (PSCs) and copper indium gallium diselenide (CIGS) solar cells. Their power conversion efficiency can surpass the single-junction Shockley-Queisser limit [1], by combining the two thin-film materials together in a tandem configuration [2].

Perovskite solar cells are especially suitable for use in tandem cells, stacked on top of a CIGS bottom cell, because their band gap is naturally quite wide. Consequently, the absorption range of the material is restricted to the higher energetic wavelengths and a large fraction of the sunlight transmits to the CIGS tandem partner. Moreover, the band gaps of both thin-film materials are easily tunable by variations of the composition, which allows engineering the absorption ranges of both subcells in order to achieve maximum power output. The wide band gaps of efficient PSCs can be adjusted in between 1.6 eV to 1.8 eV [3], while the band gap of CIGS can be narrowed down to ≈ 1.0 eV [4, 5] to maximize the absorption range.

Highly efficient perovskite–CIGS tandem cells have already been reported for mechanically stacked, four-terminal (4T) architectures (25.9 %) [6] or monolithic, two-terminal (2T) architectures (22.4 %) [7], demonstrating their great potential.

Although it is an ongoing debate whether the 4T or 2T architecture will be the most efficient, cost-effective and reliable solution in the future [8–12], these tandem architectures share a joint restriction: They are limited in their efficiency by parasitic near-infrared (NIR) absorption within the perovskite top cell. It ideally collects all light within its absorption range, typically up to 700 nm or 800 nm, while the CIGS bottom cell uses the transmitted near-infrared (NIR) light. Hence, any parasitic absorption in the layers of the top cell leads to a direct decline of the power generated by the bottom cell. The electrodes of the top cell often cause the largest contribution to the NIR absorption.

Reducing the parasitic absorption in the transparent electrodes is most challenging since they have to be both an electrical conductor and optical transmitter. Commercial transparent conductive oxides (TCOs) such as fluorine doped tin oxide (FTO) or indium tin oxide (ITO) are prominently used for single-junction perovskite cells. Given their high free carrier density, they have excellent conductivity, but also high free carrier absorption in NIR, which makes them unfavourable for tandem solar cells.

Advanced TCOs such as hydrogen-doped indium oxide (IO:H) and indium zinc oxide (IZO) provide the possibility to achieve a much lower NIR absorption due to their low charge carrier density, which is compensated by their exceptionally high electron mobility that simultaneously allows for high conductivity. Especially annealed IO:H promises suitable properties with a reported charge carrier density range from $1.1 \times 10^{20}\,\mathrm{cm}^{-3}$ to $2.1 \times 10^{20}\,\mathrm{cm}^{-3}$ and a charge carrier mobility range from $80\,\mathrm{cm}^2\,\mathrm{V}^{-1}\mathrm{s}^{-1}$ to $140\,\mathrm{cm}^2\,\mathrm{V}^{-1}\mathrm{s}^{-1}$ [13–16]. Although these TCOs have already been reported in previous perovskite-based tandem architectures [2, 17, 18], this research aims to develop a more detailed understanding of the parasitic absorption mechanisms in semitransparent PSCs and the complete tandem setup.

Compared to single-junction devices, the evaluation of the losses becomes increasingly difficult in tandem solar cells because of the high number of layers. Computed simulations are needed to determine the parasitic absorption of each layer, but the simulation itself requires precise input data from supplementary measurements to generate a correct model of the optical properties of the complete architecture. Such modelling capabilities are the basis for a systematic future development of tandem cells.

An additional concern regarding the development of tandem cells is that previous studies often estimated the 4T tandem efficiency by adding the efficiency values of small-area semitransparent perovskite cells on $\approx 0.1\,\mathrm{cm}^2$ with those of larger bottom cells $>0.5\,\mathrm{cm}^2$. In that case, the CIGS bottom cell is covered by a filter that shall represent the optical response of a large-area perovskite top solar cell [2, 19, 20]. However, this is a very idealized scenario that disregards realistic losses from which the tandem setup would suffer when the PSC area is large enough to match the bottom cell size. On the one hand, the power conversion efficiency of the PSC would be reduced, mainly because of the lateral conductive resistance of the TCO electrodes, but also due to the challenges to produce high-quality devices on a larger area with the usual solution-based deposition techniques. On the other hand, metal grids would likely be implemented to improve current transport in the electrodes — a standard for other solar cell technologies. A grid causes an additional shadow cast on the bottom cell leading to a reduced current generation, an effect which is not accounted for in a filter-based estimation.

In order to overcome the above-mentioned challenges, the tasks of this dissertation formulate as follows:

- Development of efficient PSCs

- Optimization of highly transparent IO:H and IZO electrodes

- Implementation of the transparent electrodes into PSCs

- Increasing the cell size of the PSC to $0.5\,\mathrm{cm}^2$

- Fabrication of 4T tandem cells with matching cell sizes and integrated metal grids

- Modelling and analysis of the loss mechanisms in tandem cells

Breaking down the single tasks to different subtopics generates the outline of this thesis. After discussing the necessary theoretical background for this study in Chapter 2 and presenting the methodological approaches in Chapter 3, Chapter 4 evaluates the results of the development of the PSC top cell, followed by the investigation of the tandem solar cells in Chapter 5.

The strategy chart in Figure 1.1 illustrates how the development of the tandem device is organized throughout the Chapters 4 and 5 with the corresponding subsections.
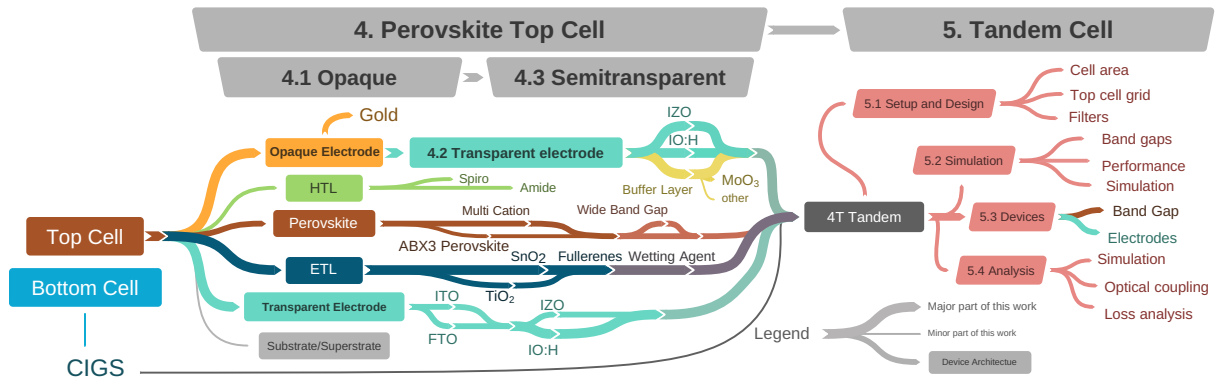

Figure 1.1: Strategy for developing a perovskite–CIGS based 4T tandem cell with the respective chapter numeration.

From left to right, following the coloured branches of the top cell to Section 4.1 'opaque', reveals the schematic device architecture of the PSC. Here, the fundamental components such as the transparent electrode, the selective electron transport layer and the perovskite itself are evaluated based on opaque PSC with gold electrodes. The thickness of branches indicates how intensely the research focuses on the development of the corresponding subtopics, which are labelled along the branch at key positions. Consequently, Section 4.1 concentrates on the interactions of the perovskite absorber layer with different electron transport materials and ITO or FTO front electrodes.

Coming from the opaque rear electrode, Section 4.2 'transparent electrode' denotes a separate subtopic, where the sputter deposition of IO:H and IZO electrodes to replace the gold electrode is discussed. A highlight of the topic is a profound evaluation of the crystallization of IO:H with x-ray diffractive methods.

In Section 4.3 'semitransparent cell' the newly developed transparent electrodes are introduced into the solar cell architecture, not only as a replacement for gold but also for ITO and FTO front electrodes. Here, the focus is on increasing the overall transmittance of the PSC and achieving high PCEs.

The implementation of the semitransparent into a tandem architecture with CIGS is part of Chapter 5, which divides into four subtopics. Section 5.1 discusses important design aspects regarding the cell size increase and application of a grid in the PSC. Furthermore, it evaluates the possible errors caused by the usage of filters instead of areal PSC device for tandem efficiency measurements.

An efficient method for simulating the theoretical efficiency of CIGS bottom cells is presented in Section 5.2 'simulation', using fictional transmittance spectra from the semitransparent PSC and the diode parameters of the CIGS cells as input data. This represents a reliable and quick method for screening and predicting possible tandem PCEs, without the necessity for time-consuming measurements.

Section 5.3 'devices' evaluates the performance of actual tandem setups comprising different PSC top cells and CIGS bottom cells. As a highlight, a champion tandem cell with 23.0 % PCE on $0.5\,cm^2$ is presented.

The optical and electronic properties of the tandem cells are investigated with a detailed current loss analysis in the last Section 5.4 'analysis'. The analysis follows a transfer matrix method (TMM) approach in which an optical model comprising all optical functions of the individual layers of the architecture is created, in order to track the loss mechanisms of the tandem cell. This method demonstrates how large the impact of the new highly transmissive IO:H and IZO electrodes is compared to a standard electrode like conventional ITO. Furthermore, the findings address the most relevant remaining losses in the other layers, which can be targeted in future development steps. Following the discussion for further improvements, the application of immersion oil as an optical coupling material between the PSC and the CIGS cell is tested, and the impact of PSC top cells with an optimized, higher band gap and close-to-perfect NIR transmission is estimated.

Chapter 6 concludes this dissertation with a summarizing of the most relevant results.

2 Basics of perovskite- and tandem solar cells

This chapter gives an overview on the specific theories and recent progress in research related to the topics that are of concern for this thesis. After introducing perovskites as photovoltaic absorbers and discussing their relevant features and challenges in Section 2.1, a brief introduction on tandem solar cells is given in Section 2.2, focusing on 4T perovskite–CIGS tandems. Subsequently, Section 2.3 introduces the relevant aspects of the functionality and deposition of TCOs, specifically IO:H and IZO. Section 2.4 refers to the special optical properties of the multilayer structures of tandem solar cells and Section 2.5 is dedicated to specified features of x-ray diffraction (XRD) for strain analysis in thin films.

2.1 Perovskite solar cells

The following sections explain, why the perovskite material is a highly promising absorber material for PV, introduce the architectural concept of PSCs and evaluate reasons for the occurrence of current-voltage hysteresis.

2.1.1 Perovskites as photovoltaic absorbers

Originally, Gustav Rose gave the name 'Perovskite' to the novel mineral calcium titanate $(CaTiO_3)$ in the year 1839, honouring the Russian mineralogist Lev Perovski [21]. Since then, the nomenclature has been used for materials that exhibit the same crystal structure ABX_3.

The organic-inorganic perovskite material, that is of interest in this study, first emerged in 1978 [22] and the first perovskite solar cell was published in 2009 [23].

The cubic structure of ABX_3 perovskite is shown in Figure 2.1, but depending on the tilt of the central octahedron, the crystal may exhibit a lower orthorhombic or tetragonal symmetry. This reversible phase change depends on external parameters such as temperature and pressure, but also on the ionic radii of the compounds.
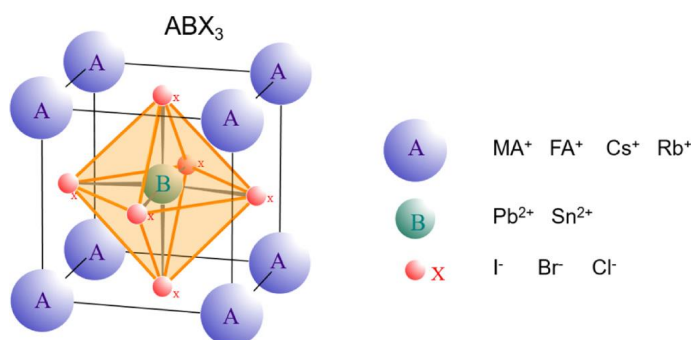

Figure 2.1: ABX_3 perovskite structure with possible ions for each side, adapted from Powalla et al. [24]

The most commonly used compounds for photovoltaic applications are methylammonium (MA^+)[1] at site A, lead (Pb^{2+}) at site B and iodine (I^-) at site X, resulting in the final formulation of $MAPbI_3$ (MAPI) with reported band gaps around 1.55 to 1.6 eV [24]. The basic features that make MAPI a good absorber material for photovoltaic application are

- a high absorption coefficient over 1.5×10^4 cm^{-1} [25],

- a low exciton binding energy below 30 meV [141] [26, 27],

- high diffusion lengths over 1 µm [28, 29],

- long carrier lifetimes over 1 µs [30],

- and high carrier mobilities of 10 to 40 cm^2 V^{-1}s^{-1} [31].

A partial replacement of the ions opens up a wide field of mixed ion perovskites, which brings several advantages. On one hand, the band gap of the material is easily tunable with the replacement of the X site cation (e.g. with Sn^{2+}) or the B site anion (e.g. Br^- or Cl^-) or the A site (e.g. formamidinium (FA^+)[2], Cs^+ or Rb^+), which makes the perovskites fascinating for tandem application. On the other hand, an increased level of mixing different anions and cations proved beneficial effects on the stability, reproducibility and overall efficiency of the perovskite material. [32] This study comprises the simple MAPI approach, as well as the prominent mixed ionic perovskite $(CsFAMAPIBr)$[3], as introduced by Saliba et al. [33].

2.1.2 Perovskite solar cell architectures

The principle setup of a planar perovskite solar cell, how it is used in this study, consists of the perovskite absorber itself, a hole transport layer (HTL) and an electron transport layer (ETL) for charge carrier separation and contact layers for charge carrier extraction. Figure 2.2 demonstrates the working principle of the solar cell with selective contacts as proposed by Peter Würfel [34].

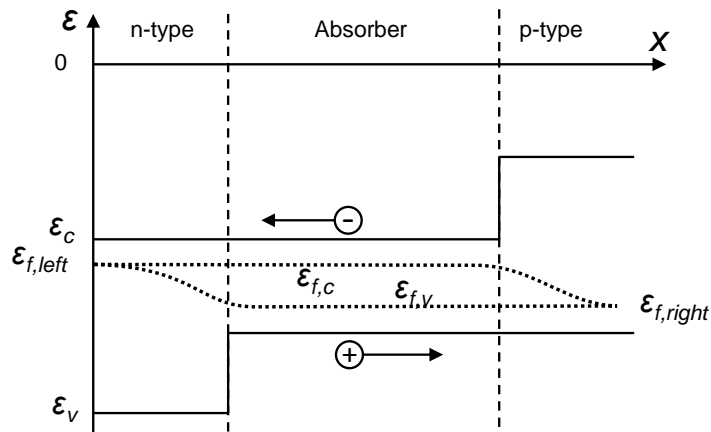Figure 2.2: Illustration after Würfel [34] showing a setup for extraction of electrons and holes with the use of n-type and p-type selective membranes (ETL and HTL). Because of the barriers introduced by the selective layers, the charges are effectively separated to the different contacts on both sides.

---

[1] $(CH_3-NH_3)^+$

[2] $(NH_2-CH=NH_2)^+$

[3] $Cs_{0.5}(FA_{0.83}MA_{0.17})_{0.95}Pb(I_{0.83}Br_{0.17})_3$

All common PSCs facilitate a transparent superstrate (e.g. glass) coated with a transparent front electrode, such as a TCO. The superstrate usually represents the illuminated side of the solar cell. The sequence of the following layers is used for distinction of two main sub architectures of PSCs, because the polarity of the selective contacts decides, whether the architecture exhibits a n-type–intrinsic–p-type (n-i-p) or p-type–intrinsic–n-type (p-i-n) character. A sequence of front electrode/ETL/perovskite/HTL/rear electrode is historically labelled as the 'standard' architecture. Consequently, the inverse order front/HTL/perovskite/ETL/rear is labelled 'inverted'. Figure 2.3 depicts the schematic layer stacks of both architectures.

Figure 2.3: Different architectures of perovskite solar cells in a) standard and b) inverted architecture.

The opaque metal rear electrode can be modified to create semitransparent cells by substituting the corresponding opaque metal contact layers with transparent alternatives. Herein especially traditional TCO materials are used like ITO and FTO [24]. Alternatives are IZO, IO:H (which are investigated in this work) and TCO double layers like ITO/IO:H as well [24].

Current record efficiencies of semitransparent PSCs are reported by Shen et al. with 18.1 % stabilized power conversion for a band gap of 1.62 eV and 16.0 % for an increased band gap of 1.75 eV [2].

The standard architecture comprises typically organic HTL materials such as a conductive fluorene (Spiro-OMeTAD)[4] or a conductive polyamine (PTAA)[5], which are sensitive to high temperatures and high energy ions as they occur in a plasma during a sputtering process. To protect these underlying layers in standard architecture from sputter damage, often a second protective HTL such as molybdenum oxide (MoO_3) is evaporated before a sputtering process [35,36]. Without MoO_3, charge extraction would be strongly inhibited after sputtering, resulting in a strong S-shape in the current-voltage characteristics. The damaging of Spiro-OMeTAD during sputtering is a well known phenomenon, which leads to a Schottky type barrier at the Spiro-OMeTAD/TCO interface. [37] After all, MoO_3 is a suitable choice for a protective buffer layer, because the valence band level of thin MoO_3 layers align well with Spiro-OMeTAD, which has proven for an effective hole extraction [38–40].

---

[4] 2,2',7,7'-Tetrakis[N,N-di(4-methoxyphenyl)amino]-9,9'-spirobifluorene
[5] poly[bis(4-phenyl)(2,4,6-trimethylphenyl)amine]

For inverted architecture common used ETL materials on top of the cell stack are for example a combination of a C_{61} fullerene derivate (PCBM)[6] and a conductive copper complex (BCP)[7], where damage can be healed by annealing [144].

Generally, a great variety of materials is available for the application as HTL and ETL. Figure 2.4 shows the energy band levels of a selection of the most important ones. In the present work, the ETLs are predominantly represented by tin oxide (SnO_2), titanium oxide (TiO_2) and PCBM, whereas the HTLs is restricted to Spiro-OMeTAD and MoO_3.
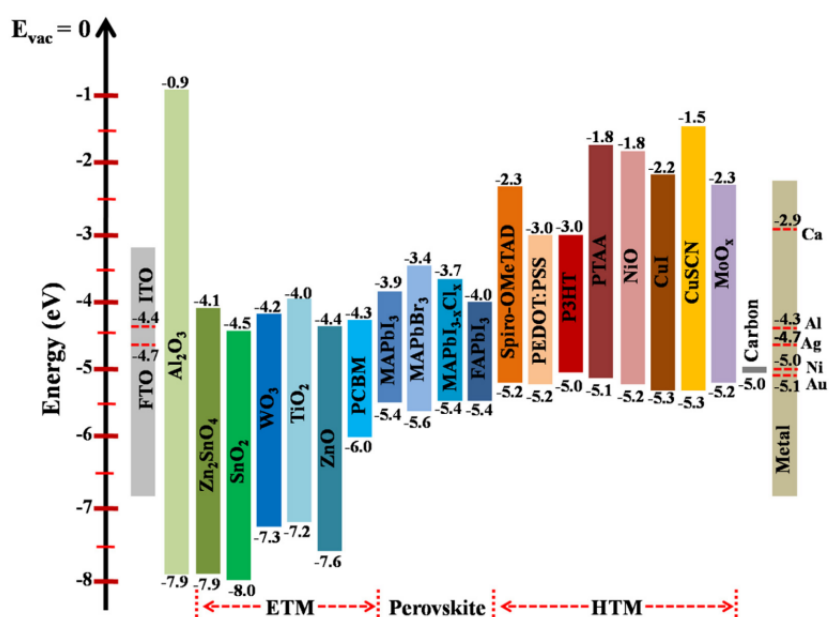
Figure 2.4: Original graphic from Ye et al. [41] showing the band alignment of different materials.

The sheer number of possible combinations of layer sequences point out, how much improvement potential there is by just focusing on interface engineering and architectural design. To discuss this in detail would be beyond the scope of this work. The interested reader may be referred to some comprehensive review papers for the different topics:

- Perovskite precursor chemistry [42, 43]

- Interfaces and energy band alignment [41, 44, 45]

- Stability and degradation [46]

---

[6] [6,6]-phenyl-C_{61}-butyric acid methyl ester
[7] 2,9-Dimethyl-4,7-diphenyl-1,10-phenanthroline (bathocuproine)

2.1.3 Current–voltage hysteresis due to ion displacement

Already in early stages of the development of PSCs researchers noticed something peculiar about the devices: The current-density–voltage dependency (JV) scans show different responses depending on the sweep direction, scan speed and light biasing [47–49]. Figure 2.5 shows two representative examples of the hysteresis observed in this study. The main difference between the JV curves originating from the forward (*fwd*) scan and the reverse (*rvs*) scan is observed in the fill factor (FF) as demonstrated in Figure 2.5a, but also the open circuit voltage (V_{OC}) may be affected as shown in b.

	rvs	fwd
PCE (%)	12.0	4.5
FF (%)	62.3	**23.6**
V_{OC} (mV)	1070	1059
J_{SC} (mA cm^{-2})	18.0	17.8
F_{HYS} (%)	**62.2**	

	rvs	fwd
PCE (%)	15.8	9.8
FF (%)	73.6	**60.0**
V_{OC} (mV)	1136	**866**
J_{SC} (mA cm^{-2})	18.8	18.9
F_{HYS} (%)	**38.0**	
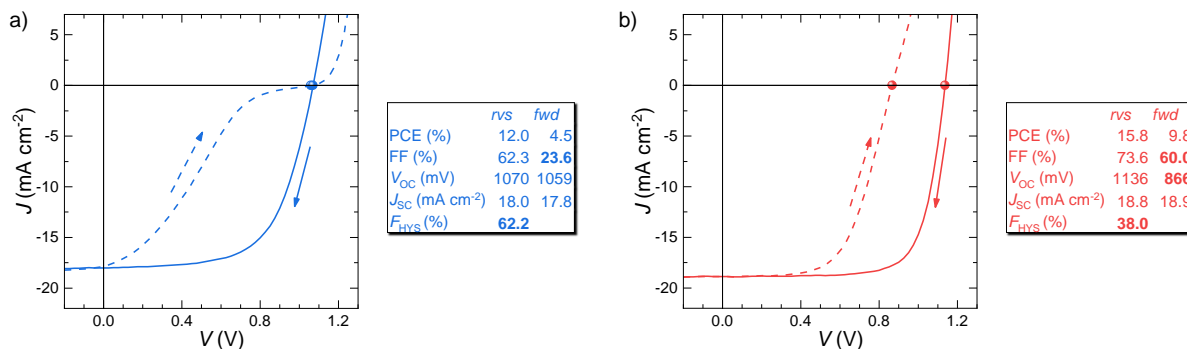
Figure 2.5: Representative examples of JV responses of two PSCs that exhibit strong hysteresis between the forward and reverse scan direction as indicated by arrows. In a) the hysteresis mainly affects the FF, whereas in b) FF and V_{OC} are affected.

Since the discovery, there is a continuing tremendous effort to understand the origin of the hysteresis. A broad consensus claims that the hysteresis is mainly the result of mobile ions and their vacancies in the perovskite structure. Several review papers have been published over the last years, giving a very detailed insight over the different approaches to study and overcome the hysteresis [50–52].

Figure 2.6 explains schematically how mobile ions in the perovskite accumulate at the interfaces and hinder the charge extraction and injection by screening the contact potential in a fast *fwd* scan.
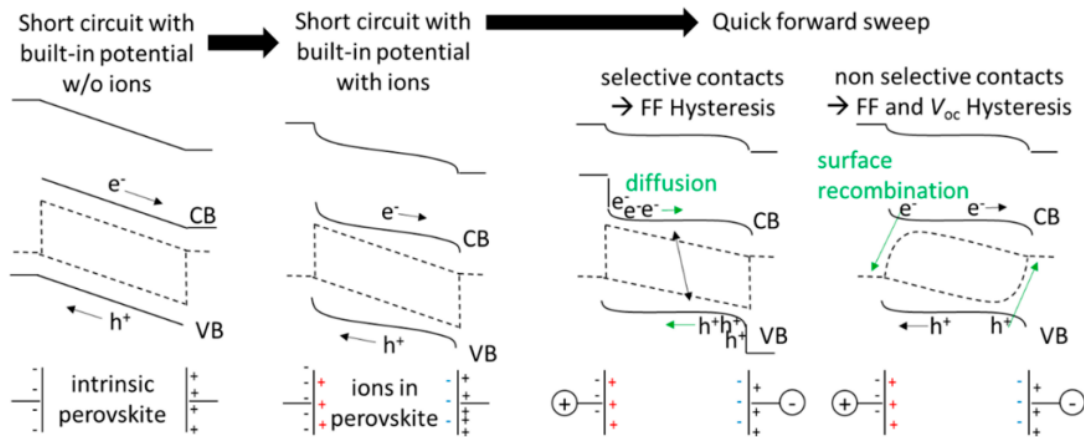
Figure 2.6: Original Figure from Tress et al. [51] showing different hypothetical states of the simplest energy band alignment of a PSC under illumination. The quasi-Fermi levels are indicated as dashed lines and the solid lines mark the valence band (VB) and conduction band (CB) edges, ions are marked with coloured + and − signs, electrons and holes by e⁻ and h⁺. From left to right: The built-in electric field under short circuit conditions; Mobile ions accumulate at the interfaces, resulting in band bending; Accumulations remain when a forward bias is quickly applied, thus screening the electrodes and slowing charge extraction to diffusive speeds; non-selective interfaces or recombination centres enhance surface recombination.

The movement and accumulation of ionic charges at the interfaces with the ETL and HTL effectively means a huge modification of the interface. Depending on the nature of the materials, the energy band alignment and the morphology, the presence of ions or vacancies may introduce severe defects such as trap states or recombination centres and the like. This also explains, why the modification of the interfaces has a high impact on the observed hysteresis. The full complexity of the coupled interdependence of the parameters has been represented in an excellent way in a graphic by Wolfang Tress in Figure 2.7 [51].

For this study, the modification of the ETL interface by fullerene derivates is of the highest importance, since it was shown to reduce the density of trap states at the interface with the perovskite. [53, 54] By this, the quality of the interface improves significantly, resulting in a effective minimization of the hysteresis.
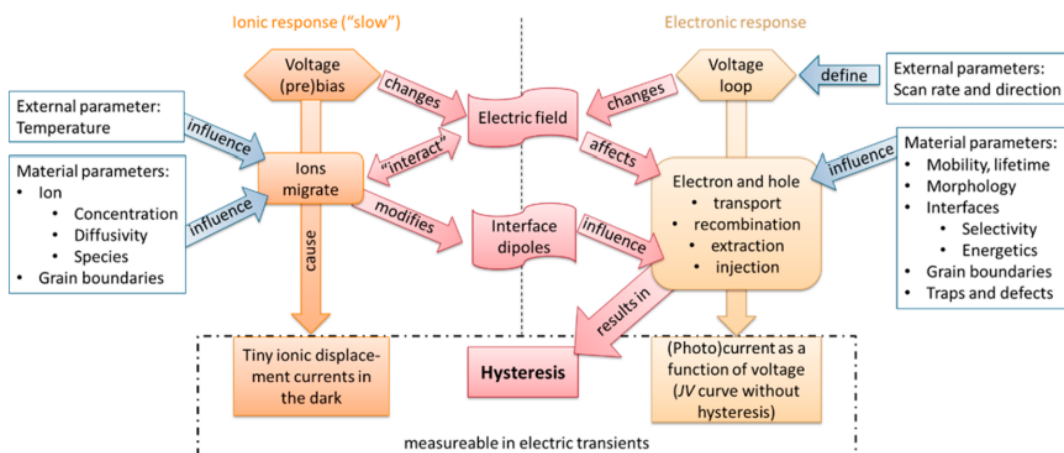

Figure 2.7: Original Figure from Tress et al. [51] indicating the complex interplay of ionic and electronic responses upon applying a voltage, which eventually cause hysteresis.

In order to quantify the hysteresis or in other words the discrepancy between *fwd* and *rvs* scan, a hysteresis factor (F_{HYS}) is introduced as following

$$F_{\text{HYS}} = \frac{\text{PCE}_{rvs} - \text{PCE}_{fwd}}{\text{PCE}_{rvs}} \tag{2.1}$$

with the PCE extracted from both scan directions, respectively. Compare also Section 3.2.2

Using the F_{HYS}, the hysteresis behaviour of different samples can be compared, under the precondition that they have been measured in the same manner. Since the measured PCE of the *JV* scan is dependent on a whole set of measurement parameters, such as scan direction, scan speed, measurement delay, pre biasing, light soaking, and even environmental conditions, the absolute PCE value of neither *fwd* nor *rvs* scan has a real quantitative meaning. [50]

A much more reliable measure of the PCE is a smart, iterative maximum power point (MPP) tracking under illumination in order to record the steady state power output from the device. From this measurement, the power conversion efficiency at steady state conditions (PCE_{MPP}) is received. In devices with a large hysteresis the steady state condition might be reached only after several tens of seconds, indicating itself a bad quality of the interface. If the device reaches the steady state condition quickly, and shows a stable power output, a close agreement of the MPP efficiency and the *JV*-based PCE value would be a strong indicator for a good interface.

2.2 Tandem solar cells

The principle of a tandem cell is the combination of a high band gap top cell with a low band gap bottom cell which absorb different parts of the solar spectrum. It is possible to classify tandem solar cells as two- or four-terminal (2T and 4T, respectively) devices. Figure 2.8 shows an example with a perovskite top cell and a CIGS bottom cell.

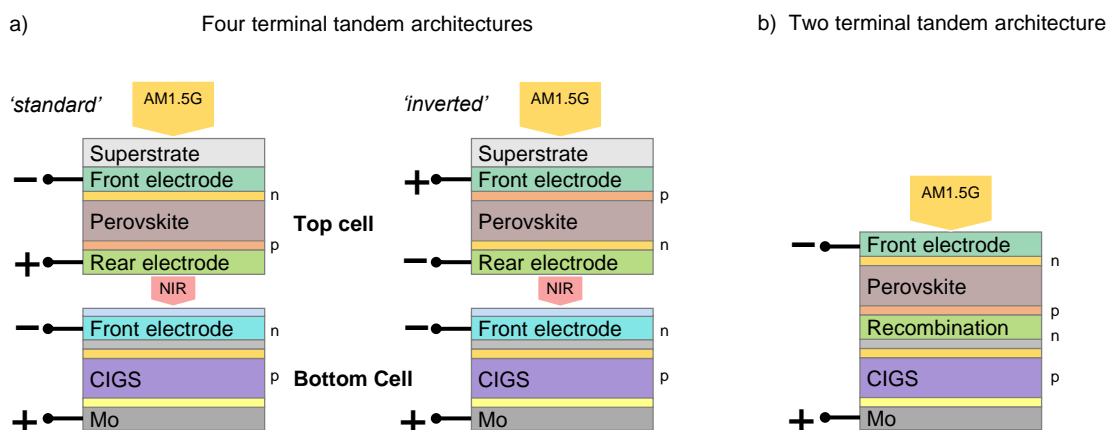Figure 2.8: Schematic illustrations of a) 4T tandem architectures comprising PSCs of the 'standard' or 'inverted' polarity and b) of a two-terminal (2T) tandem architecture.

In the 2T devices, the top cell is monolithically built on the TCO layer of the bottom cell, which is used as a recombination layer. In this configuration a current matching is essential because the sub cells are connected in series.

In the 4T tandem cell, the two devices are prepared individually and stacked mechanically. The theoretical efficiency limit for tandem devices depends on the type of stacking and the band gaps of top and bottom cell but is about 45 %. The PCE of a 4T tandem solar cell is calculated by addition of the PCE of the top cell and the PCE of the bottom cell. To distinguish the solo PCE of the bottom cell from the PCE in the tandem configuration the term power conversion efficiency under a filtered AM1.5G spectrum (PCE_f) is introduced.

Prominent partners for tandem devices with PSCs as a top cell are silicon solar cells, CIGS and low band gap PSCs. Until now, the highest efficiencies are achieved with silicon tandem devices. A prominent example for a 2T device with a silicon bottom cell is reported by Oxford PV with a certified 28 % efficiency [55]. But also with thin film CIGS very high efficiencies were reported. Shen et al. present a mechanical stacked PSC CIGS tandem device with 23.9 % efficiency [2]. An all-perovskite 4T tandem device is reported by Zhao at al. with an steady state efficiency of 22.9 % [56].

2.3 Transparent conductive oxides

In this chapter fundamentals of TCOs are discussed, which are the most widely used transparent electrodes in thin film PV technology [57]. TCO materials offer simultaneously optical transparency and electrical conductivity. The first section (2.3.1) covers the description of these properties. In Section 2.3.3 and 2.3.4 an overview of the state-of-the-art of the used materials IZO and IO:H is given, respectively.

2.3.1 Physics of transparent conductive oxides

Transparent conductive oxides TCOs are highly doped (degenerated) metal oxide semiconductors with metal like conduction but nevertheless conductivities σ two orders of magnitude lower than metals. This is due to a low carrier concentration (10×10^{20} cm^{-3}) compared to that of metals (10×10^{22} cm^{-3}) while the carrier mobility is comparable in these material systems [58]. In general the conductivity is given by:

$$\sigma = q\mu N_e = \frac{1}{\rho} \tag{2.2}$$

with the elementary charge (q) of an electron, charge carrier mobility (μ) and electron density (N_e). The inverse of the conductivity is defined as the resistivity (ρ).

According to the following equation:

$$\mu = \frac{e\overline{\tau}}{m_e^*} \tag{2.3}$$

the μ depends on the average time between two scattering events, the relaxation time ($\overline{\tau}$) and the effective electron mass (m_e^*). Determined by the band structure of the semiconductor, the values of m_e^* are fixed in the range between $0.2m_0$ and $0.3m_0$ where m_0 is the electron resting mass [57]. Thus there is only one possibility to increase μ via $\overline{\tau}$.

$\overline{\tau}$ is influenced by all scattering mechanisms that govern the electron transport in semiconductors. The main mechanisms, reducing $\overline{\tau}$ and hence μ are the following [59].

- grain boundary scattering in polycrystalline materials

- ionized impurity scattering caused by the deflection of free carriers by electrostatic fields associated with intentional dopants and defects such as interstitials and vacancies

- neutral impurity scattering caused by non-ionized impurities

- lattice vibration scattering (optical phonons)

The single scattering mechanisms are independent from each other but are strongly influenced by the carrier density. For low carrier concentrations, the mobility is mainly limited by scattering at grain boundaries. For increasing concentrations, the influence of grain boundary scattering decreases and scattering at ionized impurities becomes more severe [59].

The amount of free carrier concentration can be increased by doping of the TCO. For high doping concentrations, the Fermi level E_F shifts into the conduction band, forming a degenerated n-type semiconductor. This increase in carrier concentration has a direct influence on the optical properties of the TCO material. With the shifting of the Fermi-level into the conduction band, a beneficial widening of the optical band gap E_g is implicated. This so called Burstein-Moss effect follows the relation [60]:

$$\Delta E_g \approx N_e^{\frac{2}{3}} \tag{2.4}$$

Additionally, increasing the carrier density has a detrimental optical effect in the NIR region. From Drude theory a direct relation between N_e and the absorption coefficient (α) is given by:

$$\alpha = \frac{\lambda^2 e^3 N_e}{4\pi^2 \epsilon_0 c^3 (m_e^*)^2 \mu_{opt}} \tag{2.5}$$

with the wavelength λ, the vacuum permittivity ϵ_0 and the optical mobility μ_{opt} (which might differ from μ obtained from hall measurements). The effect of parasitic optical absorption by free carriers in the conduction band is called free carrier absorption [57]. Hence, α increases especially for long wavelengths (quadratically) and with increasing N_e (linear). This shows, that electrical and optical properties of a TCO are fundamentally interlinked. Depending on the application a compromise for low absorption either in the ultra violet to visible (UV/Vis) or NIR region has to be found. Especially for tandem solar cell approaches, which will be discussed later in Section 2.2, the development of TCO materials with low N_e and high μ is important.

2.3.2 Prerequisites for TCO contacts in solar cells

In general, a suitable TCO for application in solar cells needs to be designed in such a way, that the possibly highest PCE can be achieved with it. Inevitably, this leads to a balancing problem between the electrical and the optical properties of the TCO. Thereby, the respective demands are highly dependent on the geometry of the solar cell architecture. For instance, a large cell area demands a highly conductive TCO contact, in order to keep resistive losses low. A very small cell would benefit more from a highly translucent TCO, because the resistive losses are reduced.

For a given solar cell geometry, the optimization problem is reduced to finding the thickness of the TCO layer that allows for an optimal balance between optical and electrical losses. Eventually, if good conductive properties are needed, a metal grid could be applied to increase the conductivity. However, the implementation of a grid introduces additional shadowing losses that must be taken into account in the optimization process.

In tandem solar cells, the demands for the TCOs become more extended. The complete tandem cell needs a front TCO with high optical quality over a broader spectral range, because both subcells are more sensitive to losses in their share of the spectrum. TCOs that positioned in between both subcells need to be translucent mainly to light with long wavelengths. Furthermore, the thickness of all TCOs in tandem solar cells may be decreased, because the current densities produced by the subcells are generally lower.

The following TCOs resemble materials, that are generally suitable for the high demands of tandem solar cells, because they offer good optical qualities over a broad spectrum with a decent conductivity. Next to the development of these TCOs, a major aspect of this thesis is their implementation into tandem cells. All optimization steps including thickness variations and grid integration depend on the specific solar cell geometries that are used in this work.

2.3.3 Indium zinc oxide (IZO)

In contrast to traditional TCO materials, which are highly crystalline, IZO is an amorphous material with good optoelectronic properties. It shows electron mobilities up to $60 \, \text{cm}^2/\text{V/s}$ for free densities between $1 \times 10^{20} \, \text{cm}^{-3}$ to $3 \times 10^{20} \, \text{cm}^{-3}$ and high optical transparency [61] and is therefore a suitable candidate for low NIR absorption transparent contact in solar cell devices. The doping of IZO is controlled by the amount of oxygen vacancies, as described by Morales-Masis et al. [57]. Moreover it shows optical band gaps in the range of 3.44 eV to 3.76 eV [62, 63] depending on the sputtering parameters. Since the deposition of amorphous IZO can be carried out by direct current (DC) or radio frequency (RF) magnetron sputtering at ambient temperatures and without any additional annealing steps, it is of great technological interest for the application on temperature sensitive devices [64].

2.3.4 Hydrogen doped indium oxide (IO:H)

Recently, hydrogen-doped indium oxide (IO:H) has increasingly received considerable attention due to the high carrier mobilities reaching up to $130 \, \text{cm}^2/\text{Vs}$ at moderate carrier concentrations of below $2 \times 10^{20} \, \text{cm}^{-3}$ [65]. Its optical transmittance is superior compared to commonly used TCO materials like ITO or aluminium doped zinc oxide $Zn_x Al_{1-x} O$ (ZAO) in both ultra violet (UV) and NIR spectral ranges [66]. Koida et al. developed this material in 2007 by adding small amounts of water vapour during the sputter process of indium oxide (In_2O_3) [15,67]. In the meanwhile another approach was developed by introducing hydrogen gas instead of water during the process, because the introduction of water over a needle valve lacks in reproducibility [68,69]. The presence of hydrogen is crucial for the growing of amorphous layers at room temperature and the mentioned superior optical and electrical properties [69]. The bonding of hydroxide groups at indium atoms suppresses crystalline and favours amorphous growing. A subsequent annealing

step at approximately 200 °C induces solid-phase crystallization. The In(OH)$_3$ transforms into In$_2$O$_3$ due to water elimination. Additional hydrogen incorporation at grain boundaries is considered to passivate defects, hence reducing transport barriers and increasing carrier mobility [66, 70].

2.3.5 Deposition of TCO thin films via magnetron sputtering

This section covers a basic introduction to important aspects of the magnetron sputtering process. Sputtering is a physical vapor deposition (PVD) method for thin film deposition. The basic principle is the removing of material from a target by accelerated ions from a glow discharge. The required plasma is generated by the application of electrical power to the target, technological relevant are RF and DC power generators. The sputtering chamber with base pressures in the ultra high vacuum (UHV) range, is filled with gas, typically with argon (Ar). The Ar$^+$ ions generated in the glow discharge are accelerated at the cathode fall (sheath) and sputter the target resulting in the deposition of thin films on the substrate.

For magnetron sputtering, the electrical field is superposed with a magnetic field at the cathode, which forces the electrons in a cycloidal motion and increases the collision rate between electrons.

If a reactive gas like oxygen (O$_2$) is introduced into the chamber sputtering of thin films with different compounds is possible. The reactive species not only adsorb on the substrate surface, but also lead to a compositional change of the surface target. Thus the partial pressure of reactive gas like oxygen in the chamber is a crucial parameter for the resulting thin film parameters. In conclusion, the properties of deposited films is influenced by deposition parameters including deposition rate, substrate temperature, substrate material and deposition atmosphere [71, 72].

2.4 Optics of single- and multi-junction solar cells

For evaluation of the optical mechanisms that take place inside the multilayered structure of a tandem solar cell, profound knowledge of the optical properties of the individual layers is necessary. The following sections discuss the theoretical concepts that are used in this study to investigate these properties and how the knowledge is applied in the modelling and quantification of spectral loss mechanisms.

2.4.1 Optical functions

The optical constants of a material are commonly described by the complex refractive index $N(\lambda)$ and the complex dielectric function $\epsilon(\lambda)$. They define the propagation of electromagnetic waves in media unambiguously and are related by:

$$\epsilon(\lambda) = \epsilon_1(\lambda) - i\epsilon_2(\lambda) = N(\lambda)^2 = (n(\lambda) - ik(\lambda))^2 \tag{2.6}$$

where all quantities $\epsilon_1(\lambda)$, $\epsilon_2(\lambda)$ $n(\lambda)$ and $k(\lambda)$ are functions of the wavelength. The dielectric functions $\epsilon(\lambda)$ of dielectric materials can be described by the equations A.2 and A.3 in the appendix. The refractive index n represents the modification of the wavelength λ within a material, while the extinction coefficient k is representing the absorption of electromagnetic

waves. Real and imaginary part of both expressions are linked with each other by Kramers-Kronig relation. This means n and k are not independent, and can be calculated from each other. The Kramers-Kronig-consistency is one fundamental relation which has to be fulfilled for the determination of optical functions [73]. The imaginary part of the complex refractive index or extinction coefficient ($k(\lambda)$) may be also converted to the absorption coefficient (α) via equation 2.7. More details are presented in the appendix A.1.

$$\alpha = \frac{4\pi k}{\lambda} \tag{2.7}$$

2.4.2 Reflection and transmission on multilayer structures

The optical properties of a (tandem) solar cell rely on real part of the complex refractive index or phase velocity ($n(\lambda)$) and $k(\lambda)$ (or α) of each single layer and the individual film thickness (d). As a light beam travels through a layer, its initial intensity $I = I_0$ gets attenuated following the Lambert-Beer law

$$I = I_0 \cdot e^{-\alpha(\lambda)d} \tag{2.8}$$

Because the attenuation scales with α and d, a high α is preferable for the absorbing layer, while for the other layers a low α is demanded in order to reduce parasitic absorption. This is usually the case for the semiconductor or dielectric materials, that are used in the solar cell. Of course, the prerequisite is a wide enough band gap of the material, because when interband transitions are possible, fundamental absorption edges are observed with a drastic change of α. Also, the rise of α due to free carrier absorption is critical in case of a high N_e, as it is observed in highly doped layers such as in TCOs (compare Section 2.3.1).

At each interface between the layers, Fresnel reflection takes place. Usually during the measurements, the incident light is perpendicular to the solar cell surface. In that case, the reflectance (R) at the interface between the materials a and b is dependent on the respective $n_{a,b}(\lambda)$:

$$R(\lambda) = \left(\frac{n_b(\lambda) - n_a(\lambda)}{n_b(\lambda) + n_a(\lambda)} \right)^2 \tag{2.9}$$

Fresnel reflection is of the most importance in the front- and rear interface of a semitransparent solar cell, because of the great difference of the refractive indices between glass and air or TCO and air.

However, the solar cell consists of a multilayer stack with many interfaces and layer thicknesses in the range of visible light wavelengths. This causes a more complicated response of the transmission or reflection of the device. When looking at a set of two interfaces and the sandwiched material has a low α and the R values are high, multiple reflection is expected. Then, similar to a Fabry-Perot resonator, the distance between two plane parallel interfaces interferes with coherent wavelengths of appropriate phases. There will be constructive interference, when

an integer number m of half waves fits into the resonator, and thus the transmission increases. In the opposite case, mainly destructive interference causes a rise in the reflection. The measured transmittance (T) and R responses of the devices will exhibit a series of interference minima and maxima over the spectral range, originating from the internal multiple reflections.

The calculation of the internal reflection demands for a computational solution via transfer matrix method (TMM) [74] or other approaches using a direct extension of the Fabry-Perot resonator model [75]. All of the methods require a profound knowledge on the optical functions of the layers and the respective thicknesses. A great uncertainty is introduced by the non ideally flat interfaces (scattering) and partial intermixing of phases, e.g. the diffusion of material a into a scaffold of material b (undefined $n(\lambda)$ and $k(\lambda)$).

2.4.3 Measurement and simulation of optical losses in terms of current density

Experimentally, for a semitransparent sample such as a single TCO layer on glass or a complete semitransparent PSC, the R and T can be measured to calculate the absorptance (A) via

$$A = 1 - T - R. \tag{2.10}$$

For opaque solar cells, T equals zero and the equation simplifies to

$$A = 1 - R. \tag{2.11}$$

As discussed in the previous section, the R and T spectra of a thin layer or a set of thin layers exhibits interferences, which makes a comparison between samples of different thicknesses or materials quite difficult because of the shifting positions of the interference fringes.

In order to make the spectra comparable in a range between $\lambda_1 < \lambda_2$, an integration function $J(\lambda_1, \lambda_2)$ is introduced, utilizing the current density equivalent of the photon flux (qN_{ph}) of the incident spectrum for weighting:

$$J_{Trn}(\lambda_1, \lambda_2) = \int_{\lambda_1}^{\lambda_2} T \cdot qN_{ph} \, d\lambda \tag{2.12}$$

$$J_{Abs}(\lambda_1, \lambda_2) = \int_{\lambda_1}^{\lambda_2} A \cdot qN_{ph} \, d\lambda \tag{2.13}$$

$$J_{Ref}(\lambda_1, \lambda_2) = \int_{\lambda_1}^{\lambda_2} R \cdot qN_{ph} \, d\lambda \tag{2.14}$$

The weighting by the photon flux, rather than the incident intensity is on purpose because the efficiency of a solar cell rather scales with the number of photons than with the energy that they carry. Especially in the long wavelength regime with less energetic photons, this makes a substantial difference. By multiplication with the q, the unit conversion to a current density with the units $mA\,cm^{-2}$ is achieved. This is not only more practical than comparing large particle flux numbers, but it has a direct relation to the photovoltaic application, since the photo current density obtained by EQE measurement (J_{EQE}) is calculated in the same manner:

$$J_{\text{EQE}} = \int \text{EQE} \cdot qN_{\text{ph}} \, d\lambda \qquad (2.15)$$

By creating the ratio of current density equivalent of the transmission (J_{Trn}) and the integral of qN_{ph}, a single weighted average transmittance (T_{wt}) value for the chosen spectral range is presented:

$$T_{\text{wt}}(\lambda_1, \lambda_2) = \frac{J_{\text{Trn}}(\lambda_1, \lambda_2)}{\int_{\lambda_1}^{\lambda_2} qN_{\text{ph}} \, d\lambda}. \qquad (2.16)$$

In analogy the same may be performed for the current density equivalent of the parasitic absorption loss (J_{Abs}) with a weighted average absorptance (A_{wt}):

$$A_{\text{wt}}(\lambda_1, \lambda_2) = \frac{J_{\text{Abs}}(\lambda_1, \lambda_2)}{\int_{\lambda_1}^{\lambda_2} qN_{\text{ph}} \, d\lambda}. \qquad (2.17)$$

The measured values of the T and R only allow an outside view on the mechanisms inside the PSC, indicating the sum of the manifold internal reflections. Measuring the external quantum efficiency (EQE) of a solar cell, allows for further assessment of the parasitic losses that are introduced by the single layers. A principle EQE investigation is shown in Figure 2.9 for an opaque solar cell. It demonstrates how the EQE of a solar cell is qualitatively affected, when additional layers are implemented in the architecture.
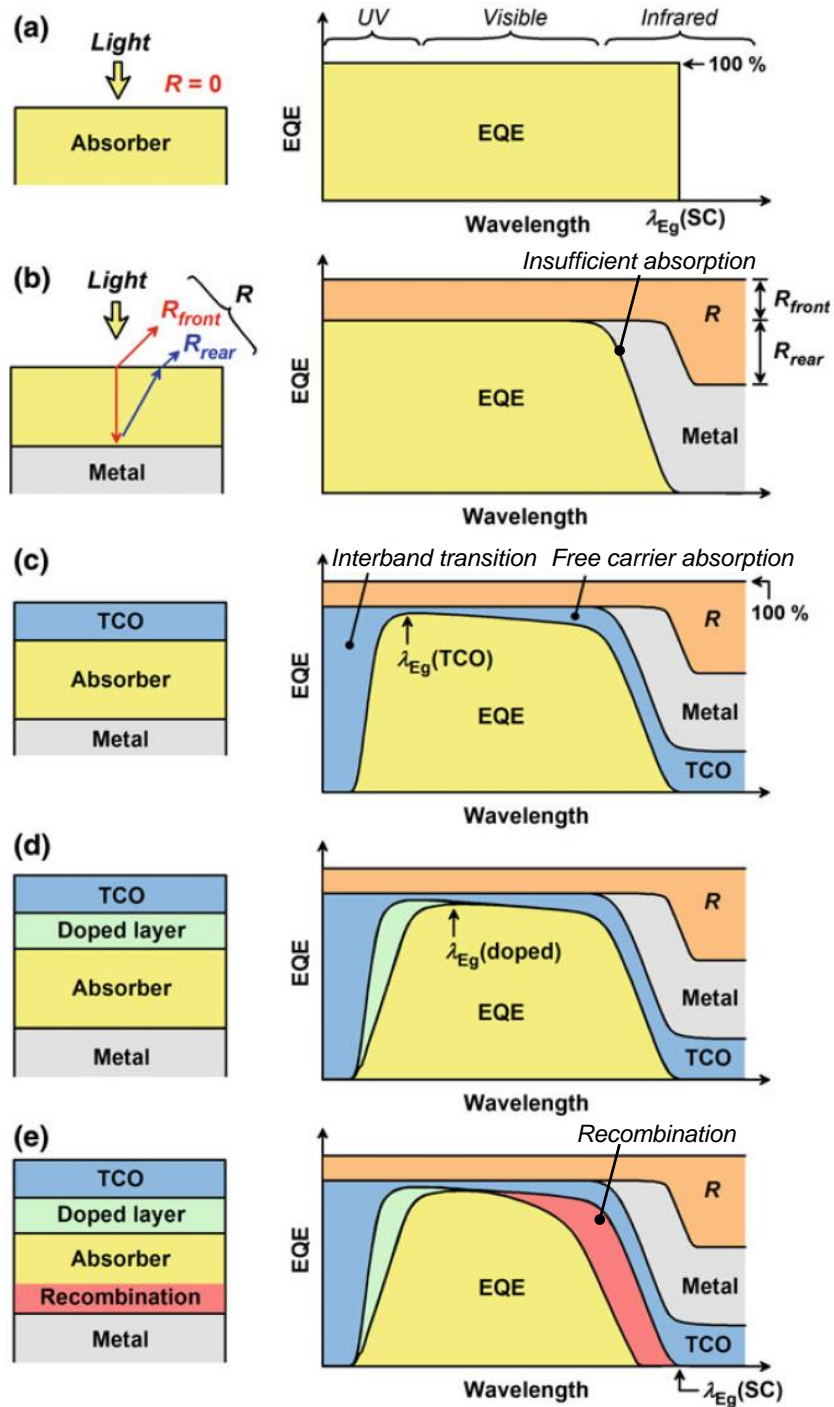
Figure 2.9: Schematic illustration of the EQE spectrum under variation of the solar cell architecture. Original graphic from Fujiwara et al. [76]. a) Hypothetical perfect absorber without R, b) Absorber/metal interface with losses due to reflection and insufficient absorption of photons with long wavelengths that are lost to the metal rear interface, c) TCO/absorber/metal with additional parasitic absorption in the TCO, d) TCO/doped layer/absorber/metal with losses due to the narrow absorption edge of the doped layer, e) the similar architecture with a recombination layer at the rear interface with the metal.

It shows that the EQE is affected by optical effects, such as reflection (b) and parasitic absorption in TCOs (c) and doped interlayers (d). Additionally, it demonstrates, how insufficient absorption in the absorber (b) and increased recombination at the rear interface (e) reduce the EQE response. These effects are difficult to distinguish without the knowledge of the absorption in each single layer.

However, a quantitative statement about the individual contribution of each sublayer to the total J_{Abs} is only possible with aforementioned computational methods. Here, the program e-ARC is used to carry out a TMM based simulation of the tandem architecture. A comprehensive study on the methods and functionalities provided in e-ARC is presented by Fujiwara et al. [76].

For the determination of the absorption A_j in each layer j, a flat optical model is created using the optical functions of each layer material and the measured R as an input. By using the measured R rather than calculating it from the model, the actual solar cell structure with rough interfaces and scattering effects can be approximated much more precisely. Figure 2.10 demonstrates the working principle of the flat model approach. The calculation of A_j follows

$$\sum A_j = 1 - R. \tag{2.18}$$
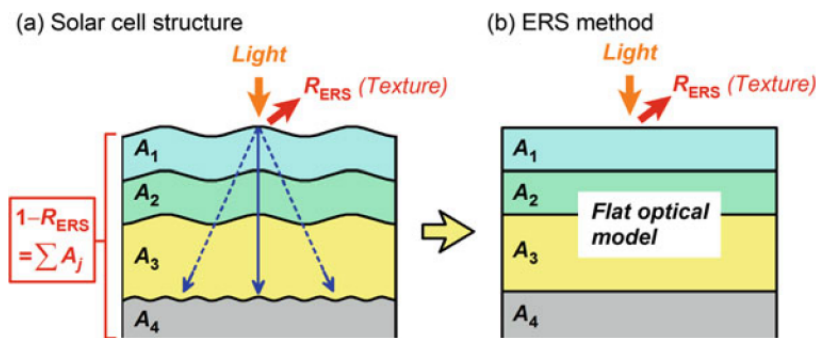
Figure 2.10: Original graphic from Fujiwara et al. [76]. a) Structure of a solar cell with rough interfaces b) optical model for the simulation in e-ARC. The R_{ERS} represents the experimental reflectance spectrum.

After calculation of the absorptance A_j in each layer including the absorber layer, the result is compared to the measured EQE. When there are differences between the absorption and the EQE, additional losses must be considered, that impede the charge collection. In perovskite solar cells, a higher charge recombination at the front interface is often observed, which is modeled in e-ARC via a additional recombination layer [76]. Possible recombination losses at the rear interface may be approximated by an additional parameter called effective carrier collection length. Using these two methods, the measured EQEs of both subcells can be fitted via the simulation, resulting in a complete description of the recombination and parasitic absorption losses of the tandem cell.

2.5 Structural analysis of thin films with XRD

Being a powerful tool for thin film analysis, a typical x-ray diffraction (XRD) pattern contains a variety of information:

- Peak position: Identification of phases, structures and lattice parameters

- Peak width: Information about the crystallite size, microstrain and defects

- Peak area or intensity ratio: Determination of a preferential crystal orientation

- Peak tails: Diffuse scattering and point defects

- Background: Amorphous contents

In its basic application, XRD is used for detection of the characteristic diffraction pattern of a phase and determination of the corresponding crystal structure from the peak positions. The technique is well-known and will not be explained in more detail at this point.

However, the evaluation of the crystallite size or strain from the width and shape of the diffracted peaks requires further calculation steps, which will be briefly discussed here.

Also, special considerations for XRD measurements under grazing incidence angles will be highlighted.

2.5.1 Williamson-Hall analysis

The observed breadth of a diffracted peak may be described by its full width at half maximum (FWHM), which is a convolution of the structural diffraction peak broadening ($\text{FWHM}_{\text{struct}}$) of the specimen and instrumental diffraction peak broadening ($\text{FWHM}_{\text{inst}}$) due to the optical setup [77]:

$$\text{FWHM} = \text{FWHM}_{\text{struct}} + \text{FWHM}_{\text{inst}} \tag{2.19}$$

The $\text{FWHM}_{\text{struct}}$ of a specimen is obtained by correction of the measured FWHM with the $\text{FWHM}_{\text{inst}}$. The latter is usually determined by measuring a reference standard material that shows no structural broadening with the same optical parameters.

Following Scherrer's equation [78] for crystallite size related broadening, including the peak broadening due to microstrains, the $\text{FWHM}_{\text{struct}}$ calculates to

$$\text{FWHM}_{\text{struct}} = \frac{K\lambda}{L\cos\theta} + 4\epsilon\frac{\sin\theta}{\cos\theta} \tag{2.20}$$

with the Scherrer constant (K), the crystallite size (L), the wavelength (λ), the diffracted angle (θ), and the microstrain (ϵ).

From this relation, the Williamson-Hall equation is obtained in the form $y = a + bx$, which can be used to determine the amount of crystallite size broadening (a) and microstrain broadening (b), when fitting a linear regression to the observed $\mathrm{FWHM_{struct}}$:

$$\mathrm{FWHM_{struct}} \cdot \cos\theta = \underbrace{\frac{K\lambda}{L}}_{\text{crystallite size}} + \underbrace{4\epsilon}_{\text{microstrain}} \cdot \sin\theta \qquad (2.21)$$

2.5.2 Grazing incidence XRD

In grazing incidence x-ray diffraction (GIXRD), a highly asymmetric Bragg measurement geometry is used with an incident angle (ω) below or close to the critical angle (ω_c), typically in the range of 0.1° to 3°. Under the conditions of total reflection, Bragg diffraction takes place only at the very surface of the sample. With increasing ω, the beam penetrates deeper into the layer, enabling a depth scan of the film thickness. The penetration depth (τ) depends on the measurement geometry and the material properties. ω defines the travel path length of the beam through the layer and the linear attenuation coefficient (μ_{att}) of the material is used to calculate the amount of attenuation regarding the Lambert-Beer law. The calculation of τ follows [79]

$$\tau = \frac{\sqrt{2}\lambda}{4\pi} \left(\left((\omega^2 - \omega_c^2)^2 + \beta \right)^{-\frac{1}{2}} - (\omega^2 - \omega_c^2) \right)^{\frac{1}{2}} \qquad (2.22)$$

with $\beta = \lambda\mu_{att}/4\pi$ being the imaginary part of the refractive index ($N = 1 - \delta - i\beta$). The penetration depth into a In_2O_3 layer is shown in Figure 4.19 and is e.g. $\approx 2\,\mathrm{nm}$ at an angle of 0.3° and $\approx 100\,\mathrm{nm}$ at 0.9°.

At low angles around ω_c, the incident x-ray beam gets refracted at the sample surface by a significant amount, resulting in a angular change of the beam direction in the material. In consequence the observed diffracted peaks are shifted from the expected Bragg positions by an angle of $2\Delta\theta$. The shift may be as high as several tenths of degrees at its maximum at ω_c, so in order to prevent misinterpretation, the observed peak positions must be corrected by $2\Delta\theta$ [80]

$$2\Delta\theta = \omega - \frac{1}{\sqrt{2}} \left(\left((\omega^2 - \omega_c^2)^2 + 4\beta^2 \right)^{\frac{1}{2}} - (\omega^2 - \omega^2) \right)^{\frac{1}{2}}. \qquad (2.23)$$

3 Experimental methods for preparation and characterization of perovskite-CIGS tandem cells

The first part of this chapter describes the preparation techniques that are used for PSCs and the corresponding layers. It is divided into three sections, that cover the solution based methods (Section 3.1.1), the PVD by thermal evaporation (Section 3.1.2) and by sputtering (Section 3.1.3).

The second part introduces the analytical methods that are utilized for the general characterization of thin films (Section 3.2.1) and for evaluation of the optical and electrical performance of solar cells (Section 3.2.2).

3.1 Preparation of perovskite solar cells

This section covers the experimental techniques of fabrication of high efficiency PSCs via solution based spin coating (SC) and PVD. The experimental setup for TCO deposition is demonstrated and the detailed proceedings of IZO and IO:H via PVD by magnetron sputtering are described. Figure 3.1 illustrates the layer preparation sequence for PSCs.
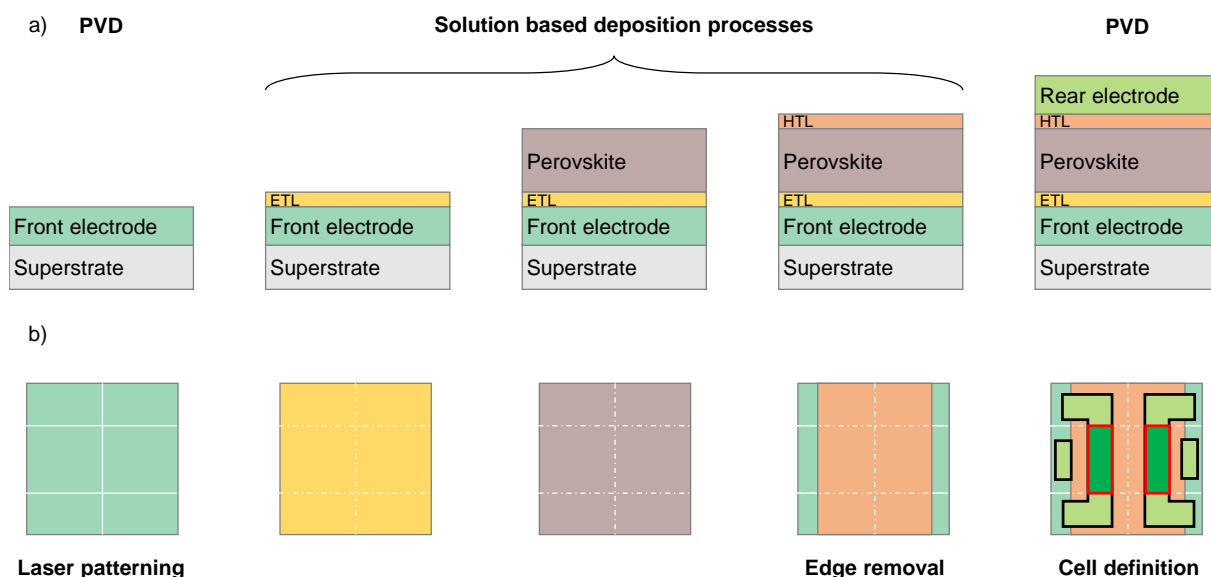

Figure 3.1: Preparation sequence and deposition methods for fabrication of PSCs in a) side view and b) top view.

3.1.1 Solution based preparation of high efficiency perovskite solar cells

Substrates, coated with TCO[1] were patterned by pulsed laser ablation for cell area definition (done by ZSW colleagues). They were plasma-cleaned in oxygen plasma for 180 s at 100 W[2] before the deposition of the electron transport layer consisting of tin oxide nanoparticle (SnO_2-NP). For SnO_2-NP deposition, a 15 wt% aqueous colloidal dispersion of SnO_2[3] was diluted in deionized H_2O to a concentration of 2 wt%. 300 µl of this dispersion was spin coated in a clean room in ambient air on 30×30 mm^2 substrates by static droplet deposition. The spin speed was 4000 rpm for 30 s with an acceleration of 2000 rpm/s. The coated samples were dried on a 200 °C hotplate for 30 min.

After a second plasma cleaning step for 60 s at 30 W in oxygen, the substrates were transferred into a glovebox and a C_{60}–SAM[4] layer was spin coated at 2000 rpm for 30 s on top and dried at 100 °C for 10 min.

Subsequently a nanoparticle (NP) based wetting agent was deposited on top [142] by spreading a 0.3 wt% dispersion of silicon oxide nanoparticle (SiO_2-NP) in ethanol at 2000 rpm for 30 s followed by a drying step at 100 °C for 5 min. The SiO_2-NP were synthesized following Bogush et al. [81] using fixed amounts of ethanol[5], ammonia[6] and tetraethyl orthosilicate[7] and deionized water[8]. After stirring at 30 °C for 3 h the weight-concentration of the stock dispersion was 1.2 wt% in ethanol with an approximate size of the nanoparticles of 20 nm. For more details see Section 4.1.2.

Simple perovskite MAPI

The MAPI perovskite was deposited from a 1.4 M solution, which was prepared from equal parts of PbI_2[9] and MAI[10] dissolved in GBL[11] and DMSO[12] (ratio 7:3). 50 µl of the solution was spin-coated dynamically on a 15×15 mm^2 substrate at 1000 rpm for 10 s and 5000 rpm for 25 s. To initiate fast crystallization of the film, 500 µl toluene was dispensed on the film 10 s prior to the end of the spin-coating step. Subsequently, the film was annealed at 100 °C for 10 min.

---

[1] ITO (Visiontek), FTO (Sigma-Aldrich) or IZO and IO:H in-house

[2] Diener electronic Pico Plasma Cleaner

[3] SnO_2 colloids: 15 wt%, Alfa Aesar

[4] C_{60}-based self-assembled monolayer (C_{60}–SAM), 0.5 mg/ml in chlorobenzene, 4-(1',5'-Dihydro-1'methyl-2'H-[5,6]fullereno-C_{60}-I$_h$-[1,9-c]pyrrol-2'-yl)benzoic acid, Sigma-Aldrich

[5] ethanol, 2.71 ml, 99.5 %, Sigma-Aldrich

[6] ammonia, 101 µl, 99.9 %, Roth

[7] TEOS, 114 µl, 98 %, Sigma-Aldrich

[8] H_2O, 27 µl

[9] lead iodide (PbI_2), 99.99 %, TCI

[10] methylammonium iodide (MAI), DyeSol

[11] γ–butyrolactone (GBL), Sigma-Aldrich

[12] dimethylsulfoxide (DMSO), Sigma-Aldrich

Mixed ionic perovskite CsFAMAPIBr

The mixed ionic perovskite CsFAMAPIBr was deposited from a 43 wt% solution, in which the precursor salts FAI[13], PbI_2[14], MABr[15], $PbBr_2$[16], and CsI[17] were dissolved in the solvents DMF[18] and DMSO (ratio 8:2) in a certain order. Firstly FAI and MABr were dissolved in the mixed solvents at ambient temperature. Afterwards, the lead salts PbI_2 and $PbBr_2$ were added to this precursor solution and dissolved on a hotplate at 100 °C. After cooling down, the solution was filtered[19] and 42 µl/ml of a CsI solution was added. The CsI solution was prepared by solving 1.5 M CsI in DMSO at 100 °C. To prepare the perovskite layer, 80 µl of the final precursor solution was spin coated dynamically on 30×30 mm^2 substrates at 1000 rpm for 10 s and 6000 rpm for 20 s. To initiate fast crystallization, 500 µl chlorobenzene was dispensed on the film 5 s before the end of the spin coating. The film was annealed at 100 °C for 60 min.

On top, a Spiro-OMeTAD[20] layer was deposited from a 75 mg/ml solution in chlorobenzene. Prior to the deposition two dopants were added to the solution.[21][22] The SC was conducted at 2500 rpm for 45 s. After the deposition of Spiro-OMeTAD, the samples with a size of 30×30 mm^2 were broken into 4 samples of 15×15 mm^2. Subsequently, the rear contact is deposited with an aperture mask to define the active areas of the two cells on each 15×15 mm^2 sample.

3.1.2 Deposition of buffer and contact layers by thermal evaporation

For opaque cells a 64 nm layer of gold was deposited as an electrode under high vacuum conditions ($<10 \times 10^{-5}$ mbar) through a metal aperture mask defining active areas of 0.24 cm^2. For semitransparent PSCs a buffer layer of 10 nm MoO_3 was deposited on the samples by thermal evaporation within a UHV chamber. Transparent contacts of IZO or IO:H were deposited subsequently via magnetron sputtering as described in the following Section 3.1.3.

3.1.3 Magnetron sputtering of high quality TCO films

TCO layers were deposited in a laboratory UHV system[23] by magnetron sputtering. Figure 3.2 illustrates the principle setup of the system. It is equipped with three magnetron sources and high purity targets and connected to power generators, which supply either a RF or DC electrical power signal. Circular outlets for the gas supply are mounted directly at the targets. All layers were deposited with Argon (Ar) as sputtering gas. For reactive sputtering a 5 % O_2 mixture

---

[13] formamidinium iodide (FAI), 1 M, 99 %, Sigma-Aldrich

[14] lead iodide (PbI_2), 1.1 M, 99.99 %, TCI

[15] methylammonium bromide (MABr), 0.2 M, 99 %, DyeSol

[16] lead bromide ($PbBr_2$), 0.2 M, 98 %, TCI

[17] caesium iodide (CsI), 99.9995 %, Sigma-Aldrich

[18] dimethylformamide (DMF), 99.8 %, Sigma-Aldrich

[19] polyethylene terephthalate (PET) filter, 0.45 µm

[20] conductive fluorene (Spiro-OMeTAD), 99 %, Sigma Aldrich

[21] Li-TFSI, bis(trifluoro-methane)sulfonimide lithium salt, 3 vol%, Sigma-Aldrich, in acetonitrile 170 mg/ml

[22] TBP, 4-tert-butylpyridine, 1 vol%, 96 %, Sigma-Aldrich

[23] von Ardenne CS 370 S

in Argon[24] was available as reaction gas. A 8 % H_2 mixture in Argon was added as hydrogen doping source. Power densities between $0.96\,W/m^2$ to $3.18\,W/m^2$ were applied with a standard deposition power density of $2.55\,W/m^2$ which relates to a power of $800\,W$. The base pressure of the process chamber was below 10^{-6} mbar.
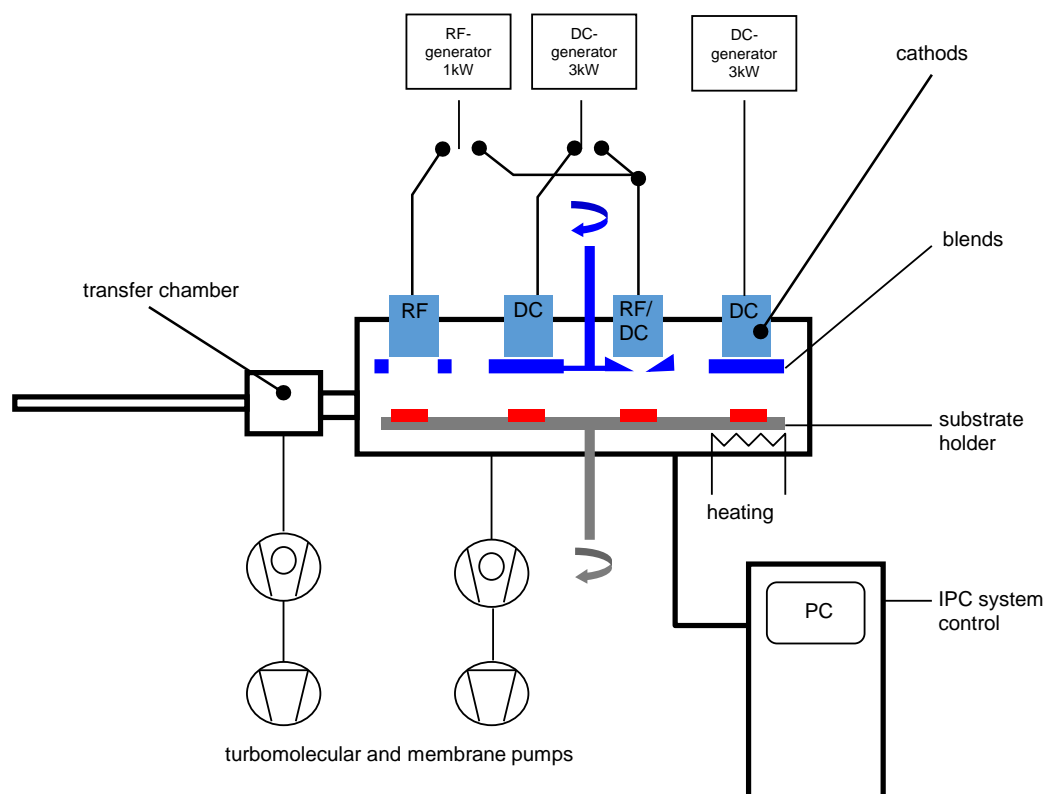
Figure 3.2: Principle setup of the laboratory sputtering system.

IZO layers were deposited by sputtering from an In_2O_3:ZnO target[25] with Argon as working gas and O_2 as reaction gas. The process pressure was fixed at $15\,\mu bar$. IO:H layers were prepared by sputtering from a In_2O_3 target[26] with Argon and Ar/O_2 and additional Ar/H_2 as hydrogen doping source. The process pressure was fixed at $5\,\mu bar$. The standard procedure for IO:H films included a subsequent annealing step at $200\,°C$ for $30\,min$ on a hotplate in air. The principle workflow of TCO depositions is defined by customized programs.

After the introduction of the samples into the deposition chamber via the transfer chamber, the substrates are moved below the selected target by rotating the substrate holder. The gas flows are adjusted by dedicated mass flow controllers (MFC). The process pressure is regulated via a butterfly valve. With the shutter closed, the initial plasma discharge was started at $15\,\mu bar$ at $300\,W$. The power was then increased in steps of $25\,W$ each $10\,s$. After reaching the targeted power for deposition, the pressure was adjusted to the process value and a subsequent sputtering step with constant parameters and closed shutter was conducted for $30\,s$ for conditioning of the target. Afterwards, the actual deposition process was carried out by opening the shutter and closing after deposition time. Finally all gas inlets were closed, generators switched off and samples were transferred.

---

[24] Argon, 99.9999 %
[25] In_2O_3:ZnO, 99.99 %, Composition ratio of 90:10, diameter 200 mm, Toshima
[26] In_2O_3, 99.99 %, diameter 200 mm, Toshima

All films for characterization were deposited on cleaned borosilicate glass[27] as substrate material. TCO layers for the application in PSC as superstrates or substrates were grown on 1.1 mm borosilicate glass. The transparent back contacts of PSCs were deposited through a metal aperture mask with the same layout as used for the gold references.

3.2 Characterization methods for solar cells

This study comprises a variety of analytical methods for characterization of the optical, electrical and structural properties of thin films and complete solar cells. The corresponding experimental setups and measurement parameters are described in the following sections.

3.2.1 Thin film characterization

This section covers the experimental techniques for the characterization of thin films. Herein the most important analysis techniques are UV/Vis to determine transmittance and reflectance and four-point-probe (4P) measurements to determine the sheet resistance of conductive films such as TCOs. For detailed analysis of specific optical, electrical or structural proberties, Hall measurements, XRD, spectroscopic ellipsometry (SE), scanning electron microscopy (SEM) and confocal laser scanning microscopy (CLSM) were carried out.

UV/Vis for the determination of optical properties and film thickness

In order to analyze the optical properties of the films their transmittance T and reflectance R spectra were measured with an Ulbricht-sphere setup in a Perkin Elmer Lambda 900 Spectrometer. From this the absorptance A was calculated via $A = 100 - R - T$. The weighted average transmittance (T_{wt}) and weighted average absorptance (A_{wt}) are then calculated via equations 2.16 and 2.17.

For the absorption edge calculation of TCO materials, the absorption coefficient α was calculated by following equation:

$$\alpha = \frac{1}{d} \cdot \ln \frac{1 - R^2}{T} \tag{3.1}$$

with the layer thickness d [82, 83]. The direct optical band gap E_g is extracted from a Tauc-plot where $(\alpha h\nu)^2$ is plotted over $h\nu$ and h is the Planck constant and ν the frequency of the electromagnetic field. E_g can be estimated by the intercept of $(\alpha h\nu)^2 = 0$ of a linear regression following the equation

$$(\alpha h\nu)^2 = A(h\nu - E_g) \tag{3.2}$$

where A is a constant [83, 84].

From transmittance spectra thicknesses of the thin films were determined by an optical simulation with a computational software for data processing and visualization (Diplot), based on the pattern of interference [85].

---

[27] borosilicate, D263 T, 0.55 mm, Schott

4-point probe to determine sheet resistances

The sheet resistance was measured with a Jandel four-point-probe, in the in-line 4P geometry with the distance s between the contacts. The voltage V between the two inner contacts is measured while a current I is injected through the outer contacts. The measured resistance $R = \frac{V}{I}$ corresponds only to the sample resistance and is independent of any contact and wiring resistances. For the ideal case with $d \ll s$ and infinitely large thin film surface, where d is the film thickness, the sheet resistance R_{sheet} is defined by

$$R_{\text{sq}} = \frac{\rho}{d} = \frac{\pi}{\ln 2} \cdot \frac{V}{I} \tag{3.3}$$

with the resistivity ρ. [86]. In order to indicate a sheet resistance value, the unit is given as $[R_{\text{sq}}] = \Omega_{\square}$.

Hall measurements for investigating the charge transport

For a detailed electrical characterization Hall measurements were carried out. The measurement is based on the deflection of charge carriers with a velocity perpendicular to a magnetic field B which generates a measurable voltage. From this voltage resistivity ρ, carrier concentration N_{e} and carrier mobility μ are obtained [87]. Therefore TCO samples were cutted into a size of $1 \times 1\,\text{cm}^2$ and contacted in the corners. The measurements were performed with a PhysTech RH2010 system in van der Pauw configuration at a magnet field of $B = 0.5\,\text{T}$ and different currents of $0.1\,\text{mA}$, $1\,\text{mA}$ and $10\,\text{mA}$.

X-ray diffraction for structural analysis

For crystallographical analysis XRD measurements (2θ-scans, $10°$ to $70°$) were performed with a Panalytical Empyrean system in Bragg-Brentano geometry with a CuK_α line as radiation source. Acceleration voltage and current were set to $40\,\text{V}$ and $40\,\mu\text{A}$, respectively. The GIXRD measurements were performed at different ω ranging from $0.1°$ to $3°$ with the same current and voltage parameters. The used software was Highscore version 3.

Spectroscopic ellipsometry to determine optical functions

Spectroscopic ellipsometry (SE) measurements were performed with a Sentech SE800 PV system in order to determine the optical functions $n(\lambda)$ and $k(\lambda)$ of the PSC layers. All investigated layers were deposited on quartz glass. The SE spectra of the polarization angles Ψ and Δ were measured in a range from $280\,\text{nm}$ to $1630\,\text{nm}$ for six different incidence angles Φ between $50°$ to $75°$ in steps of $5°$. The measurements and the subsequent simulation of $n(\lambda)$ and $k(\lambda)$ were carried out by Tim Helder with the software SpectraRay 4 from Sentech. Detailed information of the ellipsometry models and the model parameters are given in the appendix A.1.

Scanning electron microscopy

SEM images of surfaces and cross sections were taken with a FEI Sirion XL30S FEG at a voltage of 5 kV. Measurements were carried out by Tina Wahl and Daniela Müller.

Confocal laser scanning microscopy

Confocal laser scanning microscopy images were taken with a Keyence VK-9700K Color 3D Laser Microscope. The software for image processing was VK Analyzer from Keyence.

Contact angle measurements

Droplets of the perovskite precursor solution (3 μl) were applied on top of the sample surface. A customized setup was used to take photographs of contact angles inside a nitrogen-filled glovebox. The program ImageJ [88] with the contact angle measurement tool by Marco Brugnara [89] was used for evaluation of the data and contact angle fitting.

3.2.2 Solar cell analysis

For the characterization of the photovoltaic performance and the spectral response of the solar cells, *JV* measurements, EQE spectroscopy and current loss analyses were conducted.

Current-voltage characterization

The photovoltaic device performance was measured with a Keithley 2400 source meter at a scan speed of 0.2 V/s under ambient conditions and illumination of standard test conditions by a Wacom WXS-90S-L2 Super Solar Simulator (class AAA, AM 1.5G, 1000 W/m^2). All devices were prebiased at 1.5 V for 5 s and measured from 1.5 V to -0.2 V (*rvs*) and from -0.2 V to 1.5 V (*fwd*).

The *JV* response is used to obtain the characteristic solar cell parameters short circuit current density (J_{SC}), V_{OC}, FF, MPP and consequently the PCE.

Generally, the PCE is defined as the ratio of the incident radiative power of the AM1.5G solar spectrum (AM1.5) P_{in} at standard test conditions (25 °C, normal incidence) and the maximum generated electrical power output P_{max} and it is connected to the other parameters via

$$\text{PCE} = \frac{P_{max}}{P_{in}} = \frac{\text{FF} \cdot V_{OC} \cdot I_{SC}}{P_{in}} \tag{3.4}$$
.

Due to the hysteresis in the PSCs, the PCE obtained from the *fwd* and from the *rvs* scan is named PCE$_{fwd}$ and PCE$_{rvs}$, respectively. The same holds for steady state efficiencies obtained from MPP tracking which are labelled PCE$_{MPP}$. Compare also Section 2.1.3.

When a CIGS cell is not illuminated by AM1.5 but by the transmission spectrum of a PSC top cell ('filtered') the notation follows PCE$_f$.

Quantum efficiency

The external quantum efficiency (EQE) was determined with a Bentham PVE 300. The spectral range of measurement for the tandem cells was from 300 nm to 1300 nm. The setup was calibrated with standardized silicon (300 nm to 1100 nm) and germanium (800 nm to 1600 nm) photodiodes prior to the measurements. A measurement spot size of $0.05\,cm^2$ was chosen in order to fit between the grid bars of the solar cells. Additional details of the measurements are given in the appendix A.2.

Current loss analysis with e-ARC

The current loss analysis and EQE simulation was performed with the program e-ARC v2.0 by AIST [90]. The layer stack model of the tandem solar cell was created using the optical functions $(n(\lambda), k(\lambda))$ obtained from SE measurements in Section 5.4.1, as well as from literature data for ITO ($N = 1.2 \times 10^{21}\,cm^{-3}$) [91], spiro-OMeTAD [92], air [93], CIGS [94], MoSe [95], and molybdenum, MgF_2, CdS, and i-ZnO [96].

4 Development of perovskite solar cells for tandem application

The first central part of this study is the development of the perovskite top cell for application in tandem cells. Figure 4.1 depicts the branch of the strategy chart from Chapter 1, that is schematically explaining the development of the top cell in standard n-type–intrinsic–p-type (n-i-p) configuration. The chapter is divided into three main sections, that guide through the principle development process from comparably simple and low performing, opaque solar cells to more complex and highly efficient, semitransparent solar cells.
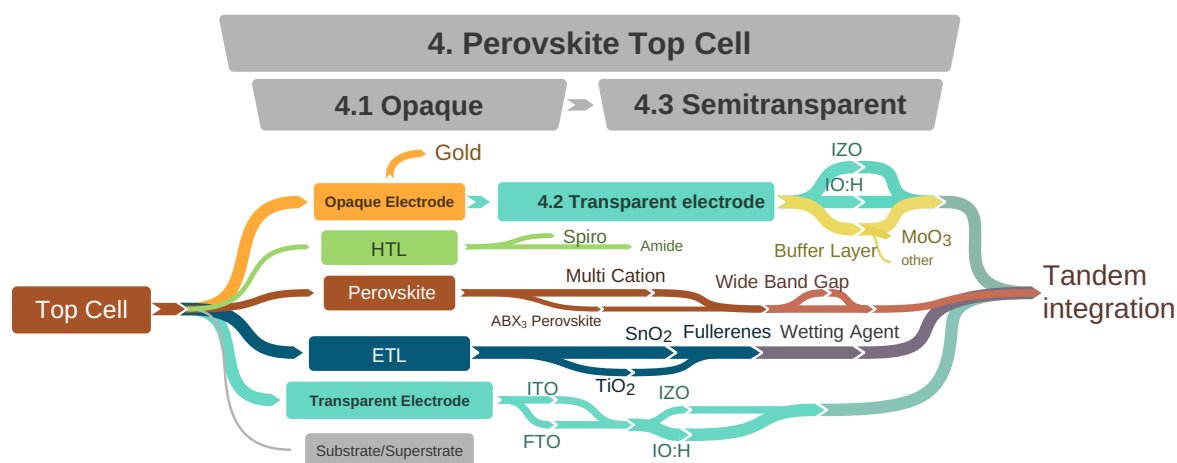

Figure 4.1: Strategy for developing the n-i-p–perovskite top cell.

The first section 4.1 focuses on the most important steps in the optimization of the electrical performance of single perovskite cells. Most of this work is related to the materials and interfaces at the electron selective layer and has been predominantly but not exclusively conducted on opaque cells with a metal back contact. Highlights are the evaluation of different TCO-ETL-absorber combinations, the introduction of fullerenes for hysteresis suppression and the development of a nanoparticle based interlayer for enhanced wetting on hydrophobic interfaces.

Secondly in Section 4.2, for the transition to semitransparent solar cells, the sputter deposition of suitable transparent and conductive layers of IO:H and IZO is discussed. For the designated application as front and rear electrodes in the top cell, the demanded material properties are a high conductivity and a low absorption. Special focus lies on post deposition crystallization of the promising IO:H, which allows for a superiorly low NIR absorption.

The subsequent Section 4.3 evaluates the implementation of the TCOs into the PSC architecture. An important step is the damage-free sputter deposition of a TCO layer as rear electrode onto the perovskite cell, replacing the opaque metal electrode. Major optical advantages are expected from the replacement of the traditional front electrodes ITO or FTO. With the adjustment of the TCO layer thicknesses, the semitransparent PSC are finally prepared for the implementation into tandem devices.

4.1 Opaque perovskite solar cells

This section is devoted to the implementation, optimization and evaluation of different materials in the development of opaque perovskite solar cells towards a high efficiency. The aim of the section is a successive advancement of the opaque solar cells in order to prepare them for the transition to semitransparent architectures.

In the n-type–intrinsic–p-type (n-i-p) perovskite solar cell, the n-type layer is on the light incident side as seen in Figure 4.2. Due to the superstrate setup of PSCs the n-layer is about to be deposited at first in the production process of the solar cell stack. Since the subsequent layers have to be deposited on top of the n-layer, it is influencing the following film quality and morphology. It is reasonable to begin with optimizing the n-interface and to proceed with the absorber material, then the p-type and finally the electrode materials, because any change in the very first layers may require a re-optimization of all the layers that follow on top of it. For this reason, this section begins with a brief evaluation of a simple glass/TCO/ETL/absorber combination in Section 4.1.1.

Section 4.1.2 introduces a new approach based on nanoparticles to enhance the wettability of hydrophobic interfaces. This is needed for the subsequent implementation of desirable fullerene interlayers, which are often of a hydrophobic nature. Their repellent behaviour causes severe de-wetting issues in the attempt to deposit a perovskite layer by sin coating on top of it. The working principle of the wetting agent is mainly investigated by means of contact angle measurements.

Section 4.1.3 discusses the beneficial effects of fullerene interlayers for the perovskite solar cell performance. Furthermore, a mixed cation perovskite is introduced, that shall increase the efficiency of the opaque solar cells.
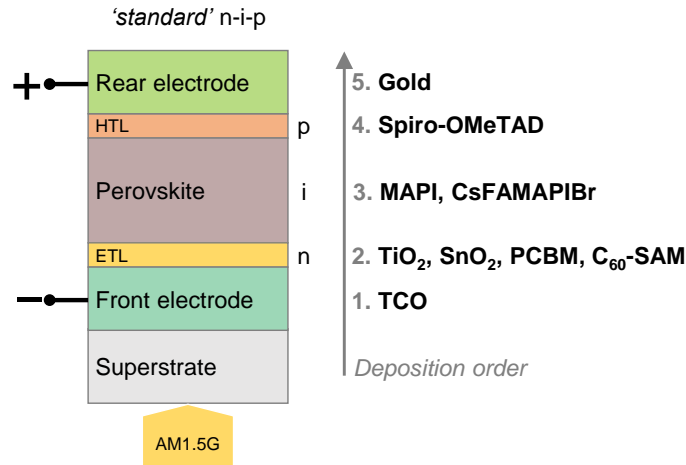
Figure 4.2: Schematic illustration of the perovskite solar cell architecture and the deposition order.

4.1.1 Principle investigations on MAPI based solar cells

As already mentioned, the optimization progress starts with the superstrate–sided n-type interface of the perovskite layer stack.

Historically, the n-side of the PSC consists of FTO as the transparent front contact and TiO_2 in the role of the electron selective layer. [23] Now, SnO_2 proves to be a promising alternative replacing the TiO_2, exhibiting a slightly lower band alignment as seen in Figure 2.4. [41, 97]

When a single oxidic ETL such as SnO_2 is used in the solar cell architecture, a perovskitetypical hysteresis is observed (compare also Section 2.1.3). This is partly reasoned by a misalignment of the Fermi-levels of SnO_2 and the perovskite, which in turn is controllable by precise annealing of the SnO_2 [98].

The following experiment is designed to find the optimum annealing temperatures for the compact tin oxide (c-SnO_2) that is used in a simple PSC setup with FTO/c-SnO_2/MAPI/Spiro-OMeTAD/Au.

Figure 4.3 displays the box plot of the characteristic solar cell parameters for the different annealing temperatures of the c-SnO_2 ranging from $180\,°C$ to $240\,°C$. The best mean efficiencies of $13\,\%$ to $14\,\%$ (*rvs* scan direction, black) are reached when the SnO_2 is annealed at $200\,°C$ or $240\,°C$. The forward scans (red) witness a pronounced hysteresis and show a reduced efficiency of about $4\,\%$ to $5\,\%$ in absolute values.
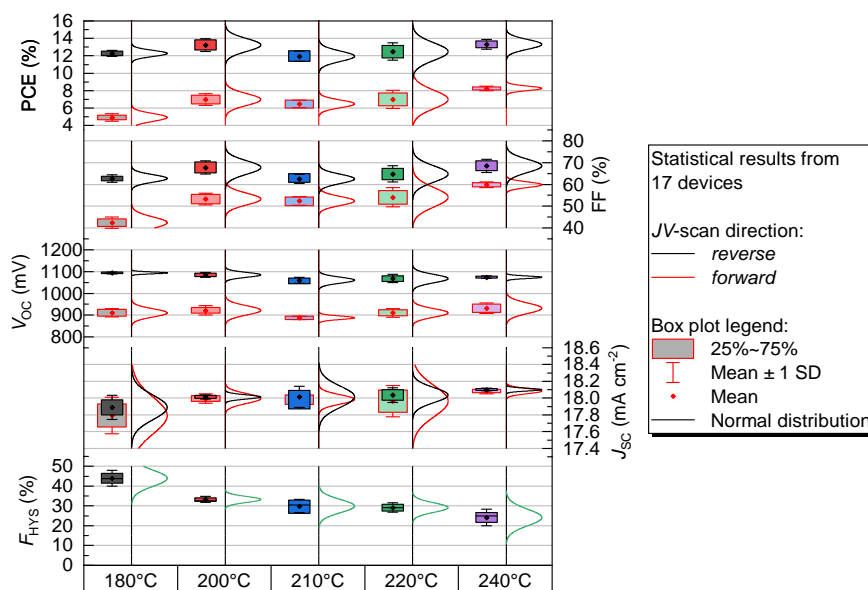
Figure 4.3: Box chart of *JV*-characteristics of PSCs with different annealing temperatures of the c-SnO$_2$ in the configuration FTO/c-SnO$_2$/MAPI/Spiro-OMeTAD/Au.

The values of the fill factor (FF) follow the same trend of the PCE, reaching the best mean values at 200 °C and 240 °C in reverse scan direction. From the large deviation of the results in forward scan directions, it is obvious that the main hysteretic difference in the efficiency is caused by the fill factor (FF).

Additionally, a V_{OC} difference between forward and reverse scan of about 200 mV contributes to the overall hysteretic losses. The V_{OC} seems to decrease slightly by less than 50 mV with increasing annealing temperature, but this trend is difficult to separate from the statistical results as a significant difference.

In contrast to the decrease of V_{OC}, the J_{SC} rises by a total of 0.3 mA/cm^2 when the c-SnO$_2$ annealing temperature is raised from 180 °C to 240 °C.

The hysteresis is minimized at an annealing temperature of 240 °C as indicated by the significant, almost linear improvement of the F_{HYS} from 45 % to 25 %. This is explained by the convergence of the reverse and forward values of the FF at elevated temperatures.

The results qualitatively confirm the findings of Aygüler et al. [98] that the performance of the PSCs is influenced by the annealing temperature of the SnO$_2$ ETL. Their study on atomic layer deposited SnO$_2$ demonstrated an optimum Fermi-levelling that leads to an effective energy band alignment when the annealing temperature is set to 200 °C. Here, also good performance values are reached at similar annealing temperatures, but the hysteresis could be significantly reduced with even higher temperatures up to 240 °C, which indicates a further interface improvement. This could be a hint for a different temperature dependency of the Fermi energy of the sol-gel deposited c-SnO$_2$ compared to the previously reported findings on atomic layer deposited SnO$_2$.

However, later on in Section 4.3 different transparent conductive oxides (TCOs) will be introduced that do not comply with temperatures larger than 200 °C. Therefore, these results are an indicator for the incompatibility of the temperature treatment of SnO_2 and the following cell setups.

A different approach is needed in order to gain control over the hysteresis and improve the solar cell efficiency. In the following Sections 4.1.2 and 4.1.3 the optimization of the interface will be targeted from another direction by introducing an additional interlayer comprising fullerenes like PCBM and C_{60}–SAM.

4.1.2 Nanoparticles for efficient wetting on hydrophobic fullerene interfaces

The nanoparticle wetting agent used in the following sections is based on collaborative findings by Nadja Giesbrecht (LMU) and the author. The following contact angle study and solar cell preparations represent original work by the author. Further information and additional highlights of the complete study are published in the corresponding journal paper [142].

In order to overcome the hysteresis related issues of the previous Section, an additional interlayer of fullerenes may be applied at the interface between ETL and perovskite. Prominent fullerene derivates such as PCBM are also n-type materials and the band alignment is matching closely to the existing ETLs such as SnO_2 or TiO_2, which can be seen from Figure 2.4.

Fullerenes have already proven to be an effective tool for suppressing hysteretic effects due to the prevention of trap states [54, 99], but they often exhibit a hydrophobic surface due to their comparably low polarity. This leads to severe wetting issues in the subsequent layer deposition, if the process utilizes a solution with a high polarity as it is the case for perovskite precursors. As a result, spin coating a perovskite solution on fullerene covered substrates leads to incomplete coverage and defective layers. Before using these hydrophobic materials in the device, a method needs to be established that overcomes the wetting related issues.

The severity of the wetting issues depends on many parameters such as the substrate interface material and morphology, the solution solvents, ingredients and temperature, the ambient atmosphere, deposition parameters and possible preconditioning steps. Partly successful enhancement of the wetting behaviour may be achieved by spin coating hot solutions on preheated substrates, by plasma aided preconditioning, by mechanical distribution of the solution droplet on top of the interface or by adding surfactants to the precursor solution. But each of the method introduces new disadvantages such as damaging the fullerene layer or deteriorating the sensitive perovskite crystallization.

To avoid all of these issues, a new approach was investigated together with collaboration partners from Ludwig-Maximilian-Universität München (LMU), mainly Nadja Giesbrecht. The method comprises oxidic, insulating nanoparticles such as aluminium oxide nanoparticles (Al_2O_3-NPs) and silicon oxide nanoparticles (SiO_2-NPs), which are coarsely distributed among the surface of the fullerene layer. By application of this wetting agent, the surface energy increases in such a way that the perovskite solution spreads easily and homogeneous coverage is achieved. In return, covering only a fraction of the interface, the wetting agent preserves the advantageous properties of the fullerene/perovskite interface and ensures full functionality of the device.

The next sections briefly discuss the working principle of the wetting agent with the aid of contact angle measurements. The influence of the diameter and distribution of the nanoparticles on different surfaces is investigated and the impact on the perovskite performance.

Wetting and pinhole formation evaluated by contact angle studies

In order to understand how nanoparticles improve the wetting on variant low-energy surfaces, contact angle measurements were conducted with perovskite precursors based on different solvents. Following Young's theory, the contact angle of a liquid droplet directly relates to the surface energy and therefore indicates the surface wettability by perovskite solutions. [100] These investigations indicate that the density of particle distribution on the surface and the particle size have the strongest influence on the wettability. Figure 4.4 illustrates the general mechanism how the nanoparticles decrease the contact angle and improve the droplet spreading that results in homogeneous perovskite layers without de-wetting issues regardless of the solution deposition technique.
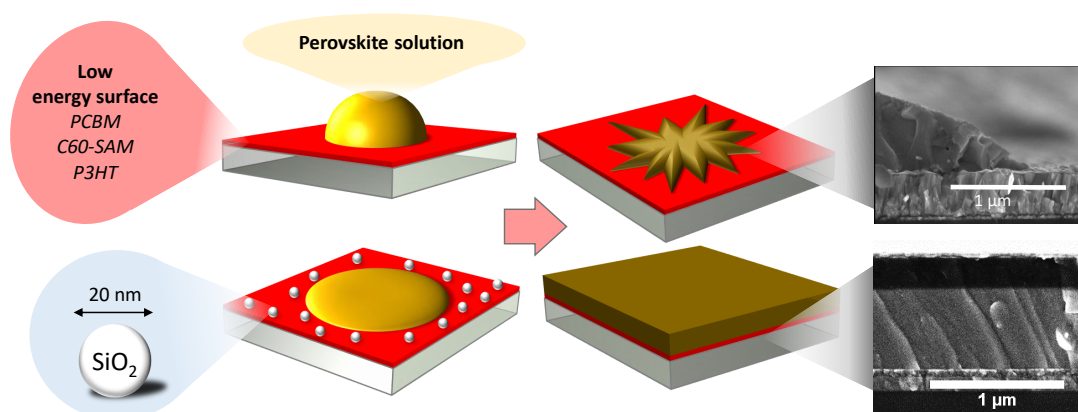
Figure 4.4: Schematic illustration of the wetting improvement by nanoparticles and exemplary SEM micrographs.

The following study investigate the contact angle under three main aspects: (i) The number of particles distributed on the interface; (ii) The size or diameter of the particles; (iii) The type of material of the particles. Therefore, commercially available Al_2O_3-NPs nanoparticles are utilized next to synthesized SiO_2-NPs of different diameters following Bogush et al. [81]

Figure 4.5 shows that the Al_2O_3-NPs have a mean diameter of (35 ± 26) nm, while the SiO_2-NPs show a narrow size distribution around 20 nm, 40 nm and 60 nm. The diameters are obtained by statistically relevant analysis of SEM images.

Figure 4.5: Distribution of calculated diameters of different NPs.

To investigate the effect of size and distribution of nanoparticles on the surface, they were deposited by spin coating from differently diluted alcoholic dispersions. Figure 4.6 shows SEM images of a fullerene (PCBM) surface and the spatial distribution of nanoparticles deposited from differently diluted dispersions. As expected, the su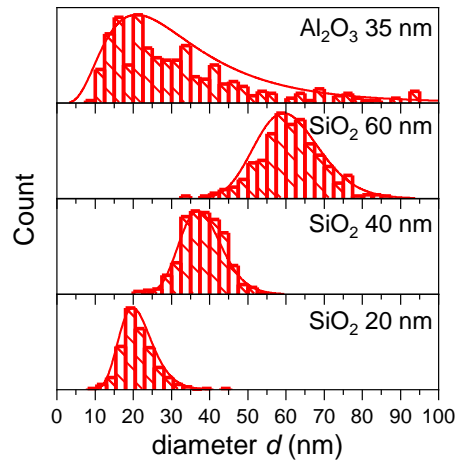rface coverage is strongly dependent on the NP size and the initial concentration. For instance the deposition of Al_2O_3-NPs from 0.2 wt% solution leads to a covered area of about 14 %.
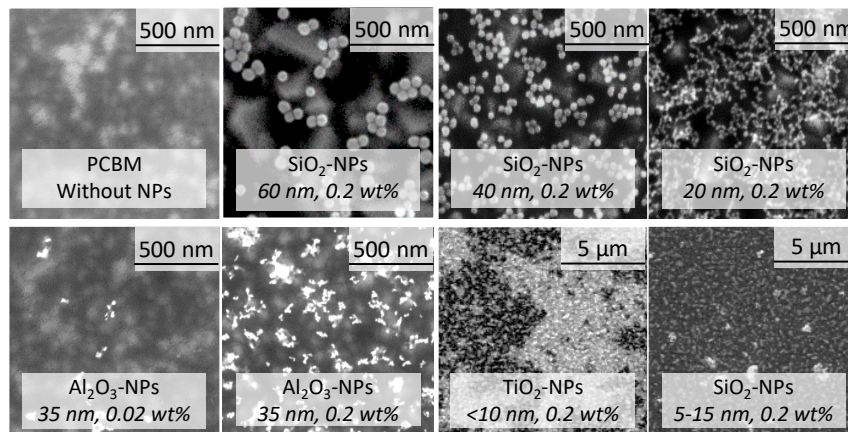
Figure 4.6: SEM micrographs of various nanoparticles on PCBM-surface.

At first, the impact of the number of particles is investigated. Therefore, a series of differently diluted Al_2O_3-NP dispersions is utilized to generate interfaces with different coverage ratios. Following the graphs in Figure 4.7a, different combinations of hydrophobic interlayers (PCBM or C_{60}–SAM) and perovskite precursors based on the solvents DMF, GBL and DMSO reveal the strong decrease of the contact angle with increase of the nanoparticle concentration. The graph shows that the initial contact angle is strongly dependent on the type of solvent–interface combination. This means that the wetting e.g. of a DMF based solution on a PCBM interface is much more difficult, than using a GBL based solution on a less hydrophobic C_{60}–SAM interface.

In all cases, increasing the nanoparticle concentration and overcoming a critical surface coverage leads to contact angle reduction to less than 10° and a change in the droplet wetting behaviour. The perovskite precursor solution then spreads almost perfectly flat on top of the substrate, regardless of the initial hydrophobicity of the interface.

Figure 4.7: a) Contact angles of DMF or GBL based perovskite solutions on fullerene interface (PCBM or C_{60}–SAM) covered with Al_2O_3-NPs from differently concentrated solutions; b) contact angle of a DMF based perovskite solution on PCBM interface covered with differently sized SiO_2-NPs.
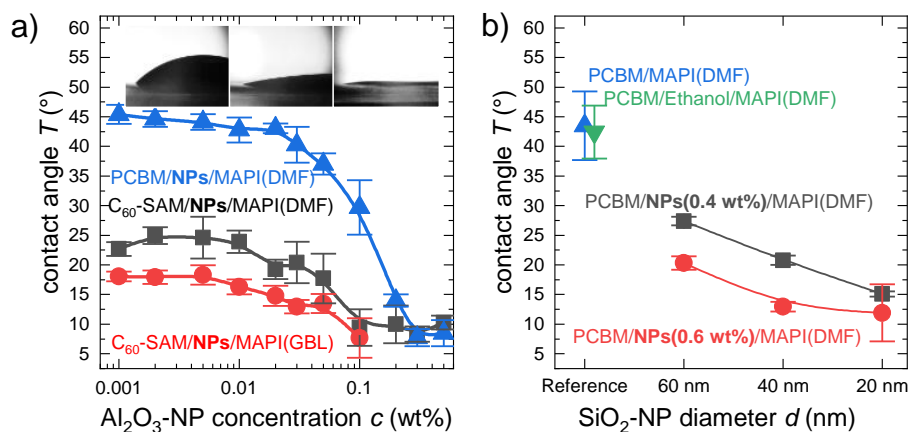
Secondly, the impact of the size of the NPs is investigated. Figure 4.7b shows, that particles with a smaller diameter lead to a stronger decline of the contact angle. For this study, ethanol based dispersions with 0.4 and 0.6 wt% concentration of SiO_2 nanospheres of diameters of 20, 40 and 60 nm (see Figure 4.5) were applied. Reference samples with untreated- and ethanol pre-treated PCBM surfaces have both high contact angles of about 45°, indicating a weak effect of pure solvent pre-treatment. Alternative solvents pretreatments with DMF, GBL or isopropanol seem to have similarly little influence on the contact angle.

The results indicate that the wetting behaviour is mainly influenced by concentration and size of the nanoparticles. The type of material has a lesser impact in this case where two oxidic NPs are applied, both capable of reducing the contact agle dramatically. Here with silicon oxide (SiO_2), the contact angle declines below 10° in case of the smallest particles (20 nm) at 0.6 wt% concentration. Notably, the variation of the diameter has a stronger effect on the contact angle than increasing the concentration. The same relation between contact angle and nanoparticle size is shown by Munshi et al. [101] in a different case study.

The well-established contact angle theories of Wenzel and Cassie predict that the roughness has a strong influence on the contact angle. They describe also the transitions from the non-wetting Cassie state, in which the droplet sits on top of a rough morphology with air trapped underneath, to a wetting Wenzel state, where the droplet completely penetrates the surface. [102, 103] In this case, a rising number of nanoparticles increases the roughness of the interface and leads to a direct decline of the wetting angle. In consequence, wetting behaviour indicates a Wenzel-like mechanism, at which the high surface energetic oxide particles increase the overall surface energy dominated by the fullerenes and act as capillary features that force the liquid to spread in between the gaps of the energetically favoured particles. Other fields of research, e.g. the fabrication of solution-processable organic transistors on hydrophobic surfaces, confirmed the validity of the Wenzel-like wetting mechanism. [104, 105]

There are two reasons why a decrease of the particle diameter favors the wetting even more. By keeping the mass concentration in the precursor dispersion constant, a reduction of the particle diameter leads to a significantly increased particle density at the interface. This can be observed as a higher surface roughness, which generally improves the wetting mechanism. [101, 106] An increased number of gaps between small particles with a higher surface energy exhibit a strong capillary force and therefore enable the perovskite solution to spread more easily. Furthermore, this explains why nanoparticles smaller than 20 nm show negative effects on the wetting. Due to their increased surface energy, the particles agglomerate (see Figure 4.6 $TiO_2 - NPs$) and thereby the capillary action is inhibited by the large distance between the clusters.

Following the results of the contact angle measurements, a good wettability of a typical perovskite solution on a fullerene interface usually requires a nanoparticle concentration of no more than 0.2 wt% at a diameter of 20 nm. Then the contact angle is so low, that a good spreading of the droplet allows for a complete coverage of the substrate. However, despite good coverage, when dealing with very hydrophobic surfaces like PCBM compared to C_{60}–SAMs, pinhole formation in the perovskite layer is often an additional issue, which is highly critical especially for the upscaling of perovskite solar cells. [107] In order to analyse this effect in more detail, two substrates (ITO and FTO) with different surface roughness have been prepared by treating the hydrophobic PCBM interface by a 0.2 wt% Al_2O_3-NP wetting agent layer to enable full wetting.

Figure 4.8a and c shows the formation of macroscopic pinholes in the crystallized perovskite layer in the top-view photographs and confocal micrographs after spin coating a MAPI based perovskite along with a toluene anti solvent step. The first surface $ITO/SnO_2/PCBM$ has a low roughness, which decreases the surface energy, and shows more and larger pinholes in contrast to the second rougher $FTO/SnO_2/PCBM$ sample.
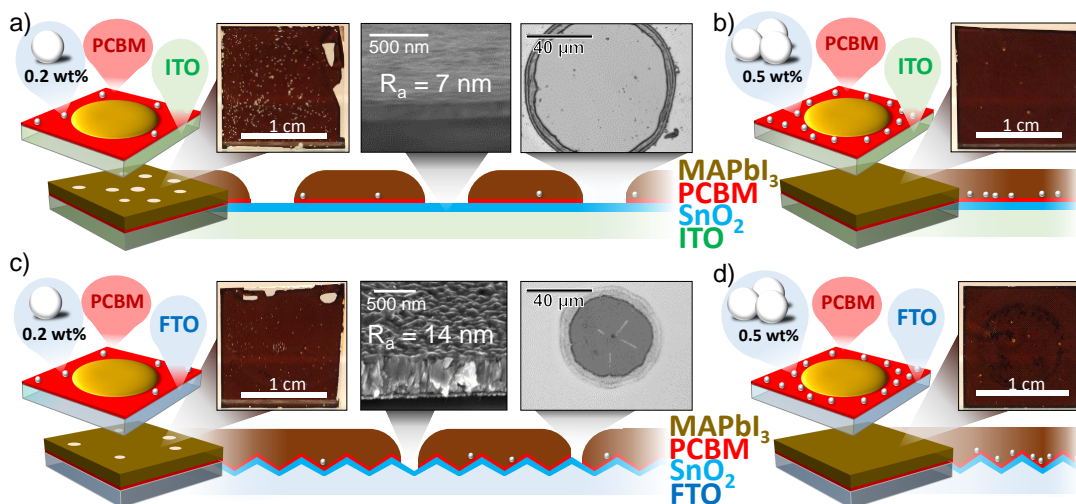

Figure 4.8: a-d) demonstration of pinhole defect suppression on different substrates (ITO/SnO_2, FTO/SnO_2) with PCBM as fullerene layer.

The pinholes form due to de-wetting of the still-wet precursor solution during spin coating prior to the perovskite crystallization. When the addition of toluene induces the phase transition, the shape of the pinhole freezes. Simultaneously, the toluene dissolves and removes the PCBM from the pinhole bottom. This example shows how substrate morphology, choice of materials and solvents can lead to different wetting issues. In both cases however, the pinholes are effectively suppressed by increasing the surface energy with the application of a higher concentration of Al_2O_3-NPs of 0.5 wt% as shown in Figure 4.8b and d.

Performance of perovskite solar cells employing nanoparticle wetting agent

In order to study the impact of the wetting strategy on the solar cell performance, full device stacks with variation in type, size and distribution of NPs and fullerene–absorber combinations were prepared. As described in the previous section, the concentration of the nanoparticle precursor dispersion coordinates the NP–distribution at the interface after spin coating, which has a direct influence on the wetting behaviour. A bad wetting at low concentrations requires a manual spreading of the droplet onto the PCBM interface with the pipette tip. In a setup with a simple MAPI absorber and PCBM fullerene interface ($FTO/SnO_2/PCBM/Al_2O_3$-NPs/MAPI/ Spiro/Au) the concentrations influence on the JV–characteristics was tested (Figure 4.9).
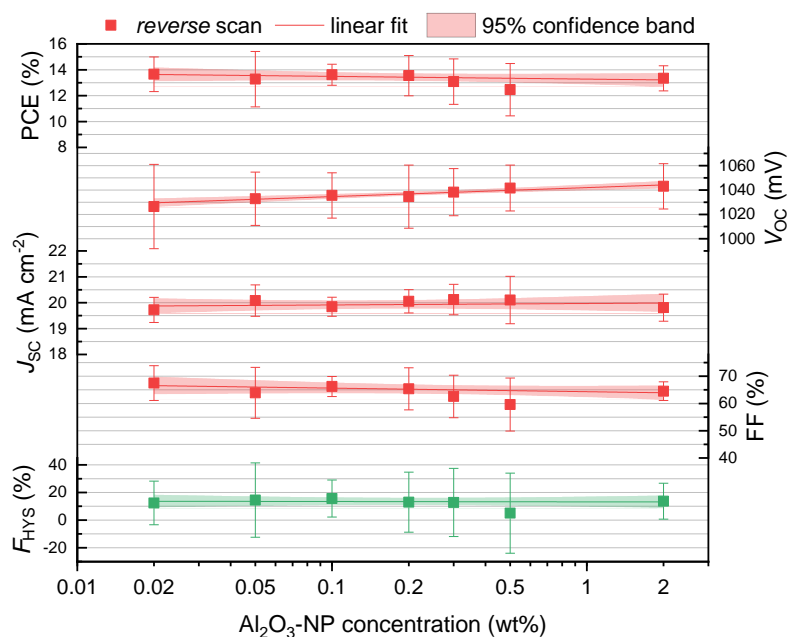
Figure 4.9: JV–characteristics of PSCs ($FTO/SnO_2/PCBM/Al_2O_3$-NPs/$MAPbI_3$/Spiro/Au) using different concentrations of Al_2O_3-NPs as a wetting agent.

Steady average PCE-results between 13 % and 14 % were achieved in all setups, which indicates that the inert metal oxide nanoparticles do not take negative effect on the device functionality. Even at a very high concentration of 2.0 wt%, which results to full NP-coverage of the interface, no significant loss in J_{SC} can be observed. This must be attributed to the transparent nature of the wide band gap Al_2O_3-insulator and in consequence very little parasitic absorption.

Additionally, although the interface may be covered by a large fraction when observed in top-view, the Al_2O_3-NP-layer is completely penetrable by the perovskite. This is validated by the cross-sectional micrograph in Figure 4.10a. In this perovskite-filled scaffold, the charges move unhindered, resulting in a normal charge extraction at the PCBM-interface. For this reason, the FF remains steady between 60 % to 70 %. It is also suggesting, that the passive NPs do not create deep trap states or recombination centres at the perovskite interface.
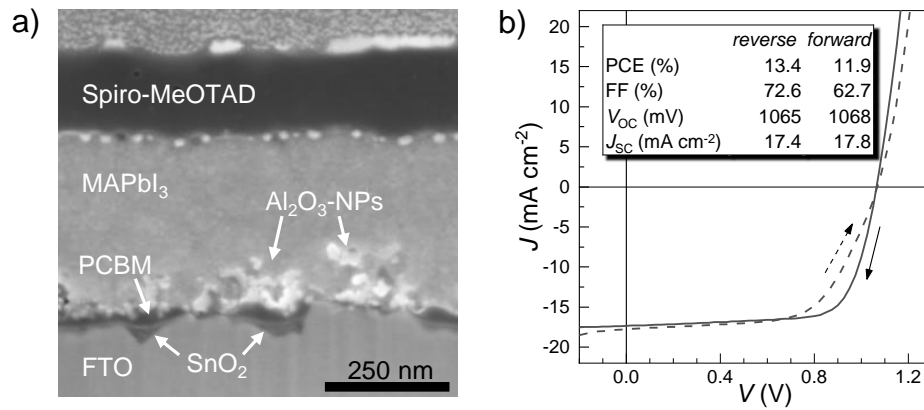
Figure 4.10: a) FIB–SEM through-lens-detector (TLD) back scattered electron imaging of a cross-section of a PSC ($FTO/SnO_2/PCBM/Al_2O_3$-NPs/$MAPbI_3$/Spiro/Au) using Al_2O_3-NPs as a wetting agent and b) the corresponding JV-response of the device.

The corresponding JV–curve which is displayed in Figure 4.10b resembles a typical behaviour. Despite the presence of the fullerene interlayer, the device is not free of hysteresis, because the PCBM layer is not optimized at this stage. But the presence of hysteresis gives the possibility to examine the influence of the nanoparticle density on F_{HYS}, which is displayed in Figure 4.9 at the bottom. There, no significant change can be observed, which implies that neither additional charge accumulation is inflicted by the NPs nor that they introduce a counteracting mechanism.

Concluding, the wetting agent based on nanoparticles can be used to guarantee homogeneous perovskite layers even on very hydrophobic fullerene interfaces. They also provide full device functionality, because the presence of the NPs does not show significant influence on the JV parameters of devices.

4.1.3 Increased efficiency and reduced hysteresis with fullerene interlayers

This section describes the final optimization steps that result in a reliable and efficient, opaque PSC architecture that can be used for the further development of a semitransparent setup. Here, two types of fullerenes PCBM and C_{60}–SAM are utilized in different setups in order to find the most efficient architecture. Additionally, a mixed cation perovskite absorber CsFAMAPIBr is introduced that promises higher efficiencies [33].

Due to the hydrophobic character of the fullerene layers, the previously (Section 4.1.2) developed wetting agent is used to enhance the deposition of a homogeneous perovskite layer.

Fullerenes (PCBM and C_{60}-SAM) in MAPI based solar cells

Next to PCBM, the following experiment utilizes C_{60}–SAM, which has selective side groups that preferably bond to the oxide surface of the ETL. In consequence a very thin and dense layer, referred to as a monolayer, forms at the interface. Devices with ITO/c-SnO$_2$/PCBM and ITO/c-SnO$_2$/C_{60}-SAM are fabricated in order to evaluate the influence of both approaches.

The performance of the corresponding PSCs benefits from both approaches. Figure 4.11 a–c) compares the $JV–$ and MPP–data of the ITO/c-SnO$_2$ reference device without fullerene interlayer and the setups with either PCBM or C_{60}–SAM. Obviously, both fullerene types effectively suppress the hysteresis that is strongly pronounced in the reference device. The hysteretic difference of FF and V_{OC} of between *rvs* and *fwd* scan is equalized with application of the fullerenes. Moreover, the absolute V_{OC}–value is improved by 30 mV to 40 mV. As a result of the hysteresis-free behaviour and the increased voltage, the stable power output at MPP is improved from 12.0 % to 13.5 % and 15.1 % for PCBM and C_{60}–SAM respectively.
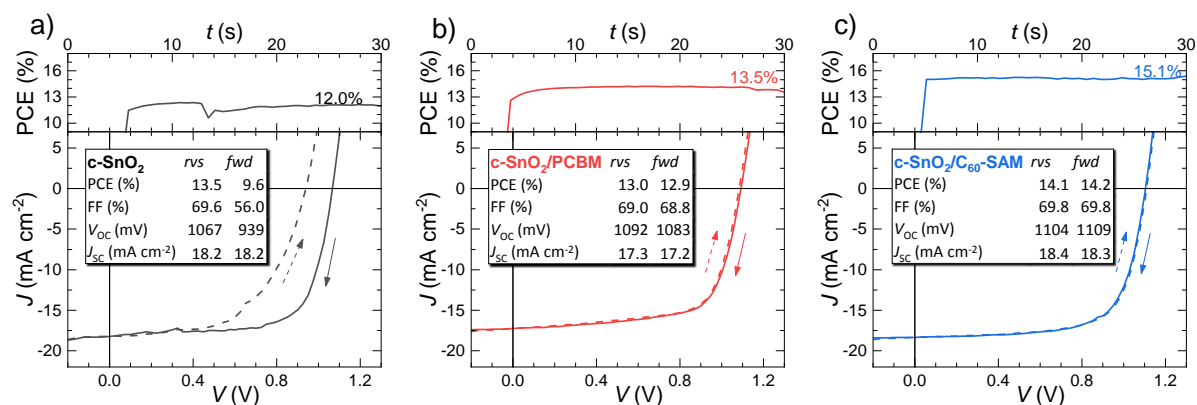
Figure 4.11: JV–characteristics and MPP responses of MAPI–based devices a) without fullerene interlayer, b) with PCBM and c) with C_{60}–SAM.

Similar to the previously discussed devices employing FTO, the PCBM–based cells of this study experience a J_{SC} loss of $-1\,\text{mA cm}^{-2}$ compared to the reference and the C_{60}–SAM device. This is most likely related to parasitic absorption by comparably thick PCBM layer. Here, a spin parameter set[1] was chosen to create a PCBM-film with a thickness 30 nm to 40 nm, which more effectively suppresses hysteresis than thinner layers.

Conclusively, in this setup with simple MAPI–absorber the combination of ITO/c-SnO$_2$/C_{60}-SAM as an ETL outperforms ITO/c-SnO$_2$/PCBM. Reducing the fullerene film thickness proved to be a decisive factor for a high current density. Moreover, C_{60}–SAM has an advance over PCBM regarding its wetting behaviour, because of a higher polarity.

Fullerenes (PCBM and C_{60}-SAM) in mixed cation CsFAMAPIBr solar cells

Utilizing the mixed cation perovskite absorber CsFAMAPIBr instead of the simple MAPI approach promises a higher efficiency, reproducibility, and stability [33]. But after the application of this absorber in a similar setup with ITO and compact c-SnO$_2$ a pronounced hysteresis in their JV–responses is observable. The results are displayed in Figure 4.12. In all scans a significant

---

[1] rotational frequency (f_{rot})= 2000 min^{-1}; $c_{PCBM} = 20\,\text{mg ml}^{-1}$; chlorobenzene (CB)

s-shape is observed around V_{OC} in either *rvs* or *fwd* scan direction or both. Additionally, the dotted curves that were measured under dark conditions have a very low current density at voltages above V_{OC}, when the diode is in a conducting state. Both observations imply that there is an energy barrier at the interface restricting charge injection/extraction. [108]

Figure 4.12: *JV*–characteristics of PSCs (ITO/c-SnO$_2$/(fullerene/SiO$_2$-NPs)/CsFAMAPIBr/Spiro/Au) a) without fullerene interlayer, b) with PCBM and c) with C$_{60}$–SAM.
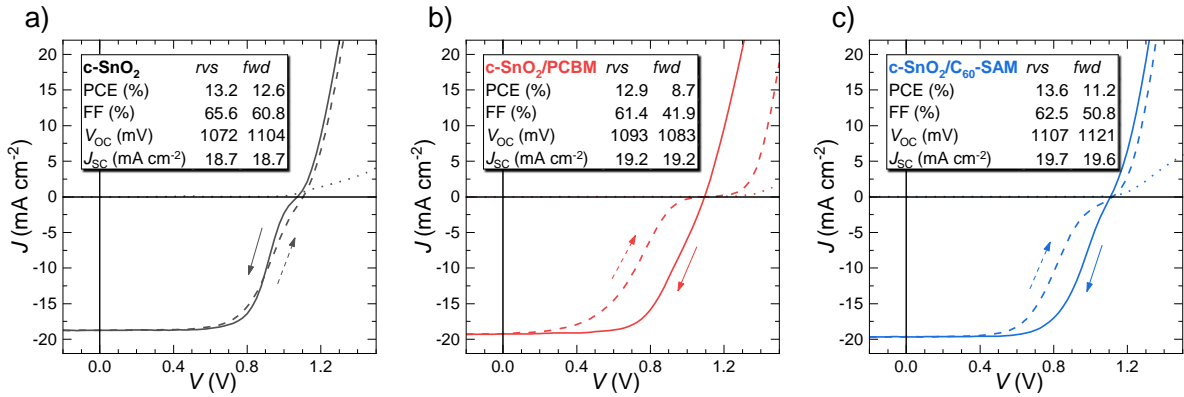
The occurrence of an energy barrier at the c-SnO$_2$/CsFAMAPIBr interface (Figure 4.12 a) could have two reasons. Due to the additional bromine content in the CsFAMAPIBr–absorber its band gap is slightly increased by ≈ 0.1 eV, which shifts both conduction and valence band relatively to the Fermi-level and thereby possibly introducing a barrier in connection to the SnO$_2$. Furthermore Aygüler et al. showed that the Fermi-level of SnO$_2$ — synthesized by atomic layer deposition — can be aligned via different annealing temperatures. [98] A misaligned Fermi-level would also lead to an energetically unfavourable band bending when it is in connection with the perovskite. Unfortunately the production process of the compact c-SnO$_2$ is based on an oxidation reaction at elevated temperatures and a controlled tuning of the Fermi-level did not prove to be feasible.

In both cases with PCBM and C$_{60}$–SAM as an interlayer the *JV*–response of the *rvs*–scan has only a minor s-shape, indicating a reduced energy barrier. On the other hand in *fwd*–direction it is notably stronger pronounced, especially with PCBM employed. Fullerenes are known to trap migrating ions [53, 109] and control unwanted charge accumulation, which both are strongly connected to hysteresis. Probably those properties introduce a dynamic ion- and charge–migration related mechanism to the interface, which adds a sweep-direction sensitive modulation of the energetic barrier. A very practical approach for overcoming this issue is the replacement of the sensitive sol-gel based c-SnO$_2$–synthesis by a more robust process.

SnO$_2$ layer deposition from SnO$_2$–nanoparticles in aqueous dispersion — developed by collaborators Hossain et al. — allows a more favourable operation in CsFAMAPIBr–based devices. Even without a fullerene interlayer, the device with a nanoparticle based SnO$_2$ as an ETL in Figure 4.13a shows no energy barrier indicators such as an s-shape or a unusual flat dark response. V_{OC} hysteresis is present though, so that the stabilized efficiency at MPP reaches only 13.8 %. Introducing C$_{60}$–SAM together with SiO$_2$-NPs for hysteresis suppression and a homogeneous layer formation leads to an improvement of the PCE up to 15.7 %. The corresponding data is shown in Figure 4.13b.
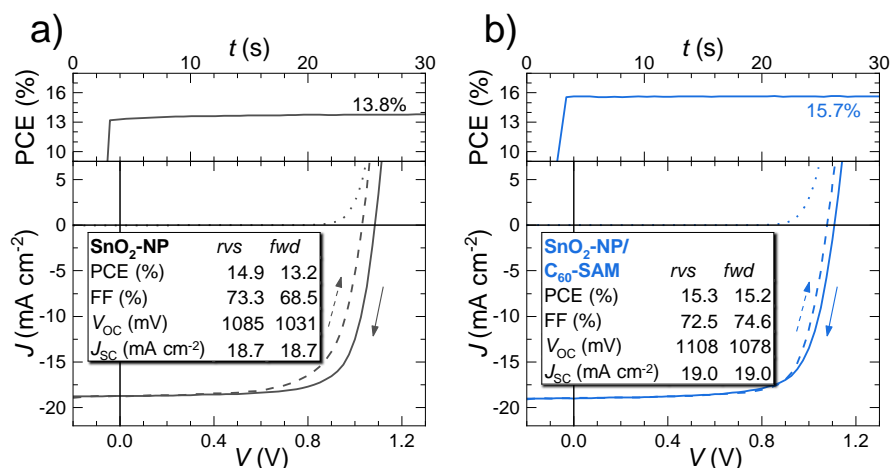
Figure 4.13: JV–characteristics of a) PSCs ITO/SnO$_2$-NP/CsFAMAPIBr/Spiro/Au and b) ITO/SnO$_2$-NP/C$_{60}$-SAM/SiO$_2$-NPsCsFAMAPIBr/Spiro/Au.

This section demonstrates how engineering the morphology and the ETL interface of the solar cells can lead to significantly increased efficiencies. With the introduction of fullerene interlayers at this interface, the hysteresis of the devices could be reduced to a minimum. The developed wetting agent based on NPs enables a reproducible deposition of the perovskite layer preventing the formation of de-wetting defects. These optimization steps combined with a more capable CsFAMAPIBr perovskite lead to an even higher performance of the PSC.

Concluding, the ETL interface at the front side of the devices is successfully optimized. This new base process is utilized for the upcoming integration of transparent electrodes at the rear interface. The development of suitable transparent contact materials for this purpose is part of the next section.

4.2 Sputter-deposition of suitable transparent conductive oxides as transparent electrodes

The following sputter depositions were conducted by Tim Helder under guidance of the author and the results reflect the main findings of his master thesis. [110]

For the transition from opaque to semitransparent PSCs, the metal rear electrode needs to be replaced by a transparent one. Considering the sensitive PSC layers, this requires a deposition process with a low thermal impact. Additionally, for implementation in a tandem cell, all electrodes must have a high overall transmittance, but especially a low parasitic absorption in the NIR range is demanded. Hence, the unfavourable front electrodes ITO or FTO should be also exchanged, as they only offer a good transparency in the visible range.

IO:H and IZO have been identified in Section 2.3 as suitable electrode materials promising to fulfil these high demands. In the following, the parameters for sputter deposition of these TCOs are evaluated, targeting to match the demanded properties. Thereby, all optimizations of the processes are carried out on glass substrates, while the implementation of the TCO layer into PSC devices follows later on in Section 4.3.

At first, Section 4.2.1 discusses the sputter deposition of IZO at ambient temperature conditions for low thermal impact. Focusing on controlling the doping level and the thickness, the aim is to find the optimal process for depositing a suitable rear electrode.

Subsequently, Section 4.2.2 discusses the sputter deposition and annealing of IO:H. A special focus lies on the post deposition recrystallization, which allows for extraordinary optical properties and makes IO:H the most promising material as a front electrode.

Finally, the new materials are compared to the traditional electrode layers FTO, ITO and ZAO.

4.2.1 Amorphous indium zinc oxide deposited with low thermal impact

The tuning of the optical properties of the amorphous IZO layers is accomplished only by variations of the sputter parameters, since is deposited from a target with a fixed In_2O_3:ZnO composition of 9:1 and the whole process is restricted to ambient temperature conditions. The next section discusses the influence of the pressure and the oxygen content on the doping level and the corresponding electrical and optical properties. Thereafter, the demanded electrode properties are fine-adjusted by means of controlling the layer thickness.

Optimization of doping level in IZO by variation of the pressure and oxygen content

The doping level of amorphous IZO films is controlled mainly by the partial pressure of oxygen in the sputter gas. [62, 64] With control over the doping level, the desired optical and electrical properties can be engineered. This section is about to evaluate the process parameters needed for a highly conductive and yet transmissive IZO electrode.

A series of IZO layers was prepared via DC sputter deposition varying the O_2 content from 1 % to 3 % at different process pressures of 10 µbar and 15 µbar. Figure 4.14a shows the results of Hall measurements in terms of resistivity (ρ), charge carrier mobility (μ) and electron density (N_e) with respect to the O_2 content. N_e decreases from high values of about 6×10^{20} cm^{-3} to values below 1×10^{20} cm^{-3} with increasing oxygen content, due to a decreased doping density by oxygen vacancies in the layer. [65]

Reasoned by the reduction of the vacancies, the scattering at ionized impurities is reduced, hence μ increases inversely to N_e. Additionally, abundant oxygen in the sputter gas prevents metal inclusions and metal pairs (In–In and In–ZnO) as further scattering centres.

At an oxygen content of 1.2 % and a pressure of 15 µbar ρ reaches a minimum with a moderate N_e and a high μ as labelled in the graph, which is comparable to the state of the art. [61, 62, 65]
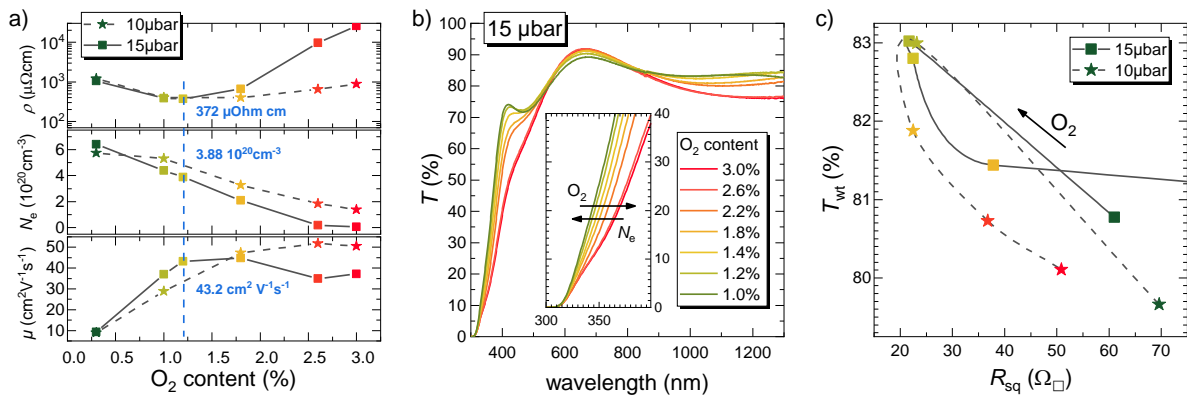
Figure 4.14: a) ρ, N_e and μ of IZO layers deposited at different O_2 contents in the sputter gas and pressures of 10 µbar and 15 µbar. The data is obtained by Hall measurements. b) Spectral T data of the layers deposited at 15 µbar. The inset shows the shift of the optical band gap according to the N_e. c) T_{wt} versus sheet resistance (R_{sq}) plot of the IZO layer series for determining the optimum process parameters.

The influence of the reduction of N_e (increase of O_2) on T is demonstrated in Figure 4.14b, where a redshift of the optical band gap is observable (inset), known as Burstein-Moss effect. On one hand, a high band gap (high N_e) would be beneficial for the application of the TCO as a front electrode, but on the other hand – as mentioned in Section 2.3.1 – a high N_e increases the free carrier absorption in NIR, which would be disadvantageous for tandem applications, where a high NIR transmittance is mandatory.

In order to find a compromise between conductive and optical properties, Figure 4.14 demonstrates the correlation between T_{wt} and R_{sq} from IZO layers with d of 170 nm deposited at varying O_2 contents. T_{wt} was obtained over the integration range from 400 nm to 1300 nm. Best results were achieved for a process with pressure of 15 µbar and an oxygen content of 1.2 %.

Controlling the absorptance and sheet resistance by adjustment of the layer thickness

Having control over the IZO layer thickness, enables a final balancing of its optical and conductive properties. [82, 111] Here, an IZO thickness variation is evaluated with respect to the R_{sq} and A.

Other than the expected inverse proportionality $R_{sq} \propto 1/d$, a power law dependency between the R_{sq} and d is observed from the linear regression in the double logarithmic plot in Figure 4.15a. These findings coincide with other studies and can be attributed to the thin dimension of the layers. [82]

With increasing d from 100 nm to 330 nm, the spectral A increases accordingly, as shown in Figure 4.15b. A quantification of the absorption up to a wavelength of 1300 nm in terms of J_{Abs}, shows that the increased absorption in the 330 nm layer leads to losses of almost 5 mA cm^{-2} compared to 2.5 mA cm^{-2} in the thinnest layer of 100 nm. An increasing contribution to the losses is contributed from the NIR range above 800 nm.
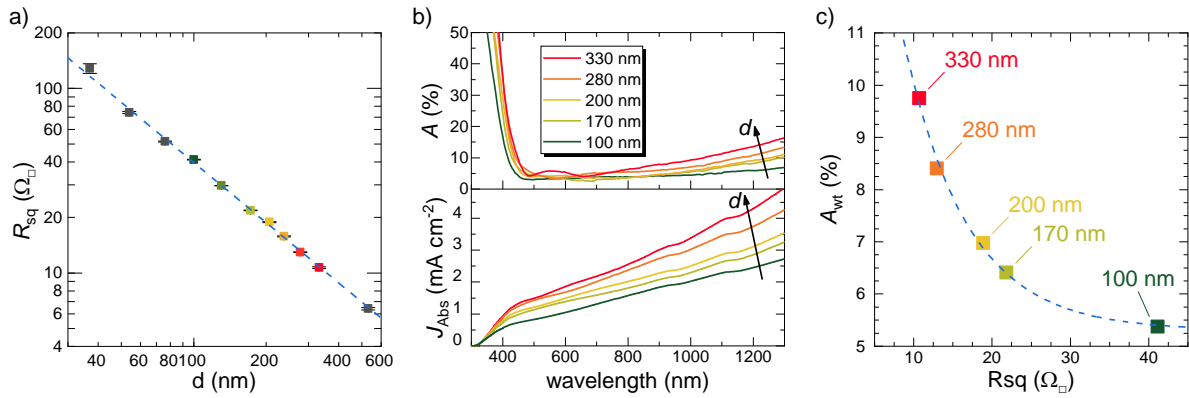
Figure 4.15: a) Double log plot of R_{sq} versus d for different IZO layers deposited at 1.2 % O_2 and 15 µbar indicating an inverse proportionality. b) Spectral A and J_{Abs} data of equivalent layers with d from 100 nm to 330 nm. c) A_{wt} versus R_{sq} plot of the IZO layer series for determining the optimum d.

The correlation between the R_{sq} and the weighted average absorptance (A_{wt}) (300 nm to 1300 nm) in Figure 4.15c indicates that a suitable compromise is matched for combinations of low A and R_{sq}. From the tested data set the combination with a layer thickness of 170 nm, an A_{wt} of 6.3 % and a R_{sq} of 22 $\Omega_\square$ is chosen to suit the demanded properties of a rear electrode for PSCs in the best way.

4.2.2 Hydrogen doped indium oxide with ultra-low absorption

In contrast to amorphous IZO, pure In_2O_3 grows in a crystalline form during sputter deposition. It is due to the incorporation of hydrogen in the crystal lattice during that process, that IO:H can be deposited as an amorphous layer, which in turn allows for a subsequent controlled annealing step in order to crystallize it. The prerequisites and consequences of this method will be discussed in the following. Subsequently, the doping level of the IO:H layers is adjusted in order to optimise the optical and electrical properties for the targeted application as a front electrode on the glass superstrate of PSCs.

Post deposition crystallization of hydrogenated, amorphously grown Indium oxide layers

The outstanding conductive and optical properties of IO:H rely on the controlled post-deposition-crystallisation (PDC) from a formerly amorphous hydrogenated indium oxide (a-IO:H) film. By this, the N_e is reduced, which in turn is compensated by a high μ to maintain sufficient conductivity. [15, 16] The amorphous growth, most likely induced by hydroxylation, [112] demands sufficient hydrogen doping of the pure In_2O_3 during the sputter deposition, which is traditionally accomplished by water vapor (H_2O) injection into the sputter gas (Ar). [15] Here, argon and hydrogen (Ar/H_2) are used as a mass flow controllable reactive gas component for initiating the hydroxylation of the IO:H layers.

The H_2 induced amorphous growth of a-IO:H is investigated by XRD. The resulting patterns in Figure 4.16a reveal that for low amounts of hydrogen $<2.0\%$ H_2 the as-deposited layers (dashed lines) grow already in a polycrystalline (*PC*) phase with a preferential (222) orientation. The preferentially oriented crystalline character of the layer remains throughout the subsequent annealing step (solid lines), visible in the dominant intensity of the (222) peak $**$ and related crystallographic reflections $\circ$ (332) and $\diamond$ (444).

As expected, raising the H_2-content to $>2.8\%$ leads to completely amorphous growth and allows for the aforementioned controlled PDC. After the transformation from amorphous to crystalline, further dominant reflections (+) of the indium oxide structure are apparent, indicating no preferential lattice orientation. A less intense signal of the (222) peak ($*$) supports the observation.

Furthermore, at low amounts of hydrogen (H_2), a shift of the peak positions towards lower angles is observed, if compared to the reference structure data of In_2O_3, which is indicated by the vertical lines. [113] In contrast, the post-deposition-crystallised hydrogenated indium oxide (PDC–IO:H) layers do not show this effect. The shift may be reasoned by lattice strains originating from crystal defects, which are effectively outmanoeuvred by the PDC approach. This effect is evaluated by GIXRD in more detail later in this Section.
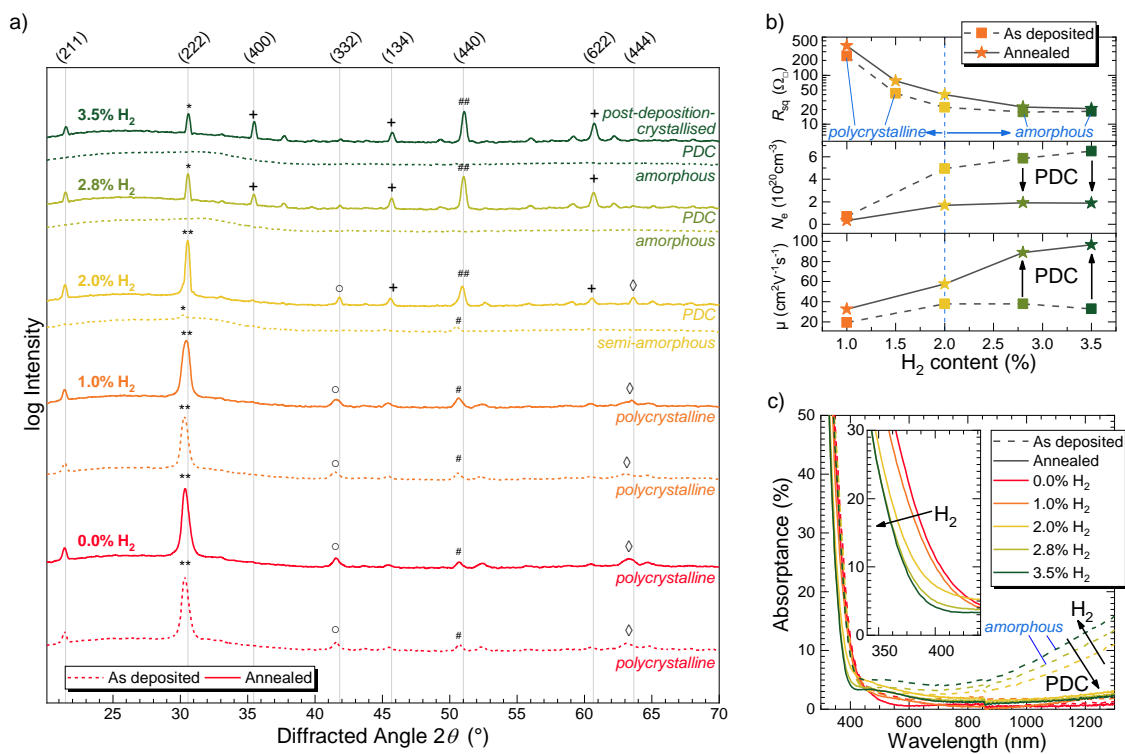
Figure 4.16: a) XRD patterns of IO:H layers deposited at different H_2 contents in the sputter atmosphere. The dashed lines represent the as deposited layers, while the solid lines represent data from the same layers after annealing at 200 °C for 30 min. The vertical lines indicate the pure In_2O_3 structure. [113] b) R_{sq}, N_e and μ data and c) spectral A data of equivalent layers. The inset shows the shift of the optical band gap.

As demonstrated in Figure 4.16b, the H_2 content and the PDC profoundly influence the R_{sq}, N_e and μ. In general, the R_{sq} decreases significantly with a higher hydrogen doping. Above 2.8 % H_2 the R_{sq} reaches $20\,\Omega_\square$ to $22\,\Omega_\square$ before and after PDC, respectively. The hydrogen doping of the as deposited layers leads to a significant increase of N_e from $1 \times 10^{20}\,cm^{-3}$ to $6 \times 10^{20}\,cm^{-3}$, which is the main cause of the improvement of the R_{sq}. But the higher doping level also limits μ to $30\,cm^2\,V^{-1}s^{-1}$ to $40\,cm^2\,V^{-1}s^{-1}$ due to ionized impurity scattering. [114]

After annealing, it is only due to the PDC of the amorphously grown layers, that μ is fundamentally improved up to nearly $100\,cm^2\,V^{-1}s^{-1}$ while N_e is decreased again to moderate $2 \times 10^{20}\,cm^{-3}$. By this, a low R_{sq} is achieved in combination with a favourably low N_e, that aids the optical properties of the PDC–IO:H.

Figure 4.16c proves that the PDC treatment leads to an exceptionally low spectral A in the NIR beneath 3 %, while the as deposited, amorphous layers exhibit a much higher A above 10 % due to free carrier absorption. Furthermore, the controlled PDC of samples with high H_2 doping results in a beneficial shift of the optical band gap as shown in the inset.

Optimization of high mobility PDC–IO:H layers with excellent NIR transmission by oxygen doping

Similar to IZO, the amount of O_2 doping controls the conductive and optical properties of a-IO:H and PDC–IO:H. Here, a variation of the O_2 content in the sputter gas is used to optimise N_e and μ for the demanded low A and low R_{sq}, while the other sputter parameters H_2 content, pressure and gas flow are adapted from the previous findings.

Results from Hall measurements in Figure 4.17a demonstrate how the addition of O_2 to the sputter gas decreases the N_e in a-IO:H (dashed, boxes), which is attributed to the decreased formation of metal inclusions and metal pairs (In–In) and defect states. [115] Correspondingly, μ increases to $\approx 40\,cm^2\,V^{-1}s^{-1}$, which leads to a minimum ρ of $292\,\mu\Omega\,cm$ at the highest O_2 content of 3.2 %. For comparison, the ρ, N_e and μ of the O_2-optimized IZO layer are also depicted in the graphs (blue boxes).

After PDC (solid, stars), N_e is reduced drastically, but shows almost no correlation to the former O_2 content. This may be due to the annihilation of oxygen vacancies or the outgassing of H_2 during annealing. Exact knowledge about this mechanism is still missing. Now, μ is the remaining decisive factor for controlling the resistivity. μ is limited mainly by the free mean path of electrons, which is in the range of the grain size and hence related to scattering mechanisms like grain boundary scattering. [116] Here, a maximum μ of $95\,cm^2\,V^{-1}s^{-1}$ is observed at a O_2 content of 2.8 %, which leads to a minimum ρ of $380\,\mu\Omega\,cm$ — a disadvantage of 23 % compared to a-IO:H.

However, the optical properties of PDC–IO:H are superior to a-IO:H as demonstrated by the spectral A and J_{Abs} graphs in Figure 4.17b. Along with the increase of O_2, the A of both a-IO:H (dashed) and PDC–IO:H (solid) declines greatly. According to the higher N_e of a-IO:H, the effect is dominantly visible in the NIR due to free carrier absorption. The quantification of A in terms of J_{Abs} in the range of 300 nm to 1300 nm shows that an O_2 content of 2.8 % or more reduces the amount of parasitic absorption loss to less than $3\,mA\,cm^{-2}$ for a a-IO:H layer of 185 nm thickness. The PDC (solid lines) leads to an additional reduction down to $2\,mA\,cm^{-2}$, mainly due to a reduced absorption in NIR above 800 nm.
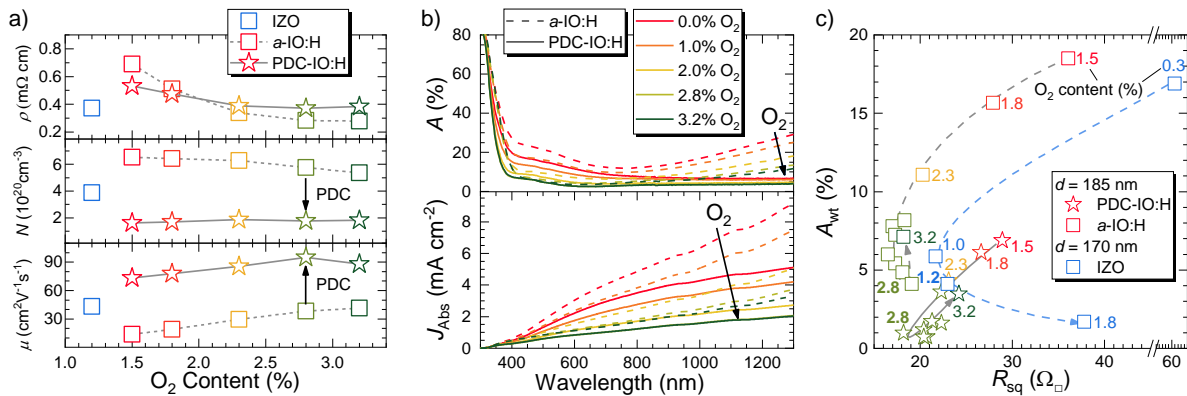
Figure 4.17: a) ρ, N_e and μ of IZO, a-IO:H and PDC–IO:H, deposited at different O_2 contents in the sputter atmosphere. b) Spectral A and J_{Abs} of equivalent layers with a d of 185 nm (without IZO). c) A_{wt} versus R_{sq} plot of the layer series for determining the optimum O_2 content.

Since the parasitic NIR absorption is of great importance for tandem application, Figure 4.17c shows the A_{wt} in the range of 800 nm to 1300 nm versus R_{sq} for the series of IO:H layers in order to find the a suitable O_2 content for the best compromise (see equation 2.17). For comparison, a similar series of IZO layers is also shown in the graph.

As intended, the PDC–IO:H (stars) exhibits superior low A_{wt} values of less than 2 % and R_{sq} of around 20 $\Omega_\square$ at an O_2 content of 2.8 %. The variety of data points indicate that the replication of the exact properties with the chosen parameters is not always possible. Since the deviations are already observed in the as deposited a-IO:H layers (boxes), they are likely to be a result of different preset conditions of the target material, e.g. partial depletion or enrichment of oxygen or indium, likewise.

Despite the deviations in reproducibility, it is obvious from this 'figure of merit' that PDC–IO:H outperforms a-IO:H as well as IZO in terms of NIR transparency and conductivity. Because of the necessary annealing step it is particularly suitable as an alternative front electrode for PSCs which is deposited on the superstrate glass. For the rear electrode, both a-IO:H and IZO are promising candidates, showing similar properties if preparation parameters are chosen well.

Lattice strain analysis by GIXRD on annealed, crystalline IO:H layers

In the XRD patterns of annealed IO:H layers in Figure 4.16, a general diffraction peak shift towards smaller angles was observed for specimen, which were deposited at low amounts of H_2. This section evaluates, how the hydrogen doping affects the structural properties of the annealed IO:H films via a more detailed XRD data analysis and the use of additional GIXRD measurements.

Figure 4.18a demonstrates the observed shift of the peaks exemplarily for the (222) reflection, which has the highest intensity. For being able to compare the peak positions and their shapes, the patterns were normalized because (222) peaks of the low H-doped films exhibit a much higher intensity due to the preferentially oriented crystal growth, as shown previously in Figure 4.16. A 2θ shift of $\approx 0.3°$ is observed, comparing the In_2O_3 film with 0.0 % H_2 to the IO:H film deposited at 2.8 % H_2. Remarkably, the lattice parameters of the highly H-doped films match better with the reference lattice of pure In_2O_3, indicating a low lattice strain despite the high

hydrogen doping. This may be due to the out-gassing of H_2 during the PDC of the amorphous layers in the annealing step. The low H_2 samples, which grow already in a polycrystalline form during deposition, do not exhibit a significant phase change during annealing and the peak positions remain shifted. The shift towards lower angles indicates a de-compressional strain on the lattice with increased interatomic distances in the unit cell.
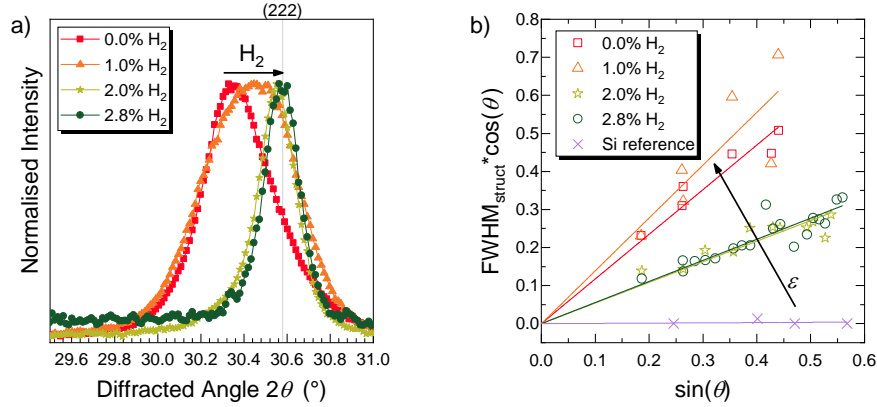
Figure 4.18: a) Shift of the (222) diffraction peak (normalized) in the XRD patterns of annealed IO:H films that were sputter deposited at different H_2 gas contents. In addition to the peak shift, the variation in the FWHM indicates a structure related broadening. Similar observations are made for the other reflections over the full scan range (compare Figure 4.16a). b) Williamson-Hall plot for the same films for evaluation of the structural diffraction peak broadening ($FWHM_{struct}$) of all peaks that are distinguishable from background and neighbour peaks. The regressions reflect cases where only microstrain contributes to the broadening at the absence of crystallite size induced broadening (y intercept = 0). Then, the slope of the regression relates to the lattice strain $d/dx = \epsilon$ induced peak broadening, following equation 2.21. Reference data from a polycrystalline Si sample shows neither crystallite size nor microstrain broadening.

Additionally, the films with 2.0 % and 2.8 % H_2 show a narrower FWHM compared to the other films. The broadest peak is observed for the 1.0 % H_2 specimen. A peak broadening generally indicates either a non-uniform influence of microstrain – caused by defects such as dislocations or antiphase grain boundaries – or contribution of nanometre sized crystallites (compare Section 2.5).

With the aid of a Williamson-Hall plot, the different contribution to the peak broadening can be distinguished from another following equation 2.21. Therefore, the measured FWHM of all peaks of the specimens are corrected by the instrumental contribution via a standard reference measurement with the same scan parameters. The corrected values are called structural diffraction peak broadening ($FWHM_{struct}$). Figure 4.18b depicts the resulting Williamson-Hall plot for the different IO:H specimen and a polycrystalline silicon reference sample.

For fitting the regressions in Figure 4.18b, it is assumed that only microstrain contributes to the $FWHM_{struct}$:

$$FWHM_{struct} \cdot \cos\theta = \underbrace{\frac{K\lambda}{L}}_{y \text{ intercept=0}} + \underbrace{4\epsilon \cdot \sin\theta}_{\text{microstrain}} \tag{4.1}$$

If crystallite size term is included, the residual of the fit does not change significantly, which indicates that crystallite size broadening is insignificant in these measurements. Comparing the slopes of the regressions, which directly correlate to the microstrain ϵ, no strain is observed for the reference Si specimen, but the IO:H samples all show a significant amount of microstrain. The highest microstrain is present in the sample deposited at 1.0 % H_2, but due to the preferentially oriented crystals, only a few diffraction peaks are visible, which reduces the precision of the fit. All microstrain values that are obtained from the Williamson-Hall plot are listed in Table 4.1.

H2 content (%)	Microstrain ϵ (%)
0.0	0.293 ± 0.011
1.0	0.314 ± 0.192
2.0	0.135 ± 0.005
2.8	0.138 ± 0.004

Table 4.1: Results of the microstrain ϵ evaluation from the Williamson-Hall plot in Figure 4.18 for annealed IO:H samples which were sputter deposited at different H_2 sputter gas concentrations.

So far, the strain analysis was based on the XRD data that was obtained from scans in the Bragg-Brentano geometry, which is a focused setup with a high penetration depth of the x-rays into the material. In case of the thin IO:H layers with a thickness of about 180 nm, the beams petrate the full depth of the film. If possibly different In_2O_3 phases are apparent, the diffracted patterns contain only the averaged information of the phases.

As a matter of fact, Muydinov et al. have already reported such different phases in IO:H layers with different morphological and electrical properties. [66] Hence, the following GIXRD measurements are designed to evaluate, if the observed microstrain of these specimens also originates from local phase differences, e.g. strains at the front surface or at the rear interface on the glass substrate.

Therefore, a series of GIXRD scans was performed at different ωs ranging from 0.1° to 3° for each specimen. Thereby, the penetration depth of the x-rays into the material increases with ω as demonstrated in Figure 4.19 for a pure In_2O_3 layer following equation 2.22. It shows that the incident beam penetrates only the first few nanometres of the layer surface at low incident angles of 0.1° to 0.3° below ω_c. With higher angles, the penetration depth increases and reaches the full layer thickness of the specimen at about 1.5°. Since the diffracted beam must travel a second time through the layer, the actual information depth is lower than the penetration depth. [79]
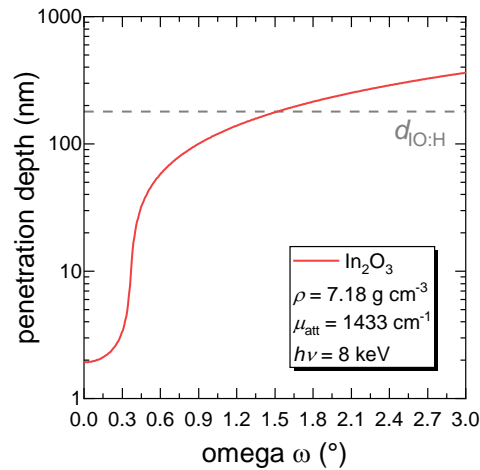
Figure 4.19: Penetration depth of x-rays into a In_2O_3 layer in dependence of small incidence angles ω. The data is calculated via equation 2.22 using the linear attenuation coefficient (μ_{att}) of pure In_2O_3 for the x-ray photon energy of $h\nu= 8\,keV$ (Cu Kα). [117] The reference line marks the thickness $d_{IO:H}$ of the specimens in the experimental series.

The diffracted angle (2θ) was scanned from 28° to 32° in order to monitor the position of the (222) reflection in each iterative measurement. The same procedure was conducted on the Si reference sample in the 2θ range from 27° to 30°, monitoring the (111) peak. The close vicinity of the reference peak is important for a reliable correction calculation, because for each set of ω and 2θ angles in the measurement series, the instrumental influence on the peak broadening changes.

Figure 4.20 depicts the (222) reflection of the four specimen measured at an incident angle ω of 3.0°, already corrected for the instrumental broadening and the Cu Kα_2 reflection. At this high angle the penetration depth of the beam is sufficient to reach the rear of the layer and so the diffracted peak carries the information of the complete sample thickness. In order to find a satisfying fit to the peaks, it is necessary to use two superimposed peak functions (pseudo-Voight) ϵ_1 and ϵ_2, which generally indicates the presence of two different phases. In all cases, the broad function ϵ_1 has a lower intensity and accounts for the small shape asymmetry of the measured peaks, while the narrow function ϵ_2 has a higher intensity and describes the main shape of the peak. In case of the samples with higher hydrogen content, ϵ_2 is significantly shifted against ϵ_1, resulting in a asymmetric convoluted peak shape.
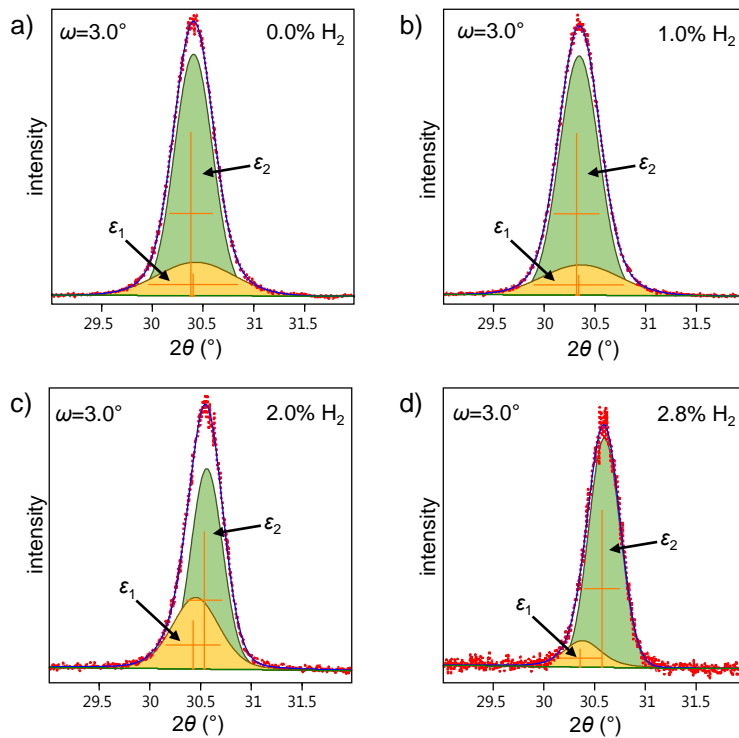
Figure 4.20: Fitting of the (222) diffraction peak of IO:H layers which were sputter deposited at different H_2 contents a) 0.0 %, b) 1.0 %, c) 2.0 % and d) 2.8 %. The diffraction data is obtained from GIXRD measurements at an incident ange ω of 3.0° and has been corrected for the Cu Kα_2 diffraction and the instrumental contribution to the peak broadening. The fitting is only satisfactory accomplished by using two pseudo-Voight functions as indicated by ϵ_1 and ϵ_2.

These double peaks, indicating the presence of two phases ϵ_1 and ϵ_2, appear in most of the measurements. Their position, intensity and shape is strongly dependent of the specimen and the incident agle ω. The evaluation focuses on three main factors: (i) The low intensity of the ϵ_1 peak indicates a smaller volume fraction of the phase compared to ϵ_2. (ii) The angular positions of the maximums of ϵ_1 and ϵ_2 indicate the d-spacings of the (222) diffraction planes, and thus the lattice parameters of the unit cell. (iii) The broader FWHM$_{struct}$ of ϵ_1 indicates a higher microstrain as in ϵ_2.

Figure 4.21 evaluates the intensity, the d-spacing and FWHM$_{struct}$ with respect to the incident angles ω for the fitted high strain phase peaks ϵ_1 (a) and the fitted low strain phase peaks ϵ_2 (b). The d-spacing values have been corrected for the shift of the Bragg reflection around ω_c using equation 2.23.

54
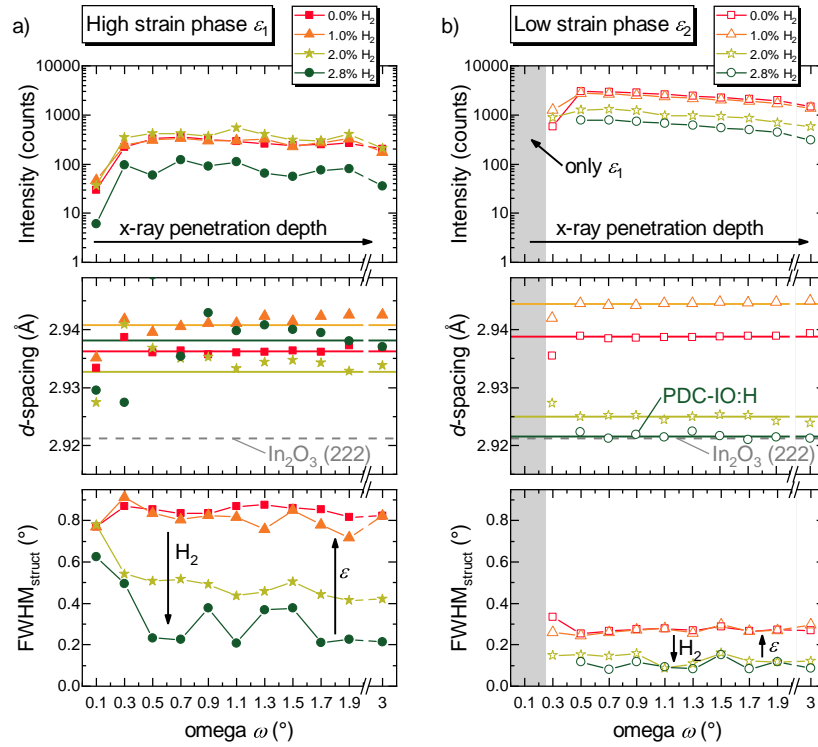
Figure 4.21: Intensity, d-spacing, and FWHM$_{struct}$ versus incidence angular (ω) of the (222) peaks of a) the high–microstrain phase ϵ_1 and b) of the weak–microstrain phase ϵ_2 of the IO:H films that were sputter-deposited at different H_2 gas concentrations. The d-spacing value is calculated from the maximum of the peak-fits to the corresponding phase-reflection at the (222) position around $2\theta=30.5°$. The reflections were recorded with GIXRD under different incident angles ω.

(i) First of all, comparing the intensities of the ϵ_1 and ϵ_2, the low strain phase ϵ_2 generally exhibits a higher intensity of about one magnitude for all specimen. But at a low ω angle of 0.1°, the diffracted peak can be fitted by only a single broad ϵ_1 function, indicating the absence of the low strain phase ϵ_2 at the surface of the layers.

(ii) Due to their broader appearance and lower intensity, the precision of the determination of the peak positions of the ϵ_1 phase is not very accurate. Hence, the calculated values for the d-spacing, show a relatively high variance especially at low angles, where the intensity drops. The straight lines indicate the corresponding d-spacing value that is obtained during the fitting procedure for the Bragg shift correction. All specimens show a larger d-spacing in the high strain phase ϵ_1, than expected from the simple In_2O_3 structure. Additionally, different ϵ_1 d-spacing are observed for the specimen deposited at different H_2 contents, but no clear trend is conceived here.

However, the lattice parameters of the low strain phase ϵ_2 are significantly dependent on the H_2 content and the effect of the PDC treatment. The d-spacing of the PDC–IO:H layer shows a high agreement with the reference In_2O_3 structure. A small offset is observed, for the sample with a lower H_2 content. This sample was not completely amorphous after sputter deposition (compare Figure 4.16a), which implies that during PDC the lattice was not completely reorganized, leaving a residual strain of the unit cell. The largest d-spacing is observed in the sample deposited at

55

1.0 % H_2. Probably the strain of the unit cell originates from the interstitial hydrogen doping. It seems, that the annealing step did not release the stress of the lattice. A large d-spacing is also obtained from the sample that was deposited without H_2 addition. Here, the strain might be introduced by oxygen doping.

(iii) Evaluation of the $FWHM_{struct}$ indicates that the H_2 content has also a high influence on the broadening of both peak functions ϵ_1 and ϵ_2. A reduced broadening speaks for a low microstrain ϵ, which would indicate a low density of defects. As expected, the high strain phase ϵ_1 exhibits large FWHM, especially in the samples with low H_2 content. In ϵ_2, these samples show also a higher strain, than the PDC–IO:H layers.

In order to quantify the amount of strain broadening, that each phase contributes to the diffraction pattern at a certain incident angle, Figure 4.22 shows the relative peak intensities of ϵ_1 and ϵ_2 normalized to 100 % versus ω. The colour coding describes the amount of microstrain ϵ that is calculated from the $FWHM_{struct}$ for each phase.
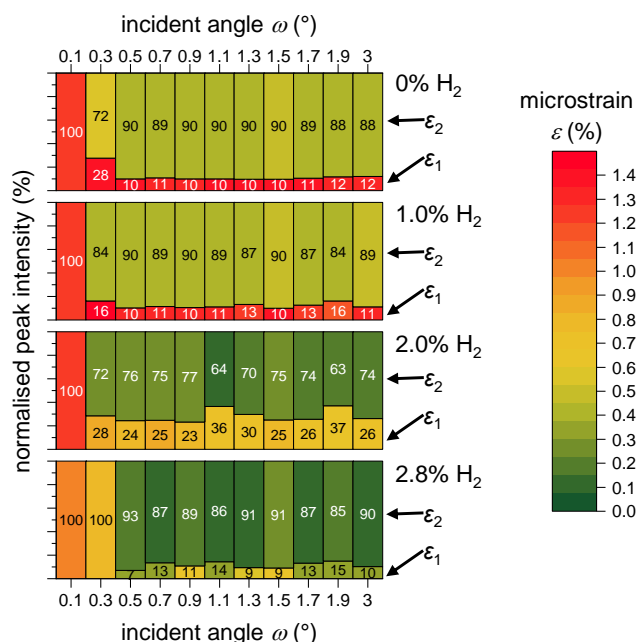
Figure 4.22: Bar diagrams showing the ratio of the maximum intensity (denoted in %) of the ϵ_1 and ϵ_2 (222) peaks versus ω for IO:H samples, which were deposited at different H_2 gas concentrations. The colour code indicates the corresponding microstrain (ϵ) that is obtained from the $FWHM_{struct}$ of each peak.

At a small ω of 0.1°, only the high strain phase ϵ_1 is observed in all specimens. At this angle close to ω_c, the penetration depth of the incident beam is only several nanometres, indicating a ϵ_1 layer with a high density of defects at the surface of the samples. The strain in this layer is higher than 1 %. Noticeable, the PDC–IO:H sample (2.8 % H_2) exhibits a thicker ϵ_1 surface layer up to 0.3°, but here the strain of ϵ_1 is generally lower (0.7 % to 0.8 %) as indicated by the color code.

At higher ω, the contribution of ϵ_2 dominates, which implies that ϵ_2 has a dominant presence in the bulk. A higher strain between 0.3 % to 0.4 % is determined for the bulk phase ϵ_2 of samples with low hydrogen content, compared to the samples deposited at 2.0 % and 2.8 % H_2 that exhibit a low ϵ_2 strain of 0.1 % to 0.2 %. The contribution of the ϵ_1 phase is measurable at all angles, most likely originating from the ϵ_1 surface layer, but an additional presence of ϵ_1 in the bulk may not be excluded.

In case of the 2.0 % H_2 sample, the ϵ_1 to ϵ_2 signal ratio is higher as compared to the other samples, which is due to the lower maximum intensity of the (222) peaks in the samples. Hence, the ϵ_2 signal is reduced. In contrast, the preferential lattice orientation in the samples deposited at a low H_2 content leads to a higher ϵ_2 peak intensity (compare Figure 4.21b).

Comparing the ϵ values obtained from the Williamson-Hall evaluation in Table 4.1 with the ones for ϵ_2 from the GIXRD investigation, a good match is observed, indicating a rather homogeneous microstrain level throughout the layer thickness. The GIXRD results prove, that a thin layer at the surface of all samples exhibit an increased microstrain, which implies a higher defect density.

For the application of the IO:H layers as front electrodes in solar cells, two main conclusions may be conceived.

(i) PDC–IO:H deposited at 2.8 % H_2 shows the best crystallographic properties in terms of a low microstrain, thus a low defect density, and a undistorted unit cell, thus a low doping level. The low defect density contributes to a high charge carrier mobility (μ), because defects act as scattering centres. The low doping level results in a low N_e, which reduces the free carrier absorption at in the NIR range. Both properties are only achievable, when the IO:H layer is deposited amorphously prior to a PDC. Some residual microstrain in the layer indicates that there is still room for improvements, to decrease the defect density even further and achieve even higher μ values.

(ii) The thin top layer that exhibits a higher amount of microstrain, might not contribute much to the macroscopic optical and electrical properties of the film, but it could cause deviations of the interface properties, when it is in contact with the ETL in the solar cell. Without knowledge of the nature of the strain causing defects, it is difficult to foretell, if they have a significant effect on the charge extraction or injection in the final device.

4.2.3 Comparison between optimized IZO and IO:H layers and commercial available TCO substrates

This section compares the optimized IO:H and IZO materials to the commercially available TCOs such as FTO and ITO that are primarily used in PSC. Additionally, ZAO is included in the comparison, because it represents the standard TCO in CIGS solar cell technology, [67] which is also utilized in the CIGS cells that are introduced later on in this study.

Figure 4.23a shows representative absorptance spectra of the set of TCO layers. Their individual thickness is denoted in the diagram legend. As expected, the in-house prepared TCOs exhibit a smaller A than the commercial TCO layers.

Big differences are also observed in the position of the optical band gap (E_g). For the compared materials, FTO and ITO show the highest optical band gaps with approximately (3.95 ± 0.05) eV. a-IO:H exhibits an optical band gap of (3.85 ± 0.03) eV, increasing up to (3.90 ± 0.03) eV after the annealing step (PDC–IO:H). For these high band gap values of FTO, ITO, as-deposited and annealed IO:H a larger uncertainty is assumed because the absorption edge of the glass substrate may affects the TCO absorption edge. Nevertheless, the calculated band gap values agree within the accuracy with the stated values in literature [115, 118, 119]. IZO and ZAO exhibit smaller band gaps of (3.79 ± 0.02) eV and (3.63 ± 0.02) eV and hence can be determined with a higher accuracy. These values are comparable as well with values given in the literature [63, 83]. Optical band gap calculations are performed as described in Section 3.2.1.

For illustrating the impact of the different A responses, Figure 4.23b depicts the cumulative J_{Abs} of the layers in the range from 300 nm to 1300 nm. With respect to application in tandem cells, it is meaningful to divide the solar spectrum in the UV/Vis range and the NIR range. The insets of the diagram show the J_{Abs} of the layers in these two ranges. Over the full spectrum range, FTO exhibits the largest J_{Abs} of over 7 mA cm^{-2}, partly reasoned by the large layer thickness of 550 nm. ITO has also a high loss of about 5 mA cm^{-2}, followed by ZAO. IZO and a-IO:H show low losses of about 2 mA cm^{-2} and PDC–IO:H stays below 1 mA cm^{-2}. In the UV/Vis range, the IZO and ZAO layers have quite high losses of up to 1.6 mA cm^{-2} due to their comparably narrow band gap. The NIR regime sees the highest losses in ITO and FTO.

In order to compare the optical properties of the layers to the conductive ones, 4.23c shows the A_{wt} versus R_{sq} for the set of TCO layers and for the different spectrum ranges as indicated. Here, two a-IO:H and PDC–IO:H layers are added, which have an increased film thickness of 230 nm. With the R_{sq} reduced by 5 $\Omega_\square$, they are suitable candidates for a more efficient front electrode compared to the thinner layers. The increased film thickness also leads to an increased A_{wt}. However, even with the larger thickness PDC–IO:H outperforms all other TCOs with a ultra low A_{wt} of about 2 % over the full spectrum at an R_{sq} of 15 $\Omega_\square$. ITO and FTO exhibit both a better conductivity with R_{sq} values down to 7 $\Omega_\square$, but they have a significant A_{wt} deficit, especially in the NIR range.
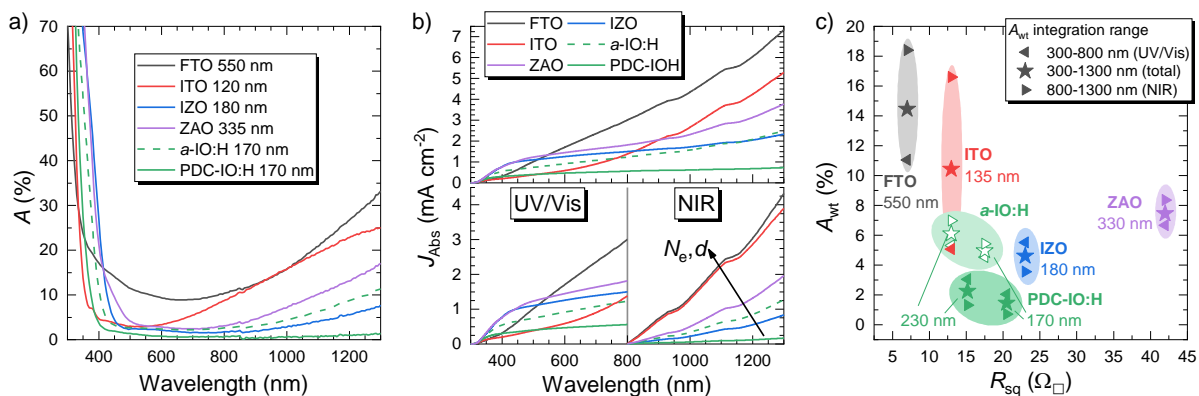
Figure 4.23: a) Absorptance spectra of different TCO materials. IZO, a-IO:H and PDC–IO:H layers are compared with standard process ZAO, ITO and FTO. b) J_{Abs} curves for the respective TCOs over the total spectral range from 300 nm to 1300 nm and in the UV/Vis and NIR range (insets). c) A_{wt} versus R_{sq} plot for the same layers in the respective spectral ranges. Additionally, the data for IO:H layers with an increased thickness of 230 nm is shown as indicated.

The significant differences between the materials are attributed to their electrical properties. Hall measurements of both, in-house and commercial materials, revealed strong variation in carrier concentration and mobility as depicted in Figure 4.24. The benchmark for the optical properties is set by PDC–IO:H with its low N_e of 1.83×10^{20} cm^{-3}. Due to the high μ, it reaches also good conductive properties with a ρ of 380 $\mu\Omega$ cm, making it the best candidate for the front electrode. ZAO has also a low N_e, hence a low A_{wt} in NIR, but suffers from a low μ. In order to reach an acceptable R_{sq}, the layer thickness has to be chosen quite large. IZO shows the third lowest N_e of 3.88×10^{20} cm^{-3}, which makes it a good NIR transmitter. In combination with a fairly low ρ, IZO resembles the most promising material for application as a rear electrode. FTO has a increased N_e and a mediocre μ and the film thickness of the commercial product is large in order to achieve a good R_{sq}. In total, this combination results in the worst optical properties. a-IO:H shows similar values, so even with a reduced film thickness, the A_{wt} stays behind the one of IZO. ITO sets the benchmark for the lowest ρ of 162 $\mu\Omega$ cm, but the good conductive properties can not compensate for the high A_{wt} introduced by the exceptionally high N_e of 11.4×10^{20} cm^{-3}.
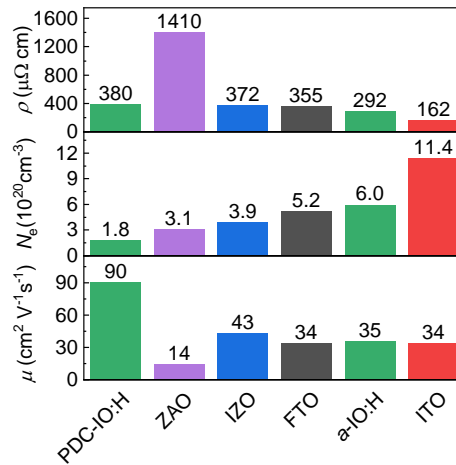
Figure 4.24: Hall measurements of different TCO materials. Depicted are ρ, N_e, and μ for in-house and commercial (FTO, ITO) TCOs.

Concluding, annealed PDC–IO:H is particularly suitable as a front electrode in PSCs with superstrate configuration, because of the high band gap, the outstanding NIR absorption and low sheet resistance. Importantly, the annealing step can be carried out after deposition on the glass superstrate. It outperforms the commercial TCOs mainly in terms of NIR transmittance. For the rear electrode, both IZO and a-IO:H seem to be suitable candidates, with IZO having an advantage over a-IO:H as it has a better NIR transmission and good conductivity.

4.3 Semitransparent perovskite solar cells

The transition from opaque to semitransparent PSCs requires the exchange of the metal rear electrode with a transparent alternative. In the last chapter, IZO and a-IO:H have been identified as suitable candidates, offering a high transmittance and a good conductivity. The task of the first Section 4.3.1 is the deposition of the new electrodes on to the PSC without damaging the sensitive underlying layers.

For a better optical transmission of the complete semitransparent PSC the traditional front electrodes FTO or ITO need to be exchanged too. Section 4.3.2 discusses the prerequisites for implementing the newly developed PDC–IO:H or IZO as front electrodes and compares the electrical and optical properties of the final devices.

The complex interplay of reflections that take place at every interface in the layer stack results in a strong modulation of the final device transmittance, depending on the wavelength and the d of each individual layer. By tuning the d of the TCO electrodes, the T, R, and A is optimized in Section 4.3.3 with the goal to find a compromise with the electrical device performance.

4.3.1 Sputter deposition of transparent rear electrodes with protective layers against damages

During the sputter deposition of the rear electrode on the PSC, the underlying charge transport layer must not be damaged in order to maintain a high photovoltaic performance. In this n-i-p architecture, the charge transport layer is represented by Spiro-OMeTAD. Without protection, sputter damages lead to a significant loss in the PCE, hence usually a protective buffer layer of MoO_3 is previously applied via thermal evaporation. An exemplary schematic cross-sectional illustration and a corresponding SEM image in Figure 4.25 demonstrate the principle architecture.
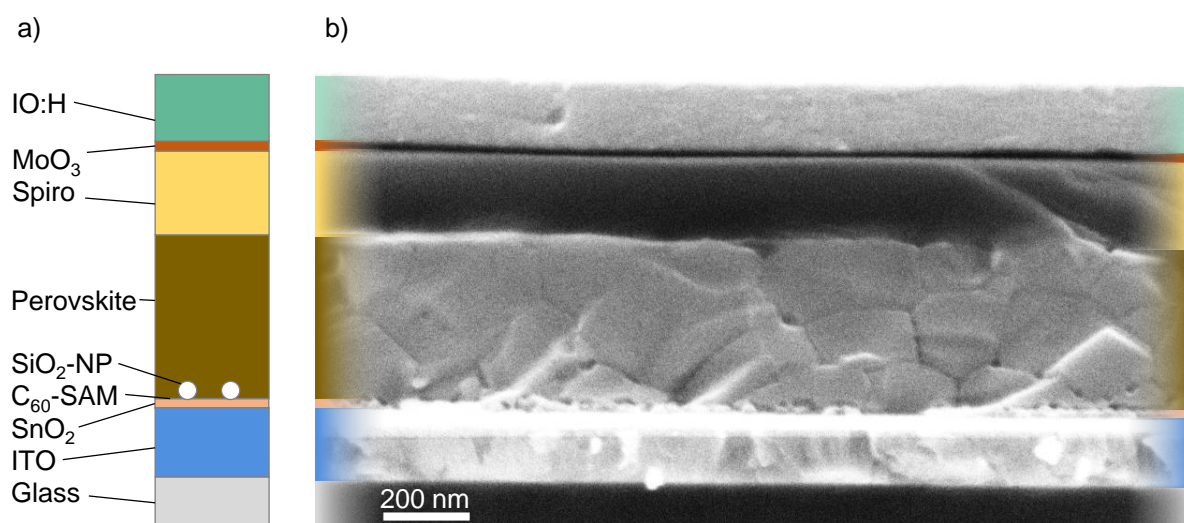
Figure 4.25: a) Schematic illustration and b) SEM cross section of a semitransparent PSC.

The thermal evaporation of a thin MoO_3 layer may serve well as a sputter damage protection, but it introduces quite a large extra effort in the preparation of the solar cells, which is otherwise dominated by solution based processes.

MoO_3 itself resembles not only a physical protection layer but takes an active part as a HTL in the solar cell. Figure 2.4 demonstrated that the band alignment of MoO_3 is very similar to Spiro-OMeTAD, which makes it a suitable HTL material in this architecture. In the following, the influence of the thickness of the MoO_3 layer is briefly evaluated.

Furthermore, two alternative protection layer free concepts will be investigated. Reports on the possibility to heal sputter damages by annealing steps [144] raise the question whether the sputter damages to Spiro-OMeTAD could be cured similarly, when no protection layer was used. Another approach includes the avoidance or reduction of the initial damaging using milder sputter conditions.

Recovery from sputter damage through annealing

In order to investigate if the sputter damage to the Spiro-OMeTAD could be cured with an annealing step, a series of different annealing temperatures and times was applied to PSCs. The results of the according JV scans are reported in Figure 4.26a and b. The first graph shows the JV responses of a single PSC, that was annealed at 50 °C, 60 °C, 65 °C and 70 °C for 300 s before each measurement in consecutive order. It proves, that up to 65 °C there is indeed a curing effect observable, resulting in a beneficial shift of the curves towards higher voltages. However, at 70 °C the JV response indicates a thermal damage by J_{SC} loss and a reduced parallel resistance (R_p).

The second graph in Figure 4.26b demonstrates with a second PSC, that increasing the annealing to 30 min at the temperature of 65 °C leads to a further curing, as the s-shape of the JV response is significantly reduced. Unfortunately, further heating for another 30 min, in total 60 min, has again a disadvantageous effect on the performance.
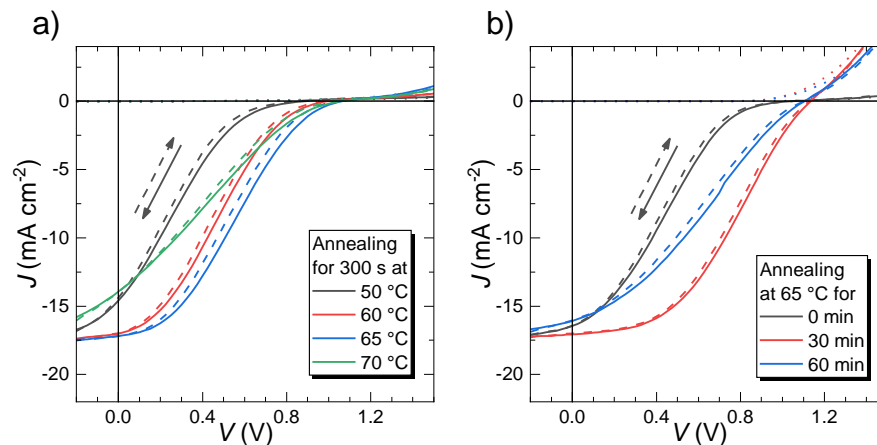
Figure 4.26: Impact of the a) annealing temperature and b) annealing time on the JV-responses of PSCs employing no protective layer in the architecture ITO/SnO$_2$-NP/C$_{60}$-SAM/SiO$_2$-NP/CsFAMAPIBr/Spiro-OMeTAD/IZO.

The results indicate, that the sputter damage can partly be cured by annealing. Presumably, the damaged parts of the HTL get cured by mechanisms related to interdiffusion and reorganization of the molecules at elevated temperatures. However, since the Spiro-OMeTAD itself is vulnerable to elevated temperatures, the curing effect is soon overcome by a degradation effect. In conclusion, annealing is not applicable to fully recover the sputter damages dealt to a PSC of this architecture.

Thickness variations of MoO₃ protective hole transport layer

For investigating how the MoO$_3$ buffer layer influences the electrical and optical performance of the PSC, a series of PSC is evaluated in this chapter with respect to its transmission and its photovoltaic response in JV measurement. Furthermore, the influence of the exposure of the MoO$_3$ coated samples to air after deposition is briefly discussed.

For evaluating the thickness of the MoO$_3$ even in the nanometre regime, x-ray reflectometry (XRR) has proven to be a powerful tool. Hence, a reference glass was coated with MoO$_3$ along with solar cells in every evaporation process. The results of the XRR measurements in Figure 4.27a show that the four different MoO$_3$ layers have thicknesses of approximately 6 nm, 9 nm, 12 nm and 17 nm.
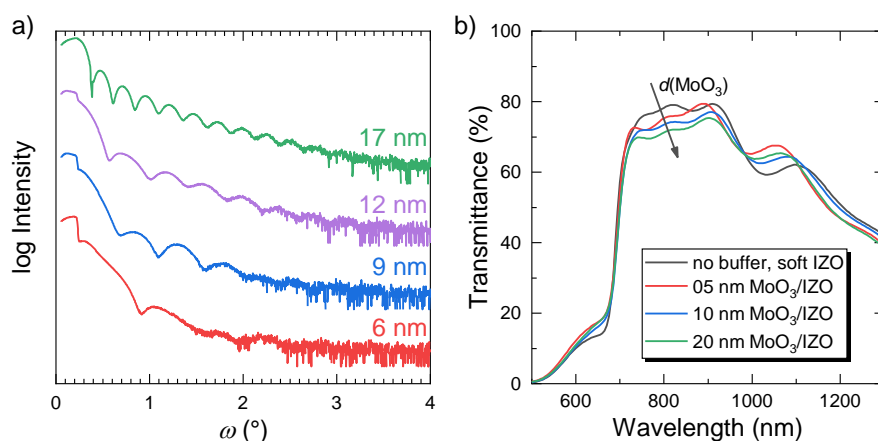
Figure 4.27: a) XRR data of MoO$_3$ layers on glass with different thicknesses; b) Spectral T of PSCs (ITO/SnO$_2$-NP/ C$_{60}$-SAM/SiO$_2$-NPs/CsFAMAPIBr/Spiro-OMeTAD/MoO$_3$/IZO) employing different thicknesses of the MoO$_3$ buffer layer.

Figure 4.27b indicates the principle effect of the MoO$_3$ layers on the T spectra of complete PSC devices. A reduction of the maximum T after the absorption edge is observed with the introduction of MoO$_3$ and with its increasing thickness. As MoO$_3$ itself has no fundamental absorption in this regime, the impeded T is most likely caused by unfavourable reflection at the interfaces. The amount of reflection varies with increasing film thickness due to interference effects.

Figure 4.28 shows the statistical results from the JV measurements of PSCs compromising the different MoO$_3$ layer thicknesses d. Significant differences are observable in the PCE, where the best performance of $\approx$12 % is achieved by the PSCs with 9 nm MoO$_3$ layers. The main cause of the performance difference is an improvement of the FF, which speaks for a better diode behaviour of the solar cells. At larger or smaller d than 9 nm, the FF shows significant differences between fwd and rvs scan direction up to 10 % absolute. Additionally, the J_{SC} reaches an average maximum of 18.5 mA cm^{-2} at 9 mm, whereas the V_{OC} shows no significant differences except for a decrease of nearly 100 mV, when d increases to 17 nm. The F_{HYS} is also strongly influenced by the MoO$_3$ thickness originating from the hysteretic behaviour of the FF.
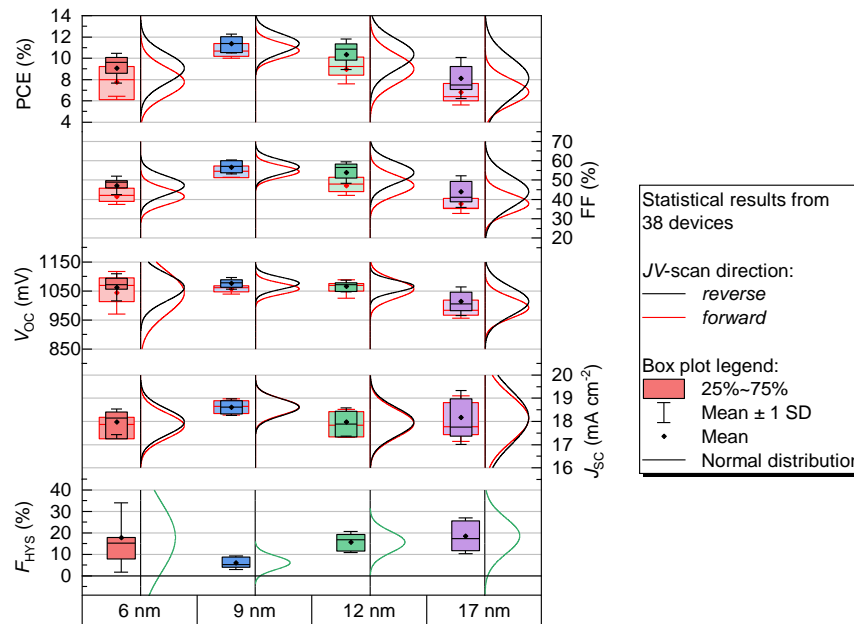
Figure 4.28: Box chart of *JV*-characteristics of PSCs (ITO/SnO$_2$-NP/C$_{60}$-SAM/SiO$_2$-NPs/CsFAMAPIBr/ Spiro-OMeTAD/MoO$_3$/IZO) employing different thicknesses of the MoO$_3$ buffer layer.

Concluding from the *JV* results, a MoO$_3$ thickness of about 9 nm allows for the best solar cell performance. Larger *d* lead to impeded charge extraction and injection, causing a bad diode behaviour and hysteresis. Smaller *d* introduce a similar negative effect, probably caused by insufficient protection against sputter damages.

Between the sequence of deposition processes of different MoO$_3$ layers and the sputter deposition of the rear electrode, inevitable waiting times could cause an additional ageing effect, if the MoO$_3$ layers are exposed to air for different time periods. The degree of oxidation of the MoO$_3$ could actually change in presence of the oxygen in air, if the material would be deposited in a non-stoicheometric form. Even small deviations from the stoicheometry could have a large effect on the electric properties, because charged oxygen vacancies represent doping centres. However, a precise determination of the oxygen to molybdenum ratio with the common analytical methods is practically impossible.

Therefore, the influence of a possible oxidation is investigated by a simple experiment, where a set of solar cells is prepared each with a similar MoO$_3$ layer thickness, but different air exposure times of 30 min, 90 min and 210 min before the deposition of the rear IZO electrode. The *JV* responses in Figure 4.29 serve as an indicator for any significant differences in the diode properties.
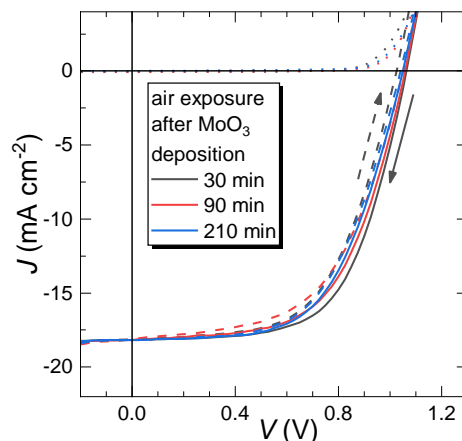
Figure 4.29: *JV*-responses of PSCs (ITO/SnO$_2$-NP/CsFAMAPIBr/Spiro-OMeTAD/MoO$_3$/IZO), that were exposed to ambient air for a different time duration after the deposition of the MoO$_3$ buffer layer, before the sputter deposition of the IZO rear electrode.

Fortunately, the *JV* responses of the devices exhibit very similar progressions in *fwd* and *rvs* scan directions after the different exposure times. Based on these observations, a severe change of the MoO$_3$ structure seems to be unlikely.

Avoiding sputter damage through reduced sputter power

A reduced target power during DC sputtering leads to a reduction of the deposition rate and a possible reduction of the damage present at a PSC. Here, several attempts are investigated to prepare samples without a protection layer by using such 'soft' processes.

With the reduction of the power, the sputter conditions need to be adapted in order to maintain the optical properties of the selected TCO. At lower powers, the amount of a specific species of ionized atoms decreases, hence the addition of reactive gas can be lowered (at constant pressure), as less of the atoms are 'consumed' by the plasma. Following this approach, Figure 4.30 proves that IZO and *a*-IO:H layers with very similar absorption properties may be prepared at target powers ranging from 300 W to 800 W (0.96 W m^{-2} to 2.55 W m^{-2}).

Four experiments were conducted using different PSC architectures each with Spiro-OMeTAD as a HTL, where different soft TCO processes are applied without a protection layer. The resulting *JV* data is shown in Figure 4.31a-d. The red and green curves indicate PSCs with soft IZO or soft *a*-IO:H (300 W) rear electrodes. Reference samples with a gold or MoO$_3$/TCO electrodes are represented by black or blue curves.
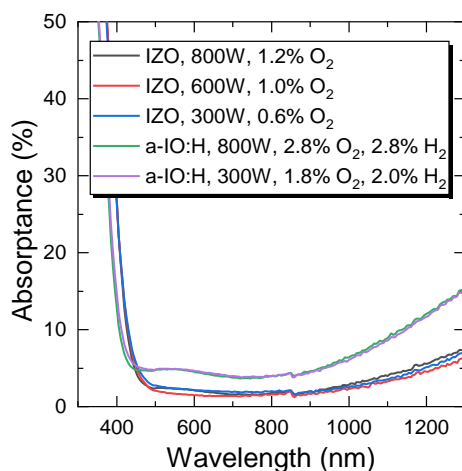
Figure 4.30: Spectral absorptance of different IZO and IO:H layers from sputter processes with varied power.
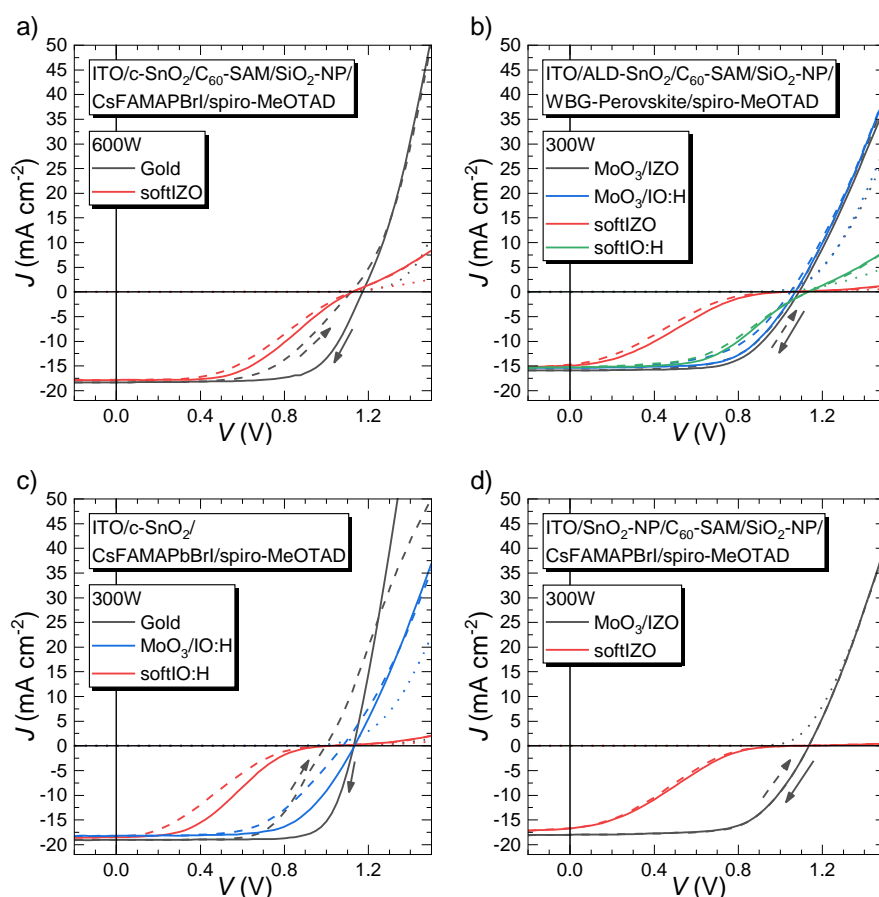
Figure 4.31: Current voltage characteristics of devices with and without MoO$_3$ buffer layer, applying different sputter processes with reduced power.

Despite the reduced power, a strong s-shape is present in the JV responses of the cells with soft TCO rear electrodes, which indicates a corrupted interface and the evidence of sputter damages. The simple reduction of the target power is not effectively avoiding the damaging of the HTL. One reason could be that the reduction of the power is reducing mainly the current flow through

65

the plasma, but the target voltage for establishing the plasma stays relatively constant. As a result, the number of accelerated ions may be reduced that hit the sample surface per time interval, but their kinetic energy is still high enough to deal damage. Therefore, the sputter conditions should be varied so that the kinetic energy of the bombardment is reduced.

4.3.2 Implementation of IZO and PDC-IO:H as front electrodes with ultra-low NIR absorption

IZO and IO:H demonstrated their superior optical performance in comparison to ITO and FTO already in Chapter 4.2.3 and they were successfully implemented as a transparent rear electrode in perovskite solar cells. These results promise a further improvement of the optical properties of the PSCs, if also the front electrode is replaced by IZO or IO:H. Therefore, this section evaluates the optical and photovoltaic properties of PSCs with FTO, ITO, PDC–IO:H and IZO as front electrodes.

Figure 4.32 depicts the statistical results of the photovoltaic performance of opaque and semitransparent PSCs employing the different front electrodes. The PSC architecture is front electrode/SnO$_2$-NP/C$_{60}$-SAM/SiO$_2$-NP/CsFAMAPIBr/Spiro-OMeTAD/rear electrode. As the normal distribution curves of the PCE values of the opaque cells in Figure 4.32a indicate, a narrow distribution is only reached with ITO with an average PCE over 15 %. PSCs with other TCOs struggle with a lower average PCE, despite the capability of FTO and PDC–IO:H to reach high maximum PCE values close to 17 %. The main cause of the scattered distribution are deviations in the FF. Since ITO is the electrode material predominantly used for development of the architecture, the well optimized processes could explain the small statistical deviations. In case of FTO, the comparably rougher surface might be one reason for the reproducibility problems and also for the larger F_{HYS}. The PSCs with in-house developed TCOs front electrodes might be impeded by particle contaminations of the glass superstrate, which are believed to cause local shunts.

However, the results of the J_{SC} indicate a significant improvement with PDC–IO:H. An average gain of $\approx 1\,\mathrm{mA\,cm^{-2}}$ is observed compared to the other TCOs, which is probably due to the exceptional transmission of the PDC–IO:H.

Similar results are observed with semitransparent PSCs in Figure 4.32b, where the gold rear contact is replaced by a-IO:H. Here the J_{SC} gain of PDC–IO:H is not as large as in the opaque setup, due to the missing back reflection from the gold rear electrode.
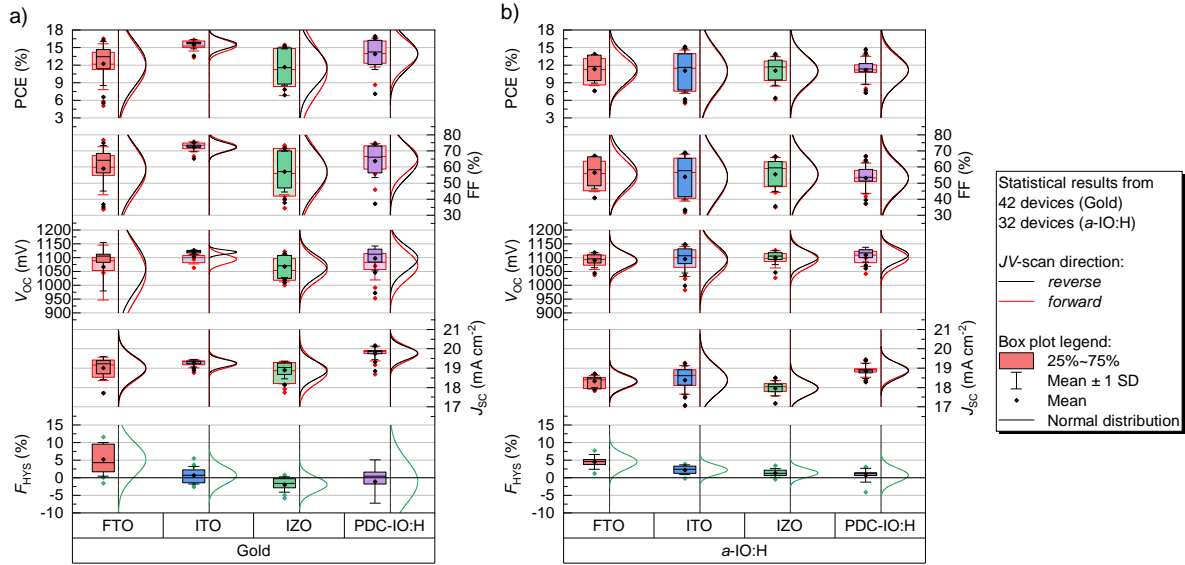
Figure 4.32: Box plots of the *JV* parameters of PSCs employing different front TCOs (FTO, ITO, IZO, PDC–IO:H) and a) an opaque gold rear electrode or b) a semitransparent *a*-IO:H rear electrode.

Quantum efficiency measurements on semitransparent PSC in Figure 4.33a reveal the relation of the spectral current generation and the optical properties of the front electrode. At small wavelengths, the EQE of the PSC (solid lines) is completely limited by the E_g of the TCO, which is conceived from the progression of the spectral *A* of the TCO layers (dashed lines). At longer wavelengths, the EQE is influenced mainly by reflection mechanisms at the interfaces, because the EQE curves show typical signs of interference modulation. Due to the interference patterns, it is difficult to evaluate the effect of the *A* in the front electrode on the quantum efficiency.

Therefore, Figure 4.33b shows the integrated curve of the J_{EQE} for the same devices. As anticipated, the low E_g of IZO leads to a strong current loss at small wavelengths. As a result, the J_{EQE} remains the lowest compared to the other TCOs over the whole absorption range, despite the low parasitic *A* of IZO at longer wavelengths. The highest J_{EQE} is reached by the PSC with PDC–IO:H, followed by ITO. Both have a sufficiently high band gap and a low parasitic absorption in the absorption range of the perovskite. FTO shows a higher *A* due to the large layer thickness compared to the other TCOs, which results in a reduced J_{EQE} of the PSC, especially at longer wavelengths. The inset shows the final J_{EQE} of the devices after the fundamental absorption edge of the perovskite.

As expected, the J_{SC} of the devices follows the same trend of the J_{EQE}, which is demonstrated by the *JV* measurements in Figure 4.33c (see inset). The comparison of the characteristic J_{SC} and J_{EQE} values in Table 4.2 prove a good match between *JV* and EQE measurement conditions.
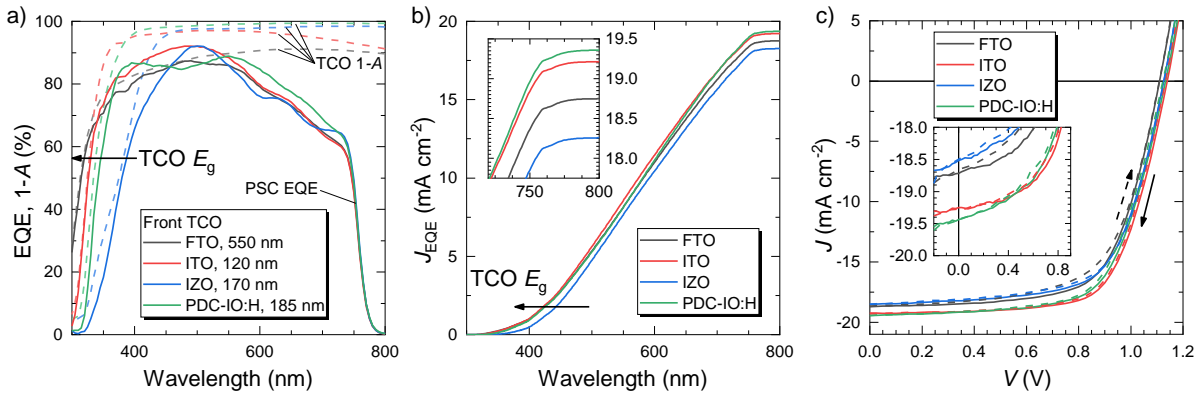
Figure 4.33: a) EQE and *A* responses of semitransparent PSCs with different front TCOs (FTO, ITO, IZO, PDC–IO:H); b) J_{EQE} curves of the same samples, the inset shows the integrated J_{EQE} at the absorption edge; c) *JV* curves of the same PSCs, the inset allows a more detailed investigation of the J_{SC}.

Regarding the optical performance of the PSCs for future tandem application, the transmittance (*T*), reflectance (*R*) and absorptance (*A*) of the devices are evaluated in Figure 4.34a and b. As intended, the use of PDC–IO:H and IZO as front electrodes leads to a significant increase of *T* and a reduction of *A*. Notably, the device with ITO exhibits a strong *R* between 100 nm to 1200 nm due to the high N_e of ITO compared to the other TCO materials. This leads to a strong reduction of *T*, while the highest *A* is observed in the PSC with FTO.

In order to quantify the parasitic absorption of the PSC in the spectral range after the absorption edge of the perovskite, Figure 4.34c shows the integrated J_{Abs} from 800 nm to 1300 nm. Both PSCs with PDC–IO:H and IZO exhibit significantly reduced J_{Abs}, which corresponds to a reduction of about 50 % compared to the commercial TCOs. The exact values are listed in Table 4.2.
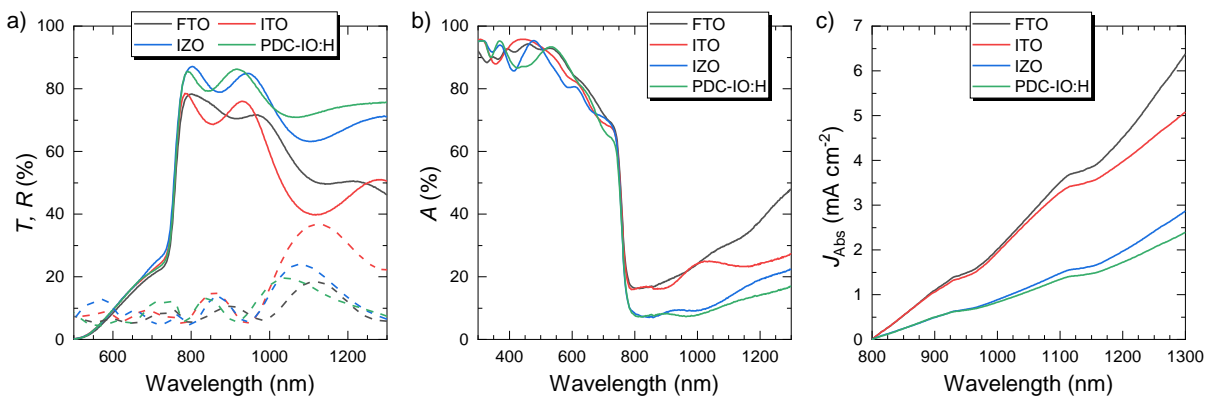
Figure 4.34: a) Transmittance (solid), reflectance (dashed) and b) absorptance spectra for perovskite solar cells with different front TCO contacts of commercial (ITO, FTO) and in-house materials (IZO, PDC–IO:H). Amorphous IO:H was used as TCO back contact. c) J_{Abs} of the same samples in for wavelengths after the absorption edge of the perovskite, indicating the equivalent current losses due to free carrier absorption in the front TCOs.

The results promise a great impact on the performance of the bottom cell in a tandem setup, when the front TCO of the semitransparent top cell is replaced by PDC–IO:H or IZO. Their reduced parasitic absorption will allow for a increased quantum yield in the bottom cell. But the comparably low band gap of IZO is unfavourable for the tandem performance, since it cuts off part of the blue light, hence reducing the current generation in the top cell. PDC–IO:H offers full potential for efficient top and bottom cells. A detailed evaluation of tandem architectures comprising different TCO combination follows in Section 5.3.

4.3.3 The optical influence of TCO layer thickness

In order to determine the influence of the thickness of the front- and rear electrodes on the optical properties of semitransparent PSCs, this section evaluates the T, R and A of devices with a variety of IO:H contact layers. The PSCs of the architecture PDC–IO:H/SnO$_2$/C$_{60}$-SAM/ SiO$_2$-NP/CsFAMAPIBr/Spiro-OMeTAD/MoO$_3$/a-IO:H use PDC–IO:H as front electrodes with d_{front} of 100 nm, 160 nm, 220 nm and 300 nm and a-IO:H as rear electrodes with d_{rear} of 90 nm, 160 nm and 240 nm.

Figure 4.35 depict the spectral R, T and A of the PSCs with all combinations of d_{front} and d_{rear} in form of colour maps.

The R data is shown for the range from 300 nm to 1300 nm, covering the absorption and transmission range of the PSC. In the absorption range up to $\approx$800 nm, R is dominated by reflection at the front electrode, which leads to interference patterns strongly related to d_{front}. A dominant green colour indicates a small amount of reflection in this range regardless of the thickness of the front electrode. In the transmission range after 800 nm, the reflection at the rear electrode interface with air causes a great effect on the spectral R. Depending on d_{rear}, R is modulated strongly by interference effects. This leads to R values of over 25 %, especially when the rear electrode layer is thin.

In correspondence to the reflection, the spectral T is also affected strongly by d_{rear}. Generally, following $1 = T + R + A$, T is low, when R is high, so a thick rear electrode seems to be favourable. But increasing d_{rear} leads to higher absorption, which counteracts the effect.

The increase of A with d is observed in Figure 4.35c. Especially d_{rear} has a strong impact on the absorptance ratio. This is due to the higher N_e in the a-IO:H compared to the PDC–IO:H of the front electrode. A higher N_e leads to increased free carrier absorption and reflection.

Front Electrode	A_{wt} (%)	J_{Abs} (mA cm^{-2})	PCE* (%)	FF* (%)	V_{OC}* (mV)	J_{SC}* (mA cm^{-2})	J_{EQE} (mA cm^{-2})	F_{HYS} (%)
FTO	27.2	6.4	14.0	67.1	1110	18.7	18.7	5.0
ITO	21.6	5.1	15.1	68.7	1149	19.1	19.2	2.0
IZO	12.2	2.9	13.9	66.7	1126	18.5	18.3	0.7
PDC-IO:H	10.2	2.4	14.7	66.9	1132	19.4	19.4	1.4

* values from reverse JV scan

Table 4.2: A_{wt} and J_{Abs} data in the range of 800 nm to 1300 nm and JV characteristics of perovskite champion cells with different front electrodes and a a-IO:H rear electrode in the architecture glass/front electrode/ c-SnO$_2$/C$_{60}$-SAM/SiO$_2$-NPs/CsFAMAPIBr/Spiro-OMeTAD/MoO$_3$/a-IO:H.
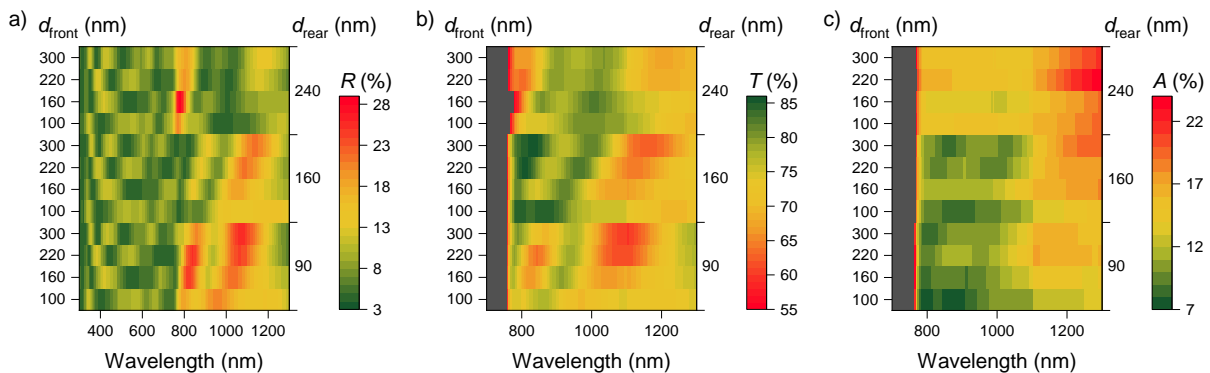
Figure 4.35: Colour coded spectra of a) R, b) T, and c) A of a set of semitransparent PSCs with different thicknesses of the front- (d_{front}) and rear electrodes (d_{rear}) as denoted on the axes. The PSC architecture is PDC–IO:H/SnO$_2$/C$_{60}$-SAM/SiO$_2$-NP/CsFAMAPIBr/Spiro-OMeTAD/MoO$_3$/a-IO:H.

In order to quantify the amount of reflected, transmitted and absorbed light, Figure 4.36 depicts the corresponding integrated curves of current density equivalent of the reflection loss (J_{Ref}), transmission loss (J_{Trn}) and absorption loss (J_{Abs}), respectively.

Regarding the reflection losses, J_{Ref} proves that up to 800 nm an equivalent of $\approx$2 mA cm^{-2} is reflected regardless of d_{front}. But for the thinnest rear electrode the reflection loss rises up to 6 mA cm^{-2} at 1300 nm. In contrast, the thickest rear contact reaches lower J_{Ref} of about 4.5 mA cm^{-2}.

The J_{Trn} is not as strongly affected by the thickness variations as the J_{Ref} or J_{Abs}. Since the transmittance results from the two counteracting mechanisms, on one hand a high reflection with thin rear electrodes and on the other hand a high absorption in thick electrodes, J_{Trn} profits most from the medium rear electrode with d_{rear} of 160 nm and reaches over 22 mA cm^{-2} at 1300 nm. The choice of d_{front} has only a minor influence in this case, probably due to the ultra low absorption in the PDC–IO:H and the complex interplay of the shift of the interference maximums in the reflection.

Quantifying the absorption losses in Figure 4.36c gives a difference of $\approx$1.5 mA cm^{-2} between the PSC with the thick front- and rear electrodes and the one with the combination of thin electrodes. As stated before, the d_{rear} has the greater influence on the absorption than d_{front}.
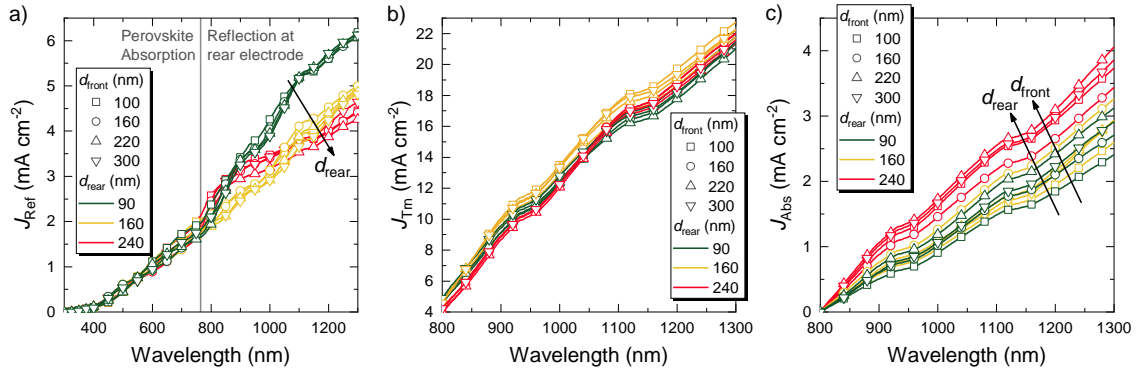
Figure 4.36: a) J_{Ref}, b) J_{Trn}, and c) J_{Abs} curves of semitransparent PSCs with different thicknesses of the front- (d_{front}) and rear electrodes (d_{rear}) as denoted by the colours and symbols. The PSC architecture is PDC–IO:H/SnO$_2$/C$_{60}$-SAM/SiO$_2$-NP/CsFAMAPIBr/Spiro-OMeTAD/MoO$_3$/a-IO:H.

Following the previous optical results it would make sense to reduce the thickness of both TCO layers of front and rear electrode as much as possible in order to minimize A. However, the sheet resistance increases strongly with decreasing thickness, as shown in Section 4.2.1, finally limiting the photovoltaic performance of the PSC. Furthermore, the R modulates strongly with the thickness of the rear electrode. Following the fresnel equation 2.9, the amount of reflection at the rear interface can be reduced by a anti reflection coating (ARC) coating with suitable refractive indices. Tuning the thickness of all layers, including the ARC layer, could further reduce the internal reflection losses by minimizing the interference effects.

In order to investigate the influence of the sheet resistance of the rear electrode on the performance of the PSC, Figure 4.37a and b show the JV responses of PSCs with different rear electrodes gold, IO:H and IZO. Additionally, the sheet resistances of the corresponding TCO layers on glass are denoted in the graph. As expected, the series resistance for thinner TCO layers with higher R_{sq} increases, which is noticeable from the decreased slope of the JV response at V_{OC}. To quantify the series resistance, the slope $dV/dJ(V)$ at V_{OC} is used to extract a resistance value normalized to the cell area. This resistance can be used as a measure for series resistance (R_s), but does not correspond exactly to it [120].

Figure 4.37c shows a box plot of the resulting resistance in comparison to the R_{sq} of the corresponding rear electrode. The application of thin TCO layers with a R_{sq} of $40\,\Omega_\square$ results in much higher resistance values of over $15\,\Omega\,cm^2$ compared to a gold rear electrode with $7\,\Omega\,cm^2$. As the thickness increases, the resistance decreases significantly. For the 220 nm layer with a R_{sq} of $15\,\Omega_\square$ the resistances drop to $10\,\Omega\,cm^2$ to $12\,\Omega\,cm^2$. This corresponds to a reduction of 30 % with an approximate doubling of the layer thickness.
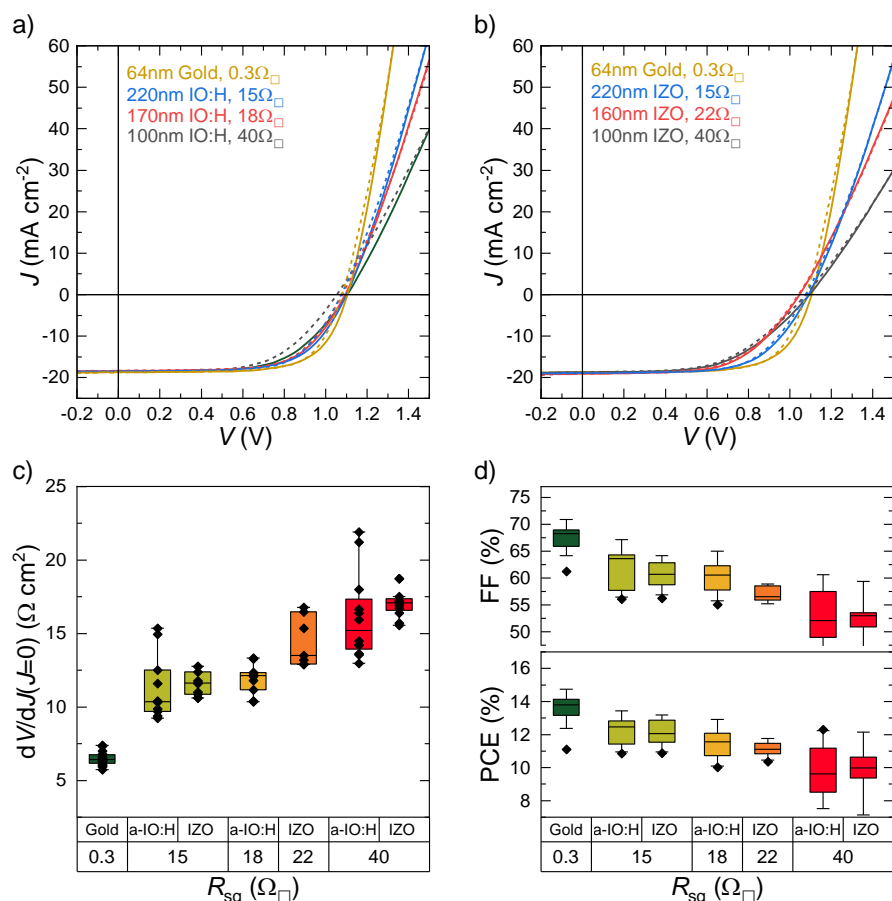
Figure 4.37: Representative *JV* scans for perovskite solar cells with a) IO:H and b) IZO back contacts of different thickness. Solar cells with gold contact were measured as reference samples. c) Box plot of the slope dV/dJ at $V = 0$ as quantification of the R_s and d) effect on FF of the *JV* curves.

The lower series resistance directly influences the FF and thus the PCE as depicted in Figure 4.37d. The FF of the semitransparent cells increase in average from $\approx 50\%$ to over 60% when d_{rear} increases from 100 nm to 220 nm and the R_{sq} drops from $40\,\Omega_\square$ to $15\,\Omega_\square$, respectively. In terms of PCE this corresponds to a gain of 2% absolute.

Nevertheless, the PCE of the semitransparent PSCs are significantly lower than the value of the gold reference with a fill factor of 67.5% in average. This is partly due to the superior R_{sq} of $0.3\,\Omega_\square$ (gold on glass) which is 40 times lower than of the 220 nm TCO layer.

In conclusion, the layer thickness of the transparent electrodes is a decisive factor for the optical and photovolatic performance of the PSC. Especially the rear electrode has a major influence on the absorption and the reflectance in the NIR regime. Here, a rather thin layer would be beneficial, but this limits the PCE of the PSC by a high series resistance.

Generally, the series resistance is also interlinked with the geometry of the solar cell. In this setup, the active area has a size of $7 \times 3.25\,\text{mm}^2$. If the cell dimensions would be much smaller and the contacts close to the active area, then the R_s would be also less important for the PCE. This is a fundamental aspect that has to be acknowledged, when it comes to optimizing the optical and electrical properties of the PSC for tandem applications.

For implementing the PSC in a 4T-tandem cell with CIGS, the PSC active area needs to be even increased, which would cause additional losses due to a higher R_s. One possible solution to reduce the R_s of the semitransparent PSCs is the application of a metal grid to the rear electrode, which is part of the discussion about tandem solar cells in the next Chapter 5.

5 Four-terminal perovskite–CIGS tandem cells

In this chapter the semitransparent perovskite cells are integrated into four-terminal tandem cells with CIGS as a bottom cell. Figure 5.1 gives a schematic overview of the development steps that are discussed in the following.
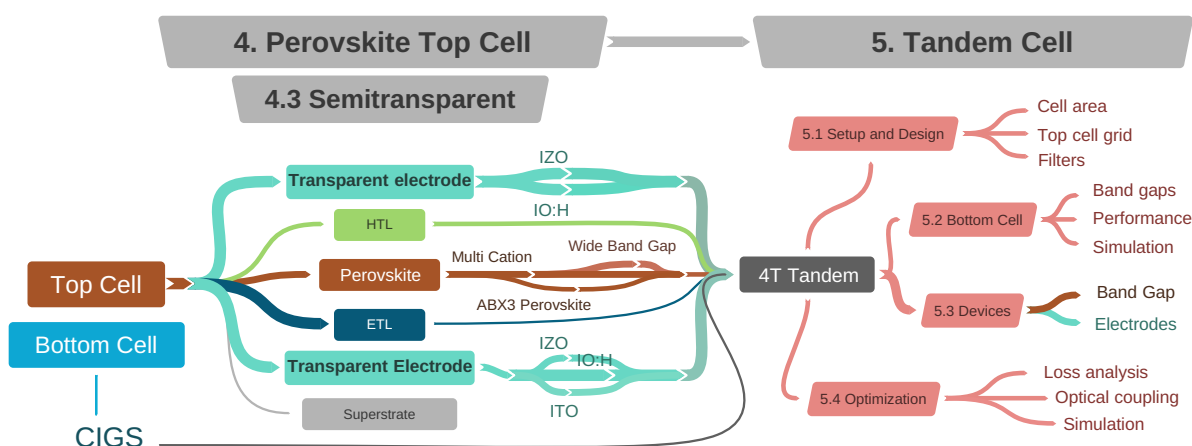
Figure 5.1: Strategy for developing the 4-terminal tandem cell using a n-i-p–perovskite top cell and CIGS bottom cell with indicated chapter numeration.

The first Section 5.1 covers the general design aspects of the tandem cell, considering the cell size matching and grid integration. Secondly, in order to estimate the CIGS bottom cell photovoltaic performance, modelling approach is discussed in Section 5.2. Section 5.3 evaluates the actual performance of tandem devices with different architectures, comprising perovskite and CIGS solar cells with different band gaps and electrodes. For a deeper understanding of the optical and electrical mechanisms that limit the tandem power conversion efficiency, current loss analyses are performed in Section 5.4.1. From the findings of the loss analysis, further development steps such as the use of optical coupling materials and anti reflective coatings are tested. Additionally, also the impact of wide band gap PSCs with ultra-high transmission is simulated in order to find the maximum achievable bottom cell efficiency.

5.1 Design and performance aspects of four-terminal tandem architectures

For the development of four-terminal tandem architectures, two different approaches are chosen in this work. The first approach is often used for estimating the tandem device performance by combining an optical filter that shall represent the PSC with the CIGS bottom cell as shown in Figure 5.2a. This approach gives the opportunity to fabricate smaller sized PSCs along with a larger filter of a nominally identical layer stack. Both the PSC and the filtered CIGS solar cell are measured separately and the single values are used for estimating a theoretical value for the PCE of a possible tandem device.

Since it is more convenient and reproducible, to achieve high performance PSCs on a small active area, this approach is commonly used to assess different possible tandem setups. Furthermore, as the filter does not need electrical connections, the mechanical integration is simplified. This allows for e.g., the use of optical coupling materials to fill the air gap between the CIGS cell and the filter, such as immersion oil.

A more sophisticated approach is to stack a semitransparent PSC and a CIGS cell of the same size as depicted in Figure 5.2b. This represents a fully functional 4T-tandem cell. Electrical and optical measurements are performed simultaneously with this architecture and the results are representative for a real 4T-tandem device as all relevant aspects are already included in the design. These aspects include variations of the transmittance of the perovskite, cell size dependent losses originating from the lateral conductivity of the electrodes or losses introduced by the shadow casting of the grids of the subcells.
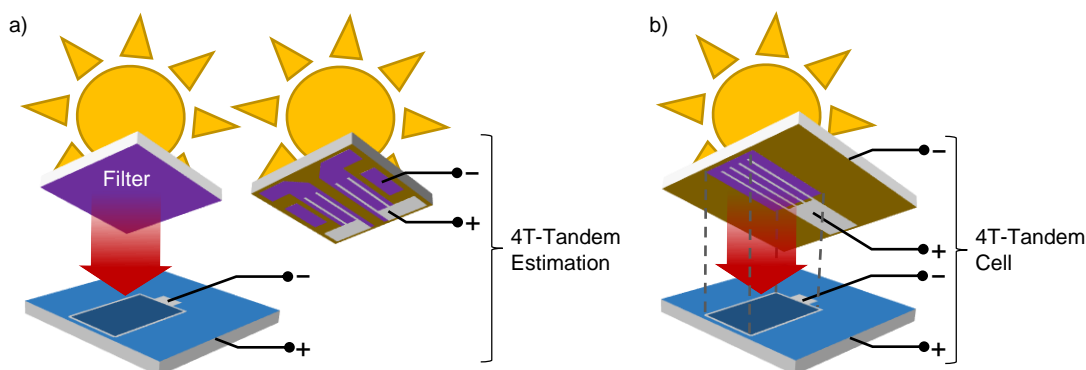
Figure 5.2: Schematic illustrations of different approaches to tandem solar cell development: a) For estimating the performance of the bottom cell in a tandem setup, an optical filter is used that shall represent the top cell. The top cell itself has a non-matching geometry and is measured separately. b) The top and the bottom cell with matched cell sizes are mechanically stacked on top of each other. Optical and electrical measurements are performed simultaneously.

In the following, the mismatch of the transmission between different filters and the corresponding PSCs is discussed briefly in Section 5.1.1. The impact of the increase of the active area of the PSC is discussed in Section 5.1.2 along with the integration of a metal grid, for the use in 4T-tandem cells.

5.1.1 Optical mismatch between perovskite solar cells and representative filter devices

Quite commonly, tandem performances are estimated by using a representative filter in place of the actual PSC as a top cell, with the belief that the actual transmittance is represented precisely enough by the filter. But due to many layer preparation steps and variations in the processes, most likely the filter exhibits a certain deviance from the sister PSC, even if prepared in the same run with the same process parameters. This chapter investigates briefly the possible optical differences between filters and cells.

Figure 5.3a shows two typical transmittance (T) curves of PSCs with different electrodes (solid lines) and alongside the corresponding T of a similarly prepared set of filter stacks (dashed). Obviously, the coarse trend of the PSC T is followed by the filters, but the exact positions of the interference maxima and minimums are shifted quite significantly. Even small deviations in the film thicknesses or roughness can cause a significant shift of the maxima, because of the wavelength sensitive internal reflection mechanisms at the interfaces between the layers. This has been already demonstrated by variations of the electrode thicknesses in Section 4.3.3.

The question remains, if this resembles a significant impact on the average transmittance or more precisely on the transmitted photon flux. Additionally to the T curves, Figure 5.3a shows the current density equivalent of the photon flux (qN_{ph}) of the AM1.5. As the photon flux declines with longer wavelengths and exhibits some gaps, the deviations of the T should be weighted according to qN_{ph}.
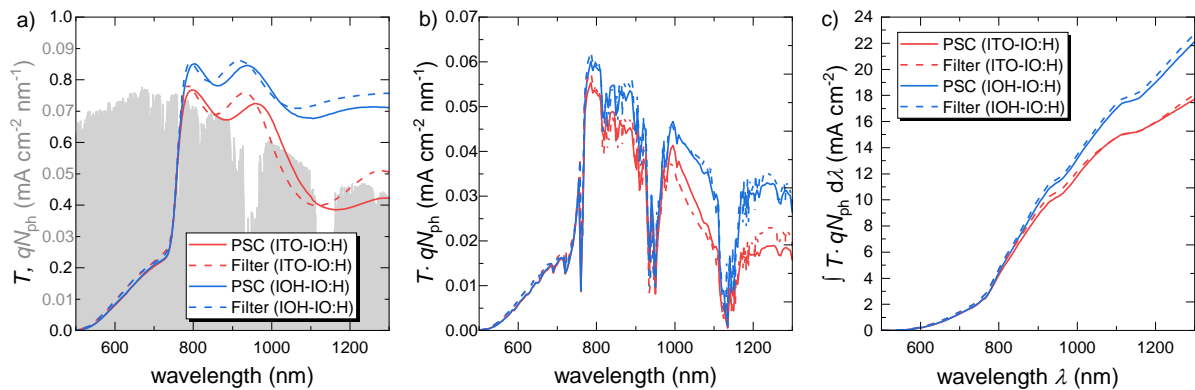
Figure 5.3: a) Transmittance T of PSCs and representative filter samples of the same architecture with different front TCOs (TCO/SnO_2-NP/C_{60}-SAM/SiO_2-NPs/CsFAMAPIBr/conductive fluorene/MoO_3/IO:H); The gray coloured data shows the photon flux of the AM1.5G spectrum in equivalents of current density qN_{ph}. b) Transmittance of the same samples multiplied by the photon flux $T \cdot qN_{ph}$. c) Integral curves of b.

By multiplication of $T \cdot qN_{ph}$ a direct weighting is achieved as shown in the graph of Figure 5.3b. Usually, these graphs are not convenient to compare, but the integral curve from Figure 5.3c can be used to estimate the maximum number of photons that are transmitted through the PSC up to a certain wavelength limit. The integrated value expresses the current density equivalent of the transmission (J_{Trn}) (see equation 2.12), which represents the maximum current density given directly in the units $mA\,cm^{-2}$ that a perfect solar cell could gain from the transmitted photon flux in the dedicated wavelength range.

The integrated curves demonstrate that the J_{Trn} of the filters does not largely deviate from the J_{Trn} of the cells. Actually, depending on the upper integration limit, the J_{Trn} values might match precisely.

In order to set the J_{Trn} in proportion to the incident photon flux, a weighted average transmittance (T_{wt}) value is introduced in analogy to T, following equation 2.16.

Using these two values J_{Trn} and T_{wt} for evaluation the T spectra of filters and cells, gives a directly understandable and comparable quantification of the principle mismatch.

Table 5.1 shows the results for a set of PSCs and corresponding filters with a variety of different TCO combinations. The integration limits are chosen from 300 nm to 1200 nm. Remarkably, the filters all exhibit a higher T_{wt} than the PSC samples. The relative mismatch is below 1 % for the samples with ITO or FTO front electrode, but for IZO and IO:H it reaches up to 3.6 %. In terms of J_{Trn}, the absolute mismatch of the filter would account for an additional transmission of over 0.5 mA cm^{-2}.

Setup		PSC		Filter		Abs. Mismatch		Rel. Mismatch
Front TCO	Rear TCO	J_{Trn} (mA cm^{-2})	T_{wt} (%)	J_{Trn} (mA cm^{-2})	T_{wt} (%)	ΔJ_{Trn} (mA cm^{-2})	ΔT_{wt} (%)	Δ (%)
ITO	IZO	16.1	40.2	16.1	40.4	+0.07	+0.18	+0.45
ITO	IO:H	15.9	39.8	16.0	40.0	+0.05	+0.12	+0.31
FTO	IZO	16.9	42.2	17.0	42.5	+0.12	+0.30	+0.70
FTO	IO:H	16.8	42.1	16.9	42.2	+0.03	+0.08	+0.18
IZO	IZO	18.6	46.5	19.1	47.9	+0.54	+1.35	+2.91
IZO	IO:H	18.5	46.4	19.2	48.0	+0.66	+1.66	+3.58
IO:H	IZO	19.0	47.7	19.6	49.0	+0.54	+1.35	+2.84
IO:H	IO:H	19.0	47.6	19.5	48.7	+0.45	+1.13	+2.37

Table 5.1: The current density equivalent of the transmission (J_{Trn}) and the weighted average transmittance (T_{wt}) of PSCs and representative filter samples of the same architecture with different front- and rear TCOs (front TCO/SnO$_2$-NP/C$_{60}$-SAM/SiO$_2$-NPs/CsFAMAPIBr/conductive fluorene/MoO$_3$/rear TCO); The values are calculated from the spectral transmittance of the samples using the equations 2.12 and 2.16 within the integration limits of 500 nm to 1200 nm. The relative mismatch Δ is calculated by (J_{Trn}(Filter)/J_{Trn}(PSC) − 1).

Since the highest mismatch is observed with IZO and IO:H front electrodes, which are prepared in-house, this suggests that there are greater deviations in the layer thickness homogeneity compared to the commercial TCOs such as FTO and ITO. Moreover, the rear electrode is sputter deposited on the full area of the filter samples, while framed metal aperture masks are used for the PSCs in order to define the active area. This may have a significant influence on the temperature of the samples and the plasma properties during sputtering, which could result in different optical properties of the rear TCOs. The general trend of the increased transmission of the filters may be explained by this.

Furthermore, the absorption limit of the bottom cell, resembles the practical wavelength limit, at which the filter transmission mismatch has to be evaluated. Depending on the E_g of the CIGS cell, its absorption limit may vary between approximately 1100 nm and 1250 nm. Since also the mismatch of the J_{Trn} is varying with the wavelength of the upper integration limit, the practically applicable mismatch between a filter and a real PSC top cell actually depends on the E_g of the bottom cell.

Following the spectral progression of the mismatch ΔJ_{Trn} in Figure 5.4, raises attention to the strongly varying mismatch values of the PSC setups with increasing wavelength. For comparison, the upper integration limit of 1200 nm is indexed in the graph. A bottom cell with an absorption range reaching beyond this limit would soon be faced with a larger mismatch, as the ΔJ_{Trn} curves tend to increase strongly afterwards.
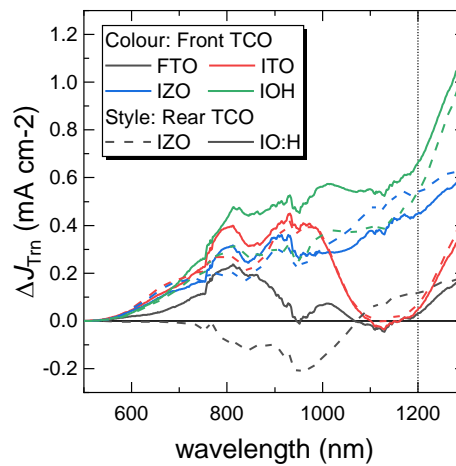
Figure 5.4: Mismatch ΔJ_{Trn} between PSCs and representative filter samples of the same architecture with different front- and rear TCOs (front TCO/SnO$_2$-NP/C$_{60}$-SAM/SiO$_2$-NPs/CsFAMAPIBr/conductive fluorene/MoO$_3$/rear TCO).

However, for tandem performance simulation, a relative mismatch of about 3 % between the transmission of the PSC and the corresponding filters may be acceptable, considering the principle method being a rather basic estimation tool, which makes use of many additional approximations in the first place. Still, the error introduced by the use of filters instead of the actual PSC should be considered as significant in the evaluation of the results.

5.1.2 Reducing the series resistance of the perovskite solar cell by implementation of a metal grid

In finding a compromise between satisfying conductive properties, serving a good PSC top cell performance, and good optical properties for a high bottom cell performance, the application of metal grids may bring the solution. Optimally, a metal grid, which is applied to the rear electrode of the PSC, increases the conductivity so that the TCO may be reduced in thickness and optimized for a high transmission. Since the grid is applied to the rear of the solar cell, it does not cast a shadow on the active area so that the generated current should remain constant, but in tandem application the shading effect needs to be accounted for the bottom cell.

Grid implementation in PSCs with a cell area of 0.24 cm²

This section introduces a principle design of a metal grid, which is suitable for the application in semitransparent PSC with an active area (A_{act}) of $0.24\,cm^2$. For sake of simplicity, the same grid material architecture Ni-Al-Ni is chosen as it is utilized for the CIGS bottom cells, which brings a great time saving advantage in the sequence of deposition processes. Here, the grid is deposited under UHV conditions by electron-beam physical vapor deposition (EBPVD). It compromises a $\approx 2.5\,\mu m$ aluminium layer sandwiched between two $\approx 50\,nm$ thin nickel layers.

A specially designed metal aperture mask is used to define the grid bar dimensions. The mask is made of $50\,\mu m$ thin steel foil that is laser patterned with a minimal line width of $\approx 35\,\mu m$. An image of the grid on a semitransparent PSC sample is depicted in Figure 5.5a along with a schematic illustration (b) that denotes the principle architecture.
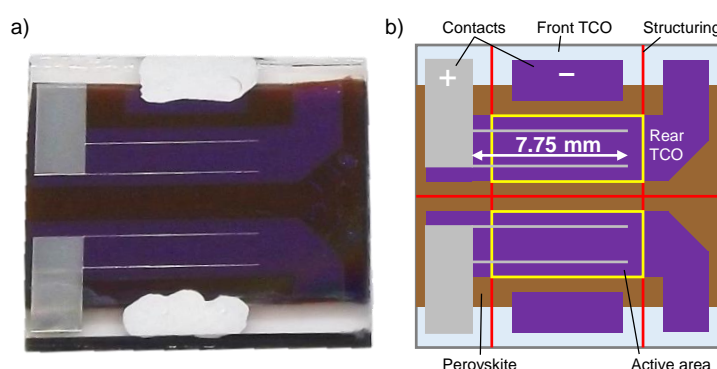
Figure 5.5: a) Photograph of a perovskite solar cell with metal grid applied to the rear electrode. (ITO/SnO$_2$-NP/ C$_{60}$-SAM/SiO$_2$/mixed ionic perovskite/Spiro-OMeTAD/MoO$_3$/IZO/grid); b) Schematic drawing of the same indicating the dimension of the grid bars and the general architectural design. The active area is defined by the front TCO structuring and the rear TCO to $0.2431\,cm^2$.

For determining the actual dimension of the grid bars, confocal laser scanning microscopy (CLSM) has been conducted at different positions. Figure 5.6a shows the colour coded height mapping of a grid bar close to the contact pad, where the bar crosses the laser structuring line of the front TCO that defines the outline of A_{act}. The second mapping (b) is recorded at the tip of a grid bar. The insets show the average line profiles along the cross section of the bars from the denoted area (red box). Since the sample holder rotates during the deposition, the cross sections exhibit asymmetric shapes. From the line profiles the average width (w_{avg}), the maximum height (h_{max}) and the average cross sectional area (A_{avg}) are obtained.
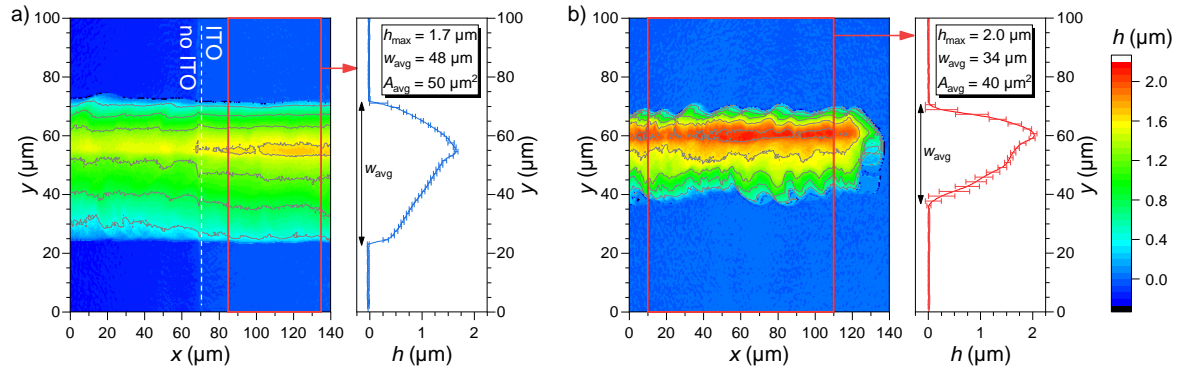
Figure 5.6: Coloured topographical scans from CLSM of solar cells (ITO/SnO$_2$-NP/C$_{60}$-SAM/SiO$_2$/ mixed ionic perovskite/Spiro-OMeTAD/MoO$_3$/IZO/grid) at different positions of the grid bars: a) near the contact pad at the laser line defining the active area, and b) at the tip. The insets show averaged line scan profiles along the marked areas.

Due to the aperture mask design, the grid bar is wider near the pad and narrower at the tip. From tip to pad, w_{avg} changes approximately linearly from 34 µm to 48 µm. Additionally, h_{max} decreases from 2.0 µm to 1.7 µm, respectively. As a result the A_{avg} increases from 40 µm^2 to 50 µm^2, which is reasonable because the current density increases in direction of the pad and a larger cross section aids the conductivity. Because the single grid bars do not show large deviations in their aspect ratios, mean values of $A_{avg} \approx 45$ µm^2 and $w_{avg} \approx 41$ µm can be estimated for further calculations.

In order to evaluate the effect of the grid on the performance of a PSC, Figure 5.7a compares the *JV* responses of PSCs with grid (blue curve) and without grid (red) to a reference solar cell with a gold rear electrode (black). The inset shows the PCEs during dynamic MPP tracking. From the slope of the *JV* curves at forward bias, a significant improvement of the R_s is anticipated when the grid is applied. Compared to the sample without grid, this results in a better FF and the diode behaviour converges the one with gold electrode. This leads to an efficiency leap so that both PSCs with IZO/grid and gold electrode achieve PCEs well over 16 % in MPP tracking, while the sample with simple IZO electrode reaches only 14 %.

81
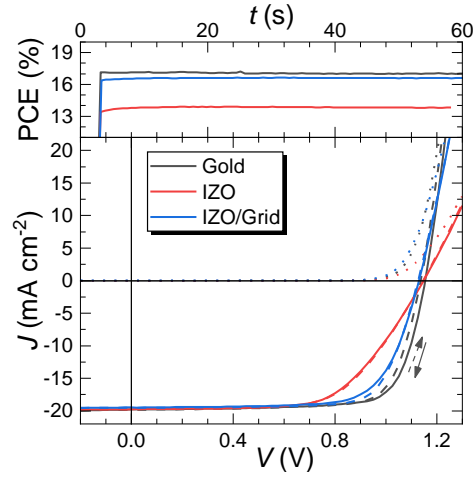
Figure 5.7: *JV* responses and MPP tracking (inset) of PSCs (ITO/SnO$_2$-NP/C$_{60}$-SAM/SiO$_2$/mixed ionic perovskite/ Spiro-OMeTAD) with different rear contacts: gold, MoO$_3$/IZO, and MoO$_3$/IZO/Ni-Al-Ni grid. The cells have an active area of 0.24 cm^2.

For quantification of the improvement in R_s, the well-established single diode model is applied, which follows the relation

$$ J = J_0 \cdot \left[\exp\left(\frac{V - J \cdot R_s}{n \cdot kT/q}\right) - 1 \right] + \frac{V - J \cdot R_s}{R_p} - J_{ph} \tag{5.1} $$

with the current density (J), the reverse saturation current density (J_0), the v (V), the parallel resistance (R_p), the diode ideality factor (n), and the photo current density (J_{ph}). The temperature dependent term kT/q is often referred to as the thermal voltage with Boltzmann constant (k) and the elementary charge (q).

The *JV* responses of the different PSCs are fitted by computational methods using 5.1. The J_{SC} shifted semi logarithmic plots in Figure 5.8 demonstrate the quality of the fits, which are weighted in such a way that the data is best fitted in the R_s and R_p ranges. The middle part, where the diode behaviour is described by n, shows some deviations. These are not particularly affecting the R_s and R_p evaluation, but they indicate that in principle a more complex model would be needed to simulate the curves in full detail.
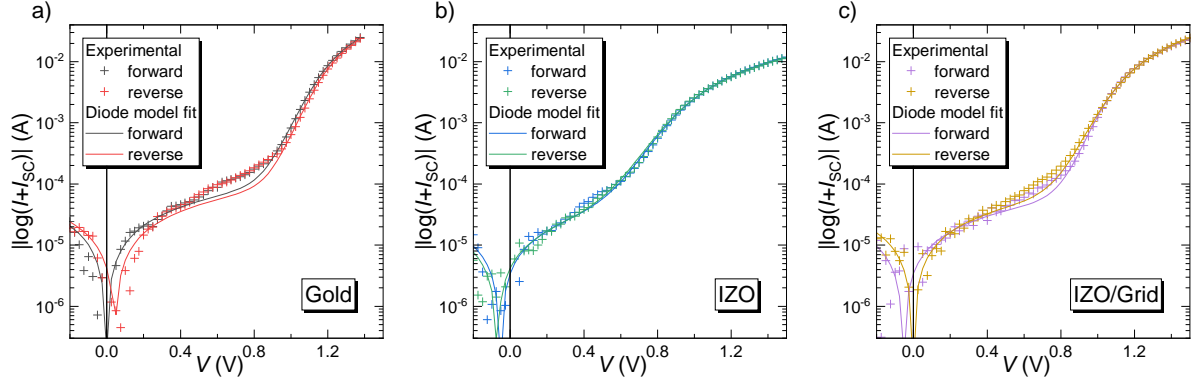
Figure 5.8: One diode model fits to the current–voltage dependency (*IV*) responses in *fwd* and *rvs* scan direction of PSCs with a) gold, b) IZO and c) IZO/Grid as rear contacts.

The characteristic parameters of the *JV* measurements and the diode model fits are listed in Table 5.2. Here, the beneficial effect of the grid for the PCE is evidently a result of a major increase of the FF from 61.6 % to 74.8 % when comparing the data of *fwd JV* scans of the IZO and IZO/grid setups. Some remanent hysteretic effects are responsible for the minor differences between *fwd* and *rvs* scan, mainly caused by deviations in the FF. The IZO/grid sample reaches almost a similar efficiency as the opaque sample with gold electrode, which has still a slight advantage in all *JV* parameters.

When comparing the diode parameters, the reduction of the R_s can be identified as the most significant factor for the performance gain and the increase of the FF. After the grid is applied, the R_s drops from $9.4\,\Omega\,cm^2$ to $3.5\,\Omega\,cm^2$, which is a reduction of over 60 %. The R_s of $1.6\,\Omega\,cm^2$ of the opaque sample is not quite reached, which partly explains the remaining difference in the performance. The other diode parameters also benefit from the application of the grid.

Sample		Experimental *JV* data					Parameters from one diode model fit				
Rear contact	Scan direction	PCE (%)	MPP (%)	FF (%)	J_{SC} (mA cm^{-2})	V_{OC} (mV)	R_s (Ω cm^2)	R_p (kΩ cm^2)	n	J_{ph} (mA cm^{-2})	J_0 (nA cm^{-2})
Gold	*fwd*	17.1	17.0	75.9	19.8	1136	1.64	2.33	2.41	19.9	0.02
	rvs	17.4		76.1	19.8	1154	1.60	2.44	2.26	19.8	0.45
IZO	*fwd*	13.9	13.9	61.6	19.7	1146	9.46	3.72	3.32	19.8	28
	rvs	13.8		61.1	19.7	1148	9.43	4.10	3.50	19.8	56
IZO/Grid	*fwd*	16.4	16.6	74.8	19.5	1126	3.52	3.69	2.24	19.5	0.58
	rvs	15.8		71.6	19.5	1129	3.14	3.02	2.65	19.5	1.25

Table 5.2: Solar cell parameters for architectures with different rear contacts: gold, IZO, and IZO/Grid. The *JV* data was obtained experimentally from the curves in Figure 5.7. The fitting parameters series resistance (R_s), parallel resistance (R_p), diode ideality factor (n), photo current density (J_{ph}), and reverse saturation current density (J_0) were obtained from the one diode model fits in Figure 5.8.

These results not only demonstrate a great performance gain for the PSC but promise to be a crucial factor for the development of efficient tandem devices. By introduction of the grid, the use of highly transparent TCOs with a limited thickness is now possible without limiting the top cell performance. It is also a technique that is scalable to a larger cell area, which is needed to form tandem devices with a targeted active area of $0.5\,\text{cm}^2$.

Increasing the PSC active area to $0.5\,\text{cm}^2$ with metal grid for integration in tandem solar cells with CIGS

The implementation of a metal grid into semitransparent PSCs with $0.24\,\text{cm}^2$ active area brings a significant reduction of the solar cells series resistance, as demonstrated in Section 5.1.2. But for cell size matched 4T-tandem cells an active area of $0.5\,\text{cm}^2$ is necessary, and the architecture of the PSC has to be adapted accordingly. An increased active area leads to longer lateral travel paths for the electrons through the TCO electrodes, which results in an even higher series resistance (R_s). The aim of this section is the reduction of the R_s in PSCs with $0.5\,\text{cm}^2$ cell size by implementation of a similar metal grid, as previously introduced.

Figure 5.9 shows a photograph along with a schematic illustration of such a PSC. The position of the increased active area is close to the substrate edge, in order to still being able to contact the CIGS bottom cell while the top cell is stacked on top. The outlines of the active area match exactly to the contours of the CIGS cell. Since the active area was more than doubled, compared to the smaller devices, the number of grid bars is increased from two to four. Other then their length, which is 8.8 mm from the tip to the contact pad, the dimensions width and height are similar to the grid that is applied to the small area. The contact pad is located 0.5 mm outside of the active area.
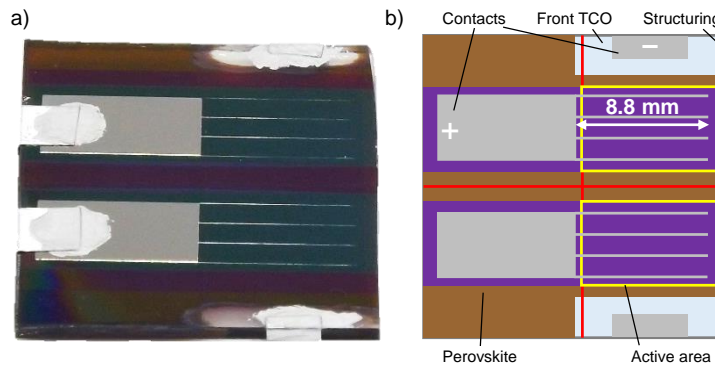
Figure 5.9: a) Photograph of a perovskite solar cell for tandem application with metal grid (ITO/SnO$_2$-NP/C$_{60}$-SAM/ SiO$_2$/CsFAMAPIBr/Spiro-OMeTAD/MoO$_3$/IZO/grid); b) Schematic drawing of the same indicating the dimension of the grid bars and the general architectural design. The active area is defined by the front TCO structuring and the rear TCO to $0.5\,\text{cm}^2$.

For calculation of the area of the shadow A_{shadow} that is cast on the CIGS active area A_{act}, the average width of the grid bars $w_{\text{avg}} = 41\,\mu\text{m}$ is multiplied by the number $n = 4$ and the length of $l = 8.3\,\text{mm}$ that reaches into the active area:

$$A_{\text{shadow}} = n * l * w_{\text{avg}} \tag{5.2}$$

The ratio of shaded area in comparison to the active area results in $A_{shadow}/A_{act} \approx 2.7\,\%$. This factor can be used for correction of the illumination intensity in measurements such as EQE spectroscopy on CIGS bottom cells with PSC filters applied on top.

For now, the effect of the grid on the PSC photovoltaic performance is evaluated. Figure 5.10 shows the statistical results of the characteristic JV values of PSCs with an A_{act} of $0.24\,cm^2$ and $0.5\,cm^2$ and with and without a metal grid applied to the rear electrode. As expected, the PCE values indicate that the application of the metal grid on the larger cells has an increasingly positive effect. A mean increase of approximately $3\,\%$ in absolute value is observed, compared to the cells without grid. On smaller area, the gain is limited to only $\approx 2\,\%$. In this experiment, the maximum PCE values reach about $16\,\%$ and $14\,\%$ for the $0.24\,cm^2$ and $0.5\,cm^2$ cells, respectively.
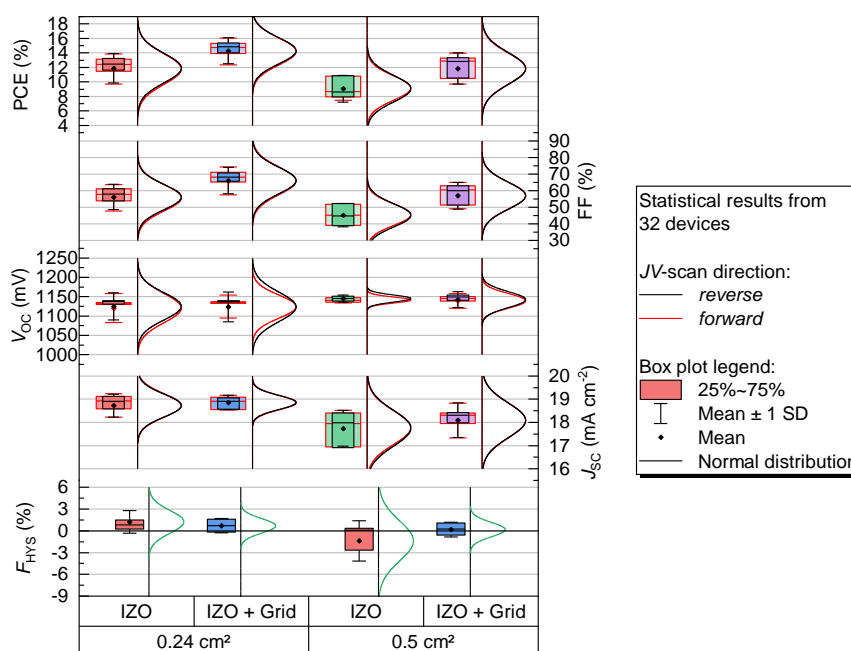
Figure 5.10: Box chart of JV-characteristics of perovskite solar cells (ITO/SnO$_2$-NP/C$_{60}$-SAM/SiO$_2$-NPs/ CsFAMAPIBr/Spiro/MoO$_3$/IZO) with different cell sizes and optional Ni-Al-Ni grid.

The performance gain is mainly related to an improved FF, which already indicates an improved R_s, as intended by the grid application. On the one hand, the V_{OC} seems to profit from the enlarged area, but the difference is not statistically significant. On the other hand a loss of up to $1\,mA\,cm^{-2}$ in average is observed in the J_{SC} on $0.5\,cm^2$. The reason for this may be related to an geometric error in the exact definition of the active area by the sputtered rear electrode. In average, all of the combinations have a F_{HYS} close to zero.

Figure 5.11a displays the JV responses of the best performing PSCs of the experiment. The steepness of the diode curves in forward bias direction demonstrates the large effect of the grid and the area of the cell on the conducting properties, hence decreasing the R_s. Comparing the $0.5\,cm^2$ cell without grid and the $0.24\,cm^2$ cell with grid, the significant reduction of the FF by the high R_s is observable.

In order to quantify the conductive properties of the solar cells, single diode model fits have been applied to the *JV* curves in Figure 5.11b and c. J_{SC}-shifted semi logarithmic plots are used in order to evaluate the quality of the fits to the *JV* responses under illumination. During the fitting procedure, the diode equation was modeled in such a way that the best precision is achieved in the regimes of the R_s and R_p. Regarding the cells with grid, the fitted curves in the part in between both regimes is deviating slightly from the experimental data, indicating that the single diode model is not sufficient for an exact replication of the measurement. However, this part of the curve is mainly a result of the quality of the diode properties of the solar cell, hence described by n and relatively unaffected by R_s and R_p.
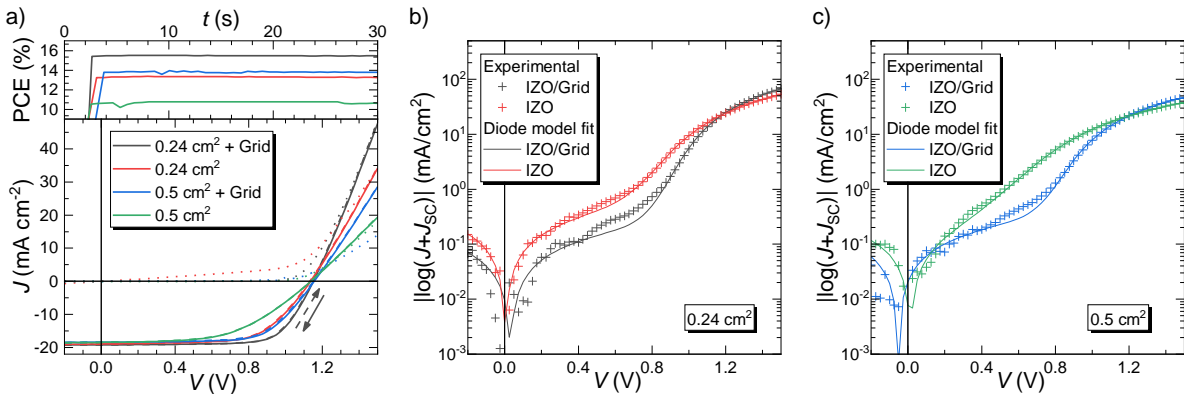
Figure 5.11: a) *JV*-responses of perovskite solar cells (ITO/SnO$_2$-NP/C$_{60}$-SAM/SiO$_2$-NPs/CsFAMAPIBr/Spiro/ MoO$_3$/IZO/grid) with different cell sizes (0.2413 cm^2 and 0.5 cm^2) and optional Ni-Al-Ni grid. b) and c) single diode model fits to the *JV*-responses (*rvs* scans) of the same cells. The data is shifted by the J_{SC} and displayed as absolute values of the logarithm.

Table 5.3 lists the characteristic parameters from the *JV* measurements and from the corresponding single diode model fits for the cells from Figure 5.11. As intended, the quantified values for R_s prove a reduction by ≈30 % on small and large area, when a grid is applied. Then, the R_s drops to 5.77 Ω cm^2 and 9.95 Ω cm^2 on 0.24 cm^2 and 0.5 cm^2, respectively. An improvement of the other diode parameters is also observed with a metal grid supported electrode.

Sample		Experimental *JV* data					Parameters from single diode model fit				
A_{act} (cm^2)	Rear contact	PCE (%)	MPP (%)	FF (%)	J_{SC} (mA cm^{-2})	V_{OC} (mV)	R_s (Ω cm^2)	R_p (kΩ cm^2)	n	J_{ph} (mA cm^{-2})	J_0 (nA cm^{-2})
0.2413	IZO/grid	15.7	15.4	71.2	19.2	1151	5.77	3.31	2.25	19.2	0.04
	IZO	13.5	13.1	63.0	18.9	1132	8.24	1.34	3.03	19.0	8.26
0.5	IZO/grid	13.9	13.7	65.4	18.4	1156	9.95	2.49	2.32	18.5	0.07
	IZO	10.9	10.5	52.1	18.4	1137	14.5	1.92	4.26	18.6	557

Table 5.3: Solar cell parameters for architectures with different cell sizes (0.2413 cm^2 and 0.5 cm^2) and IZO rear contacts with optional Ni-Al-Ni grid. The *JV* data was obtained experimentally from the *rvs* scans in Figure 5.11a. The fitting parameters series resistance (R_s), parallel resistance (R_p), diode ideality factor (n), photo current density (J_{ph}), and reverse saturation current density (J_0) were obtained from the corresponding single diode model fits in Figure 5.11b and c.

The results prove a successful implementation of a Ni-Cu-Ni grid in PSCs with a larger area of $0.5\,\mathrm{cm}^2$. For tandem devices with CIGS bottom cells this increased area is necessary in order to match an equally sized A_{act} of both sub cells. Additionally, the results indicate how important the grid is to maintain a high PCE of the PSC, because otherwise the increase of the active area leads to significant performance losses, mainly due to a large R_{s}.

5.2 Investigation of suitable CIGS bottom cells

The aim of this section is to understand the JV response of the CIGS cells, when they are exhibited to a transmission spectrum of a PSC. A simple but sufficiently accurate simulation routine is developed using a single diode model approach that allows for estimating the PCE, FF, J_{SC}, and V_{OC} of the CIGS cell under a hypothetical PSC transmission spectrum. The simulation routine may be applied for estimating the CIGS efficiency for a series of fictional transmission spectra as described in Section 5.4.3 or simply for estimating the theoretical efficiency for real transmission spectra of PSCs that are too small for tandem measurements and no representative filters are available as it is done in Section 5.3.

In this process, Section 5.2.1 investigates two different CIGS solar cells that shall be used in the subsequent experiments in various 4T tandem configurations. Their different architectures are investigated focusing on their individual spectral responses and band gaps.

Section 5.2.2 evaluates the CIGS performance under illumination by different PSC transmission spectra. Furthermore, single diode models are developed that can be used to simulate the JV responses of the CIGS under filter illumination conditions.

Subsequently, in Section 5.2.3, the models are extended so that the PCEs of the CIGS cells can be simulated for other hypothetical transmission spectra. This is achieved by using the integrated J_{SC} from the filtered EQE data of the CIGS cell as an input for the single diode model to estimate the JV response.

5.2.1 CIGS architectures with different band gaps

The CIGS solar cells that are investigated in the following were fabricated by a team of researchers at ZSW by thermal co-evaporation under different atmospheric conditions as described in [121].

This section investigates the setups of two CIGS solar cells, which are used as tandem partners in various experiments throughout the following sections. Figure 5.12 shows SEM cross sections of two different CIGS absorber layers that have different gallium content.
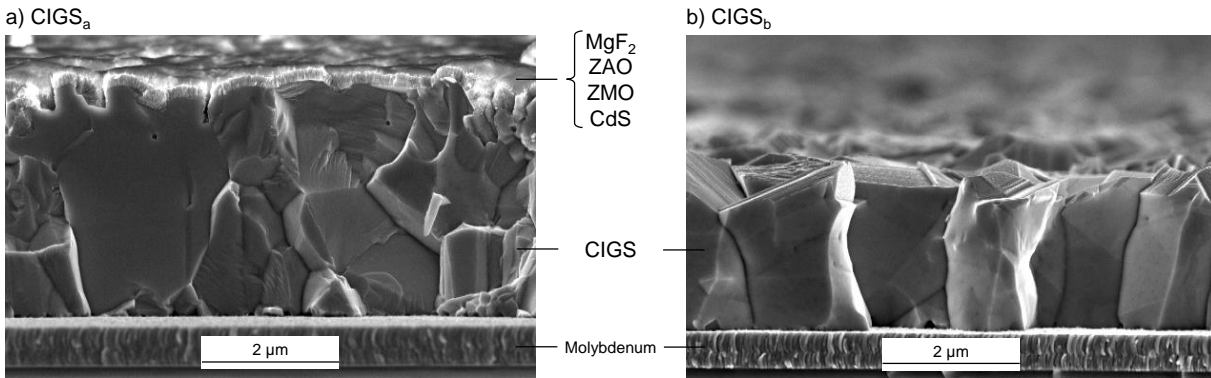
Figure 5.12: Cross sectional SEM images of a) a complete high efficiency CIGS solar cell and b) a CIGS cell with a low gallium content before buffer and window layer deposition.

The SEM images show that the absorber layer of both samples have a different thickness and morphology. Designed for high PCE in solo applications, the CIGS cell in Figure 5.12a (CIGS$_a$) has a engineered gallium gradient along the comparably thick absorber layer. The buffer layer cadmium sulfide (CdS) and the window layers zinc magnesium oxide $Zn_xMg_{1-x}O$ (ZMO) and ZAO have a optimized thickness for low parasitic absorption and the use of a metal grid. Additionally, an ARC of magnesium fluoride (MgF$_2$) has been applied for better optical yield. The CIGS layer in Figure 5.12b (CIGS$_b$) is thinner and has a very low gallium content in order to reduce the E_g. The buffer and window layers are not shown in the image.

Table 5.4 lists the thicknesses of all layers of the two final CIGS cell architectures. It shows that CIGS$_b$ comprises intrinsic zinc oxide (i-ZnO) instead of ZMO and uses a larger ZAO and CdS layer thickness than CIGS$_a$.

Layer	CIGS$_a$	CIGS$_b$
	d (nm)	d (nm)
MgF$_2$	113	-
ZAO	145	420
ZMO	50	-
i-ZnO	-	90
CdS	24	50
CIGS	3070	2340
Mo	570	510

Table 5.4: Layer thickness values of the solar cell architectures of CIGS cell with E_g = 1.1 eV (CIGS$_a$) and CIGS cell with E_g = 1.0 eV (CIGS$_b$).

The E_g of the CIGS cells can be adjusted by variation of the gallium to indium ratio (GGI). An engineered GGI gradient along the depth of the CIGS layer is generally used to optimise the solar cell performance. [122] The glow discharge optical emission spectroscopy (GDOES) data in Figure 5.13 reveals that the GGI ratio of $CIGS_a$ varies between 0.2 at the front and 0.5 at the back with a minimum of 0.15. The GGI profile of $CIGS_b$ is comparably flat and the Ga content is nearly zero in the front. As the minimum of the GGI reflects also the minimum of the E_g, it is decisive for the overall absorption range of the CIGS solar cell.
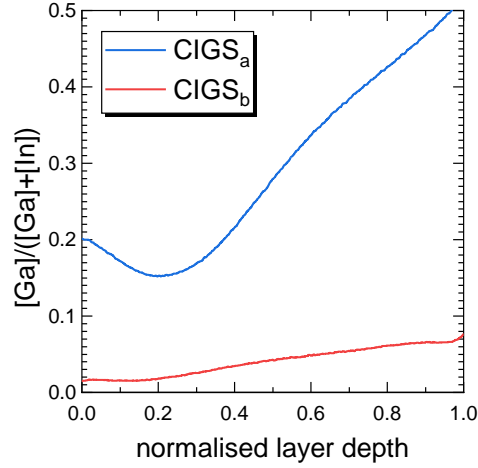
Figure 5.13: Experimental data from GDOES: GGI ratios as functions of the normalized CIGS layer depth of the high efficiency CIGS solar cell ($CIGS_a$) and a CIGS cell with a low gallium content ($CIGS_b$).

Having a much lower GGI minimum, the absorption range of $CIGS_b$ is extended up to $\approx 1300\,nm$ as demonstrated in the EQE data in Figure 5.14a compared to $CIGS_a$, which absorbs only up to $\approx 1150\,nm$. Furthermore, the relatively lower EQE of $CIGS_b$ especially in the range of $300\,nm$ to $450\,nm$ results from the increased parasitic absorption of the comparably thicker ZAO and CdS layers.

In order to determine the E_g of both cells from the EQE, two approaches are chosen here. The first method, introduced by Helmers et al. [123], is based on an exponential relationship between the absorption coefficient (α) and the photon energy ($h\nu$) (Urbach's rule) [124–126]

$$\alpha \propto \exp\left(\frac{\sigma h\nu}{kT}\right),\tag{5.3}$$

with the Boltzmann constant (k), the temperature (T) and a dimensionless steepness parameter (σ). The second method involves the square root relationship between α and E_g of a direct band transition (Tauc relation) [127, 128], which was originally developed for amorphous materials but has proven to be also accurate for crystalline materials: [129]

$$h\nu \cdot \alpha \propto \sqrt{h\nu - E_g}.\tag{5.4}$$

Assuming a sufficiently good absorption at the band edge and a sufficient diffusion length, which is the case for CIGS, the absorption coefficient is directly proportional to the EQE. [130]

Hence, following equation 5.3 the onset of the EQE exhibits an exponential behaviour in Figure 5.14b and saturates close to unity above E_g. As stated in ref. [123], the E_g is determined by the transition from the onset to the saturation regime, by fitting two exponential functions of the form $\exp(a + b \cdot h\nu)$ to the corresponding regimes and extracting E_g from their intersection, marked by a sphere symbol.

Using the Tauc relation from eq. 5.4, the linear regions in the $(h\nu \cdot \mathrm{EQE})^2$ versus $h\nu$ plots in Figure 5.14c are interpolated to derive the E_g from the intersection with the abscissa axis.
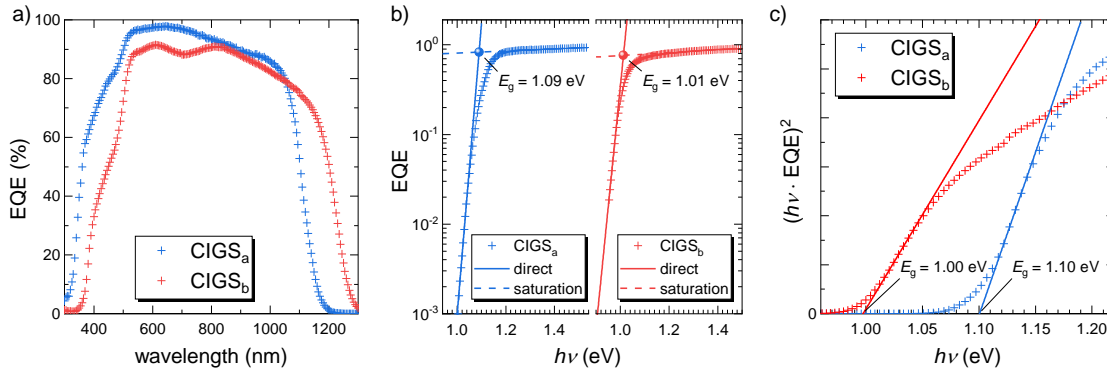
Figure 5.14: a) EQE responses of CIGS$_\mathrm{a}$ and CIGS$_\mathrm{b}$; The E_g is determined from the EQE by two methods: b) In the semilogarithmic plots of the EQEs versus $h\nu$ E_g is derived from the intersection of two exponential fits, one at the onset of the EQE and one in the saturation region. c) In the $(h\nu \cdot \mathrm{EQE})^2$ versus $h\nu$ plots E_g is determined from the intersections of the linear interpolations with the abscissa axis.

Both methods for determining the E_g give similar results with low deviations of $<10\,\mathrm{meV}$. According to the results CIGS$_\mathrm{a}$ has a E_g of 1.1 eV and CIGS$_\mathrm{b}$ with the low gallium content has a E_g of 1.0 eV, which is comparable to the E_g of pure CIS.

5.2.2 CIGS bottom cell performance estimations from single diode models

This section investigates the two CIGS cells with the band gaps of 1.1 eV and 1.0 eV, which were introduced in the previous Section 5.2.1. Their JV performance is measured under the full AM1.5G solar spectrum and under the transmission spectra of two different perovskite filters. The filters have equal layer stacks despite different front electrodes. The one comprises a highly NIR transparent IO:H electrode and the other has a less transparent ITO electrode in order to simulate significant changes in the transmitted spectrum. The spectral differences are used to investigate how the diode behaviour of the CIGS is affected.

In order to create simple and accurate simulation routines that can predict the JV respsonses of the two CIGS cells in these tandem configurations, single diode models are developed that use the input parameters R_s, R_p, n and J_0 from direct fits to these measurements. The J_SC value can be integrated from filtered EQE data using the transmission data of the PSC which is discussed in more detail in the subsequent section 5.2.3. From this set of model parameters the CIGS cells characteristic values PCE, FF, V_OC, and J_SC can be calculated using the model.

Hence, the results of the measurements and fits are plotted in Figure 5.15 for determination of the fitting parameters R_s, R_p, n, and J_0.
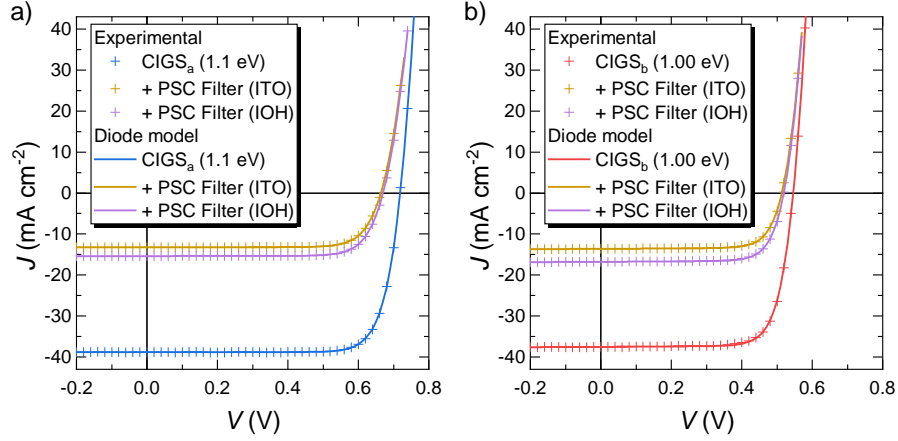
Figure 5.15: a) Experimental *JV* data of a CIGS cell with E_g = 1.1 eV (CIGS$_a$) measured without a filter (solo) and filtered by PSCs with different front TCOs (ITO and IO:H). The solid lines represent single diode model fits of the three cases. b) *JV* data and single diode model fits of a CIGS cell with E_g = 1.0 eV (CIGS$_b$) under the same conditions.

In general, the individual fits show a very good accordance with the experimental data. As intended, the filters absorb a large proportion of the light, so that the photocurrent of the CIGS is reduced. Since the perovskite filters themselves have a different transmittance, the current generated by the filtered CIGS cells varies significantly. Especially the CIGS cell with the smaller E_g of 1.0 eV (Figure 5.15b), hence broader absorption range, gains more current from the increased NIR transmittance of the PSC filter with the IO:H front electrode (blue line), compared to the PSC with ITO (red line).

Table 5.5 lists the experimental data from the *JV* measurements and the fitting parameters for the two investigated CIGS cells under the different illumination conditions.

Sample		Experimental JV Data				Parameters from single diode model fit						
ID	Filter	PCE	FF	J_{SC}	V_{OC}	R_s	R_p	n	J_{ph}	J_0	FF	PCE
		(%)	(%)	(mA cm^{-2})	(V)	(Ω cm^2)	(kΩ cm^2)		(mA cm^{-2})	(nA cm^{-2})	(%)	(%)
CIGS$_a$	solo	22.13	79.4	38.8	0.72	0.28	17.3	1.40	38.8	0.09	79.3	22.13
	ITO	6.85	78.0	13.2	0.66	0.59	14.4	1.44	13.2	0.23	78.0	6.84
	IO:H	8.04	78.0	15.4	0.67	0.57	14.3	1.45	15.4	0.25	77.9	8.03
CIGS$_b$	solo	15.61	76.3	37.5	0.55	0.25	2.3	1.27	37.5	1.95	76.4	15.64
	ITO	5.27	75.3	13.6	0.51	0.32	2.3	1.24	13.6	1.29	75.9	5.31
	IOH	6.58	75.5	16.8	0.52	0.31	2.3	1.25	16.8	1.55	76.0	6.62

Table 5.5: Experimental *JV* data and parameters of the corresponding single diode model fits for a CIGS cell with E_g = 1.1 eV (CIGS$_a$) and CIGS$_b$ measured without a filter (solo) and filtered by PSCs with different front TCOs (ITO and IO:H).

A difference of the diode parameters is observed comparing the filtered and unfiltered CIGS cells. Especially the fitting parameters R_p, R_s, and J_0 show large deviations under filtered conditions. This is true for both types of CIGS with different band gaps. The variations can be explained by the different charge carrier generation profiles along the depth of the CIGS cell under the changing spectral conditions.

However, it is also observed that the fitting parameters for the filtered JV curves prove to be very similar between the two types of applied filters. Hence, the set of fitting parameters for the simulation routines is determined for the two CIGS cells, resulting in the average values in Table 5.6. With these sets of parameters JV curves for the filtered $CIGS_a$ and $CIGS_b$ cells can be simulated from the implicit single diode model equation 5.5 using the J_{ph} as an additional input. One benefit of using the single diode model approach is that it allows for an iterative numerical calculation of the solar cell parameters PCE, FF, V_{OC} and J_{SC}. [131, 132]

$$ J = J_0 \cdot \left[\exp\left(\frac{V - J \cdot R_s}{n \cdot kT/q} \right) - 1 \right] + \frac{V - J \cdot R_s}{R_p} - J_{ph} \tag{5.5} $$

Sample	Parameters for single diode model simulation			
ID	R_s	R_p	n	J_0
	($\Omega\,cm^2$)	($k\Omega\,cm^2$)		($pA\,cm^{-2}$)
$CIGS_a$	0.58	14.35	1.45	237
$CIGS_b$	0.32	2.27	1.24	1422

Table 5.6: Parameters for the single diode model simulations for CIGS cell with $E_g = 1.1\,eV$ ($CIGS_a$) and $CIGS_b$ as bottom cells under filter conditions.

For validation of the equations the coefficient of determination (R^2) is reviewed for the four tandem setups, using the experimental J_{SC} values for J_{ph} in the calculation of the JV curve models. The residual results and the experimental PCE_f and simulated PCE_{Sim} values are listed in Table 5.7 and indicate that both models achieve a very high accuracy in all cases with a R^2 of over 0.995 and a close match of the PCE.

Sample			Experimental	Single diode model	
ID	E_g	Filter	PCE_f	PCE_{Sim}	R^2
	(eV)		(%)	(%)	
$CIGS_a$	1.1	ITO	6.85	6.85	1.000
		IO:H	8.04	8.03	0.9995
$CIGS_b$	1.0	ITO	5.27	5.28	0.9966
		IOH	6.58	6.61	0.9988

Table 5.7: Comparison of the experimental PCE data of filtered $CIGS_a$ and $CIGS_b$ with the simulated values obtained by the single diode models. The CIGS cells are filtered by PSCs with different front TCOs (ITO and IO:H). R^2 denotes the coincidence of the experimental and simulated JV curve.

The single diode models for $CIGS_a$ and $CIGS_b$ can be used to precisely determine the performance of these cells in a hypothetical tandem setup under two conditions: (i) the photo current density (J_{ph}) of the filtered CIGS is known and (ii) the illumination spectrum matches roughly with the transmitted spectrum of the perovskite filters.

5.2.3 Estimation of the CIGS performance under different illumination conditions

For estimating the PCE of the bottom cells by the single diode models in real or fictional tandem setups, the J_{ph} has to be measured or simulated in the most precise manner. Typically, the $J_{ph} = J_{EQE}$ is obtained from EQE measurements by integration and multiplication with the AM1.5G solar spectrum following equation 2.15.

Here, the possibility to estimate the J_{ph} from simulated EQE data of the CIGS is discussed and compared to experimental data. Therefore, the T of real PSC devices is used to modulate the EQE responses of the CIGS cells. The photo current density obtained by EQE simulation (J_{Sim}) is calculated via equation 5.6 using the EQE of the sample and the current density equivalent of the photon flux (qN_{ph}) of the AM1.5G solar spectrum:

$$J_{Sim} = \int T \cdot EQE \cdot qN_{ph} \, d\lambda \qquad (5.6)$$

J_{Sim} is used as an input for J_{ph} in the single diode model equation, in order to calculate the theoretical PCE. This procedure allows for estimating the hypothetical tandem efficiency for any PSCs by measuring only the T spectrum.

Figure 5.16 shows the T spectra of the two PSCs with different front electrodes IO:H and ITO, which have been also used for the development of the single diode models in the previous Section 5.2.2.
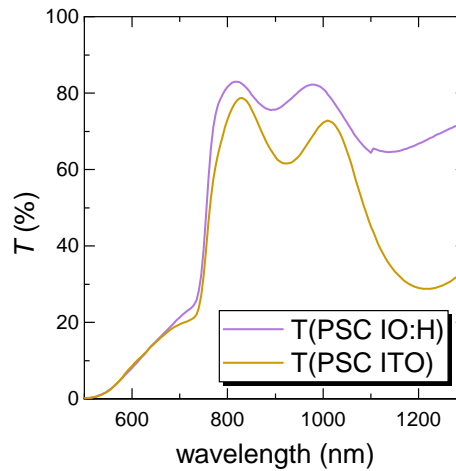
Figure 5.16: Transmittance data of two PSCs with different front electrode (IO:H and ITO). The E_g of the perovskite is 1.6 eV.

Between 500 nm to 750 nm the transmittance of the devices increases up to $\approx 20\%$ due to insufficient absorption of the perovskite layer. At the perovskite absorption edge at ≈ 750 nm, the T increases and is then limited only by parasitic absorption and reflection losses in the NIR regime. Here the improved NIR transmittance of the PSC filter with IO:H front electrode becomes visible, although the T is still strongly limited by reflection losses, which can be seen from the interference patterns.

By multiplication of the T spectra of the filters with the EQE responses of the previously introduced CIGS cells (CIGS$_a$ and CIGS$_b$ with E_g =1.1 eV and 1.0 eV, respectively) under illumination of the AM1.5G solar spectrum, Figure 5.17 shows the simulated EQE as they would appear in the actual tandem configuration. For comparison, also the experimental EQE of the CIGS cells is shown, when the cells are filtered by the two real PSC devices, denoted as PSC-IO:H and PSC-ITO.
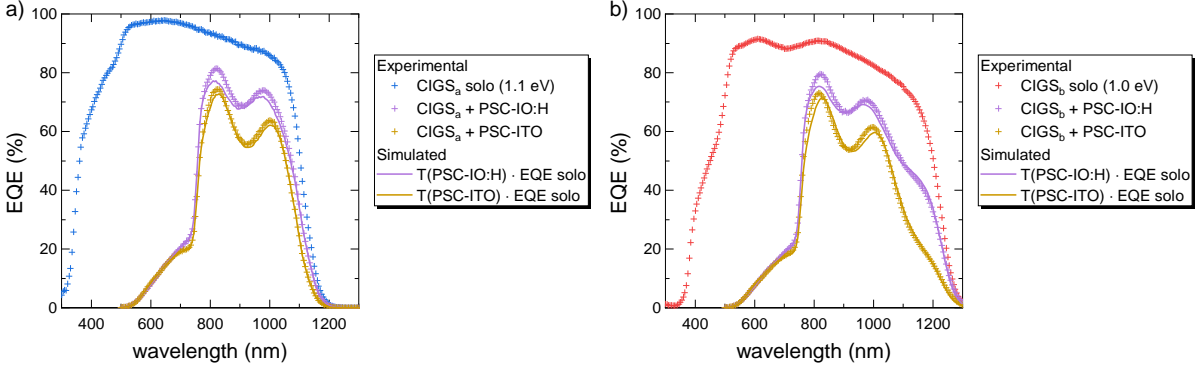
Figure 5.17: a) Experimental EQE data (+) of a CIGS cell with an E_g of 1.1 eV under the AM1.5G solar spectrum (solo) and under two PSC filters with different front electrode (IO:H and ITO). The simulated EQE data (—) is obtained from multiplication of the EQE with transmittance data from Figure 5.16. b) Similar data for a CIGS cell with an E_g of 1.0 eV.

Comparing the experimental and simulated EQE responses of the two CIGS cells in Figure 5.17a and b, the simulated curves seem to underestimate the quantum efficiency to some extent, especially in the regimes of the interference maxima, where most light is transmitted. This effect is reasoned by the additional back reflection of light at the PSC that got partially reflected from the CIGS bottom cells surface in the first place. In experiment, this double back reflection takes place naturally, increasing the quantum efficiency of the bottom cell. But when using only the T spectrum as an input for the EQE simulation, the additional amount of back reflected light is neglected.

Since the double back reflection is dependent on T and the refractive indices of all contributing layers in the tandem stack, this effect cannot be easily included in this simple simulation approach. However, by calculating the mismatch between experiment and simulation, the error introduced by this effect can be estimated and respected in the simulations for the fictional PSC filters. When calculating the J_{EQE} from the measured and J_{Sim} from the simulated EQE responses with the filters PSC-IO:H and PSC-ITO applied, the maximum relative errors summarise to <3.5 % and <2.5 % for the two CIGS cells with E_g =1.1 eV and 1.0 eV, respectively.

The calculated J_{Sim} and J_{EQE} values for the different scenarios are used to estimate the corresponding PCE of the CIGS cells according to the single diode model equation 5.1. Figure 5.18 summarises the PCE results for both cells CIGS$_a$ and CIGS$_b$ as a function of the J_{ph}. The filter setups used in the calculation are colour coded and denoted accordingly. Additionally the graph contains the experimental PCE and J_{SC} values obtained from regular JV measurements for both CIGS cells with the PSC-IO:H and PSC-ITO filters applied.
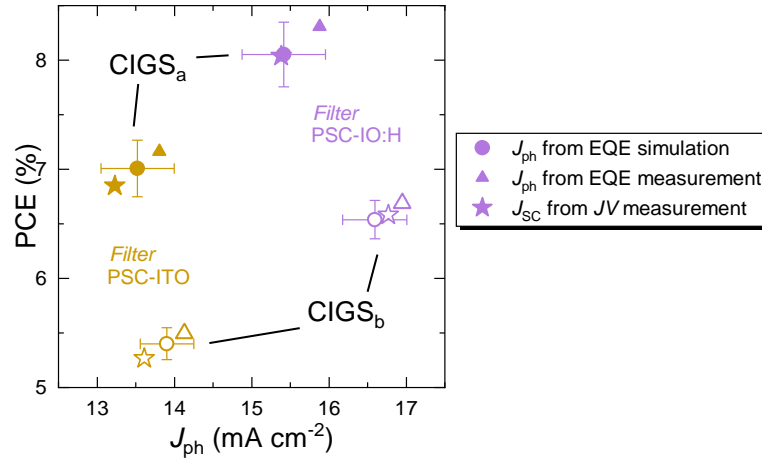
Figure 5.18: Simulated and experimental PCE and J_{ph} data of CIGS cells with E_g of 1.1 eV and 1.0 eV under different PSC filters as denoted in the diagram. The T spectra of the filters are shown in Figure 5.16. The J_{ph} was calculated from the corresponding simulated and experimental EQE data in Figure 5.17(J_{Sim} and J_{EQE}). Additionally, the corresponding J_{SC} and PCE values from JV measurements are shown for the two PSC filters with different front electrodes IO:H and ITO.

For the setups with the PSC-ITO filter, both CIGS cells show the lowest J_{ph} of about 13.5 mA cm^{-2} to 14 mA cm^{-2} due to the low transmittance of the filter. Compared to the experimental values from EQE and JV measurements, both simulated PCE values of about 5.5 % and 7.0 % lay within the error distances.

The second PSC-IO:H filter has a higher transmittance, especially in NIR, and thus the J_{ph} and PCE increases significantly. Here, the lower band gap CIGS$_b$ with 1.0 eV benefits from the wider absorption range in NIR and gains a higher J_{ph} of 16.6 mA cm^{-2} compared to the cell with 1.1 eV, which generates only 15.4 mA cm^{-2} under the same conditions.

Concluding, the approximation of the J_{Sim} of CIGS$_a$ and CIGS$_b$ via a modulation of their EQE responses with a PSC T spectrum introduces a relative mismatch of up to 3.5 % compared to the experimentally determined J_{EQE}. This error is in the same range of the optical mismatch that is to be expected, when filter stacks are utilized for the tandem PCE estimation, which was shown in Section 5.1.1. Hence, the procedure is a valid and effective alternative tool, to estimate the CIGS efficiency in hypothetical tandem setups, by measuring the T of the actual PSC top cell, rather than preparing an extra filter device for the experimental determination of the performance.

Furthermore, the approach can be used to predict the CIGS performance under the influence of fictional T spectra with e.g. higher transmittance or shifted band gaps, which will be part of Section 5.4.3 later on.

5.3 Photovoltaic performance of tandem architectures with different perovskite and TCO combinations

The aim of this section is to evaluate the tandem cell performance of the different PSC architectures as top cells in combination with CIGS as bottom cells. During the development of efficient semitransparent PSCs in Section 4.3, many optimization cycles were evaluated for the different layer materials such as the TCOs, the buffer layers and the perovskite absorber material itself. It was shown that the choice of the electrode material has the greatest influence on the NIR transmittance of the PSC. Additionally, the band gap of the perovskite, depending on the composition, is a limiting criteria for the amount of transmitted light. The two perovskite compositions MAPbI$_3$ (MAPI) and mixed ionic perovskite (CsFAMAPIBr), which were mainly part of the discussion in Chapter 4, have both a relatively close band gap between 1.61 eV and 1.65 eV. From collaboration with Karlsruher Institut für Technologie (KIT) and LMU, further PSCs with a greater range of different E_g have been thankfully provided.

Hence, the following sections cover the evaluation of 4T tandem architectures with MAPI (Section 5.3.1), CsFAMAPIBr (Section 5.3.2) in combination with CIGS bottom cells. As bottom cells serve the CIGS cell with $E_g = 1.1$ eV (CIGS$_a$) and the CIGS cell with $E_g = 1.0$ eV (CIGS$_b$), introduced in the previous section.

5.3.1 Simple perovskite based top cells

Simple MAPI based PSC represent the reference, which this work started to develop on. Before new perovskite absorber materials were introduced, suitable transparent electrodes and buffer layers were thoroughly evaluated with this architecture in Chapter 4. Although the MAPI based PSC did not reach the highest efficiencies compared to the CsFAMAPIBr perovskite, it is worth to briefly investigate the performance of this material in tandem application, which may be seen as a reference from which the development of highly transparent perovskite top cells continues.

One of the best performing semitransparent MAPI based PSC of this work is displayed as a cross sectional SEM image in Figure 5.19. For clarification, the layers in the image are shown in order of preparation from bottom to top. Because the light passes through the cell in the same direction, the FTO is named the front and IZO as the rear electrode.
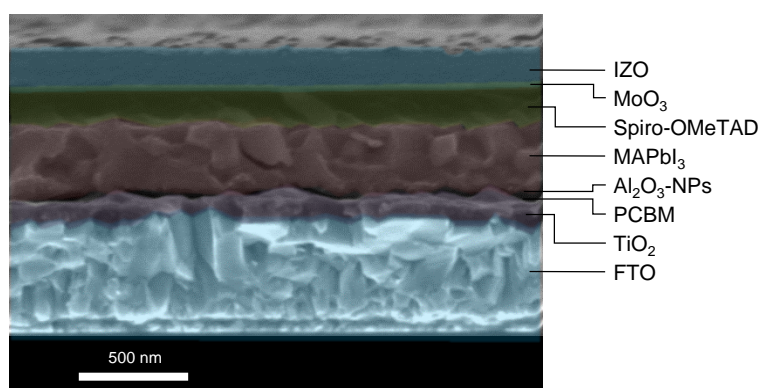
Figure 5.19: Cross sectional SEM image in false colours of a semitransparent PSC with simple MAPI absorption layer.

Despite the use of low NIR absorbing IZO, the FTO is responsible for a reduced NIR transmittance of the layer stack, which is demonstrated by the spectral T response in Figure 5.20a. Since the PSC has a very small active area (A_{act}) of $\approx 0.1\,cm^2$, it is not applicable in an actual tandem setup with a $0.5\,cm^2$ CIGS bottom cell. Additionally, no representative filter device is available for this solar cell. Hence, for estimating the performance of a principle tandem setup, the method from Section 5.2 is applied. Therefore, the spectral T of the PSC is used to modulate the EQE of the two bottom cells $CIGS_a$ and $CIGS_b$ with an E_g of 1.1 eV and 1.0 eV, respectively, as demonstrated in the same graph.
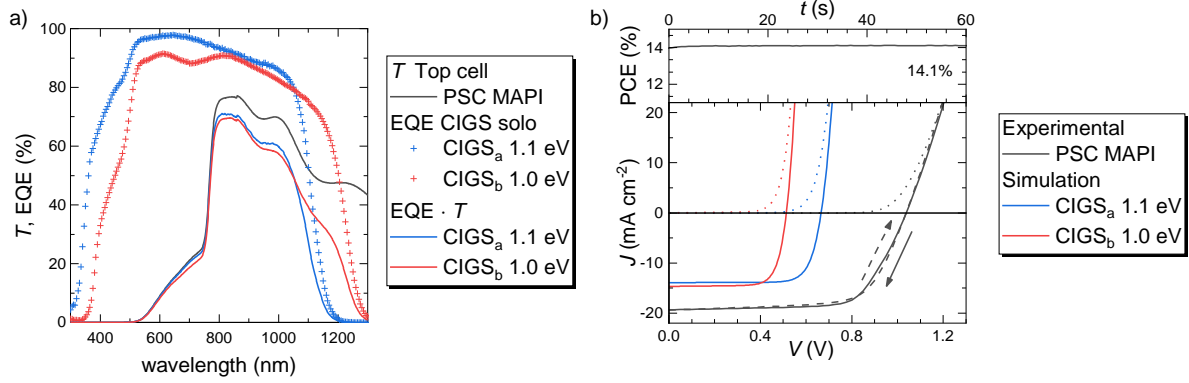
Figure 5.20: a) Spectral T of semitransparent MAPI PSC and experimental EQE data (+) of unfiltered CIGS cells with E_g of 1.1 eV and 1.0 eV (solo). The simulated EQE data (–) is obtained from multiplication of the EQE with transmittance data and shall represent the CIGS EQE in tandem application with the PSC. b) JV characteristics and MPP-response (inset) of the PSC and the simulated JV curves of the CIGS bottom cells in tandem application with the PSC. The simulation is performed by single diode model calculations with the theoretical J_{ph} values from the EQE.

Because of the relatively low T of below 80 % after the fundamental absorption edge at about 750 nm, the filtered EQE show equivalently low theoretical progression curves. Integrating the EQE leads to estimated J_{Sim} values of 13.9 mA cm^{-2} and 14.7 mA cm^{-2} for $CIGS_a$ and $CIGS_b$, respectively. Using the J_{Sim} as an input, the single diode model equation 5.1 is used to simulate the corresponding JV curves in Figure 5.20b. Additionally, the graph shows the measured JV response of the PSC along with the dynamic MPP tracking in the inset, where the PSC achieves a PCE of 14.1 % at the highest after 60 s under one sun illumination.

Table 5.8 lists the estimated PCE_{Sim} of the bottom cells and the corresponding 4T tandem setups.

Top Cell	Bottom Cell Simulated				Tandem Simulated	
MAPI	$CIGS_a$		$CIGS_b$		$CIGS_a$	$CIGS_b$
PCE*	PCE_{Sim}	J_{Sim}	PCE_{Sim}	J_{Sim}	PCE	PCE
(%)	(%)	(mA cm^{-2})	(%)	(mA cm^{-2})	(%)	(%)
14.1	7.2	13.9	5.7	14.7	21.3	19.8

* measured after 60 s of dynamic MPP tracking under one sun illumination

Table 5.8: Experimental PCE value for a MAPI based solar cell and simulated bottom cell- and tandem PCE values for setups with a $CIGS_a$ or $CIGS_b$.

As a result, the CIGS cell with $E_g = 1.1$ eV (CIGS$_a$) retains only about 7.2 % in PCE$_{Sim}$ by calculation of the performance with the single diode model and the T of the PSC (iv). Because the loss in PCE$_{Sim}$ accounts for nearly 15 % absolute compared to the solo PCE of 21.1 %, the hypothetical tandem device of the PSC and CIGS$_a$ would have a summarized PCE of 21.3 %, which is even lower than the solo PCE of CIGS$_a$.

With the extended absorption range, the CIGS cell with $E_g = 1.0$ eV (CIGS$_b$) is able to achieve a higher J_{Sim} than CIGS$_a$. Despite that the resulting PCE$_{Sim}$ from the filtered single diode model calculation is only as high as 5.7 %, the loss compared to the solo PCE is only about 10 % in absolute values. This raises the theoretical tandem setup PCE of 19.8 % above both single cell PCEs of 15.6 % in solo application (compare Table 5.5).

The results demonstrate that for high efficiency CIGS cells, also very good performing PSC cells are needed in order to make the tandem setup having a better PCE than each of the sub cells. A good performing PSC does not only demand a high PCE but a very good NIR transmittance.

5.3.2 Multi cation perovskite based top cells

A higher tandem efficiency is expected from the use of the CsFAMAPIBr perovskite absorber material in the top cell, compared to simple MAPI. The multi cation approach has proven main advantages in power conversion efficiency and hysteresis as discussed in Chapter 4, which would directly benefit the tandem performance. In Figure 5.21 the E_g of CsFAMAPIBr is determined to be ≈ 1.62 eV, which is similar to MAPI [27], hence no band gap related gain is expected for the bottom cell performance. However, the transmittance of the semitransparent PSCs with CsFAMAPIBr could be significantly increased with the introduction of low NIR absorbing TCO electrodes in Section 4.3.2, which promises great potential in tandem application.

Therefore, this chapter evaluates the performance of tandem architectures with CsFAMAPIBr based PSCs and CIGS focusing on the use of different TCO combinations for the electrodes. The discussion is divided into two sections. Firstly, the variety of combinations is compared by tandem efficiency estimations with different PSC filters. Secondly, a selection of the most promising setups is evaluated in actual tandem devices with PSC and CIGS cells of the same cell size.

Estimation of tandem device PCEs with PSC filters

Semitransparent PSC with a high transmittance (T) in the NIR regime are mandatory for a well performing bottom cell in tandem applications. The absorptance (A) of the PSC could be significantly reduced in the NIR with the introduction of IO:H and IZO as electrodes, but higher PCEs values were achieved with the traditional TCO, such as ITO. The question of which results in a better tandem performance is about to be discussed in the following.

For evaluation of the bottom cell performance, a set of perovskite filters is prepared that is used to estimate the PCE$_f$ of the CIGS cells in different possible tandem setups via simulations or experiments. The performance data of the top cell setups is collected from various experiments, comprising the best performing PSC with similar architectures to the filters. All of the PSCs have an A_{act} of 0.24 cm^2, some are equipped with an optional metal grid at the rear electrode. Finally the tandem PCE is estimated from the sum of the PCEs of each sub cell.
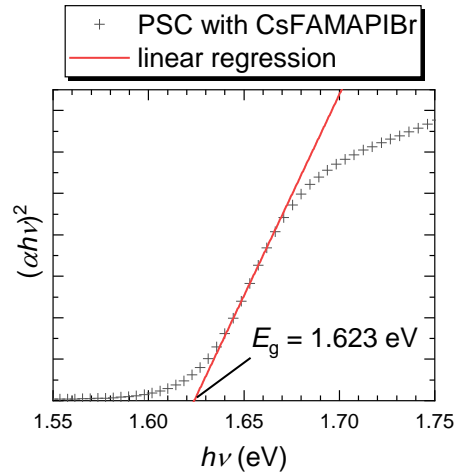
Figure 5.21: Tauc plot $(\alpha h \nu)^2$ versus $h\nu$ for a PSC with CsFAMAPIBr perovskite absorber material for determining the E_g.

Figure 5.22a shows the T of the set of PSC filters with the architecture glass/front electrode/SnO_2-NP/C_{60}-SAM/SiO_2-NPs/CsFAMAPIBr/Spiro-OMeTAD/MoO_3/rear electrode. They incorporate FTO, ITO, IZO and PDC–IO:H as front electrodes and IZO or a-IO:H in place of the rear electrodes. The graph in Figure 5.22b depicts the integral curve of the current density equivalent of the transmission (J_{Trn}) of the same setups, following equation 2.12.

As expected, the filters with the PDC–IO:H and IZO front electrodes have a superior T compared to ITO and FTO. The interference modulations of the T spectra make a direct comparison of the closely related curves with the same front TCO and different rear TCOs difficult. Hence, the integral curves of the J_{Trn} reveal that the filters with the IZO rear contact accumulate a small advantage over the ones with a-IO:H in the range up to 1200 nm.
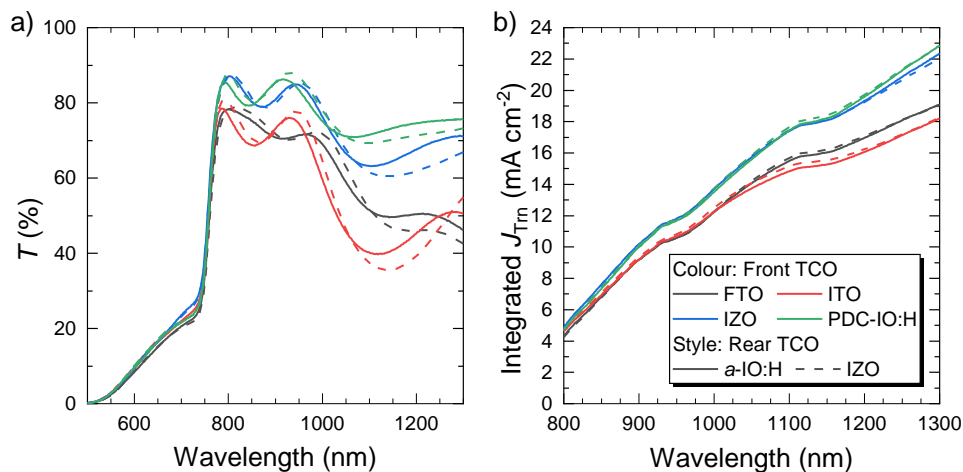
Figure 5.22: a) Spectral transmittance (T) and b) integrated current density equivalent of the transmission (J_{Trn}) versus wavelength of different PSC filters, representing complete semitransparent solar cells based on CsFAMAPIBr perovskite. The filter stacks comprise a variation of front electrodes (colour coded: FTO, ITO, IZO, and PDC–IO:H) as well as different rear electrodes (solid: a-IO:H; dashed: IZO).

Using the T of the PSC filters as the input, the estimated J_{SC} and PCE_{Sim} values are simulated via the single diode model for the two different bottom cells $CIGS_a$ and $CIGS_b$ (see Section 5.2). The results are listed in Table 5.9 along with the PCEs of the best performing PSCs corresponding to each filter architecture. For $CIGS_a$ the experimental data is also shown and the PCE_f of the hypothetical tandem setups is estimated. An additional correction was used for the tandem estimation of PSC samples with a grid. The J_{SC} of the bottom cell was reduced according to a shadowing factor of 2.7 %, as it was calculated in 5.1.2 for the PSC metal grid that is used in cells with matching active area.

|		Experimental Values Top Cell			Experimental Values CIGS$_a$			Simulated Values CIGS$_a$			Simulated Values CIGS$_b$		
		Perovskite Solar Cell Data		Filter Data	Filter + CIGS$_a$		Tandem	Filter + CIGS$_a$		Tandem	Filter + CIGS$_b$		Tandem
Electrodes		PCE*	T_{wt}**	J_{Trn}***	J_{SC}	PCE_f	PCE	J_{Sim}	PCE_{Sim}	PCE	J_{Sim}	PCE_{Sim}	PCE
Front	Rear	(%)	(%)	(mA cm^{-2})	(mA cm^{-2})	(%)	(%)	(mA cm^{-2})	(%)	(%)	(mA cm^{-2})	(%)	(%)
FTO	a-IO:H	13.70	62.80	19.09	13.97	7.30	21.00	14.04	7.29	20.99	14.84	5.80	19.50
	IZO	13.00	63.01	19.04	14.20	7.37	20.37	14.20	7.38	20.38	14.92	5.83	18.83
ITO	a-IO:H	15.10	57.81	18.20	13.49	6.97	22.07	13.50	7.00	22.10	14.15	5.50	20.60
	IZO	14.30	57.93	18.26	13.65	7.14	21.44	13.78	7.15	21.45	14.29	5.57	19.87
	a-IO:H + Grid$^+$	15.50	56.25	17.70	13.12	6.78	22.28	13.14	6.80	22.30	13.77	5.34	20.84
	IZO + Grid$^+$	16.60	56.37	17.77	13.29	6.95	23.55	13.41	6.94	23.54	13.91	5.40	22.00
IZO	a-IO:H	14.10	74.34	22.34	15.68	8.20	22.30	15.79	8.26	22.36	16.95	6.69	20.79
	IZO	12.70	73.22	22.04	15.82	8.23	20.93	15.84	8.28	20.98	16.87	6.66	19.36
PDC-IO:H	a-IO:H	14.90	77.19	22.85	15.73	8.25	23.15	15.81	8.27	23.17	17.17	6.78	21.68
	IZO	13.20	77.14	22.85	15.87	8.35	21.55	16.01	8.38	21.58	17.28	6.83	20.03
	a-IO:H + Grid$^+$	14.50	75.10	22.23	15.30	8.03	22.53	15.39	8.04	22.54	16.70	6.58	21.08
	IZO + Grid$^+$	15.40	75.05	22.23	15.45	8.12	23.52	15.58	8.14	23.54	16.81	6.63	22.03

* PCE after 30 s of dynamic MPP tracking under one sun illumination

** T_{wt} in the NIR range between 800 nm to 1300 nm

*** J_{Trn} in the range 300 nm to 1300 nm

$^+$ all values are corrected for a grid shadow area of 2.7 %

Table 5.9: *Experimental values of the top cell:* PCEs of the best performing PSC devices with A_{act} of 0.24 cm^2 and different combinations of front and rear electrodes. Equivalent PSC filters with larger area shall represent the corresponding transmission behaviour, given in terms of weighted average transmittance (T_{wt}) and current density equivalent of the transmission (J_{Trn}).
Experimental values of CIGS$_a$: measured J_{SC} and PCE_f of CIGS$_a$ when the PSC filter is stacked on top. The tandem PCE denotes the cumulative efficiency of PSC and the filtered CIGS.
Simulated values of CIGS$_a$ and CIGS$_b$: simulated J_{Sim} and PCE_{Sim} of CIGS$_a$ and CIGS$_b$, where J_{Sim} is obtained via equation 5.6 and used for calculation of the PCE_{Sim} via the single diode models from Section 5.2.2. The tandem PCE denotes the cumulative efficiency of PSC and the simulated CIGS. Since the PSC filters do not have a grid, the grid shading factor of 2.7 % (see Section 5.1.2) is used for estimation of the losses in T_{wt} and J_{Trn} of the filter and the J_{SC}, J_{Sim} and PCE values of the CIGS cells.

The results indicate that both a high PCE or high T of the PSC can lead to the highest tandem PCEs. 23.5 % is the best theoretical tandem PCE, which is simultaneously achieved by two different setups each with CIGS$_a$ as the bottom cell. One setup comprises a PSC with ITO front- and IZO+grid rear electrode, achieving a PCE of 16.6 % and a weighted average transmittance (T_{wt}) of 56.2 %. The other setup uses PDC–IO:H as a front electrode, which increases the T_{wt} to 75.1 % at a PCE of 15.4 %.

As the bottom cell PCE_{Sim} (or PCE_f) represents a direct measure for the transmission quality of the top cell, the CIGS PCE_{Sim} vs. PSC PCE data plot in Figure 5.23 effectively visualises the correlation matrix between top cell transmittance, top cell PCE and tandem PCE.
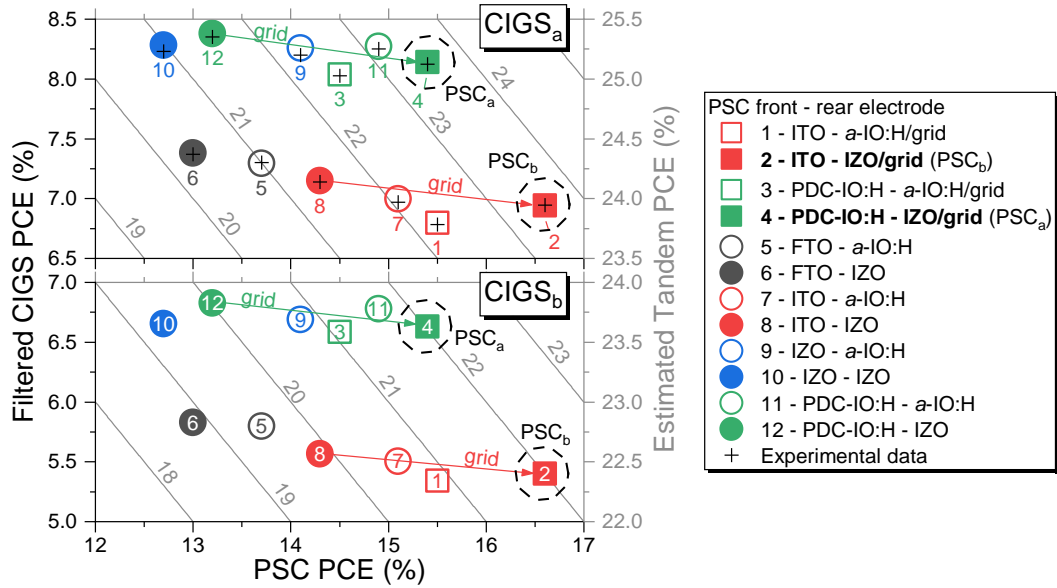
Figure 5.23: Estimated PCEs of principle tandem setups as functions of the PCEs of different top and bottom cells. The data corresponds to Table 5.9 and shows the combination of PSCs with different front and rear electrodes according to the numeration in combination with $CIGS_a$ and $CIGS_b$. The PCE of the $0.24\,cm^2$ PSCs is obtained from MPP tracking under one sun illumination, while the PCE of the CIGS is obtained from one diode model simulation or experimental JV measurement (crosses). Both methods utilize the transmission of the corresponding PSC filters. The arrows indicate how the application of a metal grid to the PSC rear electrode (square symbols) would induce a shift of the tandem PCE. A large PCE gain is observable for the PSCs with IZO-grid electrode, while the PCE of the CIGS is estimated to be reduced by a relative $2.7\,\%$ due to shading of an equivalent grid in a real tandem device.

In addition to the simulated data, also experimental data (crosses) from JV measurements with CIGS in combination with the filters is shown in this plot, which was only available for $CIGS_a$. It proves a very good coincidence with the simulated data, verifying the validity of the estimations.

The long arrows mark the significant increase of the PCE of the PSCs which have a grid applied to their IZO rear electrode. These top cells then also give reason to the highest overall tandem PCEs for each setup with $CIGS_a$ ($23.5\,\%$) and $CIGS_b$ ($22.0\,\%$). Here, the gain in PCE largely overcompensates for the grid shadow cast losses, hence bottom cell PCE losses.

When a grid is applied to the a-IO:H rear electrodes, no such efficiency boost is observable. In case of the PSCs with PDC–IO:H and a-IO:H electrodes (solid green symbols), the best PCE achieved by a cell without grid even outperforms the one with grid. Possibly, the missing improvement is an intrinsic issue, because the a-IO:H has different energy band levels which might not suit an ohmic contact as well as it is the case for IZO. Also, a possible surface defect of the IO:H could prevent a good contact, but here the deviations in the surface have been detected only by XRD in the crystalline form of PDC–IO:H (see Section 4.2.2).

From the comparison of the different TCO combinations can be concluded that the best suited top cell candidates for the further development on larger area, are represented by a highly transparent perovskite solar cell with PDC-IO:H front electrode (PSC_a) and a highly efficient perovskite solar cell with ITO front electrode (PSC_b), which both comprise a IZO-grid rear electrode.

Tandem devices with matching cell area

Real tandem devices with a matching active area (A_{act}) of $0.5\,cm^2$ have been prepared using larger PSCs of the most promising setups from the previous section — a perovskite solar cell with PDC-IO:H front electrode (PSC$_a$)[1] and a perovskite solar cell with ITO front electrode (PSC$_b$)[2] — in combination with the familiar CIGS$_a$ and CIGS$_b$. The *JV* responses of the complete setups in Figure 5.24 are measured simultaneously under the same spectral illumination conditions (one sun). The insets show the PCE of the PSCs over time from dynamic MPP tracking under the same illumination.

Figure 5.24: *JV* responses of the top and bottom cells of the best performing 4T tandem architectures with matching cell size: a) a perovskite solar cell with PDC-IO:H front electrode (PSC$_a$) and in combination with a CIGS cell with E_g = 1.1 eV (CIGS$_a$) and a CIGS cell with E_g = 1.0 eV (CIGS$_b$); b) a perovskite solar cell with ITO front electrode (PSC$_b$) in combination with the same CIGS cells. The inset denote the PSC MPP response. Both PSCs have an IZO rear electrode with additional metal grid.

Contradicting the expectations, comparing the PCE of both PSCs in Figure 5.24a and b, PSC$_a$ achieves a much better PCE of 15.0 % than PSC$_b$ with 13.7 %. The MPP response of PSC$_b$ shows some decline in PCE for about 30 s before it stabilises, which indicates some illumination dependent defects. Probably, the faulty device is a result of the difficulty of homogeneous layer preparation on lager area with the solution based deposition processes and the lack of a statistically significant number of devices that can be prepared in one experiment.

However, the optical properties of the PSCs are not strongly affected. Thus, the responses of the CIGS bottom cells on the different transmittance spectra match the expectations. With the superior transmittance of PSC$_a$, both CIGS cells gain more photocurrent than with PSC$_b$. Due to the exceptional NIR performance of PDC–IO:H, the CIGS cell with E_g = 1.0 eV (CIGS$_b$) profits the most of the extended absorption range in the NIR.

Table 5.10 lists the corresponding characteristic values from the *JV* measurements and the 4T tandem efficiency as a sum of the PCEs of both sub cells. A remarkable tandem efficiency of 23.0 % is achieved by the combination of PSC$_a$ and CIGS$_a$, which is only 0.5 % absolute lower than the estimated value from the tandem simulation with a filter and a small sized PSC (see

---

[1] PDC-IO:H/SnO$_2$-NP/C$_{60}$-SAM/SiO$_2$-NPs/CsFAMAPIBr/Spiro-OMeTAD/MoO$_3$/IZO/grid
[2] ITO/SnO$_2$-NP/C$_{60}$-SAM/SiO$_2$-NPs/CsFAMAPIBr/Spiro-OMeTAD/MoO$_3$/IZO/grid

Table 5.9). According to the results with $CIGS_a$, the tandem performance with the narrow E_g $CIGS_b$ is also close to the estimated value and reaches a PCE of 21.6 %. Due to the comparably poor PCE performance and the generally poorer transmittance, the tandem cells with PSC_b do not match the expectations from the simulation in Table 5.9.

Setup		Top Cell				Bottom cell					Tandem
Top Cell	Bottom Cell	PCE* (%)	FF (%)	V_{OC} (mV)	J_{SC} (mA cm^{-2})	E_g (eV)	PCE_f (%)	FF (%)	V_{OC} (mV)	J_{SC} (mA cm^{-2})	PCE (%)
PSC_a (IO:H)	$CIGS_a$	15.0	68.0	1178	18.6	1.1	8.0	78.0	669	15.4	23.0
	$CIGS_b$					1.0	6.6	75.5	520	16.8	21.6
PSC_b (ITO)	$CIGS_a$	13.7	62.3	1173	18.4	1.1	6.8	78.0	663	13.2	20.5
	$CIGS_b$					1.0	5.2	75.2	513	13.6	18.9

* PCE after 60 s of dynamic MPP tracking under one sun illumination

Table 5.10: *JV* characteristics of the top and bottom cells of 4T tandem setups with matching cell sizes (0.5 cm^2). The tandems are assembled by four different top and bottom cell setups: A perovskite solar cell with PDC-IO:H front electrode (PSC_a) in combination with a CIGS cell with E_g = 1.1 eV ($CIGS_a$) and a CIGS cell with E_g = 1.0 eV ($CIGS_b$) and a perovskite solar cell with ITO front electrode (PSC_b) in combination with the same CIGSs cells. The $CIGS_a$ and $CIGS_b$ have the respective solo PCEs of 21.1 % and 15.6 %. Both PSCs compromise a IZO rear electrode with a metal grid.

Additional EQE and T measurements allow for further investigation of the electrical and optical performance of the sub cells. Figure 5.25 depicts the EQE responses of the top and bottom cells of the four different tandem setups. The T of the top cells is also indicated. As expected, the superior T of PSC_a allows for an improvement of the EQE of the bottom cells compared to the setups with PSC_b. Especially for $CIGS_b$, the higher NIR transmittance of PSC_a increases the EQE in the long wavelength regime significantly.
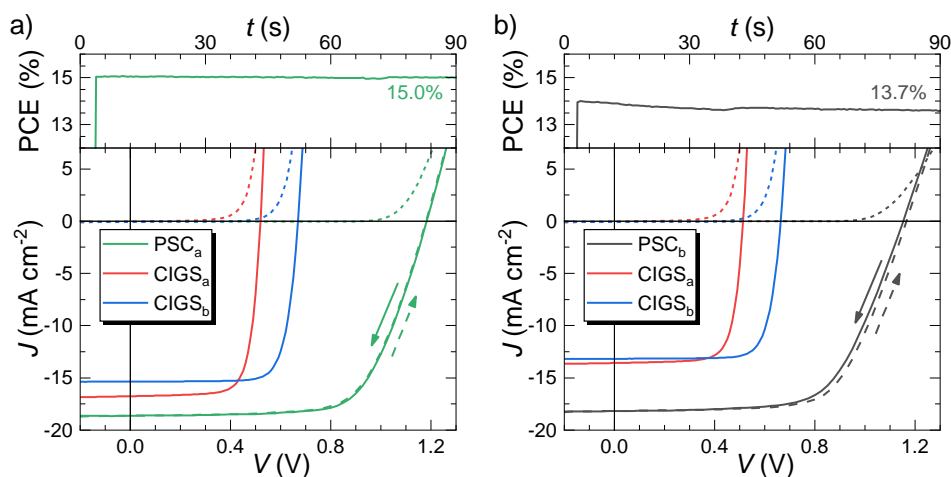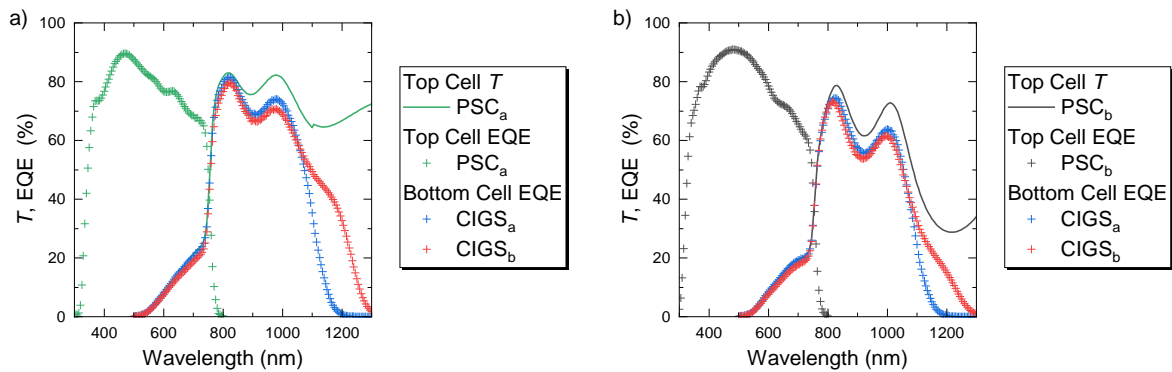

Figure 5.25: EQE responses of the top and bottom cells of the best performing 4T tandem architectures with matching cell size: a) a perovskite solar cell with PDC-IO:H front electrode (PSC_a) and in combination with a CIGS cell with E_g = 1.1 eV ($CIGS_a$) and a CIGS cell with E_g = 1.0 eV ($CIGS_b$); b) a perovskite solar cell with ITO front electrode (PSC_b) in combination with the same CIGSs cells. The solid lines denote the spectral transmittance (T) of the PSC top cells.

After quantification by calculation of the J_{EQE}, the results are compared to the J_{SC} values from the JV scans in Table 5.11. In case of PSC$_a$, the J_{EQE} of 18.8 mA cm^{-2} matches quite closely to the measured J_{SC} of 18.6 mA cm^{-2}. For PSC$_b$ the measured J_{SC} of 18.4 mA cm^{-2} seems to be too low, but this is likely an effect of the illumination sensitive behaviour of the device during the JV measurements.

Setup		Top Cell				Bottom cell			Tandem
Top Cell	Bottom Cell	J_{SC} (mA cm^{-2})	J_{EQE} (mA cm^{-2})	J_{Trn}* (mA cm^{-2})	E_g (eV)	J_{SC} (mA cm^{-2})	J_{EQE} (mA cm^{-2})	$J_{EQE,Grid}$** (mA cm^{-2})	PCE (%)
PSC$_a$(IO:H)	CIGS$_a$	18.6	18.8	22.0	1.1	15.4	15.8	15.3	23.0
	CIGS$_b$				1.0	16.8	16.9	16.4	21.6
PSC$_b$(ITO)	CIGS$_a$	18.4	19.0	17.3	1.1	13.2	13.7	13.3	20.5
	CIGS$_b$				1.0	13.6	14.1	13.7	18.9

* J_{Trn} in the range from 300 nm to 1300 nm
** J_{EQE} corrected by a shading of 2.7 % by the PSC metal grid

Table 5.11: EQE characteristics of the top and bottom cells of 4T tandem setups with matching cell sizes (0.5 cm^2).The tandems are assembled by four different top and bottom cell setups: A perovskite solar cell with PDC-IO:H front electrode (PSC$_a$) in combination with a CIGS cell with E_g = 1.1 eV (CIGS$_a$) and a CIGS cell with E_g = 1.0 eV (CIGS$_b$) and a perovskite solar cell with ITO front electrode (PSC$_b$) in combination with the same CIGSs cells. The CIGS$_a$ and CIGS$_b$ have the respective solo PCEs of 21.1 % and 15.6 %. Both PSCs compromise a IZO rear electrode with a metal grid.

Similar to the calculation of the J_{EQE}, the J_{Trn} of the top cell devices is determined from the T response, within the upper integration limit of 1300 nm. Since the J_{Trn} indicates the maximum current density that a solar cell could produce from the remaining transmitted photon flux, the fact that PSC$_a$ transmits nearly 5 mA cm^{-2} more than PSC$_b$, supports the necessity of highly transmitting electrodes.

As a direct result, the J_{EQE} of the CIGS cells with PSC$_a$ as a top cell overcome the J_{EQE} of the ones with PSC$_b$ by over 2 mA cm^{-2}. For a direct comparison to the measured J_{SC}, the J_{EQE} values have been corrected by a factor of 2.7 % that accounts for the area that is shaded by the metal grid of the PSC. An additional correction is conducted on CIGS$_a$, which has a small grid with the area of 0.23 %. For CIGS$_b$ an additional correction proved to be difficult, because it has a different grid layout than CIGS$_a$. The grid of CIGS$_b$ partly aligns with the grid of the PSC cell, so that the correct shading area is not determinable. Here, a certain error must be accepted for the PCE estimation, which is expected to be lower than 2.5 %. After correction, a good match between J_{SC} and J_{EQE} is observed, except for the combination of PSC$_a$ with CIGS$_b$, where the measured J_{SC} seems to be a little too high by 0.4 mA cm^{-2}. Since here, the bottom cell profits from a significant increase of the EQE in the long wavelength regime above 1100 nm, it might be more sensitive to fluctuations of the solar spectrum of the solar simulator lamp. This effect would not be observable with the other setups and could be the explanation of the deviation.

In order to get a deeper understanding of the current generation and losses in these tandem setups, Section 5.4.1 evaluates the optical and electrical simulation of the devices via a TMM approach.

5.4 Potential for further optimizations of perovskite–CIGS tandem solar cells

Despite the manifold reflection-, absorption- and transmission mechanisms within the multitude of layers, only the total reflectance (R) is conceivable experimentally of a complete tandem device. EQE measurements allow for further insights regarding the current generation of the absorber layers, which can be evaluated for eventual parasitic losses. Additional T spectra of the semitransparent top cell can be used to determine the absorptance (A) of different architectures. This has all been part of the previous sections, but the exact contributions of the single layers to the absorption remains unknown.

With computational methods, it is possible to access this information by using models of the tandem architecture that mimic the optical properties of the complete device and each single layer of it. The following sections discuss the development of such models and their application for determination of the parasitic absorption losses of different tandem solar cells.

Furthermore, Section 5.4.2 evaluates the application of immersion oil as an optical coupling material in 4T-tandem filter estimations and the use of anti-reflective foils for overcoming the reflection losses.

Section 5.4.3 investigates the maximum theoretical PCE of the bottom cell via a simulation approach considering a hypothetical close-to-perfect NIR transmission of PSCs with different band gaps.

5.4.1 Simulation assisted analysis of the parasitic losses

This section investigates the optical loss mechanisms of the previously introduced tandem cells. In the process, the optical properties of the individual layers are determined and

Simulation of optical properties of the top cell

The SE measurements were conducted by Tim Helder. Further information on the evaluation of the SE data by using different oscillator models is described in his masters thesis [110] and is briefly introduced in appendix A.1.

In order to get profound knowledge on the optical properties of the semitransparent PSC, this section evaluates the real part of the complex refractive index or phase velocity ($n(\lambda)$) and the imaginary part of the complex refractive index or extinction coefficient ($k(\lambda)$) of the single layer materials, which are obtained by spectroscopic ellipsometry (SE) measurements.

Figure 5.26a shows the simulated optical functions for IZO (180 nm), a-IO:H (180 nm) and PDC–IO:H (220 nm). The extinction coefficient k increases while n decreases for longer wavelengths under the effects of free carrier absorption for all the TCO layers. Because $k(\lambda)$ is correlated to the absorption coefficient (α) via equation 2.7, this increase of $k(\lambda)$ and the absorption in the NIR region is correlated to intraband transitions which increase with carrier concentration [133]. The increasing values of $k(\lambda)$ for small wavelengths <400 nm corresponds to the band gap of the TCOs.
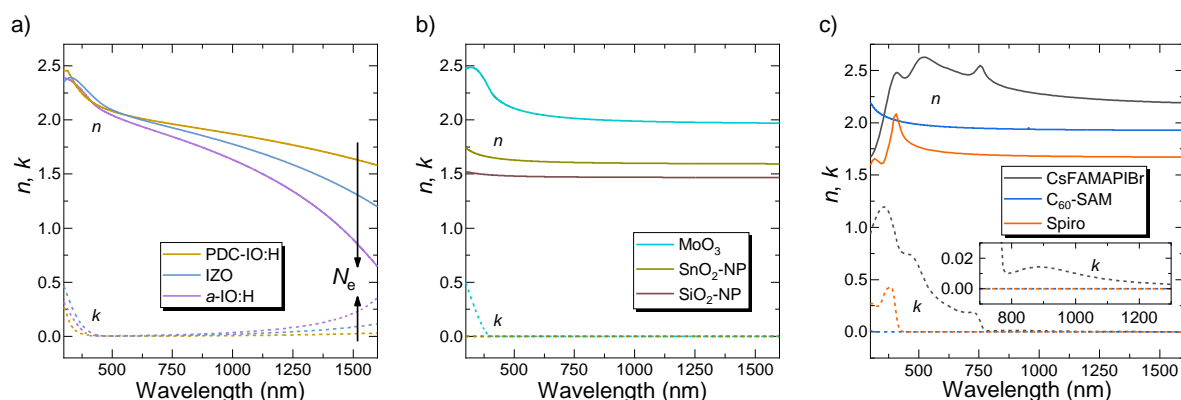
Figure 5.26: Refractive index and absorption coefficient of the layer materials utilized in the perovskite solar cell. a) TCO materials, b) other oxides and c) perovskite CsFAMAPIBr and organic materials.

The increasing differences of $n(\lambda)$ of the three TCO materials for long wavelengths is directly associated with the respective N_e of the materials, as indicated by arrows in the graph. [134] As shown before the N_e of IO:H is drastically reduced during PDC. The correlated change in the optical properties coincides with findings of Koida. [133] IZO exhibits a intermediate N_e and the resulting $n(\lambda)$ and $k(\lambda)$ data compares to reports of Martin et al. [135]

Figure 5.26b shows the $n(\lambda)$ and $k(\lambda)$ values for the layers of 10 nm MoO_3, a non-compact layer of SiO_2-NP and 20 nm SnO_2-NP. The values for the refractive index of MoO_3 correspond well with the literature [136]. For the nanoparticle layers, the values of SiO_2-NP agree with the values of Gao et al. [137] for compact SiO_2. This is noticeable because SiO_2-NP do not form a dense layer and hence different values to that of compact SiO_2 was expected. Goldsmith et al. investigated the optical properties of compact SnO_2 thin films and present $n(\lambda)$ values of approximately 2 in the visible spectral range. Further they calculated the refractive index for SnO_2 layers with different fraction of voids in the layer. For a fraction of 0.3 the refraction index decreases to approx. 1.8. Since these nanoparticle based layers are rather porous than compact the assumption of voids in the layer is reasonable. This is a possible explanation for the low values of approximately 1.7.

Figure 5.26c shows the $n(\lambda)$ and $k(\lambda)$ values of the organic layers of conductive fluorene and C_{60}–SAM and the perovskite absorber CsFAMAPIBr. The data for conductive fluorene were taken from literature because the deposition of conductive fluorene diluted in chlorobenzene on quartz glass was not possible. [92] C_{60}–SAM, which forms only monolayers or thin layers in the range of a few nanometer, shows no absorption and a constant refractive index of approximately 2 in the range of 600 nm to 1600 nm.

The results for $n(\lambda)$ and $k(\lambda)$ of the perovskite absorber shows a high $k(\lambda)$ for wavelengths shorter than 500 nm and a decrease of $k(\lambda)$ until the fundamental absorption edge. The decline indicates a significantly reduced capability to absorb photons with wavelengths longer than 500 nm, which coincides with the findings from transmittance measurements. For wavelengths exceeding the absorption edge at about 790 nm, $k(\lambda)$ is expected to reach 0, but a small parasitic absorption is observable (see inset) probably due to defects and residual non perovskite compounds in the layer.

With the knowledge of $n(\lambda)$ and $k(\lambda)$ of each individual material of the PSC architecture, it is possible to create a multi layer model in order to simulate the optical transmittance, reflectance and absorptance of a real PSC device, as demonstrated by Tim Helder. [110] Here, the $n(\lambda)$ and $k(\lambda)$ data will be used in the next Section 5.4.1 for the modelling of complete 4T tandem architectures as part of a current loss analysis.

Current loss analysis by transfer matrix method

This section contains simulation results that are original work of the author and have been published in [143].

In order to estimate the parasitic absorptance of each sublayer of a tandem cell, a simulation model is created comprising all layers with their optical parameters $n(\lambda)$, $k(\lambda)$ from the last section. The remaining optical data was taken from literature (ITO, [91] Spiro-OMeTAD, [92] air, [93] CIGS, [94] MoSe, [95] and molybdenum, MgF_2, CdS, and i-ZnO. [96]). Two cell size matched tandem devices from Section 5.3.2 with the setups PSC_a+$CIGS_a$ and PSC_b+$CIGS_b$ are chosen as the physical data basis of the simulation, aiming for a deeper understanding of the parasitic absorption in the different front electrodes of the PSCs, namely PDC–IO:H and ITO.

Via transfer-matrix-method, the absorptance losses in each layer were simulated and calculated in terms of equivalent current densities using the program e-ARC. [90] The spectral dependency of A_i of each layer i is cumulatively plotted in the colour coded graphs of Figure 5.27a and c following the relation $1 = \sum(A_i) + R$. Additionally, the measured (symbols) and simulated (lines) EQE responses are shown. Figure 5.27b and d depict schematic illustrations of the layer architectures and the results of the current loss analysis for the integration range up to 1165 nm. The simulation allows for the evaluation of the total J_{Ref}, the individual J_{Abs} in each layer, the current density equivalent of the recombination loss (J_{Rec}) and the J_{Sim} in the top and bottom cell.

To account for the shadow losses in the bottom cell introduced by the grid of the PSC top cell, the EQE and A_i are corrected for the shaded area of 2.7 % (see Section 5.1.2), assuming a negligible amount of reflection and full absorption at the grid. An additional correction is made for the grid of the CIGS cell, which is smaller and therefore shades only an area of 0.23 %.
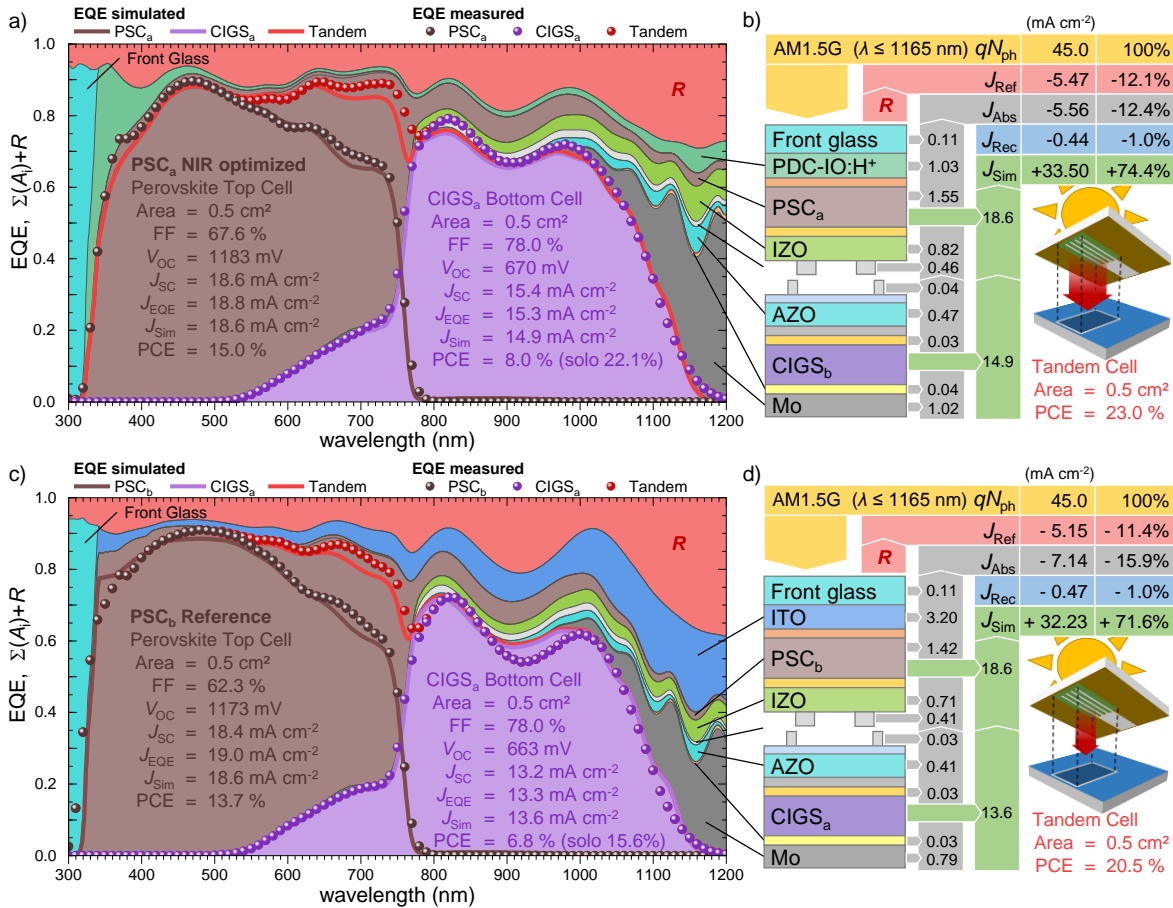
a) **EQE simulated** — PSC$_a$ — CIGS$_a$ — Tandem **EQE measured** ● PSC$_a$ ● CIGS$_a$ ● Tandem

Front Glass

PSC$_a$ NIR optimized
Perovskite Top Cell
Area = 0.5 cm²
FF = 67.6 %
V_{OC} = 1183 mV
J_{SC} = 18.6 mA cm⁻²
J_{EQE} = 18.8 mA cm⁻²
J_{Sim} = 18.6 mA cm⁻²
PCE = 15.0 %

CIGS$_a$ Bottom Cell
Area = 0.5 cm²
FF = 78.0 %
V_{OC} = 670 mV
J_{SC} = 15.4 mA cm⁻²
J_{EQE} = 15.3 mA cm⁻²
J_{Sim} = 14.9 mA cm⁻²
PCE = 8.0 % (solo 22.1%)

b)
(mA cm⁻²)

AM1.5G ($\lambda \leq 1165$ nm) qN_{ph}	45.0	100%
J_{Ref}	-5.47	-12.1%
J_{Abs}	-5.56	-12.4%
J_{Rec}	-0.44	-1.0%
J_{Sim}	+33.50	+74.4%

Front glass — 0.11
PDC-IO:H⁺ — 1.03
PSC$_a$ — 1.55 / 18.6
IZO — 0.82 / 0.46 / 0.04
AZO — 0.47 / 0.03
CIGS$_b$ — 14.9
Mo — 0.04 / 1.02

Tandem Cell
Area = 0.5 cm²
PCE = 23.0 %

c) **EQE simulated** — PSC$_b$ — CIGS$_a$ — Tandem **EQE measured** ● PSC$_b$ ● CIGS$_a$ ● Tandem

Front Glass

PSC$_b$ Reference
Perovskite Top Cell
Area = 0.5 cm²
FF = 62.3 %
V_{OC} = 1173 mV
J_{SC} = 18.4 mA cm⁻²
J_{EQE} = 19.0 mA cm⁻²
J_{Sim} = 18.6 mA cm⁻²
PCE = 13.7 %

CIGS$_a$ Bottom Cell
Area = 0.5 cm²
FF = 78.0 %
V_{OC} = 663 mV
J_{SC} = 13.2 mA cm⁻²
J_{EQE} = 13.3 mA cm⁻²
J_{Sim} = 13.6 mA cm⁻²
PCE = 6.8 % (solo 15.6%)

d)
(mA cm⁻²)

AM1.5G ($\lambda \leq 1165$ nm) qN_{ph}	45.0	100%
J_{Ref}	- 5.15	- 11.4%
J_{Abs}	- 7.14	- 15.9%
J_{Rec}	- 0.47	- 1.0%
J_{Sim}	+ 32.23	+ 71.6%

Front glass — 0.11
ITO — 3.20
PSC$_b$ — 1.42 / 18.6
IZO — 0.71 / 0.41 / 0.03
AZO — 0.41 / 0.03
CIGS$_a$ — 13.6
Mo — 0.03 / 0.79

Tandem Cell
Area = 0.5 cm²
PCE = 20.5 %

Figure 5.27: Spectral evaluation of the EQE (measured and simulated), R (measured) and A (simulated) with corresponding current loss analyses and schematic illustrations of the tandem cell architectures PSC$_a$+CIGS$_a$ (Figures a and b) and PSC$_b$+CIGS$_a$ (c and d). The main difference between both tandem setups is that PSC$_a$ is NIR optimized by comprising PDC–IO:H as a front electrode, while the reference PSC$_b$ uses ITO. The simulated absorptance spectra of each sublayer A_i are plotted cumulatively following $\sum(A_i) + R = 1$ and colour coded correspondingly to the layer materials as denoted in the schematic layer stack. The solo PCE of CIGS$_a$ is 22.1 % (compare tables 5.5 and 5.10).

Due to the superior transmittance of the PDC–IO:H and IZO (b), the losses in the top cell electrodes are confined to only $1.0\,\mathrm{mA\,cm^{-2}}$ and $0.8\,\mathrm{mA\,cm^{-2}}$, respectively. In comparison to the reference setup (d) comprising the unfavourable ITO ($3.2\,\mathrm{mA\,cm^{-2}}$), the loss in the ZAO front electrode is reduced by over $2\,\mathrm{mA\,cm^{-2}}$. In the bottom cell, the ZAO electrode of the CIGS cell introduces losses of $0.4\,\mathrm{mA\,cm^{-2}}$ to $0.5\,\mathrm{mA\,cm^{-2}}$. In the reference setup, the sum of TCO related current losses is $4.3\,\mathrm{mA\,cm^{-2}}$, which is over 60 % of the total J_{Abs}. In the NIR optimized setup the TCO losses are reduced to 40 %, which is still a significant fraction and demonstrates the impact of the electrodes on the optical properties of the solar cell.

Additional losses are contributed to recombination and parasitic absorption in the perovskite itself, while the interlayers in the tandem cell have a negligible contribution. Within the absorption range of the bottom cell up to 1165 nm, a part of the NIR spectrum is also lost ($0.8\,\mathrm{mA\,cm^{-2}}$ to $1.0\,\mathrm{mA\,cm^{-2}}$) to absorption at the molybdenum rear contact, due to insufficient NIR absorption in the CIGS and a low reflectivity of the molybdenum rear interface. The overall absorption losses accumulate to 12.4 % for the NIR-optimized tandem cell and 15.9 % for the reference setup relative to the incident photon flux of the AM1.5.

The optimized NIR transmittance translates into a simulated gain in the current generation J_{Sim} in the bottom cell of $1.3\,\mathrm{mA\,cm^{-2}}$. The measured EQE predicts a higher J_{EQE} gain of $2\,\mathrm{mA\,cm^{-2}}$, which coincides with the increase of the J_{SC} from JV-measurements. The differences between measurement and model are due to the imperfect simulation of the interference pattern of the EQE. These are strongly related to the real interface properties between the layers, which are approximated by a flat morphology in the simulation. Besides that, the simulated curves of the EQE show a reasonable coincidence with the measured data, as well as the values for J_{Sim} and J_{EQE} for each sub cell.

It is expected that tandem setups comprising a CIGS cell with lower E_g benefit even more from the increased NIR transmittance of PSC_a, because the extended CIGS absorption range allows for collecting low energetic photons for current generation. Specifically engineered CIGS cells for tandem applications have been lately demonstrated by Feurer et al. gaining a PCE of $16.1\,\%$ at an E_g of $1.0\,\mathrm{eV}$ [5].

In this thesis, Section 5.3.2 (Table 5.10) presented a similarly engineered CIGS cell with $E_g = 1.0\,\mathrm{eV}$ ($CIGS_b$) with a solo PCE of $15.6\,\%$, for which was shown that the current generation J_{EQE} in the tandem setup increases from $15.3\,\mathrm{mA\,cm^{-2}}$ to $16.4\,\mathrm{mA\,cm^{-2}}$ compared to the regular $CIGS_a$. The architecture of PSC_a and $CIGS_b$ demonstrated $21.6\,\%$ tandem PCE, surpassing the solo PCEs by $\approx 6\,\%$. The corresponding spectral evaluation is shown in Figure 5.28a. In comparison to the reference setup with PSC_b in place of the top cell in Figure 5.28b, the necessity of highly NIR translucent TCOs is demonstrated, because due to the steadily increasing NIR absorption of the ITO layer at long wavelengths, the $CIGS_b$ hardly gains profit from the extended absorption range. The J_{EQE} remains at a low yield of $13.7\,\mathrm{mA\,cm^{-2}}$, which is only slightly more than was achieved with the $CIGS_a$ ($13.3\,\mathrm{mA\,cm^{-2}}$).
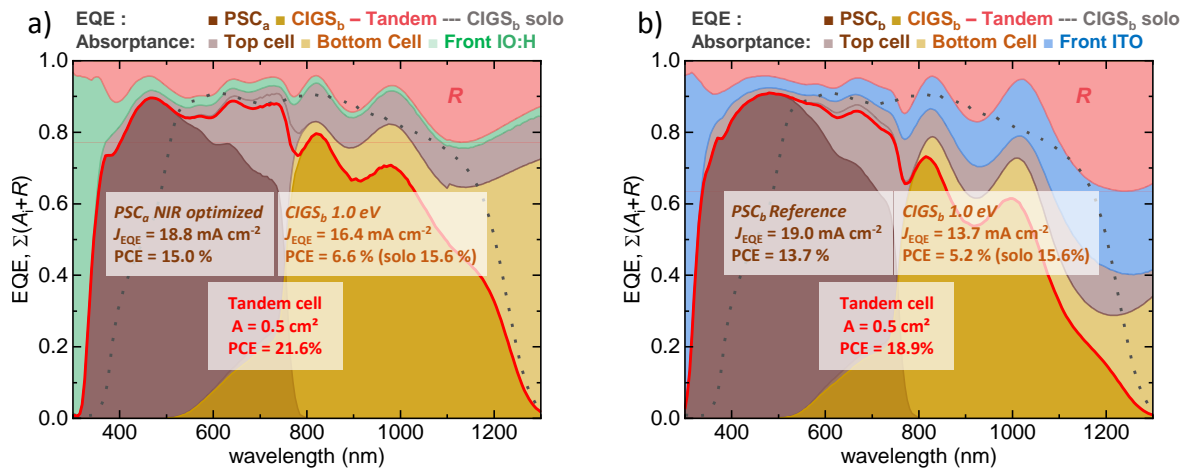
Figure 5.28: Spectral evaluation of the reflectance $(1 - R)$, absorptance (A) and external quantum efficiency (EQE) of both sub cells of 4T-Tandem devices with a) NIR optimized PSC_a (comprising PDC–IO:H as the front electrode) and $CIGS_b$ ($E_g = 1.0\,\mathrm{eV}$; PCE = $15.7\,\%$), b) reference setup with PSC_b (comprising ITO as the front electrode) and $CIGS_b$.

Concluding, the current loss analysis demonstrates that the reduction of the parasitic absorption in the TCO layers has a significant impact on the CIGS performance. But it also shows that the remaining absorption and reflection losses accumulate to nearly $25\,\%$. To challenge the remaining parasitic absorption losses, replacing the ZAO of the bottom cell with a NIR optimized IZO is a promising approach. Previous studies have shown that the implementation

of IZO may also lead to an improved stability and comparable efficiency values of the CIGS. [138] Additionally, the front electrode of the bottom cell CIGS could be adapted to the lower current density in the tandem application by decreasing the TCO thickness and grid bar dimensions, reducing parasitic absorption even further.

In order to diminish the reflection losses, familiar concepts of light management such as anti-reflective coatings (ARC), surface structuring or optical coupling materials may be applied. The following Section 5.4.2 introduces a simple approach using immersion oil to fill the air gap in between the top and bottom cell. By this, the Fresnel reflection at the rear electrode to the PSC device shall be minimized. Furthermore, the option of using a structured anti reflection foil (ARF) will be evaluated to realize a better light incoupling at the PSC surface. A greater reduction of the overall reflection is expected from a simulation assisted engineering of the individual layer thicknesses, which could reduce the amount of disadvantageous interference reflection patterns. On the one hand, the freedom of thickness variations is strongly limited by the prerequisite to maintain full electrical functionality of the solar cell architecture, but on the other hand, the perovskite technology has proven to serve a great variety of different materials and layer stack options, so that the development of an optically and electrically enhanced device is feasible in the future. Further development of the proposed optical models could be of valuable assistance to fulfil this tasks.

In general, this study utilized only perovskite with an E_g of about 1.6 eV, because the material composition of choice provided the best efficiency and reproducibility. Lately, our collaborators at KIT showed that the band gap of the perovskite top cell can be increased, while maintaining very high efficiencies. [3] Naturally, a higher band gap in the top cell enhance the bottom cell efficiency, and thus the tandem efficiency. The optimum band gap composition is still under discussion in experiment and simulation. [9, 32, 56] In this thesis, a fine-tuning of the band gap in connection with an additional adjustment of the transmission will be evaluated on a simulation approach later on in Section 5.4.3 to estimate the maximum achievable PCE values for the bottom cells CIGS$_a$ and CIGS$_b$.

5.4.2 Improvement of the light management by using immersion oil for optical coupling and anti-reflective foil

In the so far tested 4T tandem cells, the top cell was mechanically stacked on top of the bottom cell, leaving an air gap in between. When the gap is simply left filled with air, the mismatch between the refractive indices of air and the electrode materials is causing unwanted Fresnel reflection losses. Equally, the glass surface of the superstrate of the top cell is in contact with air and causes reflection losses. This section evaluates the possibility to reduce the reflection losses by using immersion oil as an optical coupling material to replace the air in the gap in the tandem setup. Additionally, an anti reflection foil (ARF) with a pyramidal structure is used to enhance the light incoupling at the surface. The ARF has been kindly provided by collaborators from IMEC, who utilized a similar foil in perovskite–silicon tandem solar modules for optimal light harvesting. [12, 139]

At first for comparison, Figure 5.29 shows the basic effect of a regular ARC on a CIGS solar cell. The layer thickness is chosen such that the main reflection losses for wavelength between 500 nm and 900 nm are diminished by the constructive interference effects (green area). Since the single layer ARC approach can be optimized only for certain wavelengths, this scenario

demonstrates that the ARC actually introduces additional reflection losses at longer wavelengths (red area). In summary, the gains overweight the losses and the net current generation increases. The wavelength dependency of the effectiveness of ARC coatings makes their application in multi junction solar cells more complicated and the engineering of the correct thickness requires a solid simulation model of the optical layer stack. Furthermore, the ARC coating is typically optimized for an incidence angle normal to the sample surface, but under different angles, the light path distances through the layers change and the anti-reflective effect may shift towards unwanted wavelengths.
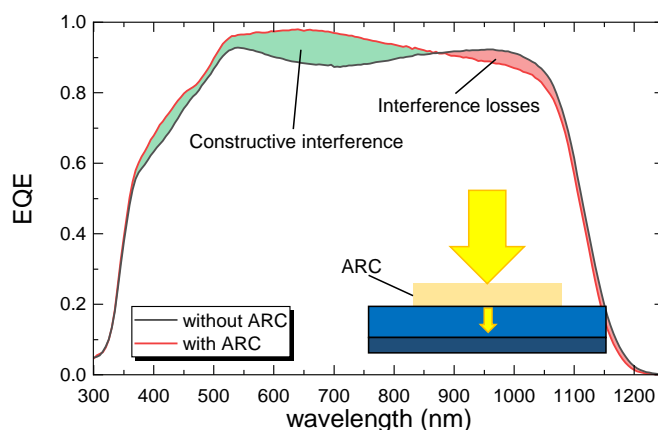

Figure 5.29: EQEs of a CIGS cell with and without an MgF_2 ARC. Schematic illustrations demonstrate the mechanisms that lead to the denoted, colour-coded gains (green) and losses (red) in the quantum efficiency.

The working principle of the ARF is different from the ARC approach, because it is not intended to prevent reflection in general, but to guide the reflected beams effectively in the desired direction of the active area. This is accomplished by the nano-scale structure of the foil with high aspect ratios, which aims for trapping escaping light beams by multiple back reflection. As a result, light of any wavelength can be effectively guided into the layer stack, but the light gets also diffusively scattered over a broad angle.

In a preliminary experiment, the ARF is tested in combination with the single cells in order to examine the principle functionality. Therefore, the ARF is placed on the surface of the ZAO electrode of a CIGS cell (without ARC) and on the sun facing glass superstrate of a semitransparent PSC comprising ITO as a front- and IZO/grid as a rear electrode[3] with an area of $0.24\,cm^2$. For optimal light incoupling, regular immersion oil with an refractive index of about 1.5 is used to connect the foil to the underlying layer material.

The spectral EQE responses of the cells with and without ARF in Figure 5.30a and b indicate in which wavelength regimes the application of the ARF proves to be ad- or disadvantageous. The resulting gains are colour coded in green and the losses in red.

---

[3] ITO/SnO_2-NP/C_{60}-SAM/SiO_2-NPs/CsFAMAPIBr/Spiro-OMeTAD/MoO_3/IZO/grid
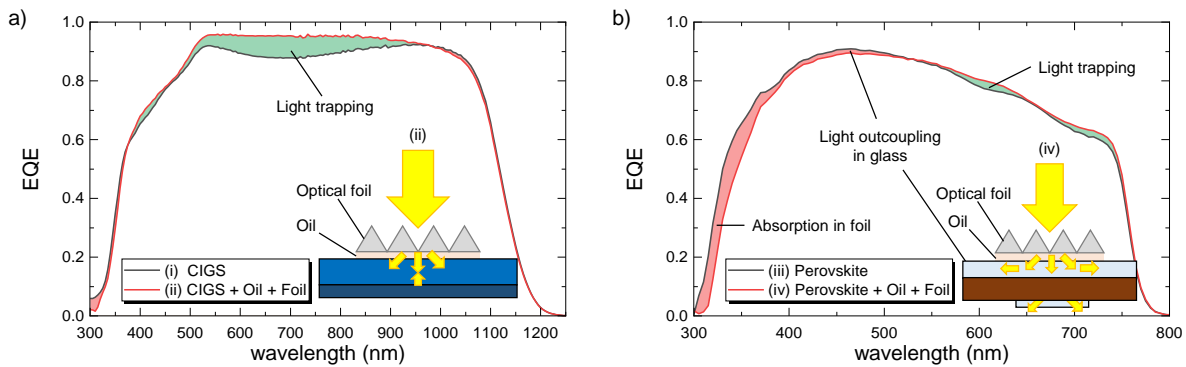
Figure 5.30: EQEs of a) a CIGS cell without ARC and b) a PSC with and without an anti-reflective foil that is placed on top of the solar cell using immersion oil for optimal light in-coupling. Schematic illustrations demonstrate the mechanisms that lead to the denoted, colour-coded gains (green) and losses (red) in the quantum efficiency.

In case of CIGS the main reflection losses without ARF (i) in the regime from 500 nm to 1000 nm can be effectively suppressed with the ARF (ii). Due to multiple scattering at the pyramidal structure, photons are effectively guided towards the solar cell or redirected towards it, if back reflected from the cells surface. This mechanism is called light trapping, as it is denoted in the graph of Figure 5.30a.

Similarly in Figure 5.30b, the same mechanism applies for the PSC with ARF (iv), but here a counteracting mechanism limits the beneficial gains of the light trapping. Due to the much longer travelling distance through the ≈1 mm thick superstrate, the omnidirectional scattered and back reflected photons are likely to be guided away from the active area and therefore lost for current generation, as it is demonstrated in the schematic drawing. This effect is named light outcoupling. As a result, the competing mechanisms cancel each other out in average, bringing no significant advantage to the PSC EQE. Furthermore, the ARF itself has an absorption edge at ≈320 nm, which reduces the EQE of the solar cell in that regime.

It should be noted here that the effect of light outcoupling is partly caused by the measurement setup, where a collimated narrow beam of ≈1 mm in diameter is used to illuminate a fraction of the PSC active area. Since the active area itself has only a width of 3.75 mm, the amount of outcoupling losses is certainly increased by the low scattering angles that are needed for light beams to escape the active area. With full size illumination, e.g. under the solar simulator, a contrary effect is observed. Then, scattered light beams from outside of the A_{act} are guided towards it, increasing the current generation through light incoupling.

In tandem setups comprising the PSC as top cell, the CIGS as bottom cell, immersion oil is expected to improve the light management, if used to fill the air gap and hence reducing the mismatch of the refractive indices along the layer interfaces from top to bottom cell. In order to investigate this, Figure 5.31a shows the EQE response of the CIGS cell in the different tandem setups with a representative PSC filter on top. The possible configurations with air (v), oil (vi) and additionally with ARF (vii) are schematically displayed in Figure 5.31b.
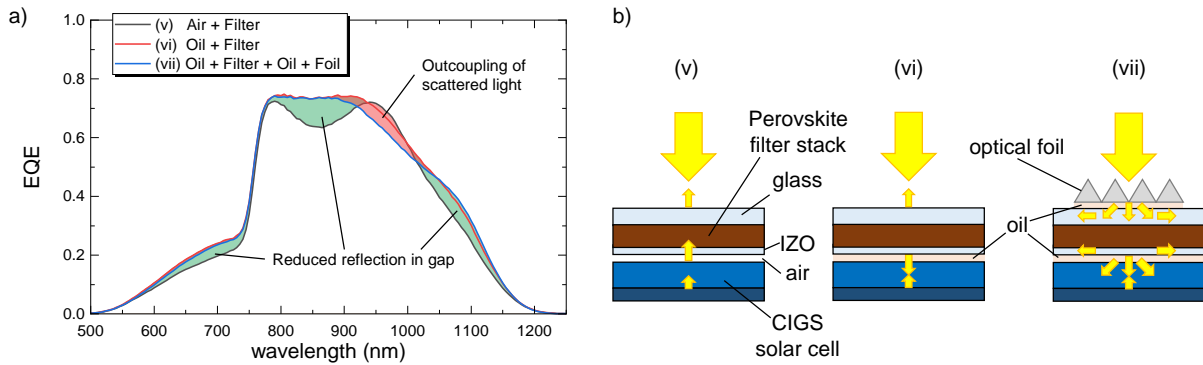
Figure 5.31: EQEs of a) a CIGS cell filtered by a representative perovskite solar cell stack with an air gap in between (v), optionally applying immersion oil (vi) and an anti-reflective foil (vii) that is placed on top of the filter. b) The corresponding schematic illustrations (v), (vi), and (vii) demonstrate the mechanisms that lead to the denoted, colour-coded gains (green) and losses (red) in the quantum efficiency.

As expected, the EQE of the CIGS bottom cell in a tandem setup with an air gap (v) shows typical losses from reflection. These are visible as in the form of local minimums due to the wavelength dependent interference patterns in the reflection. With oil in between PSC filter and CIGS (vi), the reflection losses are effectively suppressed and the EQE shows significant gains in the formerly reflecting parts (green area). When a ARF is applied to the setup (vii), the EQE is again reduced due to the light outcoupling effect (red area).

These results indicate that a tandem cell with an effective coupling material should benefit significantly from an increased current generation in the bottom cell. An ARF is unfortunately not of use in the evaluation of tandem cells of this size due to the unpredictable light in- and outcoupling effects. Alternatively, an ARC could be applied, to reduce the reflection at the air-glass interface at the top, without introducing light scattering. Since the in- and outcoupling effects that are described here, were primarily a matter of the small area solar cells, the ARF should be applied on larger areas such as tandem modules. For perovskite–silicon tandem modules, the beneficial effect has already been demonstrated. [12, 139]

In order to prove the expected performance gain of 4T tandem devices, when the air gap is filled with an optical coupling material, JV measurements have been performed with the different configurations. The results are listed in Table 5.12 along with the calculated J_{EQE} from the EQE measurements. As mentioned before, the measurements of the CIGS bottom cell (v, vi) utilise a representative PSC filter stacked on top, whereas the corresponding PSC top cell is measured separately (iii).

	Sample		JV data			EQE data
ID	Setup	PCE	FF	V_{OC}	J_{SC}	J_{EQE}
		(%)	(%)	(mV)	(mA cm^{-2})	(mA cm^{-2})
i	CIGS	20.1	76.2	695	38.1	38.3
iii	PSC	15.8	71.6	1129	19.3	18.9
v	Filter + Air + CIGS	7.1	77.5	659	13.8	13.8
vi	Filter + Oil + CIGS	7.6	76.4	661	14.9	15.1
iii + v	PSC + Air + CIGS	22.9				
iii + vi	PSC + Oil + CIGS	23.4		4T-tandem efficiency estimations		

Table 5.12: Solar cell parameters for a CIGS solar cell (i) and a semitransparent PSC (iii) as introduced in Figure 5.30. Parameters for the CIGS, when a filter representing the PSC is stacked on top with air in between (v) and using immersion oil (vi) as shown in Figure 5.31. The JV data was obtained experimentally from *rvs* JV scans and the J_{EQE} from EQE measurements. For the estimation of PCE of the theoretical 4T-tandem setups, the PCE$_f$ values of the filtered CIGS and the PSC were summarized according to the notation.

According to the JV measurements, the CIGS bottom cell profits from the use of immersion oil by a PCE$_f$ increase from 7.1 % to 7.6 % and a J_{SC} increase of 1.1 mA cm^{-2}. The measured J_{SC} values match closely to the calculated J_{EQE} values, proving the effective reduction of the reflection losses. A theoretical tandem setup with the PSC (iii), which has a PCE of 15.8 %, would reach a combined tandem PCE of 23.4 %.

As already mentioned before, the PSC comprises ITO as the front electrode, which is generally unfavourable due to its high NIR absorption. But the gain of efficiency in the bottom cell of more than 0.5 % absolute due to the immersion oil should be directly transferable to other setups with different electrode setups.

Unfortunately, the application of the oil is not easily accomplished when using actual solar cells instead of filters, because of several reasons. Firstly, the capillary forces strongly suck the top cell towards the bottom cell, so that the release of both cells after measurement likely damages the sensitive perovskite layers. Furthermore, for contacting the rear electrode of the PSC on the underside requires an electrical interconnection that the plane positioning on top of the bottom cell is difficult to accomplish without further technical arrangements. Lastly, oil that spills besides the TCO electrode of the PSC is likely to penetrate the sensitive organic layers and damage the cell. A filter is fully covered by the TCO, which is quite resistive to the oil and can be rinsed with alcohol afterwards.

For future development steps, the positive results of the immersion oil imply that an alternative coupling material could be applied to connect top and bottom cell such as a thermoplastic polymer, in order to serve a permanent encapsulation and a beneficial optical coupling. A suitable candidate could be poly(methyl methacrylate) (PMMA) since it has a similar refractive index of about 1.5 compared to immersion oil.

5.4.3 Increasing the CIGS efficiency by implementing wide band gap top cells with higher transmission

This section contains experimental transmittance data of filter stacks and PCE data of semi-transparent PSCs prepared by Saba Garibzadeh and Ihteaz M. Hossain from KIT. Detailed information is published in [3]. The following spectral analysis and simulation is original work of this thesis.

For the highest theoretical tandem PCE the E_g of the PSC should be increased to an optimum value of ≈ 1.7 eV, while keeping the PSC performance on a high level. Here, the impact of PSCs with a series of wider band gaps on the performance of the CIGS cells and hence the tandem PCE is evaluated with samples provided by collaboration partners from KIT.

Due to the increase of the E_g, the fundamental absorption edge shifts to lower wavelengths as it is observable in the T curves in Figure 5.32a for a set of different PSC filters from KIT. The transmittance after the fundamental absorption edge (T_f) is generally lower compared to the in-house prepared PSC (dashed line) due to a different electrode setup based on ITO instead of IO:H and IZO. The architecture of the KIT PSC filters is described in reference [3].

The shift of the absorption edge from 1.63 eV to 1.83 eV leads to a significant increase of the J_{Trn} of more than 4 mA cm^{-2} in the integration limit wavelength up to 1200 nm, as shown in Figure 5.32b. As expected, the higher T_f of the ZSW PSC (E_g= 1.62 eV) leads also to a gain of ≈ 2 mA.cm^{-2} in J_{Trn} if compared to the KIT sample with a similar E_g. However, the spectral response of the bottom cell is certainly higher for shorter wavelengths, so that the strongest impact on the CIGS PCE$_f$ is expected from the PSCs with a wider band gap.

Figure 5.32c shows the estimated tandem PCEs, using the single diode model approach for simulating the bottom cell power conversion efficiency obtained from single diode model simulation (PCE$_{Sim}$) of the CIGS cell with E_g = 1.1 eV (CIGS$_a$) and using the PCEs of PSCs that are equivalent to the filter architectures which are measured at the KIT.
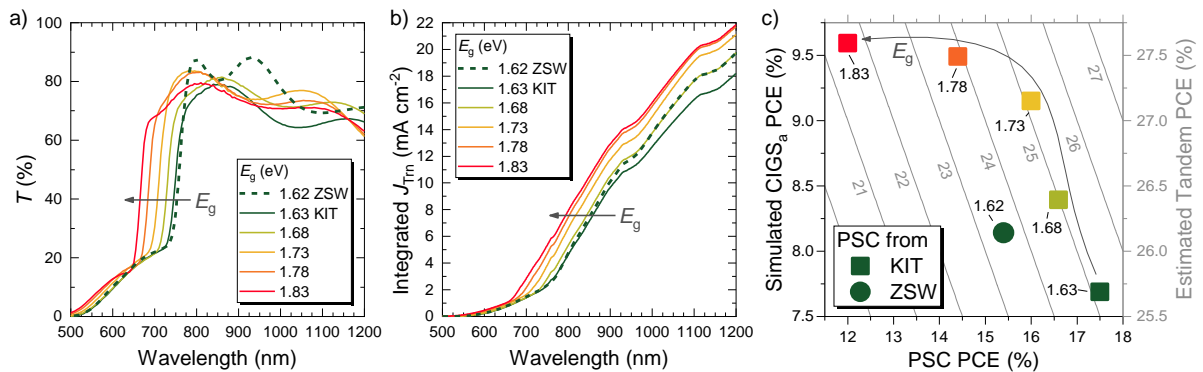
Figure 5.32: a) Spectral T of PSC filters from Zentrum für Sonnenenergie- und Wasserstoff-Forschung Baden-Württemberg (ZSW) and KIT with different E_g in the range of 1.62 eV to 1.83 eV; b) Integral curves of J_{Trn} of the same filters; c) Estimated PCEs of principle tandem setups of CIGS$_a$ as a bottom cell and the PSCs with different band gaps as top cells. Here, the PCE of the CIGS$_a$ is simulated by the single diode model, using the T of the PSC filters as an input. The PCE of the PSCs is obtained from MPP tracking of equivalent PSCs devices from KIT and ZSW.

As expected, the increase of the E_g is followed by a strong performance gain in the bottom cell. Filtered by the PSC filter with the lowest E_g of 1.63 eV, the CIGS$_a$ reaches only about 7.7 %, while the maximum bottom cell PCE$_{Sim}$ of 9.6 % is reached at 1.83 eV. However, the best tandem performance with an estimated PCE of 25.2 % is met with the PSC with 1.63 eV, which has a much higher reported PCE of 17.5 %. With the increase of the E_g, the PSCs themselves lose in PCE, which is not fully compensated by the PCE gains in the bottom cell. As a result, the three PSCs with the lower E_g values of 1.63 eV, 1.68 eV and 1.73 eV achieve quite similar tandem PCEs over 25 %, while the wider band gap setups lose tandem performance.

Comparing the tandem setups with the 1.62 eV (ZSW) and 1.63 eV (KIT) samples, a difference in the CIGS PCE$_{Sim}$ of an absolute value of ≈0.5 % is observed that is reasoned the superior transmittance of the ZSW sample. Of course the tandem performance with the ZSW PSC is lower, because of the lower perovskite performance, but it raises the question, what would be the maximum bottom cell performance, if the T_f would be higher for the PSCs with different E_g.

In order to estimate the bottom cell PCE for any setup with a fictional higher T_f, a set of PSC filter models has been generated that mimic the T of the real filters near E_g, but the T_f is set to fix values of 70 % to 95 %. The spectral T data of the set is shown in Figure 5.33a. Following the same single diode model simulation approach from Section 5.2, the PCE of CIGS$_a$ in all possible combinations is mapped in Figure 5.33b. The PCEs are plotted versus the E_g using a colour coded heat map for denoting the T_f. For comparison, also the experimental values are marked. Figure 5.33b shows a similar colour map for CIGS$_b$.

The positions of the experimental data points indicate that their actual T_f responses correlate to a theoretical linear T_f of around 75 %. Small deviations originate from the positions of the interference maxima in the real T spectra.
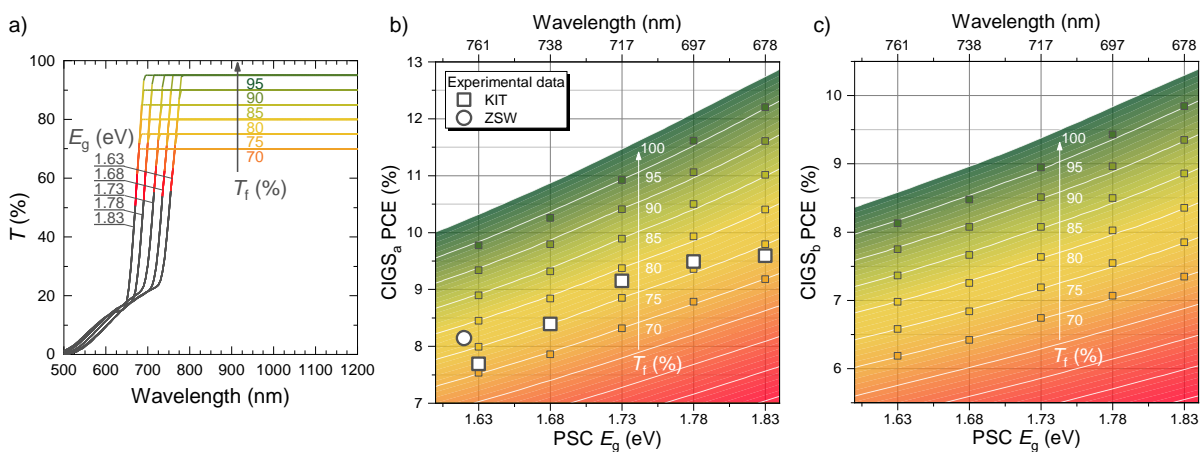

Figure 5.33: a) Spectral T of PSC filter models with different E_g and a linear transmittance after the fundamental absorption edge (T_f) up to 95 % as indicated; Simulated PCE of b) CIGS$_a$ and c) CIGS$_b$ versus E_g of the PSC filter models. The colour coded scale denote the corresponding T_f. Additional experimental data is shown in b).

However, the simulation predicts that the bottom cell PCE could be increased by an absolute of approximately 2 % for all setups, if the T_f would be increased to 95 %. It also predicts that the maximum PCE that could be reached with the CIGS cell with E_g = 1.1 eV (CIGS$_a$) in application, is limited to ≈10 % when using a top cell with a narrow E_g and ≈12 % with a wider E_g. The CIGS cell with E_g = 1.0 eV (CIGS$_b$) would reach maximum PCEs between 8 % and 10 %, respectively.

In an estimation example, CIGS$_a$ would have a PCE$_{Sim}$ of about 9.5 %, assuming perovskite solar cell with a decent transmittance of 80 % and a band gap of 1.75 eV. This would lead to a tandem efficiency of 28 % or more, only if the PSC is highly efficient with a PCE of over 18.5 %. Increasing the transmittance to 90 % would boost the bottom cell PCE$_f$ to 10.5 % and the tandem to 29 %, respectively.

For tandem PCEs to approach 30 % in the future, two consequences are conceived from these results: (i) The bottom cell must become more efficient in the collection and conversion of photons with long wavelengths and (ii) The top cell must increase the transmittance and the overall photovoltaic performance.

Both issues demand for a profound knowledge on the loss mechanisms, where incident photons are not converted to current but reflected, scattered, or parasitically absorbed. The proposed optical models in Section 5.4.1 may serve this task in the future.

6 Summary

This thesis focuses on the development of efficient perovskite–CIGS tandem solar cells with an enhanced spectral response in the near-infrared spectrum. In the process, perovskite solar cells (PSCs) were fabricated with high power conversion efficiency and high transparency. To increase their transmission in the near-infrared (NIR) spectrum, hydrogen-doped indium oxide (IO:H) and indium zinc oxide (IZO) films were investigated and implemented as front and rear electrodes for the PSC. Cell-size-matched four-terminal (4T) tandem solar cells with an active area of $0.5\,\text{cm}^2$ were developed that reach a power conversion efficiency (PCE) of 23.0 %.

In the first part of this thesis, fundamental challenges regarding the solution-based fabrication of PSC were identified and overcome by sophisticated interface engineering. A large issue is caused by ion accumulation at the electron transport layer (ETL) interface with the perovskite, which hinders charge extraction and results in a pronounced hysteresis with an irregular response of the photocurrent during a voltage scan depending on the sweep direction. Passivating the interface with a C_{60}-based self-assembled monolayer (C_{60}–SAM) effectively suppressed the hysteresis, but the highly non-polar molecules introduced severe wetting issues during the subsequent deposition of the perovskite precursor.

To increase the low surface energy of the organic fullerene layer, a wetting agent was developed on the basis of insulating oxides nanoparticles such as SiO_2 and Al_2O_3 with diameters between $20\,\text{nm}$ to $60\,\text{nm}$. Contact angle measurements revealed that the insulating nanoparticles cause a strong increase of the surface energy already when covering only fractions of 10 % to 15 % of the interface. The wetting agent thus facilitated the perovskite formation to the extent that a homogeneous layer was feasible even on larger areas.

On the pathway to semitransparent PSCs, highly NIR transparent and yet conductive IO:H and IZO electrodes were developed. Sputter deposited and subsequently crystallized IO:H was identified as a suitable front electrode on the glass superstrate with the best optical properties, using H_2 gas as the doping source during deposition. This approach achieved state-of-the-art conductive properties with a high charge carrier mobility (μ) of over $90\,\text{cm}^2\,\text{V}^{-1}\text{s}^{-1}$ and a low electron density (N_e) of under $2 \times 10^{20}\,\text{cm}^{-3}$ at an ultra-low NIR absorptance below 2 %.

For the rear electrode deposition on the sensitive organic hole transport layer (HTL), amorphous IZO in combination with a MoO_3 protective layer proved to be the best choice in terms of avoiding sputter damage, low absorption and low resistivity. The perovskite absorber followed a mixed cation approach with a band gap of $\approx 1.6\,\text{eV}$, fixing the absorption edge at about $780\,\text{nm}$. From a thorough investigation of the spectral properties of the semitransparent PSCs, it can be concluded that IO:H and IZO outperform traditional transparent conductive oxides (TCOs) such as indium tin oxide (ITO) or fluorine doped tin oxide (FTO), lowering the integral NIR absorptance from over 20 % to below 7 % while maintaining a high photovoltaic PCE of over 15 %.

Variations of the TCO layer thickness unveiled the complex balancing between optical properties and electrical performance for the given solar cell geometry. As expected, thinner rear electrodes lead to a lower parasitic absorption accompanied by higher series resistance, but it was also found that the transmittance suffers from high internal reflection interference. Hence, intermediate layer thicknesses proved to have the advantage of a better transmission and an improved electrical performance.

The second part of this thesis concentrated on combining the semitransparent PSCs with copper indium gallium diselenide (CIGS) solar cells into tandem setups. Because the race to publish perovskite record values has led to announcements of tandem device efficiencies derived from vaguely filtered bottom cells and tiny top cells, one goal of this thesis was to evaluate the discrepancy between a real cell-size-matched tandem device and a filtered cell stack estimation. A simple study of the transmittance of diverse semitransparent PSC and their sister filters quickly confirmed a spectral disparity. Especially with the use of in-house made electrodes, slight thickness variations lead to interference-induced mismatches of up to 3.6 %.

However, the comparably small transmittance mismatch should not cause concern because the real performance limiting factors hide behind the small area of the perovskite. Considering the possible challenges of a homogeneous layer deposition in the solution-based processes, it is no coincidence that the record PCE values are reported for tiny perovskite devices. Furthermore, the resistivity of the transparent electrodes becomes significantly more important upon increasing the cell size. To realize an area of $0.5\,\mathrm{cm}^2$, one dimension of the cell will be at least 7 mm wide, which is already comparable to the width of a cell in a typical module made of interconnected parallel cell stripes.

A metal grid is implemented to minimize the resistive losses in the TCO electrodes, lowering the series resistance of the solar cell by over 60 % in case of $0.24\,\mathrm{cm}^2$ PSCs and by 30 % on a larger area of $0.5\,\mathrm{cm}^2$. Remarkably, and perhaps due to the beneficial effect of the wetting agent on the perovskite layer homogeneity, the best large area PSC reached a steady-state PCE of 15.0 %. Combined with a high-efficiency CIGS solar cell of the same area, the resulting 4T tandem device demonstrated a champion PCE of 23 %.

Additional simulations with hypothetical filters to represent perovskite absorbers with a range of different band gaps showed that the required high efficiencies over 10 % for the CIGS bottom cell can only be reached when the band gap of the perovskite is increased to a minimum of $\approx 1.75\,\mathrm{eV}$ and in combination with a high transmittance after its absorption edge ($\approx 720\,\mathrm{nm}$) of about 90 %.

In order to investigate the remaining loss mechanisms in the tandem setup, a sophisticated current loss analysis was performed. In the process, spectroscopic ellipsometry measurements were conducted on the single layers of the PSC in order to determine their optical functions n and k for inclusion in a simulation model of the whole 4T tandem architecture. The model enables the parasitic absorption of each layer of the complete tandem stack to be addressed.

As a result, it shows that the main absorption losses are attributed to the TCOs while the interlayers contribute only a minor fraction. Already the replacement of the ITO front electrode of the PSC by an IO:H electrode avoids current density losses of over $2\,\mathrm{mA\,cm^{-2}}$. Hence, the overall relative absorption related current loss is reduced from 16 % to 12 %, which is equal to the current losses introduced by reflection (12 %). Further significant losses are due to imperfections of the perovskite, shadowing by the metal grid and insufficient absorption of NIR photons which are lost at the rear electrode of the CIGS bottom cell.

in conclusion, there is quite some potential to improve the performance of the tandem cell from an optical point of view. At first, the reflection losses must be minimized. A simple experiment with immersion oil as an optical coupling material in between the gap of a perovskite filter and the CIGS bottom cell demonstrated that the reflection losses at long wavelengths from the interface of the PSC rear electrode can be drastically reduced. These reflection losses are confirmed in the current loss analysis, which indicates that a suitable filler material with a matched refractive index could be used to glue top and bottom cell together. On the one hand this would serve as encapsulation and on the other hand improve light management, leading to a win-win situation.

A different approach is needed for the front interface. Here, experiments with a textured anti-reflective foil showed that due to the thick glass superstrate in the front, no beneficial effects could be achieved because if only a fraction is illuminated the light is scattered away from the active area. Illumination of a larger fraction leads to the opposite effect with more light coupling into the active area. Consequently, the texturing approach could lead to better light management, but only on large-area devices such as modules in which the scattered light would always encounter the active area at some point. Additionally, a simple anti-reflective coating on the glass side might not lead to the desired gain, because a large amount of reflection is introduced internally at the interfaces. These act as reflective resonators for wavelengths that match the interlayer distances. Hence, a sensitive fine-tuning of the interlayer thicknesses would lead to a more significant improvement of the transmissive properties of the top cell. The optical models developed in this work, will contribute to this development in the future.

Regarding the remaining parasitic absorption in the TCO electrodes, a great further reduction here is only possible under certain preconditions, because the main losses could be already effectively reduced by exchanging the front electrode ITO with post-deposition-crystallised hydrogenated indium oxide (PDC–IO:H). As long as the reflection is still high and the perovskite absorber layer itself also contributes a significant amount of parasitic absorption (including recombination losses), not much light transmits to the underlying TCO layers. As a result the implementation of even better TCOs in place of the rear electrode of the PSC or replacing the TCO of the CIGS would have only a small effect.

For future development steps, the tasks can be formulated from the above findings:

- Reduction of the reflection at the rear electrode of the PSC

- Simulation assisted adjustment of all layer thicknesses to reduce internal reflection

- Advanced perovskite absorbers with less parasitic absorption and optimal band gap

- Highly NIR optimized TCOs also for CIGS

- Improved CIGS efficiency in the NIR

There are many other challenges of the new perovskite technology which have not been addressed in this thesis, such as degradation issues, thermal stability, lead elution, upscaling, solvent toxicity, and the like. The list is long, but because there is so much research and industrial effort involved in this fascinating topic, perovskites seem to be ready to tackle all remaining challenges. I therefore believe that perovskites have an excellent chance to succeed as a new player in the PV world. I am looking forward to a bright perovskite future, especially in tandem applications and consequently with CIGS as a thin-film teammate.

A Appendix

A.1 Ellipsometry models

Drude model (D): A Drude model is used for the description of free carriers like they occur in a materials like metals or highly doped semiconductors (like TCOs). The dielectric functions is defined as:

$$\epsilon(\omega) = \epsilon_{1\infty} - \frac{\omega_p^2}{\omega^2 + i\omega_\tau \nu} \tag{A.1}$$

with the frequency ω in units of $1/s$ and where $\omega_p = \sqrt{(\frac{Ne^2}{\epsilon_0 m^*})}$ is the resonance frequency which represents the amplitude of the oscillator and $\omega_\tau = \frac{e}{\mu m^*}$ the damping constant. From this relations carrier concentration, mobility and effective mass can be determined. The value of the dielectric function in infinity $\epsilon_{1\infty}$ is typically fixed at 1.

Tauc-Lorentz model (TL): This model is mainly used to describe transparent dielectric and amorphous materials with an absorption edge. It is based on the expression for $\epsilon_2(E)$. $\epsilon_2(E)$ is obtained from Kramers-Kronig relation.

$$\epsilon_2(E) = \begin{cases} \frac{AE_0C(E-E_g)^2}{(E^2-E_0^2)^2+C^2E^2}\frac{1}{E}, & E > E_g \\ 0 & E \leq E_g \end{cases} \tag{A.2}$$

$$\epsilon_1(E) = \epsilon_{1\infty} + \frac{2}{\pi}P\int_{E_g}^{\infty}\frac{x\epsilon_2(x)}{x^2-E^2}dx \tag{A.3}$$

In the TL model, the dielectric functions are obtained from the five parameters band gap E_g, the amplitude A, the resonance frequency E_0 and the broadening of the oscillator C. The units of these parameters is eV. The given formula is for a single oscillator, but using multiple TL oscillators to describe a material may be reasonable.

Cody-Lorentz model (CL): The CL model is similar to the TL model but with an additional Urbach term in order to simulate Urbach tail for the absorption of photons with energy smaller E_g.

$$\epsilon_2(E) = \begin{cases} \frac{AE_0CE(E-E_g)^2}{((E^2-E_0^2)^2+C^2E^2)((E-E_g)^2+E_p^2)}, & E > E_t \\ \frac{E_1}{E}exp\left(\frac{(E-E_t)}{E_U}\right) & E \leq E_t \end{cases} \tag{A.4}$$

$$\epsilon_1(E) = \epsilon_{1\infty} + \frac{2}{\pi}P\int_{E_g}^{\infty}\frac{x\epsilon_2(x)}{x^2-E^2}dx \tag{A.5}$$

Parameters A, E_0, C and E_g are the same as in the TL model. E_p, E_t, E_U are additional parameters due to the Urbach term.

Cauchy model (C): A Cauchy model is often used for transparent dielectric materials. The Cauchy relation uses the first two even orders of a polynomial description of $n(\lambda)$ and $k(\lambda)$:

$$n(\lambda) = n_0 + C_0 \frac{n_1}{\lambda^2} + C_1 \frac{n_2}{\lambda^4} \tag{A.6}$$

$$k(\lambda) = k_0 + C_0 \frac{k_1}{\lambda^2} + C_1 \frac{k_2}{\lambda^4} \tag{A.7}$$

with the wavelength λ in units of nm. The optical functions are obtained by fitting the six parameters $n_0, n_1, n_2, k_0, k_1, k_2$. The coefficients $C_0 = 10^2$ and $C_1 = 10^7$ are fixed.

For the best description of the TCO materials of this study, a Drude model for the modelling of free carrier absorption is combined with another model for the interband transitions. For the interband transition modelling, Tauc-Lorentz and Cody-Lorentz models are suitable and widely used [73]. A Drude model in combination with a Tauc-Lorentz model was used for modelling the amorphous layers IZO and a-IO:H (both 180 nm). For PDC-IO:H layers (with a layer thickness of 220 nm) with polycrystalline structure, a combination of Drude and Cody-Lorentz was used.

For the modeling of MoO_3, a Tauc-Lorentz model was used to design both the band gap and the close to zero absorption for wavelengths greater than 400 nm. The values for the refractive index correspond well with the literature [136]. For the nanoparticle layers, Cauchy models were used since no absorption and no band to band transitions take place. The values of SiO_2-NP agree with the values of Gao et al. [137] for compact SiO_2. Goldsmith et al. calculated the refractive index of approx. 1.8 for SnO_2 layers with a fraction of voids of 0.3, which is comparable to our results for the non-compact nanoparticle based layers. [140]

The data for Spiro-MeOTAD were taken from literature because the deposition on quartz glass was not possible. [92] For the simulation of $C_{60}-SAM$ a Tauc-Lorentz model was used. For the simulation of the perovskite absorber, 8 Tauc-Lorentz oscillators were used in one model. For wavelength higher than 800 nm k drops to values in the range of 0 but a small residual absorption is observable (see inset).

The parameters of the optical models of the simulation are listed in Table A.1.

Layer	RMS	d (nm)	Model	Parameters						
a-IOH	3.06	156	TL	E_g (eV)	A (eV)	E_0 (eV)	C (eV)			
				2.9943	474660	2.7136	14.8437			
			D	ω_p (cm^{-1})	ω_τ (cm^{-1})					
				12313.31	774.41					
PDC-IO:H	5.58	210	CL	E_g (eV)	A (eV)	E_0 (eV)	C (eV)	E_p (eV)	E_t (eV)	E_U (eV)
				2.419	87.18	8.5978	19.1496	3.1469	4.0013	0.2507
			D	ω_p (cm^{-1})	ω_τ (cm^{-1})					
				7938.99	403.6					
IZO	0.69	168	TL	E_g (eV)	A (eV)	E_0 (eV)	C (eV)			
			1	2.5389	18237	13.0974	2.1841			
			2	4.6027	201151	5.535	18.0286			
			3	2.6258	38788	4.2672	2.4085			
			D	ω_p (cm^{-1})	ω_τ (cm^{-1})					
				10431.21	628.14					
SiO$_2$$-$NP	0.42	25	C	n_0	n_1	n_2	k_0	k_1	k_2	
				1073	39.5	25.4	0	-385	282	
SnO$_2$$-$NP	0.31	12	C	n_0	n_1	n_2	k_0	k_1	k_2	
				1223	120.6	30.2	10	-55535	50163	
Perovskite	0.95	384	TL	E_g (eV)	A (eV)	E_0 (eV)	C (eV)			
			1	0.0121	32	1.4346	0.477			
			2	1.5961	62222	1.6323	0.1019			
			3	1.5533	12133	2.0226	0.9481			
			4	1.5138	5800	2.5122	0.6366			
			5	2.0564	34779	2.6747	1.2476			
			6	2.7076	38236	3.0059	0.4939			
			7	2.8999	99772	3.1361	0.7149			
			8	4.1076	142975	4.6938	2.9157			
C$_{60}$$-$SAM	0.44	2.6	TL	E_g (eV)	A (eV)	E_0 (eV)	C (eV)			
				3.939	410001	4.1034	13.5611			
MoO$_3$	0.39	10	TL	E_g (eV)	A (eV)	E_0 (eV)	C (eV)			
				3.0485	656802	1.7095	5.4024			

Table A.1: Parameters used for the optical models for fitting the spectral ellipsometry data and for simulating the optical functions n and k of each layer. The quality of the fit is evaluated by the root mean square error RMS.

A.2 Quantum efficiency measurements

To evaluate the spectral properties of the PSC, we performed external quantum efficiency (EQE) and transmittance (T) measurements. In contrast to the JV measurements under illumination of the full cell area, the illuminated area during EQE and T measurments is restricted to $0.05\,\text{cm}^2$ in order to fit between the grid bars (see Figure A.1). By this, all incident photons of the probe beam may be either absorbed, reflected or transmitted in the layers of the tandem cell, without influence of the grid. In order to make sure, that no significant error is introduced by illuminating only a fraction of the active area, leaving a big fraction of dark area, we discuss briefly different preconditions for appropriate measurements in the following.

Layer homogeneity: Figure A.2 shows that the EQE responses of $0.24\,\text{cm}^2$ and $0.5\,\text{cm}^2$ sized cells are comparable, speaking for a equally good charge generation and collection in samples with different active areas. From the transmittance curves of the devices in the same graph, we observe a significant shift of the T patterns, which indicates layer thickness differences between the devices. This shows that – despite fabrication with equal process parameters – the exact replication of the optical properties can not be guaranteed. In contrast, the optical properties of a single device are very homogeneous, since no significant difference in EQE or T is observed by moving the measurement spot in different positions of each sample.

Shunts and dark area: Local shunts would deteriorate the EQE response, if they are close to the measurement spot or close to the contact (grid). Without significant shunts, the EQE is quite independent from the resistive properties of the solar cell since it is measured under short circuit conditions ($V = 0$). Likewise, the dark area should be irrelevant to the measurement, because it is resembled by a parallel diode that locks under short circuit conditions with a high resistance. The absence of significant shunts is proven by the high parallel resistance of several $\text{k}\Omega$ as obtained from JV measurements of the devices.
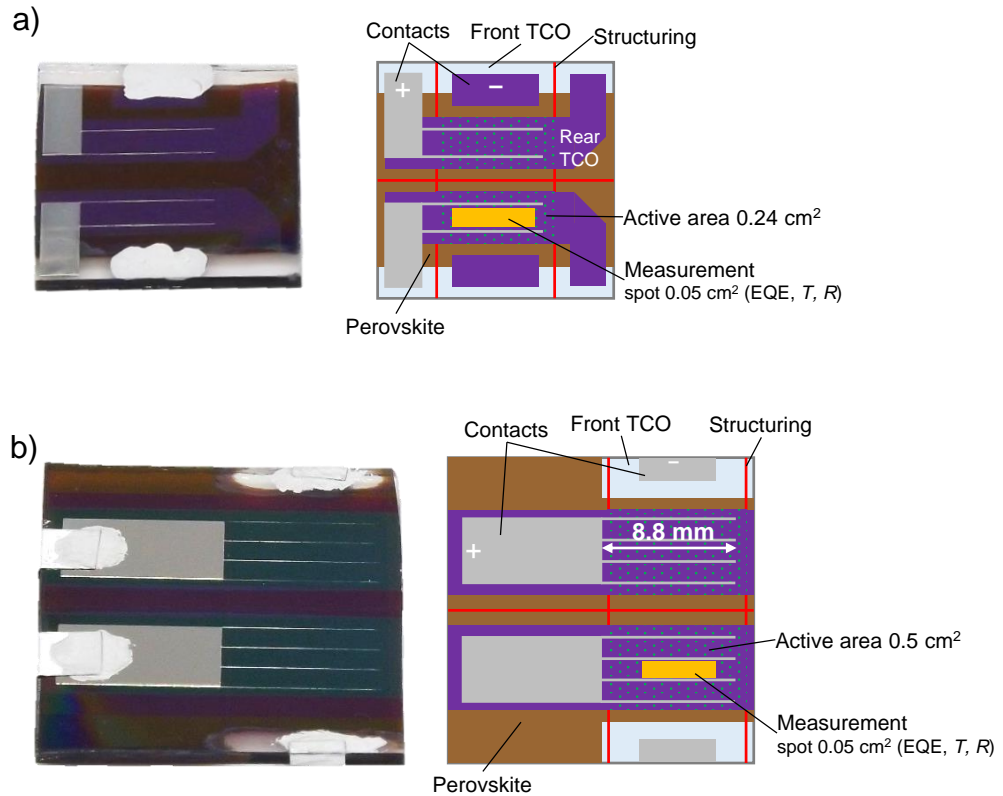
Figure A.1: a) Photograph and scheme of a perovskite device with two solar cells of an active area of 0.24 cm^2 and of b) 0.5 cm^2. The yellow spot between the grid bars denotes the area (0.05 cm^2), which is illuminated during EQE, T and R measurements of the single cells or tandem cells. During JV measurements, the full active area is illuminated.
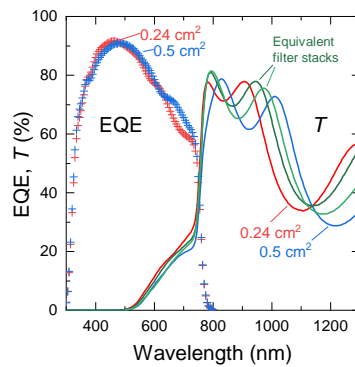

Figure A.2: EQE and T measurements of PSC of the same architecture with different active area. Additionally, T spectra of filter stacks are shown which were prepared under nominally the same conditions and process parameters at different times.

Bibliography

[1] T. Todorov, O. Gunawan, and S. Guha, "A road towards 25% efficiency and beyond: Perovskite tandem solar cells," *Molecular Systems Design & Engineering*, vol. 1, no. 4, pp. 370–376, 2016.

[2] H. Shen, T. Duong, J. Peng, D. Jacobs, N. Wu, J. Gong, Y. Wu, S. K. Karuturi, X. Fu, K. Weber, X. Xiao, T. P. White, and K. Catchpole, "Mechanically-stacked perovskite/CIGS tandem solar cells with efficiency of 23.9% and reduced oxygen sensitivity," *Energy & Environmental Science*, vol. 11, pp. 394–406, Feb. 2018.

[3] S. Gharibzadeh, B. A. Nejand, M. Jakoby, T. Abzieher, D. Hauschild, S. Moghadamzadeh, J. A. Schwenzer, P. Brenner, R. Schmager, A. A. Haghighirad, L. Weinhardt, U. Lemmer, B. S. Richards, I. A. Howard, and U. W. Paetzold, "Record Open-Circuit Voltage Wide-Bandgap Perovskite Solar Cells Utilizing 2D/3D Perovskite Heterostructure," *Advanced Energy Materials*, vol. 9, no. 21, p. 1803699, 2019.

[4] E. Avancini, R. Carron, B. Bissig, P. Reinhard, R. Menozzi, G. Sozzi, S. D. Napoli, T. Feurer, S. Nishiwaki, S. Buecheler, and A. N. Tiwari, "Impact of compositional grading and overall Cu deficiency on the near-infrared response in Cu(In, Ga)Se$_2$ solar cells," *Progress in Photovoltaics: Research and Applications*, vol. 25, no. 3, pp. 233–241, 2017.

[5] T. Feurer, B. Bissig, T. P. Weiss, R. Carron, E. Avancini, J. Löckinger, S. Buecheler, and A. N. Tiwari, "Single-graded CIGS with narrow bandgap for tandem solar cells," *Science and Technology of Advanced Materials*, vol. 19, no. 1, pp. 263–270, 2018.

[6] D. H. Kim, C. P. Muzzillo, J. Tong, A. F. Palmstrom, B. W. Larson, C. Choi, S. P. Harvey, S. Glynn, J. B. Whitaker, F. Zhang, Z. Li, H. Lu, M. F. van Hest, J. J. Berry, L. M. Mansfield, Y. Huang, Y. Yan, and K. Zhu, "Bimolecular additives improve wide-band-gap perovskites for efficient tandem solar cells with cigs," *Joule*, vol. 3, no. 7, pp. 1734 – 1745, 2019.

[7] Q. Han, Y.-T. Hsieh, L. Meng, J.-L. Wu, P. Sun, E.-P. Yao, S.-Y. Chang, S.-H. Bae, T. Kato, V. Bermudez, and Y. Yang, "High-performance perovskite/Cu(In,Ga)Se$_2$ monolithic tandem solar cells," *Science*, vol. 361, no. 6405, pp. 904–908, 2018.

[8] M. Jošt, T. Bertram, D. Koushik, J. A. Marquez, M. A. Verheijen, M. D. Heinemann, E. Köhnen, A. Al-Ashouri, S. Braunger, F. Lang, B. Rech, T. Unold, M. Creatore, I. Lauermann, C. A. Kaufmann, R. Schlatmann, and S. Albrecht, "21.6%-Efficient Monolithic Perovskite/Cu(In,Ga)Se$_2$ Tandem Solar Cells with Thin Conformal Hole Transport Layers for Integration on Rough Bottom Cell Surfaces," *ACS Energy Letters*, pp. 583–590, 2019.

[9] M. Langenhorst, B. Sautter, R. Schmager, J. Lehr, E. Ahlswede, M. Powalla, U. Lemmer, B. S. Richards, and U. W. Paetzold, "Energy yield of all thin-film perovskite/CIGS tandem solar modules," *Progress in Photovoltaics: Research and Applications*, vol. 27, no. 4, pp. 290–298, 2019.

[10] P. Mantilla-Perez, T. Feurer, J.-P. Correa-Baena, Q. Liu, S. Colodrero, J. Toudert, M. Saliba, S. Buecheler, A. Hagfeldt, and A. N. Tiwari, "Monolithic CIGS–Perovskite Tandem Cell for Optimal Light Harvesting without Current Matching," *ACS Photonics*, vol. 4, no. 4, pp. 861–867, 2017.

[11] U. W. Paetzold, M. Jaysankar, R. Gehlhaar, E. Ahlswede, S. Paetel, W. Qiu, J. Bastos, L. Rakocevic, B. S. Richards, T. Aernouts, M. Powalla, and J. Poortmans, "Scalable perovskite/CIGS thin-film solar module with power conversion efficiency of 17.8%," *Journal of Materials Chemistry A*, vol. 5, pp. 9897–9906, May 2017.

[12] M. Jaysankar, S. Paetel, E. Ahlswede, U. W. Paetzold, T. Aernouts, R. Gehlhaar, and J. Poortmans, "Toward scalable perovskite-based multijunction solar modules," *Progress in Photovoltaics: Research and Applications*, vol. 27, no. 8, pp. 733–738, 2019.

[13] G. C. E. Jost, A. N. Hamri, F. Köhler, and J. Hüpkes, "Reliability aspects of hydrogen-doped indium oxide," *physica status solidi (a)*, vol. 213, no. 7, pp. 1751–1759, 2016.

[14] H. Scherg-Kurmes, S. Seeger, S. Körner, B. Rech, R. Schlatmann, and B. Szyszka, "Optimization of the post-deposition annealing process of high-mobility In_2O_3:H for photovoltaic applications," *Thin Solid Films*, vol. 599, pp. 78–83, 2016.

[15] T. Koida, H. Fujiwara, and M. Kondo, "Hydrogen-doped In_2O_3 as High-mobility Transparent Conductive Oxide," *Japanese Journal of Applied Physics*, vol. 46, no. 7L, p. L685, 2007.

[16] T. Koida, M. Kondo, K. Tsutsumi, A. Sakaguchi, M. Suzuki, and H. Fujiwara, "Hydrogen-doped In_2O_3 transparent conducting oxide films prepared by solid-phase crystallization method," *Journal of Applied Physics*, vol. 107, no. 3, p. 033514, 2010.

[17] J. Werner, L. Barraud, A. Walter, M. Bräuninger, F. Sahli, D. Sacchetto, N. Tétreault, B. Paviet-Salomon, S.-J. Moon, C. Allebé, M. Despeisse, S. Nicolay, S. De Wolf, B. Niesen, and C. Ballif, "Efficient Near-Infrared-Transparent Perovskite Solar Cells Enabling Direct Comparison of 4-Terminal and Monolithic Perovskite/Silicon Tandem Cells," *ACS Energy Letters*, vol. 1, no. 2, pp. 474–480, 2016.

[18] F. Fu, T. Feurer, T. Jaeger, E. Avancini, B. Bissig, S. Yoon, S. Buecheler, and A. N. Tiwari, "Low-temperature-processed efficient semi-transparent planar perovskite solar cells for bifacial and tandem applications," *Nature Communications*, vol. 6, 2015.

[19] C. O. Ramirez Quiroz, Y. Shen, M. Salvador, K. Forberich, N. Schrenker, G. D. Spyropoulos, T. Heumuller, B. Wilkinson, T. Kirchartz, E. Spiecker, P. J. Verlinden, X. Zhang, M. A. Green, A. Ho-Baillie, and C. J. Brabec, "Balancing electrical and optical losses for efficient 4-terminal Si-perovskite solar cells with solution processed percolation electrodes," *Journal of Materials Chemistry A*, vol. 6, no. 8, pp. 3583–3592, 2018.

[20] A. Guchhait, H. A. Dewi, S. W. Leow, H. Wang, G. Han, F. B. Suhaimi, S. Mhaisalkar, L. H. Wong, and N. Mathews, "Over 20% Efficient CIGS–Perovskite Tandem Solar Cells," *ACS Energy Letters*, vol. 2, no. 4, pp. 807–812, 2017.

[21] G. Rose, "Beschreibung einiger neuen Mineralien des Urals," *Annalen der Physik*, vol. 124, no. 12, pp. 551–573, 1839.

[22] D. Weber, "$CH_3NH_3SnBr_xI_{3-x}$ (x = 0-3), a Sn(II)-System with Cubic Perovskite Structure," *Zeitschrift für Naturforschung B*, vol. 33, no. 8, pp. 862–865, 1978.

[23] A. Kojima, K. Teshima, Y. Shirai, and T. Miyasaka, "Organometal Halide Perovskites as Visible-Light Sensitizers for Photovoltaic Cells," *Journal of the American Chemical Society*, vol. 131, no. 17, pp. 6050–6051, 2009.

[24] M. Powalla, S. Paetel, E. Ahlswede, R. Wuerz, C. D. Wessendorf, and T. Magorian Friedlmeier, "Thin-film solar cells exceeding 22% solar cell efficiency: An overview on CdTe-, Cu(In,Ga)Se$_2$-, and perovskite-based materials," *Applied Physics Reviews*, vol. 5, no. 4, p. 041602, 2018.

[25] N.-G. Park, "Perovskite solar cells: An emerging photovoltaic technology," *Materials Today*, vol. 18, no. 2, pp. 65–72, 2015.

[26] M. Hirasawa, T. Ishihara, T. Goto, K. Uchida, and N. Miura, "Magnetoabsorption of the lowest exciton in perovskite-type compound (CH$_3$NH$_3$)PbI$_3$," *Physica B Condensed Matter*, vol. 201, pp. 427–430, 1994.

[27] F. Ruf, M. F. Aygüler, N. Giesbrecht, B. Rendenbach, A. Magin, P. Docampo, H. Kalt, and M. Hetterich, "Temperature-dependent studies of exciton binding energy and phase-transition suppression in (Cs,FA,MA)Pb(I,Br)$_3$ perovskites," *APL Materials*, vol. 7, no. 3, p. 031113, 2019.

[28] S. D. Stranks, G. E. Eperon, G. Grancini, C. Menelaou, M. J. P. Alcocer, T. Leijtens, L. M. Herz, A. Petrozza, and H. J. Snaith, "Electron-hole diffusion lengths exceeding 1 micrometer in an organometal trihalide perovskite absorber," *Science*, vol. 342, no. 6156, pp. 341–344, 2013.

[29] G. Xing, N. Mathews, S. Sun, S. S. Lim, Y. M. Lam, M. Grätzel, S. Mhaisalkar, and T. C. Sum, "Long-range balanced electron- and hole-transport lengths in organic-inorganic CH$_3$NH$_3$PbI$_3$," *Science*, vol. 342, no. 6156, pp. 344–347, 2013.

[30] D. W. deQuilettes, S. M. Vorpahl, S. D. Stranks, H. Nagaoka, G. E. Eperon, M. E. Ziffer, H. J. Snaith, and D. S. Ginger, "Solar cells. Impact of microstructure on local carrier lifetime in perovskite solar cells," *Science*, vol. 348, no. 6235, pp. 683–686, 2015.

[31] L. M. Herz, "Charge-Carrier Mobilities in Metal Halide Perovskites: Fundamental Mechanisms and Limits," *ACS Energy Letters*, vol. 2, no. 7, pp. 1539–1548, 2017.

[32] D. P. McMeekin, G. Sadoughi, W. Rehman, G. E. Eperon, M. Saliba, M. T. Hörantner, A. Haghighirad, N. Sakai, L. Korte, B. Rech, M. B. Johnston, L. M. Herz, and H. J. Snaith, "A mixed-cation lead mixed-halide perovskite absorber for tandem solar cells," *Science*, vol. 351, no. 6269, pp. 151–155, 2016.

[33] M. Saliba, T. Matsui, J.-Y. Seo, K. Domanski, J.-P. Correa-Baena, M. K. Nazeeruddin, S. M. Zakeeruddin, W. Tress, A. Abate, A. Hagfeldt, and M. Grätzel, "Cesium-containing triple cation perovskite solar cells: Improved stability, reproducibility and high efficiency," *Energy & Environmental Science*, vol. 9, no. 6, pp. 1989–1997, 2016.

[34] P. Würfel and U. Würfel, *Physics of solar cells : from basic principles to advanced concepts*. Weinheim: Wiley-VCH Verlag GmbH & Co. KGaA, 3rd edition ed., 2016.

[35] Y. Wu, D. Yan, J. Peng, T. Duong, Y. Wan, S. P. Phang, H. Shen, N. Wu, C. Barugkin, X. Fu, S. Surve, D. Grant, D. Walter, T. P. White, K. R. Catchpole, and K. J. Weber, "Monolithic perovskite/silicon-homojunction tandem solar cell with over 22% efficiency," *Energy & Environmental Science*, vol. 10, pp. 2472–2479, Nov. 2017.

[36] J. Werner, G. Dubuis, A. Walter, P. Löper, S.-J. Moon, S. Nicolay, M. Morales-Masis, S. De Wolf, B. Niesen, and C. Ballif, "Sputtered rear electrode with broadband transparency for perovskite solar cells," *Solar Energy Materials and Solar Cells*, vol. 141, pp. 407–413, 2015.

[37] H. Kanda, A. Uzum, A. K. Baranwal, T. A. N. Peiris, T. Umeyama, H. Imahori, H. Segawa, T. Miyasaka, and S. Ito, "Analysis of Sputtering Damage on I–V Curves for Perovskite Solar Cells and Simulation with Reversed Diode Model," *The Journal of Physical Chemistry C*, vol. 120, no. 50, pp. 28441–28447, 2016.

[38] Y. Zhao, A. M. Nardes, and K. Zhu, "Effective hole extraction using MoOx-Al contact in perovskite $CH_3NH_3PbI_3$ solar cells," *Applied Physics Letters*, vol. 104, no. 21, p. 213906, 2014.

[39] P. Schulz, J. O. Tiepelt, J. A. Christians, I. Levine, E. Edri, E. M. Sanehira, G. Hodes, D. Cahen, and A. Kahn, "High-Work-Function Molybdenum Oxide Hole Extraction Contacts in Hybrid Organic–Inorganic Perovskite Solar Cells," *ACS Applied Materials & Interfaces*, vol. 8, no. 46, pp. 31491–31499, 2016.

[40] E. M. Sanehira, B. J. Tremolet de Villers, P. Schulz, M. O. Reese, S. Ferrere, K. Zhu, L. Y. Lin, J. J. Berry, and J. M. Luther, "Influence of Electrode Interfaces on the Stability of Perovskite Solar Cells: Reduced Degradation Using MoOx/Al for Hole Collection," *ACS Energy Letters*, vol. 1, no. 1, pp. 38–45, 2016.

[41] M. Ye, C. He, J. Iocozzia, X. Liu, X. Cui, X. Meng, M. Rager, X. Hong, X. Liu, and Z. Lin, "Recent advances in interfacial engineering of perovskite solar cells," *Journal of Physics D: Applied Physics*, vol. 50, no. 37, p. 373002, 2017.

[42] M. Jung, S.-G. Ji, G. Kim, and S. I. Seok, "Perovskite precursor solution chemistry: From fundamentals to photovoltaic applications," *Chemical Society Reviews*, 2019.

[43] A. K. Jena, A. Kulkarni, and T. Miyasaka, "Halide Perovskite Photovoltaics: Background, Status, and Future Prospects," *Chemical Reviews*, vol. 119, no. 5, pp. 3036–3103, 2019.

[44] P. Schulz, D. Cahen, and A. Kahn, "Halide Perovskites: Is It All about the Interfaces?," *Chemical Reviews*, vol. 119, no. 5, pp. 3349–3417, 2019.

[45] J.-M. Yang, Y. Luo, Q. Bao, Y.-Q. Li, and J.-X. Tang, "Recent Advances in Energetics and Stability of Metal Halide Perovskites for Optoelectronic Applications," *Advanced Materials Interfaces*, vol. 6, no. 3, p. 1801351, 2019.

[46] C. C. Boyd, R. Cheacharoen, T. Leijtens, and M. D. McGehee, "Understanding Degradation Mechanisms and Improving Stability of Perovskite Photovoltaics," *Chemical Reviews*, vol. 119, no. 5, pp. 3418–3451, 2019.

[47] A. Dualeh, T. Moehl, N. Tétreault, J. Teuscher, P. Gao, M. K. Nazeeruddin, and M. Grätzel, "Impedance spectroscopic analysis of lead iodide perovskite-sensitized solid-state solar cells," *ACS Nano*, vol. 8, no. 1, pp. 362–373, 2014.

[48] H. J. Snaith, A. Abate, J. M. Ball, G. E. Eperon, T. Leijtens, N. K. Noel, S. D. Stranks, J. T.-W. Wang, K. Wojciechowski, and W. Zhang, "Anomalous Hysteresis in Perovskite Solar Cells," *The Journal of Physical Chemistry Letters*, vol. 5, no. 9, pp. 1511–1515, 2014.

[49] E. L. Unger, E. T. Hoke, C. D. Bailie, W. H. Nguyen, A. R. Bowring, T. Heumüller, M. G. Christoforo, and M. D. McGehee, "Hysteresis and transient behavior in current–voltage measurements of hybrid-perovskite absorber solar cells," *Energy & Environmental Science*, vol. 7, no. 11, pp. 3690–3698, 2014.

[50] S. N. Habisreutinger, N. K. Noel, and H. J. Snaith, "Hysteresis Index: A Figure without Merit for Quantifying Hysteresis in Perovskite Solar Cells," *ACS Energy Letters*, vol. 3, no. 10, pp. 2472–2476, 2018.

[51] W. Tress, "Metal Halide Perovskites as Mixed Electronic–Ionic Conductors: Challenges and Opportunities—From Hysteresis to Memristivity," *The Journal of Physical Chemistry Letters*, vol. 8, no. 13, pp. 3106–3114, 2017.

[52] P. Liu, W. Wang, S. Liu, H. Yang, and Z. Shao, "Fundamental Understanding of Photocurrent Hysteresis in Perovskite Solar Cells," *Advanced Energy Materials*, vol. 9, no. 13, p. 1803017, 2019.

[53] Y. Shao, Z. Xiao, C. Bi, Y. Yuan, and J. Huang, "Origin and elimination of photocurrent hysteresis by fullerene passivation in $CH_3NH_3PbI_3$ planar heterojunction solar cells," *Nature Communications*, vol. 5, p. 5784, 2014.

[54] L. Kegelmann, C. M. Wolff, C. Awino, F. Lang, E. L. Unger, L. Korte, T. Dittrich, D. Neher, B. Rech, and S. Albrecht, "It Takes Two to Tango—Double-Layer Selective Contacts in Perovskite Solar Cells for Improved Device Performance and Reduced Hysteresis," *ACS Applied Materials & Interfaces*, vol. 9, no. 20, pp. 17245–17255, 2017.

[55] "Perovskite world record | Oxford PV." https://www.oxfordpv.com/news/oxford-pv-perovskite-solar-cell-achieves-28-efficiency. [Online; accessed Sep. 2019].

[56] D. Zhao, C. Wang, Z. Song, Y. Yu, C. Chen, X. Zhao, K. Zhu, and Y. Yan, "Four-Terminal All-Perovskite Tandem Solar Cells Achieving Power Conversion Efficiencies Exceeding 23%," *ACS Energy Letters*, vol. 3, no. 2, pp. 305–306, 2018.

[57] M. Morales-Masis, S. D. Wolf, R. Woods-Robinson, J. W. Ager, and C. Ballif, "Transparent Electrodes for Efficient Optoelectronics," *Advanced Electronic Materials*, vol. 3, no. 5, p. 1600529, 2017.

[58] H. J. Gläser, *Dünnfilmtechnologie auf Flachglas*. Schorndorf: Hofmann, 1999.

[59] S. Calnan and A. N. Tiwari, "High mobility transparent conducting oxides for thin film solar cells," *Thin Solid Films*, vol. 518, no. 7, pp. 1839–1849, 2010.

[60] K. L. Chopra, S. Major, and D. K. Pandya, "Transparent conductors—A status review," *Thin Solid Films*, vol. 102, no. 1, pp. 1–46, 1983.

[61] Y. S. Jung, J. Y. Seo, D. W. Lee, and D. Y. Jeon, "Influence of DC magnetron sputtering parameters on the properties of amorphous indium zinc oxide thin film," *Thin Solid Films*, vol. 445, no. 1, pp. 63–71, 2003.

[62] M. Morales-Masis, S. Martin De Nicolas, J. Holovsky, S. De Wolf, and C. Ballif, "Low-Temperature High-Mobility Amorphous IZO for Silicon Heterojunction Solar Cells," *IEEE Journal of Photovoltaics*, vol. 5, no. 5, pp. 1340–1347, 2015.

[63] R. Martins, P. Barquinha, A. Pimentel, L. Pereira, and E. Fortunato, "Transport in high mobility amorphous wide band gap indium zinc oxide films," *physica status solidi (a)*, vol. 202, no. 9, pp. R95–R97, 2005.

[64] A. J. Leenheer, J. D. Perkins, M. F. A. M. van Hest, J. J. Berry, R. P. O'Hayre, and D. S. Ginley, "General mobility and carrier concentration relationship in transparent amorphous indium zinc oxide films," *Physical Review B*, vol. 77, no. 11, 2008.

[65] S. Li, Z. Shi, Z. Tang, and X. Li, "Comparison of ITO, In_2O_3:Zn and In_2O_3:H transparent conductive oxides as front electrodes for silicon heterojunction solar cell applications," *Vacuum*, vol. 145, pp. 262–267, 2017.

[66] R. Muydinov, A. Steigert, M. Wollgarten, P. P. Michałowski, U. Bloeck, A. Pflug, D. Erfurt, R. Klenk, S. Körner, I. Lauermann, and B. Szyszka, "Crystallisation Phenomena of In_2O_3:H Films," *Materials*, vol. 12, no. 2, p. 266, 2019.

[67] T. Jäger, Y. E. Romanyuk, S. Nishiwaki, B. Bissig, F. Pianezzi, P. Fuchs, C. Gretener, M. Döbeli, and A. N. Tiwari, "Hydrogenated indium oxide window layers for high-efficiency Cu(In,Ga)Se$_2$ solar cells," *Journal of Applied Physics*, vol. 117, no. 20, p. 205301, 2015.

[68] M. Boccard, N. Rodkey, and Z. C. Holman, "Properties of hydrogenated indium oxide prepared by reactive sputtering with hydrogen gas," in *2016 IEEE 43rd Photovoltaic Specialists Conference (PVSC)*, pp. 2868–2870, 2016.

[69] M. Boccard, N. Rodkey, and Z. C. Holman, "High-mobility Hydrogenated Indium Oxide without Introducing Water During Sputtering," *Energy Procedia*, vol. 92, pp. 297–303, 2016.

[70] G. C. E. Jost, A. N. Hamri, F. Köhler, and J. Hüpkes, "Reliability aspects of hydrogen-doped indium oxide," *physica status solidi (a)*, vol. 213, no. 7, pp. 1751–1759, 2016.

[71] T. A. Jäger, *Transparent Conductive Oxides by Magnetron Sputtering for Solar Energy Applications*. PhD thesis, ETH Zurich, 2015.

[72] K. V. Wasa and S. V. Hayakawa, eds., *Handbook of sputter deposition technology : principles, technology and applications*. Materials science and process technology series, Park Ridge, NJ: Noyes, 1992.

[73] H. Fujiwara and S. Fujimoto, "Transparent Conductive Oxide Materials," in *Spectroscopic Ellipsometry for Photovoltaics: Volume 1: Fundamental Principles and Solar Cell Characterization* (H. Fujiwara and R. W. Collins, eds.), Springer Series in Optical Sciences, pp. 523–563, Cham: Springer International Publishing, 2018.

[74] M. G. Moharam, D. A. Pommet, E. B. Grann, and T. K. Gaylord, "Stable implementation of the rigorous coupled-wave analysis for surface-relief gratings: Enhanced transmittance matrix approach," *Journal of the Optical Society of America A*, vol. 12, no. 5, pp. 1077–1086, 1995.

[75] O. E. Gawhary, M. C. Dheur, S. F. Pereira, and J. J. M. Braat, "Extension of the classical Fabry–Perot formula to 1D multilayered structures," *Applied Physics B*, vol. 111, no. 4, pp. 637–645, 2013.

[76] H. Fujiwara, A. Nakane, D. Murata, H. Tampo, T. Matsui, and H. Shibata, "Analysis of Optical and Recombination Losses in Solar Cells," in *Spectroscopic Ellipsometry for Photovoltaics* (H. Fujiwara and R. W. Collins, eds.), vol. 214, pp. 29–82, Cham: Springer International Publishing, 2018.

[77] B. E. V. Warren, ed., *X-ray diffraction*. Dover books on physics, New York: Dover, 1990.

[78] P. Scherrer, "Bestimmung der Größe und der inneren Struktur von Kolloidteilchen mittels Röntgenstrahlen," *Nachrichten von der Gesellschaft der Wissenschaften zu Göttingen, Mathematisch-Physikalische Klasse*, vol. 1918, pp. 98–100, 1918.

[79] M. V. Birkholz, ed., *Thin film analysis by x-ray scattering*. Weinheim: Wiley-VCH, 2006.

[80] M. F. Toney and S. Brennan, "Observation of the effect of refraction on x-rays diffracted in a grazing-incidence asymmetric Bragg geometry," *Physical Review B*, vol. 39, no. 11, pp. 7963–7966, 1989.

[81] G. H. Bogush, M. A. Tracy, and C. F. Zukoski, "Preparation of monodisperse silica particles: Control of size and mass fraction," *Journal of Non-Crystalline Solids*, vol. 104, no. 1, pp. 95–106, 1988.

[82] D.-C. Tsai, Z.-C. Chang, B.-H. Kuo, Y.-H. Wang, E.-C. Chen, and F.-S. Shieu, "Thickness dependence of the structural, electrical, and optical properties of amorphous indium zinc oxide thin films," *Journal of Alloys and Compounds*, vol. 743, pp. 603–609, 2018.

[83] A. Mosbah and M. S. Aida, "Influence of deposition temperature on structural, optical and electrical properties of sputtered Al doped ZnO thin films," *Journal of Alloys and Compounds*, vol. 515, pp. 149–153, 2012.

[84] J. Tauc, R. Grigorovici, and A. Vancu, "Optical Properties and Electronic Structure of Amorphous Germanium," *physica status solidi (b)*, vol. 15, no. 2, pp. 627–637, 1966.

[85] E. Lotter, "Diplot." http://www.diplot.de/. [Online; accessed May 2019].

[86] I. Miccoli, F. Edler, H. Pfnür, and C. Tegenkamp, "The 100th anniversary of the four-point probe technique: The role of probe geometries in isotropic and anisotropic systems," *Journal of Physics: Condensed Matter*, vol. 27, no. 22, p. 223201, 2015.

[87] D. K. Schroder, "Carrier and Doping Density," in *Semiconductor Material and Device Characterization*, IEEE, 2006.

[88] C. A. Schneider, W. S. Rasband, and K. W. Eliceiri, "NIH Image to ImageJ: 25 years of image analysis," *Nature Methods*, vol. 9, pp. 671–675, 2012. 18783.

[89] M. Brugnara, "Static contact angle analyzer." https://imagej.nih.gov/ij/plugins/contact-angle.html, 2006. [Online; accessed Sep 2018].

[90] A. Nakane, H. Tampo, M. Tamakoshi, S. Fujimoto, K. M. Kim, S. Kim, H. Shibata, S. Niki, and H. Fujiwara, "Quantitative determination of optical and recombination losses in thin-film photovoltaic devices based on external quantum efficiency analysis," *Journal of Applied Physics*, vol. 120, no. 6, p. 064505, 2016.

[91] H. Fujiwara and M. Kondo, "Effects of carrier concentration on the dielectric function of ZnO:Ga and In$_2$O$_3$:Sn studied by spectroscopic ellipsometry: Analysis of free-carrier and band-edge absorption," *Physical Review B*, vol. 71, no. 7, p. 075109, 2005.

[92] M. Shirayama, H. Kadowaki, T. Miyadera, T. Sugita, M. Tamakoshi, M. Kato, T. Fujiseki, D. Murata, S. Hara, T. N. Murakami, S. Fujimoto, M. Chikamatsu, and H. Fujiwara, "Optical Transitions in Hybrid Perovskite Solar Cells: Ellipsometry, Density Functional Theory, and Quantum Efficiency Analyses for CH$_3$NH$_3$PbI$_3$," *Physical Review Applied*, vol. 5, no. 1, p. 014012, 2016.

[93] P. E. Ciddor, "Refractive index of air: New equations for the visible and near infrared," *Applied Optics*, vol. 35, no. 9, pp. 1566–1573, 1996.

[94] S. Minoura, T. Maekawa, K. Kodera, A. Nakane, S. Niki, and H. Fujiwara, "Optical constants of Cu(In, Ga)Se$_2$ for arbitrary Cu and Ga compositions," *Journal of Applied Physics*, vol. 117, no. 19, p. 195703, 2015.

[95] M. Richter, C. Schubbert, P. Eraerds, I. Riedel, J. Keller, J. Parisi, T. Dalibor, and A. Avellán-Hampe, "Optical characterization and modeling of Cu(In,Ga)(Se,S)$_2$ solar cells with spectroscopic ellipsometry and coherent numerical simulation," *Thin Solid Films*, vol. 535, pp. 331–335, 2013.

[96] T. Hara, T. Maekawa, S. Minoura, Y. Sago, S. Niki, and H. Fujiwara, "Quantitative Assessment of Optical Gain and Loss in Submicron-Textured CuIn$_{1-x}$Ga$_x$Se$_2$ Solar Cells Fabricated by Three-Stage Coevaporation," *Physical Review Applied*, vol. 2, no. 3, p. 034012, 2014.

[97] J. P. C. Baena, L. Steier, W. Tress, M. Saliba, S. Neutzner, T. Matsui, F. Giordano, T. J. Jacobsson, A. R. S. Kandada, S. M. Zakeeruddin, A. Petrozza, A. Abate, M. K. Nazeeruddin, M. Grätzel, and A. Hagfeldt, "Highly efficient planar perovskite solar cells through band alignment engineering," *Energy & Environmental Science*, vol. 8, no. 10, pp. 2928–2934, 2015.

[98] M. F. Aygüler, A. G. Hufnagel, P. Rieder, M. Wussler, W. Jaegermann, T. Bein, V. Dyakonov, M. L. Petrus, A. Baumann, and P. Docampo, "Influence of Fermi Level Alignment with Tin Oxide on the Hysteresis of Perovskite Solar Cells," *ACS Applied Materials & Interfaces*, vol. 10, no. 14, pp. 11414–11419, 2018.

[99] K. Wojciechowski, S. D. Stranks, A. Abate, G. Sadoughi, A. Sadhanala, N. Kopidakis, G. Rumbles, C.-Z. Li, R. H. Friend, A. K.-Y. Jen, and H. J. Snaith, "Heterojunction Modification for Highly Efficient Organic–Inorganic Perovskite Solar Cells," *ACS Nano*, vol. 8, no. 12, pp. 12701–12709, 2014.

[100] Young Thomas, "III. An essay on the cohesion of fluids," *Philosophical Transactions of the Royal Society of London*, vol. 95, pp. 65–87, 1805.

[101] A. M. Munshi, V. N. Singh, M. Kumar, and J. P. Singh, "Effect of nanoparticle size on sessile droplet contact angle," *Journal of Applied Physics*, vol. 103, no. 8, p. 084315, 2008.

[102] C. Ishino and K. Okumura, "Wetting transitions on textured hydrophilic surfaces," *The European Physical Journal E*, vol. 25, no. 4, pp. 415–424, 2008.

[103] A. Marmur, "Wetting on Hydrophobic Rough Surfaces: To Be Heterogeneous or Not To Be?," *Langmuir*, vol. 19, no. 20, pp. 8343–8348, 2003.

[104] L. Torrisi and C. Scolaro, "Nanoparticles Improving the Wetting Ability of Biological Liquids," *Journal of Thermodynamics & Catalysis*, vol. 8, no. 2, pp. 1–6, 2017.

[105] J. Haapanen, M. Aromaa, H. Teisala, M. Tuominen, M. Stepien, J. Saarinen, M. Heikkilä, M. Toivakka, J. Kuusipalo, and J. Mäkelä, "Binary TiO_2/SiO_2 nanoparticle coating for controlling the wetting properties of paperboard," *Materials Chemistry and Physics*, vol. 149-150, pp. 230–237, 2015.

[106] S. Vafaei, T. Borca-Tasciuc, M. Z. Podowski, A. Purkayastha, G. Ramanath, and P. M. Ajayan, "Effect of nanoparticles on sessile droplet contact angle," *Nanotechnology*, vol. 17, no. 10, pp. 2523–2527, 2006.

[107] W. Qiu, T. Merckx, M. Jaysankar, C. M. de la Huerta, L. Rakocevic, W. Zhang, U. W. Paetzold, R. Gehlhaar, L. Froyen, J. Poortmans, D. Cheyns, H. J. Snaith, and P. Heremans, "Pinhole-free perovskite films for efficient solar modules," *Energy & Environmental Science*, vol. 9, no. 2, pp. 484–489, 2016.

[108] R. Saive, "S-Shaped Current–Voltage Characteristics in Solar Cells: A Review," *IEEE Journal of Photovoltaics*, pp. 1–8, 2019.

[109] J. Xu, A. Buin, A. H. Ip, W. Li, O. Voznyy, R. Comin, M. Yuan, S. Jeon, Z. Ning, J. J. McDowell, P. Kanjanaboos, J.-P. Sun, X. Lan, L. N. Quan, D. H. Kim, I. G. Hill, P. Maksymovych, and E. H. Sargent, "Perovskite–fullerene hybrid materials suppress hysteresis in planar diodes," *Nature Communications*, vol. 6, no. 1, 2015.

[110] T. Helder, *Development of Transparent Conductive Oxides for Semitransparent Perovskite Solar Cells in Tandem Applications*. Masterthesis, Universität Stuttgart, Stuttgart, 2019.

[111] J.-H. Lee, S.-Y. Lee, and B.-O. Park, "Fabrication and characteristics of transparent conducting In_2O_3–ZnO thin films by ultrasonic spray pyrolysis," *Materials Science and Engineering: B*, vol. 127, no. 2, pp. 267–271, 2006.

[112] R. Muydinov, A. Steigert, M. Wollgarten, P. P. Michałowski, U. Bloeck, A. Pflug, D. Erfurt, R. Klenk, S. Körner, I. Lauermann, and B. Szyszka, "Crystallisation Phenomena of In_2O_3:H Films," *Materials*, vol. 12, no. 2, p. 266, 2019.

[113] N. Nadaud, N. Lequeux, M. Nanot, J. Jové, and T. Roisnel, "Structural Studies of Tin-Doped Indium Oxide (ITO) and $In_4Sn_3O_{12}$," *Journal of Solid State Chemistry*, vol. 135, no. 1, pp. 140–148, 1998.

[114] S. Limpijumnong, P. Reunchan, A. Janotti, and C. G. Van de Walle, "Hydrogen doping in indium oxide: An *ab initio* study," *Physical Review B*, vol. 80, no. 19, 2009.

[115] T. Koida, H. Shibata, M. Kondo, K. Tsutsumi, A. Sakaguchi, M. Suzuki, and H. Fujiwara, "Correlation between oxygen stoichiometry, structure, and opto-electrical properties in amorphous In_2O_3:H films," *Journal of Applied Physics*, vol. 111, no. 6, p. 063721, 2012.

[116] S. Husein, M. Stuckelberger, B. West, L. Ding, F. Dauzou, M. Morales-Masis, M. Duchamp, Z. Holman, and M. I. Bertoni, "Carrier scattering mechanisms limiting mobility in hydrogen-doped indium oxide," *Journal of Applied Physics*, vol. 123, no. 24, p. 245102, 2018.

[117] T. Schoonjans, A. Brunetti, B. Golosio, M. Sanchez del Rio, V. A. Solé, C. Ferrero, and L. Vincze, "The xraylib library for X-ray–matter interactions. Recent developments," *Spectrochimica Acta Part B: Atomic Spectroscopy*, vol. 66, no. 11, pp. 776–784, 2011.

[118] S. Ray, R. Banerjee, N. Basu, A. K. Batabyal, and A. K. Barua, "Properties of tin doped indium oxide thin films prepared by magnetron sputtering," *Journal of Applied Physics*, vol. 54, no. 6, pp. 3497–3501, 1983.

[119] A. E. Rakhshani, Y. Makdisi, and H. A. Ramazaniyan, "Electronic and optical properties of fluorine-doped tin oxide films," *Journal of Applied Physics*, vol. 83, no. 2, pp. 1049–1057, 1998.

[120] H.-G. Wagemann and H. Eschrich, *Photovoltaik*. Wiesbaden: Vieweg + Teubner, 2010.

[121] M. Powalla, P. Jackson, W. Witte, D. Hariskos, S. Paetel, C. Tschamber, and W. Wischmann, "High-efficiency $Cu(In,Ga)Se_2$ cells and modules," *Solar Energy Materials and Solar Cells*, vol. 119, pp. 51–58, 2013.

[122] W. Witte, D. Abou-Ras, K. Albe, G. H. Bauer, F. Bertram, C. Boit, R. Brüggemann, J. Christen, J. Dietrich, A. Eicke, D. Hariskos, M. Maiberg, R. Mainz, M. Meessen, M. Müller, O. Neumann, T. Orgis, S. Paetel, J. Pohl, H. Rodriguez-Alvarez, R. Scheer, H.-W. Schock, T. Unold, A. Weber, and M. Powalla, "Gallium gradients in $Cu(In,Ga)Se_2$ thin-film solar cells," *Progress in Photovoltaics: Research and Applications*, vol. 23, no. 6, pp. 717–733, 2015.

[123] H. Helmers, C. Karcher, and A. W. Bett, "Bandgap determination based on electrical quantum efficiency," *Applied Physics Letters*, vol. 103, no. 3, p. 032108, 2013.

[124] J. D. Dow and D. Redfield, "Toward a Unified Theory of Urbach's Rule and Exponential Absorption Edges," *Physical Review B*, vol. 5, no. 2, pp. 594–610, 1972.

[125] M. V. Kurik, "Urbach rule," *physica status solidi (a)*, vol. 8, no. 1, pp. 9–45, 1971.

[126] F. Urbach, "The Long-Wavelength Edge of Photographic Sensitivity and of the Electronic Absorption of Solids," *Physical Review*, vol. 92, no. 5, pp. 1324–1324, 1953.

[127] J. Tauc, "Optical properties and electronic structure of amorphous Ge and Si," *Materials Research Bulletin*, vol. 3, no. 1, pp. 37–46, 1968.

[128] E. J. Johnson, "Absorption near the Fundamental Edge," in *Semiconductors and Semimetals*, vol. 3, pp. 154–253, Academic Press, 1967.

[129] B. D. Viezbicke, S. Patel, B. E. Davis, and D. P. Birnie, "Evaluation of the Tauc method for optical absorption edge determination: ZnO thin films as a model system: Tauc method for optical absorption edge determination," *physica status solidi (b)*, vol. 252, no. 8, pp. 1700–1710, 2015.

[130] S. S. Hegedus and W. N. Shafarman, "Thin-film solar cells: Device measurements and analysis," *Progress in Photovoltaics: Research and Applications*, vol. 12, no. 23, pp. 155–176, 2004.

[131] E. I. Batzelis, G. E. Kampitsis, S. A. Papathanassiou, and S. N. Manias, "Direct MPP Calculation in Terms of the Single-Diode PV Model Parameters," *IEEE Transactions on Energy Conversion*, vol. 30, no. 1, pp. 226–236, 2015.

[132] E. I. Batzelis and S. A. Papathanassiou, "A Method for the Analytical Extraction of the Single-Diode PV Model Parameters," *IEEE Transactions on Sustainable Energy*, vol. 7, no. 2, pp. 504–512, 2016.

[133] T. Koida, "Amorphous and crystalline In_2O_3-based transparent conducting films for photovoltaics," *physica status solidi (a)*, vol. 214, no. 2, p. 1600464, 2017.

[134] H. Fujiwara and M. Kondo, "Effects of carrier concentration on the dielectric function of ZnO:Ga and In_2O_3 : Sn studied by spectroscopic ellipsometry: Analysis of free-carrier and band-edge absorption," *Physical Review B*, vol. 71, no. 7, p. 075109, 2005.

[135] R. Martins, P. Almeida, P. Barquinha, L. Pereira, A. Pimentel, I. Ferreira, and E. Fortunato, "Electron transport and optical characteristics in amorphous indium zinc oxide films," *Journal of non-crystalline solids*, vol. 352, no. 9-20, pp. 1471–1474, 2006.

[136] L. Lajaunie, F. Boucher, R. Dessapt, and P. Moreau, "Strong anisotropic influence of local-field effects on the dielectric response of $alpha$-MoO_3," *Physical Review B*, vol. 88, no. 11, p. 115141, 2013.

[137] L. Gao, F. Lemarchand, and M. Lequime, "Refractive index determination of SiO_2 layer in the UV/Vis/NIR range: spectrophotometric reverse engineering on single and bi-layer designs," *Journal of the European Optical Society - Rapid publications*, vol. 8, no. 0, 2013.

[138] R. Menner, S. Paetel, W. Wischmann, and M. Powalla, "Indium zinc oxide window layer for high-efficiency Cu(In,Ga)Se$_2$ solar cells," *Thin Solid Films*, vol. 634, pp. 160–164, 2017.

[139] M. Jaysankar, M. Filipič, B. Zielinski, R. Schmager, W. Song, W. Qiu, U. W. Paetzold, T. Aernouts, M. Debucquoy, R. Gehlhaar, and J. Poortmans, "Perovskite–silicon tandem solar modules with optimised light harvesting," *Energy & Environmental Science*, vol. 11, no. 6, pp. 1489–1498, 2018.

[140] S. Goldsmith, E. Çetinörgü, and R. L. Boxman, "Modeling the optical properties of tin oxide thin films," *Thin Solid Films*, vol. 517, no. 17, pp. 5146–5150, 2009.

Author's Publications

Journal Papers

[141] Fabian Ruf, Alice Magin, Moritz Schultes, Erik Ahlswede, Heinz Kalt, and Michael Hetterich. Excitonic Nature of Optical Transitions in Electroabsorption Spectra of Perovskite Solar Cells. *Applied Physics Letters*, 112(8):083902, February 2018.

[142] Moritz Schultes, Nadja Giesbrecht, Johannes Küffner, Erik Ahlswede, Pablo Docampo, Thomas Bein, and Michael Powalla. Universal Nanoparticle Wetting Agent for Upscaling Perovskite Solar Cells. *ACS Applied Materials & Interfaces*, 11(13):12948–12957, April 2019.

[143] Moritz Schultes, Tim Helder, Erik Ahlswede, Meltem F. Aygüler, Philip Jackson, Stefan Paetel, Jonas A. Schwenzer, Ihteaz M. Hossain, Ulrich W. Paetzold, and Michael Powalla. Sputtered Transparent Electrodes (IO:H and IZO) with Low Parasitic Near-Infrared Absorption for Perovskite–Cu(In,Ga)Se$_2$ Tandem Solar Cells. *ACS Applied Energy Materials*, 2(11):7823–7831, 2019.

[144] Tina Wahl, Jonas Hanisch, Sven Meier, Moritz Schultes, and Erik Ahlswede. Sputtered Indium Zinc Oxide Rear Electrodes for Inverted Semitransparent Perovskite Solar Cells without Using a Protective Buffer Layer. *Organic Electronics*, 54:48–53, March 2018.

Conference Contributions

[145] Fabian Ruf, Alice Magin, Moritz Schultes, Meltem F. Ayguler, Pablo Docampo, Erik Ahlswede, Heinz Kalt, and Michael Hetterich. Temperature-Dependent Electromodulation Spectroscopy of Excitons in Perovskite Solar Cells. In *2018 IEEE 7th World Conference on Photovoltaic Energy Conversion (WCPEC) (A Joint Conference of 45th IEEE PVSC, 28th PVSEC & 34th EU PVSEC)*, pages 1550–1554, Waikoloa Village, HI, June 2018. IEEE.

[146] Moritz Schultes. Large Area Perovskite Deposition Enabled by Nanoparticle Adhesion Promoters. In *35th European Photovoltaic Solar Energy Conference and Exhibition (EU PVSEC)*, Brussels, September 2018. Oral Presentation.

[147] Moritz Schultes. Minimizing Parasitic Near Infrared Absorption in Perovskite-CIGS Tandem Solar Cells. In *5th International Conference on Perovskite Solar Cells an Optoelectronics (PSCO)*, Lausanne, 2019. Oral Presentation.

[148] Moritz Schultes, Erik Ahlswede, Jonas Hanisch, Tina Wahl, Sven Meier, Daniela Müller, Philip Jackson, Stefan Paetel, Richard Menner, Wiltraud Wischmann, and Michael Powalla. Status of CIGS-Perovskite Stacked Tandem Solar Cells. In *PSCO*, Oxford, 2017. Poster Presentation.